THE EFFECTS OF CLOUD-TOP PROCESSES ON CONVECTION IN THE CLOUD-TOPPED BOUNDARY LAYER

by Qingqiu Shao

David A. Randall, Principal Investigator

Colorado State University

DEPARTMENT OF ATMOSPHERIC SCIENCE

PAPER NO. 573

THE EFFECTS OF CLOUD-TOP PROCESSES ON CONVECTION IN THE CLOUD-TOPPED BOUNDARY LAYER

by

Qingqiu Shao

Research supported by the
National Aeronautics and Space Administration
under Grants NAG1-893 and NAG1-1137
and the
Office of Naval Research
under Contract N00014-89-J-1364

Department of Atmospheric Science
Colorado State University
Fort Collins, CO

Spring 1994

Atmospheric Science Paper No. 573

ABSTRACT

The Effects of Cloud-Top Processes on Convection in the Cloud-Topped Boundary Layer

Cloud-top processes studies in this paper include cloud-top radiative cooling and entrainment (entrainment mixing warming and evaporative cooling due to the mixing). We have studied how they drive and/or regulate convection in the stratocumulus-topped boundary layer (STBL) analytically, numerically, and through analysis of observational data and data from large-eddy simulations (LES).

An analytical second-order bulk boundary-layer model has been built in an attempt to parameterize the planetary boundary layer (PBL) for large-scale models, as well as to understand the complex physics of entrainment in a relatively simple framework. Cloud-top processes are parameterized in terms of "bulk" properties, and are related to the convection inside the PBL by the matching conditions developed. The model is able to determine the fractional cloudiness, and relaxes the "well mixed" assumption. The vertical structures of the mean state and the turbulent fluxes are determined analytically. Several aspects of this simple model's formulation are evaluated using results from LES.

For the further analysis of cloud-top processes methods which can be used to evaluate the radiative cooling, and entrainment warming of individual parcels are systematically discussed. These methods are applied to study an LES-generated STBL field, as well as a set of tethered balloon data observed during FIRE. By applying these methods to the LES-

generated STBL, some parameters used in the earlier analytical second-order bulk boundary-layer model are further investigated. Moreover, as a case study, the relative importance of radiative cooling and evaporative cooling is investigated based on the LES data.

The effects of cloud-top processes on mesoscale cellular convection (MCC) are studied both analytically and numerically by means of a two-dimensional nonlinear Boussinesq model. It is found that strong cloud-top cooling can generate closed MCC. Nonlinear processes, which are shown as mesoscale advection and interactions between convection and the basic state, are essential for generating and maintaining mesoscale convection. A conceptual model is constructed to suggest a mechanism for the formation of closed MCC. This model appears to be applicable to the atmosphere.

ACKNOWLEDGEMENTS

I wish to express my deep gratitude and sincere appreciation to my advisor, Professor David A. Randall, for all he has done for me in the past few years. His insightful suggestions for my research, his stimulating guidance on my work, and his patient help in improving my English, are not only needed for me to finish this dissertation, but also beneficial to my future career. His constant encouragement, generous understanding, and strong support, especially in the last two years after my son was born, are very impressive and unforgettable.

I also wish to thank my other committee members, Dr. Chin-Hoh Moeng, Professors Roger A. Pielke, Wayne H. Schubert, and Jon A. Peterka, for their efforts and suggestions. I learned a lot from Dr. Chin-Hoh Moeng about scientific writing. Her many suggestions based on her experience are invaluable for my future career. By studying her large-eddy simulation model with her help, I started to build up my experience as a numerical modeler. Discussions with Professor Roger Pielke and taking his classes increased my knowledge of modeling and mesoscale meteorology. Discussions with Professor Wayne Schubert and taking his classes helped me to build up a solid background in atmospheric dynamics. I also enjoyed working with him during ASTEX. Professor Jon Peterka's view of my study of MCC from a different perspective is stimulating.

I wish to extend my thanks to Professor Steven K. Krueger at the University of Utah, for his help and beneficial discussions when I used his model. Although my work related to his model is not discussed in my dissertation, I have enriched my knowledge about numerical modeling by working with him.

I am grateful to Paul F. Hein in our department and to many students and staff in our group, especially Cindy Carrick, Ross Heikes, Kelley Wittmeyer, Donald Dazlich, Dr. Kuanman Xu, and Scott Denning. Paul F. Hein provided the tethered balloon data observed during FIRE. Cindy Carrick edited chapter 2 of my dissertation. I also thank her for arranging my trips, some of which were really troublesome. Ross Heikes provided a friendly environment in our office, and he was ready to provide help for any scientific or trivial questions I had. Kelley Wittmeyer helped me in using computer software. She also provided Fig. 1.2. Donald Dazlich helped me in using computers and software, especially at the very beginning of my study. Dr. Kuanman Xu provided some help in using the CEM. Scott Denning helped me to use some software.

I am indebted to my loved ones, my husband, Dr. Xubin Zeng, and my son, David. Without Xubin's many helpful discussions and constant moral support, I could not have finished my dissertation. David cheered me up every day no matter how tired I felt due to working overtime in the office. I also wish to extend my love to my parents and my parents-in-law, who gave me strong support.

Support for this research was provided by NASA's Climate Program under Grant NAG-1-893, NAG-1-1137, and by the Office of Naval Research under Contract N00014-89-J-1364. Computing resources were provided by the Numerical Aerodynamic

Simulation Facility at NASA/Ames, NCAR's Scientific Computing Division, and the NERSC supercomputers.

TO

My parents
My husband Xubin and my son David

TABLE OF CONTENTS

1.Introduction

1.1 Overview 1

1.2 Observational studies 5

1.2.1 Experiments conducted in STBL 5

1.2.2 Observed STBL driven by cloud-top cooling 10

1.2.3 The observed mean structures and related dynamics in the STBL 11

1.2.4 Observed scales of convection in STBL 14

1.3 Theories concerning the role of cloud-top processes in driving convection 16

1.3.1 Cloud top radiative cooling 16

1.3.2 Cloud-top evaporative cooling 19

1.4 Numerical studies 21

1.5 Topics in this study 23

2. Parameterization of Cloud-Top Processes in a Second-Order Bulk Boundary-Layer Model

2.1 Introduction 26

2.2 Convective Mass Flux Model 28

2.3 Matching the fluxes 39

2.4 The convective mass flux and the turbulence kinetic energy 53

2.5 Interiors 58

2.6 Summary and conclusions 72

3. Plume Generation in the Entrainment Layer by the Cloud-Top Processes

3.1 Introduction 69

3.2 Data and methodology 74

3.2.1 The ventilation layer 80

3.2.2 The entrainment layer 83
3.3 Results 96
3.3.1 Mixing and selection processes in the ventilation layer 96
3.3.2 Mixing and selection processes in the entrainment layer 103
3.3.2.1 LES data 103
3.3.2.1.1 Turbulent mixing 103
3.3.2.1.2 Radiative cooling 107
3.3.2.1.3 Evaporative cooling 111
3.3.2.1.4 Buoyancy 116
3.3.2.1.5 Mixing and selection processes 119
3.3.2.2 Tethered balloon data 120
3.4 Concluding remarks 123

4. Effects of Cloud-top Cooling on Mesoscale Shallow Convection

4.1 Introduction 127
4.2 The model 134
4.2.1 The equations 134
4.2.2 The internal forcing, ... 135
4.3 The weak nonlinear analytical solution to the effect of coolings at the top 140
4.3.1 The nondimensional equations 140
4.3.2 A perturbation method 142
4.3.3 Solution 145
4.3.3.1 Derivation of the prognostic equation for potential temperature at the leading order 145
4.3.3.2 Steady state solution 151
4.3.3.3 The dependence of and on the forcing 153
4.3.4 Discussion 158
4.4 The fully nonlinear numerical solution to the effect of coolings at the top 159
4.4.1 Numerical method 159
4.4.1.1 Poisson equation 160
4.4.1.2 Prognostic equations 164
4.4.1.3 Boundary conditions 165
4.4.2 Parameters 166
4.4.3 Results 166
4.4.3.1 A general description of the steady state results 166
4.4.3.2 Spectral analysis 179
4.4.3.3 Vertical distributions of potential temperature and heat flux 184
4.4.3.4 -budget analysis 199
4.4.4 The sensitivity of the results to horizontal domain size 205

4.4.5 Discussion 208
4.5 Conclusions 212

5. Conclusions and Future Research

5.1 Conclusions 214
5.2 Future research 217
5.2.1 The second-order bulk boundary-layer model 217
5.2.2 MCC 219
5.2.2.1 Upgrading the present model 219
5.2.2.2 Using an existing model 220
5.2.2.3 Developing a 3-D model 220
5.2.3 Other aspects 220

References

Appendices

A. Scalar Variance Budgets For the Ventilation and Entrainment Layers ..243
B. A Method to Predict the Vertically Integrated Turbulence Kinetic Energy 252
C. Motivation for (5.8 - 9) 254
D. Calculation of Thermodynamic Variables From the Tethered Balloon Data 257
E. A numerical method for choosing the boundaries Of the ventilation and entrainment layers 259
F. An example to calculate 263
G. The profile of the filter used to select mesoscale contributions 268

LIST OF TABLES

Table 2.1 Summary of observations and simulations of the fractional area covered by rising motion in several studies. Here < > denotes the expected value. 31

Table 2.2 The LES entrainment mass flux in 10^{-2} kg m^{-2} s^{-1}, as determined by methods HA, HB, QA, QB, and Z. See text for explanation of the methods. 46

Table 2.3 Values of χ_V and χ_E determined from the LES results by various methods. Subscript q indicates that we have used $\psi = h$. In the case of $\chi'_{V,h}$ we have taken into account the weak radiative forcing of the ventilation layer. This slightly reduces the values of $\chi_{V,h}$, bringing them into better overall agreement with those of $\chi_{V,q}$. 49

Table 3.1 The cloudy grid cell numbers (n) and their percentage (%) to the total grid numbers of 6400 at each level in the entrainment layer. 76

Table 3.2 The average mixing fraction (%) and the fraction of the area covered by updrafts at each level in the ventilation layer. 98

Table 3.3 The average χ at each level for cloudy parcels in the entrainment layer....106

Table 4.1 The parameters for the internal and boundary forcings. 139

LIST OF FIGURES

Figure 1.1 Satellite-derived relative low cloud cover in percentage (%) (from Stowe et al., 1989). 3

Figure 1.2 Stratocumulus clouds observed by GOES in July 7, 1987 during FIRE. 4

Figure 1.3 A schematic description of the mean profiles in a STBL with the well-mixed subcloud and cloud layers. The values indicated are intended to give a rough idea what the values of these quantities could be in a STBL. Exact values will change from case to case. 12

Figure 2.1 Diagram illustrating the assumed structure of the PBL. The interior, which is represented by two layers, is bounded above by a thin entrainment layer and below by a thin ventilation layer. Convective circulations occur, with rising branches occupying fractional area σ. The ascending and descending branches have different thermodynamic soundings and, therefore, different cloud base levels. 28

Figure 2.2 The vertical profiles of $\bar{h}$ and $\overline{q_t}$, plotted as functions of height. 34

Figure 2.3 a) The vertical profiles of w_u and w_d obtained by the method described in Section 2.2 (solid curves), and also by directly sampling the LES results (dashed curves). b) The vertical profiles of σ (solid curve) and M_c (dashed curve), plotted as functions of height normalized by the PBL depth. Values are not plotted above the PBL top, since σ and M_c have little meaning there. 36

Figure 2.4 Profiles of ψ_u and ψ_d calculated directly by conditional sampling (based on the sign of the vertical velocity) and from the fluxes using (2.10 - 11). a) for h / c_p; and b) for q_t. The solid lines show the updraft and downdraft properties obtained from (2.10 - 11), and the dashed lines show the corresponding values based on conditional sampling. 38

Figure 2.5 For the LES results, the ratio of the subgrid-scale flux moisture flux to the total flux. The ventilation and entrainment layers are indicated by stippling. 45

Figure 2.6 Vertical profiles of τ_{dis}, as determined from the LES results for dissipation of h (solid line) and q_t (dashed line). 57

Figure 2.7 The variation of $\delta p_M / \delta p_*$ with σ, for the particular case $M_c = 0.4$ kg m^{-2} s^{-1}, $\delta p_M = 50$ mb. The solid line is for $\hat{\tau} = 1$ second, and the dashed line is for $\hat{\tau} = 10$ seconds. 60

Figure 2.8 As in Fig. 2.7, but for the variation of $\partial\overline{\psi}/\partial p$ with σ: a) potential temperature, in units of K (50 mb)$^{-1}$; b) the mixing ratio of water vapor, in units of g kg^{-1} (50 mb)$^{-1}$. 62

Figure 2.9 As in Fig. 2.7, but for the variations of the fluxes of potential temperature and moisture with height, from the surface to the PBL top: a) Potential temperature flux for $\sigma = 0.52$; b) moisture flux for $\sigma = 0.52$; c) potential temperature flux for $\sigma = 0.48$; d) moisture flux for $\sigma = 0.48$. 63

Figure 2.10 Diagram summarizing the relationship of the present model to earlier models used in boundary-layer and cumulus parameterization. 68

Figure 3.1 Diagram illustrating the mean profile of total water content for a convective boundary layer, and identifying the ventilation and entrainment layers. 75

Figure 3.2 The mean structure of dry bulb temperature from the tethered balloon data. Levels B and B+ are indicated. 77

Figure 3.3 The rawinsonde sounding obtained at the same time and place as the tethered balloon sounding of Fig.3.2. 78

Figure 3.4 The pressure at which data was collected. The hatched area indicates the time period for this study. 79

Figure 3.5 The conditionally sampled horizontal means of h (a) and s_v (b) for the updrafts, downdrafts and the total. 88

Figure 3.6 The pdf at each level in the ventilation layer. Level S-4 is closest to the surface. The vertical bar indicates $\overline{\chi}$ at each level. 97

Figure 3.7 The distribution of $\langle s'_v \rangle$, as well as its components for updrafts and downdrafts, with χ at each level in the ventilation layer. 100

Figure 3.8 $\langle w \rangle$ and $\langle s'_v \rangle$ at each level in the ventilation layer. 101

Figure 3.9 $\Pi_E(\chi)$ and its components for updrafts and downdrafts at each level in the entrainment layer. The vertical bar indicates $\overline{\chi}$ at each level, which is also the $\chi' = 0$ line for each level. 104

Figure 3.10 The radiative cooling at each level in entrainment layer for a) total and b)-f) the difference of updrafts and downdrafts from the total. Note the scale difference between different panels. 108

Figure 3.11 As in Fig.3.10 but for evaporative cooling and the amount of liquid water evaporated. 113

Figure 3.12 As in Fig.3.10 but for liquid water content. 114

Figure 3.13 The buoyancy of the total, as well as of the updrafts and downdrafts, at each level in entrainment layer. Note the scale difference between the panels. 117

Figure 3.14 The results from tethered balloon data: a) pdf, b) radiative cooling, c) evaporative cooling, d) liquid water content, and f) buoyancy. 121

Figure 4.1 The change of (a) $F/(da)$, and (b) z_0/d with n, and (c) Q/a with z/d at $n = 5$. 138

Figure 4.2 The internal heating/cooling profiles based on values listed in Table 1. Fluxes from boundaries (c_b and c_t) are not indicated here. Since $F = F_0$ is the same for all cases, the larger the n (or the more asymmetric the profile), the stronger the cooling near the top. 140

Figure 4.3 A schematic illustration of the relation between critical Rayleigh number and wave number obtained from linear theory. The minimum happens at k=0. (Chapman and Proctor, 1980) 142

Figure 4.4 The solution of (a) stream function G and (b) potential temperature F as a function of α. 152

Figure 4.5 The distribution of P(Z) with height. 154

Figure 4.6 The change of R_{ac} and α with n for class (1) on page 29 (solid line) and class (3) on page 31 (dashed line). 157

Figure 4.7 The grid for the 2-D model. 160

Figure 4.8 Cycle C for linear problems. Reproduced from Brandt (1977). Here " $\leftarrow$ " means "substitute." 163

Figure 4.9 The change of domain averaged TKE and enstrophy with time. 167

Figure 4.10 The temperature (K) and stream function (m^2/s) for case 1 (n5). The top and bottom panels for each variable are the value at the 24th hour and 1 hour average value over the 24 hour, respectively. The arrow indicates the cell appeared in the trajectory analysis in section 4.4.3.3. 168

Figure 4.11 Same as in Fig.4.10 except for case 2 (n35). 169

Figure 4.12 Same as in Fig.4.10 except for case 3 (n1). 170

Figure 4.13 Same as in Fig.4.10 except for case 4 (cb). 171

Figure 4.14 Same as in Fig.4.10 except for case 5 (n35cb). 172

Figure 4.15 The horizontal and vertical velocities (m/s) at the end of 24th hour for case 1 (n5). 173

Figure 4.16 As in Fig. 4.15 except for case 2 (n35). 174

Figure 4.17 As in Fig. 4.15 except for case 3 (n1). 175

Figure 4.18 As in Fig. 4.15 except for case 4 (cb). 176

Figure 4.19 As in Fig. 4.15 except for case 5 (n35cb). 177

Figure 4.20 Power spectrum of TKE (% of variance) at the middle level of the layer for each case. Three lines in each panel show the instantaneous results at the end of 22nd, 23rd and 24th hours, respectively. 180

Figure 4.21 The same as in Fig. 4.20 except for enstrophy. 181

Figure 4.22 The distribution of (a) total and (b) mesoscale component of TKE for case 1. 183

Figure 4.23 The vertical distribution of TKE. 184

Figure 4.24 The vertical distribution of horizontally averaged mean potential temperature, as well as that in updrafts and downdrafts. The top and bottom of the stable layers are indicated by the bars. 185

Figure 4.25 Heat fluxes (K m/s) for the five cases. 187
Figure 4.26 A composite structure of temperature (0.1 K) and vertical velocity (m/s) at the mid-level of case 1. 189
Figure 4.27 The potential temperature distribution from case 1. 190
Figure 4.28 Case 1: (a) trajectory and two small cells encircled by the trajectory (indicated by 1 and 2); (b) imposed internal heating/cooling rate $\dot{Q}$; (c) the potential temperature that the parcel would have if only $\dot{Q}$ is considered (solid line), and the potential temperature of the parcel interpolated from its environment (dashed line); and (d) the instantaneous value of $\dot{Q}$ at where the parcel is located. (See footnote on page 192 for more explanation). 191
Figure 4.29 As in Fig. 4.28 but for case 2. 192
Figure 4.30 As in Fig. 4.28 but for case 3. 193
Figure 4.31 As in Fig. 4.28 except for case 4. 194
Figure 4.32 As in Fig. 4.28 except for case 5. 195
Figure 4.33 Soundings observed during ASTEX. 198
Figure 4.34 The horizontally averaged θ-budget (K/s) for each case. 200
Figure 4.35 Total and mesoscale advections for θ-budget. 202
Figure 4.36 Total and mesoscale diffusion for θ-budget. 203
Figure 4.37 The potential temperature distribution for the different domain sizes for case 1. Note the difference of the horizontal scale between different panels. 206
Figure 4.38 The stream function for the different domain sizes for case 1. Note the difference of horizontal scale between different panels. 207
Figure 4.39 A conceptual model for closed MCCs. See discussion in the text. 208
Figure A.1 Plots of χ_V and σ_S against k_V and r_V, as given by (A.13) and (A.15). Panels (a) and (b) are for the choice of the plus sign on the discriminant, and panels (c) and (d) are for the choice of the minus sign. 247
Figure A.2 Plots of χ_E and σ_B against k_E and r_E, as given by (A.21) and (A.22). Panels (a) and (b) are for the choice of the plus sign on the discriminant, and panels (c) and (d) are for the choice of the minus sign. 249
Figure A.3 Plot of σ_B as a function of r_E, or of σ_S, or of both, as a function of r_V. 250
Figure E.1 The pdf at level S and S-. 260
Figure E.2 The pdf at level B and B+. 261
Figure G.1 The profile of the filter used to select the mesoscale contribution. 269

CHAPTER 1

Introduction

1.1 Overview

Low-level clouds (clouds below 2 km above sea level, WMO, 1956) play an important role in the climate system. In terms of the Earth's radiation energy budget, they reflect more solar energy back to space than the sea surface. At the same time, they emit almost the same outgoing infrared radiation as the sea surface, due to their warm cloud-top temperature, which is close to the sea surface temperature (SST). Therefore, low level clouds cool the Earth system (Ramanathan, 1987a, b). Randall et al. (1984) estimated that a 4% increase in the area covered by low-level clouds could offset the global warming induced by a doubling of CO_2. Since the long wave (infrared) radiation strongly cools the cloud top, low-level clouds tend to stabilize the troposphere, and destabilize the planetary boundary layer (PBL). This modification to the atmospheric stratification can affect the vertical transports of moisture and heat, and hence can modify the general circulation. Furthermore, the locally organized convection in a PBL covered by low-level clouds is essential for air-sea exchanges of heat and moisture

(Hanson and Gruber, 1982). Therefore, studying the formation and dissipation of low-level clouds is one of the important tasks in studying climate.

Low-level clouds appear mostly over the oceans, as shown in Fig.1.1 (Stowe et al., 1989). Among low-level clouds, the effects of persistent marine stratocumulus clouds on climate are believed to be most dominant. These persistent marine stratocumulus clouds occupy large portions of the eastern Pacific and eastern Atlantic Oceans. They are most extensive in the Northern Hemisphere summer, when the upward motion in the ITCZ (Inter-Tropical Convection Zone) and the downward motion in the subtropical highs are strongest (Schubert et al., 1979). Fig.1.2 shows an example of persistent stratocumulus cloud pattern off the coast of California, which was observed on 7 July 1987 by GOES satellite during the First ISCCP (International Satellite Cloud Climatology Project) Regional Experiment (FIRE) in the summer of 1987 (Randall et al., 1984; Albrecht et al., 1988). Along the trajectory of the low-level flow in the subtropical high, which is directed from northeast to southwest, the clouds change from stratus to broken stratocumulus to cumulus. The stratocumulus-topped marine boundary layer (STBL) is what we are interested in here. Cloud patterns in the stratocumulus regime show the existence of mesoscale structures.

It was realized decades ago that cloud-top processes, including cloud-top radiative cooling and entrainment (including entrainment mixing warming and evaporative cooling due to the mixing), play important roles in driving convection in the STBL. Among the earlier observational studies (Riehl et al., 1951; James, 1959; Neiburger, 1960; Neiburger et al., 1961), James (1959) analyzed the data collected by aircraft of the

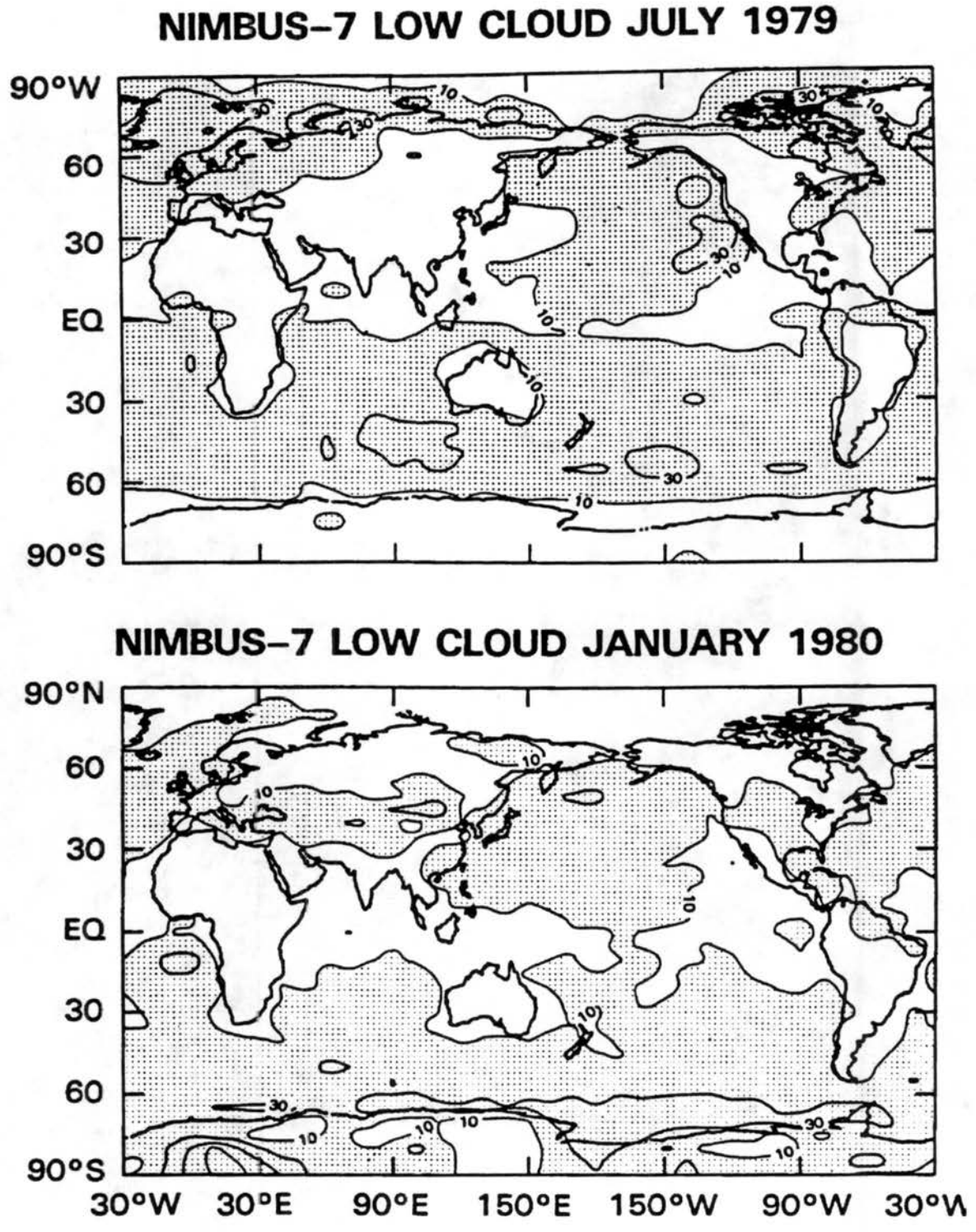

FIGURE 1.1: Satellite-derived relative low cloud cover in percentage (%) (from Stowe et al., 1989).

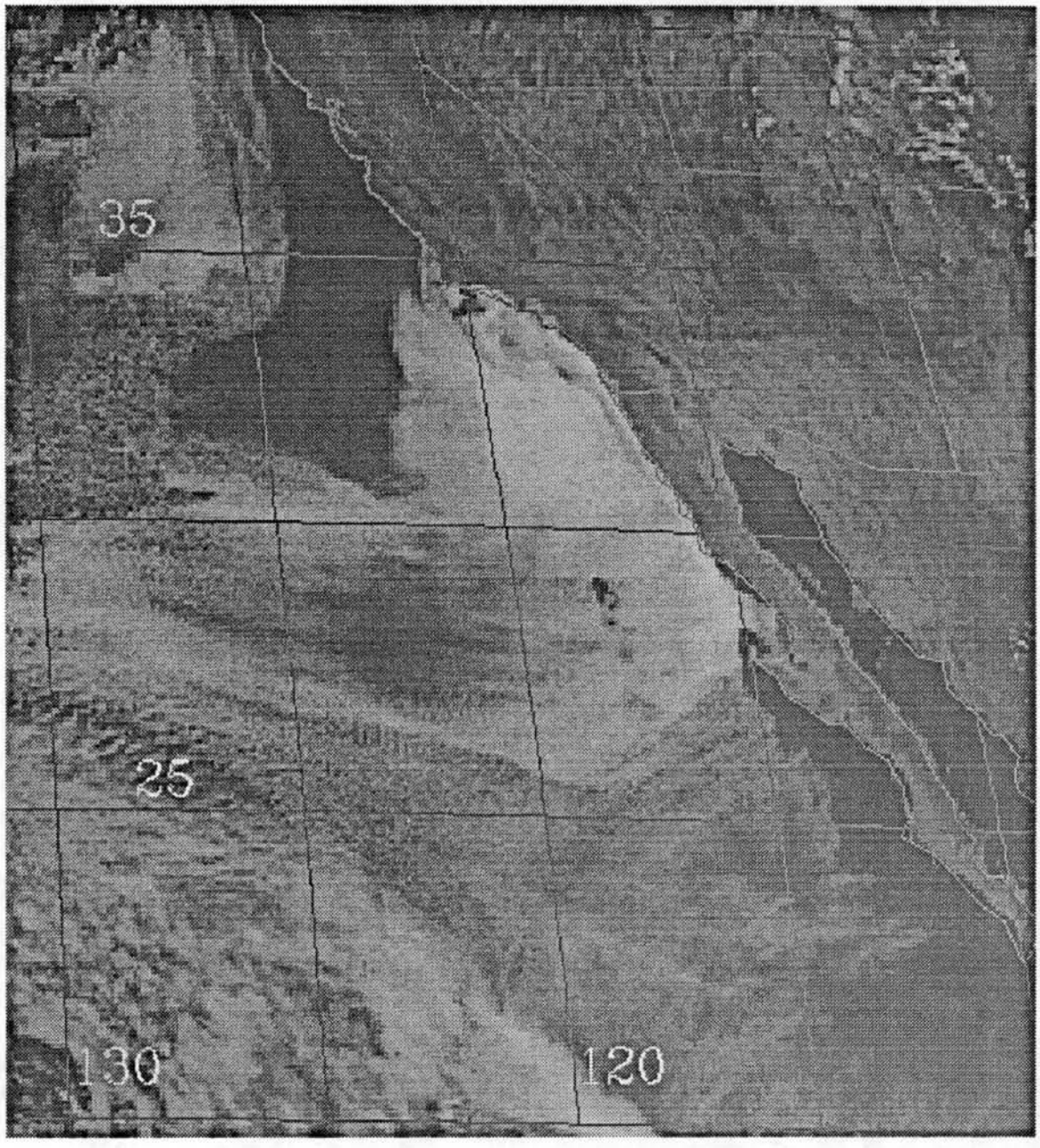

FIGURE 1.2: Stratocumulus clouds observed by GOES in July 7, 1987 during FIRE.

Meteorological Research Flight (MRF) near Farnborough (51°16′N, 00°46′W) in November 1955, and found that a strong inversion and large moisture jump exist directly above the tops of the clouds. He demonstrated that radiative cooling, entrainment and subsidence play important roles in the evolution of the layer cloud. He also attempted to relate the turbulent fluxes at cloud top to the mean profiles.

Following the experimental results and adopting the modeling philosophy of Ball (1960), Lilly (1968) developed a basic theoretical model for a well-mixed STBL, with radiative cooling and entrainment as driving forces. He recognized that radiative cooling occurs near cloud top, and demonstrated that the properties of the STBL are related to the properties in the inversion layer through entrainment. Although the cloud-top processes in his model were idealized due in part to the limitations of the observations, the remarkable insight provided by Lilly's work stimulated a lot of further observational, theoretical and numerical studies on cloud-top processes.

In the following subsection, we review observational studies first, then the theories, and then some numerical studies. All of these are previous studies on convection driven by cloud-top processes. The problems we solve in this study are listed in section 1.5.

1.2 Observational studies

1.2.1 Experiments conducted in STBL

Since Lilly's (1968) stimulating study, experiments in STBL have been emphasizing the observations of the cloud-top processes. The Marine Stratocumulus Experiment,

which was designed based on Lilly's (1968) theoretical STBL model, was conducted off the California coast near San Francisco in June 1976 (Wakefield and Schubert, 1976). The NCAR Electra aircraft measured mean and fluctuating dynamical, thermodynamical and radiative variables in the persistent STBL. The mean structures and turbulent properties based on these data were analyzed by Brost et al. (1982a, b) and Albrecht et al. (1985). Their main findings concerning cloud-top processes, for the cases they studied, are: radiative cooling is mainly located within 40 m of the cloud top. Radiative heat loss is mainly balanced by the shear-driven entrainment so that turbulence driven by the cooling is weak. Convection driven by latent heat release is also weak due to low liquid water content. The vertical velocity variance at cloud top is maintained principally by the pressure-scrambling terms through the redistribution of the shear-produced energy. These findings from observations contradicted some of the assumptions of Lilly (1968), e.g., that radiative cooling is located in the inversion layer and is the main driving force for the turbulence of the well-mixed STBL. Brost et al. (1982a, b) emphasized that nonlinear mesoscale effects could significantly modify the mean structure of the boundary layer.

In the same year, November 1976, comprehensive observations of nocturnal anticyclonic stratocumulus clouds were made with ground-based and balloon-borne equipment at Cardington, Bedford, UK (56°06′N, 0°24′W). Roach et al. (1982) analyzed the mean structure and budgets. Caughey et al. (1982) discussed turbulence structure and related it to cloud-top entrainment. Together with two further case studies (October 1977 and January 1978), Slingo et al. (1982) described detailed radiative and microphysical observations. Based on these data, Caughey and Kitchen (1984) further

examined small-scale variations in the cloud water droplet population and their relationship to the turbulence field. They found that radiative cooling is the primary driving force for downdrafts near cloud top, although it is still partly balanced by the shear-produced entrainment. Entrainment effects at cloud top result primarily in droplet concentration fluctuations, which indicates the existence of local evaporative cooling. The evaporative cooling did not play an essential role in generating downdrafts in the case they studied.

In 1982 and 1983, observations in horizontally extensive, uniform sheets of stratiform cloud over U. K. coastal waters were made by using the MRF C-130 research aircraft. Nicholls (1984), and Nicholls and Leighton (1986) described the mean structure in terms of layer averages, identified the main physical transport processes, and assessed the effects of these processes on the mean structure. In particular, the consequences of the distribution of internal energy sources within the boundary layer, especially those associated with radiation, were emphasized. Nicholls and Turton (1986) discussed the entrainment, as well as the relative importance of radiative cooling and evaporative cooling for the buoyancy of a parcel near cloud top. Nicholls (1989) discussed how downdrafts are driven by radiative cooling, entrainment mixing, and horizontal pressure gradients near cloud top. They found that the cloud layer and subcloud layer were decoupled, rather than well-mixed as often assumed earlier. Radiative cooling and the horizontal pressure gradient worked together to drive downdrafts. When the mixing fraction of dry inversion air due to entrainment was small, radiative cooling dominated over evaporative cooling in downdrafts.

The above observational results suggest several questions: To what extent do cloud-top processes drive convection in the STBL? Does the horizontal pressure gradient, which helps in the generation of downdrafts, result from locally cooled air or from the circulations inside the STBL? If it is from the locally cooled air, its existence is evidence that the cloud-top processes drive convection in the STBL. Another problem, which was missed in the above experimental studies due partly to the limitations of the observational tools, is mesoscale convection. Mesoscale convection is made visible by the mesoscale organization of cloud patches, as shown in Fig. 1.2. Is mesoscale convection also related to cloud-top processes? To answer these questions, a comprehensive field experiment with large horizontal domain as well as detailed observations of vertical structure is required.

FIRE (Randall et al., 1984; Albrecht et al., 1988) was conducted off the coast of California, from 29 June-19 July 1987, to study the extensive fields of stratocumulus clouds that are a persistent feature of subtropical marine boundary layers. A comprehensive set of measurements was obtained by using aircraft, satellite, and surface-based instruments. For the first time, measurements were made on both the regional scale and on the micro-scale, to permit the widest possible interpretation of the mean, turbulent, microphysical, radiative, and chemical characteristics of stratocumulus, as well as the interactions among these quantities that are believed to be important in controlling the structure and evolution of these clouds. Much current research is based on these data. Schubert et al. (1987) listed the sounding profiles of temperature and moisture, and tested the cloud-top entrainment instability (CTEI) criterion (Randall, 1980; Deardorff, 1980) based on the soundings. Cahalan and Snider (1989) did a spectrum analysis of the

cloud brightness observed by satellites. Fairall et al. (1990) used the surface-observed longwave irradiance data to estimate fractional cloudiness, and used the shortwave irradiance to estimate cloud albedo and integrated cloud liquid water content. Betts and Boers (1990) studied the cloudiness transition by using the in situ aircraft and lidar data. Hignett (1991) used tethered balloon data and Blaskovic et al. (1991) used surface observations to study the diurnal variations of the STBL. Based on flight data, Nucciarone and Young (1991) analyzed turbulence spectra and variance dissipation, and Moyer and Young (1991) analyzed the vertical velocity skewness within the STBL. Paluch and Lenschow (1991) studied the formation of stratiform clouds by using aircraft data. Khalsa (1993) and Wang and Albrecht (1993) studied entrainment processes by using flight data. A set of tethered balloon data was analyzed by Shao et al. (1993) to study radiative and evaporative cooling in the entrainment layer.

As a part of the continuing program of FIRE, the Atlantic Stratocumulus Transition Experiment (ASTEX), which I participated in†, was conducted in the region of the eastern Atlantic extending southeast from Santa Maria (37°N, 25°W) in the Azores to Porto Santo (33°N, 16°W), north of Maderia, in June, 1992. ASTEX focused on detailed questions concerning the formation, maintenance, and dissipation of stratocumulus clouds. Only some preliminary results based on this experiment have been published so far (e.g., Bluth and Albrecht, 1993; Bretherton, 1993; Schubert et al., 1992; Cox et al., 1993a, b).

†. I was with the CSU group on Porto Santo during June, 1992, except one week on Santa Maria staying with other groups. I participated in one flight mission while I was on Santa Maria.

The above two experiments provided further evidence that cloud-top processes can drive convection in the STBL. The results of these experiments have shown quantitatively that both mesoscale and small scale convections coexist in the STBL. Below we give detailed discussions of these problems, as well as the observed mean structure of the STBL which is supposed to be determined by the cloud-top processes and other dynamical and microphysical processes found in the STBL, such as solar radiation, drizzling, surface heating, large-scale subsidence, and cloud condensation nuclei (CCN).

1.2.2 Observed STBL driven by cloud-top cooling

The above observational studies have revealed that cloud-top processes can be the dominant dynamical processes in driving convection in the STBL. Through case studies, Nicholls (1989), Khalsa (1993), Wang and Albrecht (1993) and Shao et al. (1993) have shown that cloud-top radiative and evaporative cooling are the primary mechanisms to generate strong narrow downdrafts near cloud top. Whether or not a STBL is driven by cloud-top cooling can be seen from an analysis of the vertical velocity skewness (Moeng and Rotunno, 1990; LeMone, 1990; Moyer and Young, 1991). A positive vertical velocity skewness indicates that strong narrow updrafts are surrounded by broader, weaker downdrafts. Similarly, a negative vertical velocity skewness indicates that strong narrow downdrafts are surrounded by broader, weaker updrafts. Therefore, an STBL with a negative vertical velocity skewness should be driven by cloud-top cooling.

Examples of STBLs with negative vertical velocity skewness throughout the layer were found by Nicholls and Leighton (1986), and Moyer and Young (1991), indicating that a STBL with dynamics dominated by cloud-top cooling is common.

1.2.3 The observed mean structures and related dynamics in the STBL

The observed STBL may not always be well mixed as assumed by Lilly (1968); this differs from case to case. Based on the temperature and moisture soundings, the STBL can be divided into several sublayers (Roach et al., 1982; Nicholls and Leighton, 1986): Surface layer, subcloud layer, cloud layer, and inversion layer. These layers are indicated in Fig.1.3. The vertical structures of certain quantities and their representative values are also shown schematically in Fig.1.3. These quantities are the water vapor mixing ratio (q_v), liquid water mixing ratio (q_l), moist static energy (defined as $h = c_pT + gz + Lq_v$), dry static energy (defined as $s_v = c_pT + gz$), radiative cooling rate (Q_R), and wind speed (u). The total water ($q = q_v + q_l$) and moist static energy (h) are conservative for both moist (without ice) and dry adiabatic processes.

The surface layer can be statically neutral (Brost et al., 1982a; Albrecht et al., 1985), stable (Roach et al., 1982), or unstable (Nicholls and Leighton, 1986). This is mainly determined by the air-sea temperature difference, which could be one or two degrees. An unstable surface layer can provide more heat and moisture to the STBL than a neutral and stable surface layers, and can generate convection from below. Wind shear is generally strong in the surface layer.

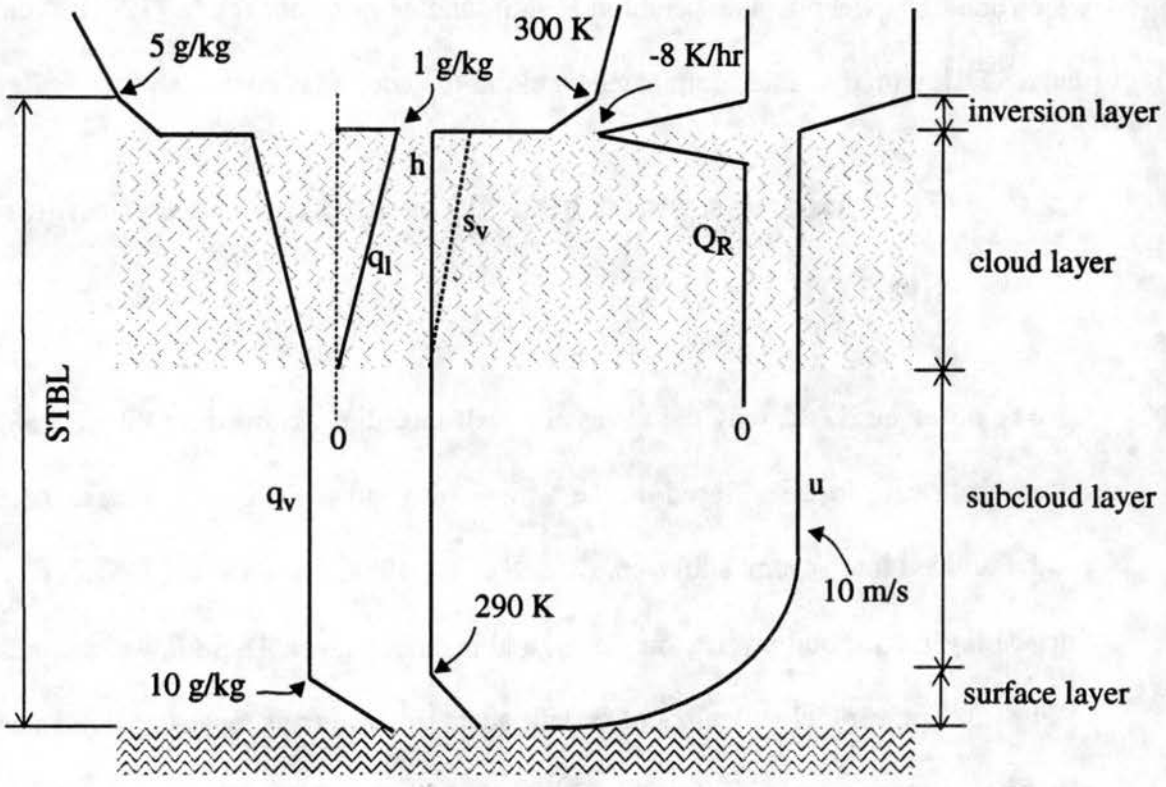

FIGURE 1.3: A schematic description of the mean profiles in a STBL with the well-mixed subcloud and cloud layers. The values indicated are intended to give a rough idea what the values of these quantities could be in a STBL. Exact values will change from case to case.

The properties of the marine surface layer follow a similarity theory like that proposed by Businger et al. (1971), and the surface fluxes are often parameterized by a bulk aerodynamic method (e.g., Kondo, 1975; Liu et al., 1979).

The subcloud layer and cloud layer are each generally well mixed, so that the observed q and h do not change with height (Brost et al., 1982a; Albrecht et al., 1985; Roach et al., 1982; Schubert et al., 1987). Turbulence in these two layers are either generated by surface heating or cloud top cooling. However, a weak inversion is often observed near cloud base (Nicholls and Leighton, 1986; Betts, 1989). Two physical

processes may be responsible for the formation of this inversion: One is the warming above cloud base due to solar absorption, and the other is the cooling of the subcloud layer due to the evaporation of drizzle. The inversion results in the decoupling of the two layers, which can block the upward transport of moisture, as well as downward transport of TKE generated by radiative cooling and entrainment at cloud top. This can result in a breakup of the clouds.

Properties in the cloud layer are closely related to the cloud-top processes, which are in turn related to microphysical properties in clouds. The liquid water content increases with height in the cloud layer, and is generally less than the adiabatic condensation value (Roach et al., 1982; Nicholls, 1989; Slingo et al., 1982). It fluctuates significantly near cloud top, possibly due to entrainment mixing and evaporation (Caughey and Kitchen, 1984), as well as radiative cooling (Curry, 1986), as discussed below. Radiative cooling is directly related to the opacity of the cloud liquid water, as well as indirectly related to CCN through the cloud droplet distribution. It is strongest near cloud top, extends weakly above the cloud. The extinction length for the cooling inside clouds is a few tens of meters (Slingo et al., 1982; Brost et al., 1982; Curry, 1986). The net effects of the cloud-top processes can be strong enough to drive convection in the whole STBL, as discussed in section 2.2.

A very dry and strong inversion generally caps the STBL. The strength of the inversion determines the relative importance of entrainment warming and evaporative cooling. The jumps of moisture and potential temperature are generally about -5 g kg^{-1} and 10 K across the inversion, respectively. According to Lilly (1968), this inversion is

maintained by the subsidence of the air in the troposphere, as well as radiative cooling near cloud top. A moist layer above the inversion, or q-reversal, which is not shown in Fig. 1.3, was often observed during FIRE and ASTEX (Betts and Albrecht, 1987; Schubert et al., 1992). There is no clear explanation for this q-reversal yet. A sharp gradient of geostrophic wind sometimes exists across inversion, due to the slope of the inversion layer.

1.2.4 Observed scales of convection in STBL

The coexistence of small-scale (a few kilometers) and mesoscale (tens of kilometers) convection was first reported by Krueger and Fritz (1961), and later by Hubert (1966) from satellite observations. They found that small-scale cumuli are organized to form mesoscale cloud patterns. Fig. 1.2 also shows that the sizes of cloud patches range from small-scale to mesoscale. Cahalan and Snider (1989) analyzed the cloud patterns quantitatively in terms of the brightness of clouds observed by satellite during FIRE, and found that both small-scale and mesoscale convection existed in the cases observed. Their results also suggested that the mesoscale brightness variations of clouds are associated with liquid water variations, and that these in turn are associated with variations in vertical velocity, or mesoscale circulations.

Nucciarone and Young (1991) did spectral analysis of turbulent fields observed by flights during FIRE. They found that all the spectra of temperature, moisture and horizontal wind show two peaks: One is at the mesoscale range, the other is at the small-scale range, with a shallow spectral gap up to a decade in width in between them.

However, the vertical velocity spectra noticeably lack any mesoscale contribution. They argued that continuity and the shallowness of the marine layer limit large-scale vertical velocity perturbations. Paluch and Lenschow (1991) showed that convection with scales larger than 5 km contributes substantially to the total heat and moisture fluxes, which indicates that a mesoscale component of vertical velocity should exist, in contrast to the Nucciarone and Young (1991) results.

From the observations, there is no doubt that small-scale convection is vigorous in the STBL. The dynamics of small-scale convection has been studied extensively, and is now fairly well understood (e.g., Moeng, 1986; Moeng and Schumann, 1991; Moeng et al., 1992). However, although mesoscale convection is also evident in the observations, it is still not clear yet how it is organized.

A very frequently observed kind of mesoscale convection in the STBL, which has been drawing a lot of attention since the Krueger and Fritz (1961) discovery, is mesoscale cellular convection (MCC), which often has a hexagonal form. Hubert (1966) reported two kinds of MCC: One consists of "open" cells, which have broad downward motion in the cell centers, and narrow upward motion in the periphery of the hexagons. The other is "closed" cells, which have circulations opposite to those of open cells. Associated with their directions of circulations, respectively, open cells have cumulus clouds scattered at the periphery of the hexagons, with clear skies at the centers, while closed cells have stratocumulus cloud decks at the centers, with narrow clear regions in between. Therefore, in this thesis we study closed MCC as related to the STBL.

Closed MCC occurs preferentially to the west of continents over cool ocean currents with warm air advection (Hubert,1966; Agee et al, 1973; and Agee and Lomax, 1978), where stratocumulus clouds often occur (Fig. 1.1). Rothermel and Agee (1980), and Lee et al. (1980) also showed that closed cells may occur over warm water. By analyzing the AMTEX (Air Mass Transformation Experiment) data, Burt and Agee (1977) found that the SST is generally about half degree cooler than the air above, which results in weak heat fluxes at the air-sea interface. But they also found that strong surface heating can also be associated with closed cells.

Agee and Dowell (1974) and Agee (1984) found that the closed cells typically have diameters of 10-100 km, and aspect ratios (the ratio of cell diameter to convective depth) of 5 to 50, with a typical value of 30. Burt and Agee (1977) found that the closed cell centers are anomalously deeper, warmer (~0.2 K) and moister (~0.4 g kg^{-1}) than the thin clear air at the edges. The horizontal wind anomalies associated with the cells are on the order of 0.5 $m\,s^{-1}$, which corresponds to rising motion on the order of 0.1 $m\,s^{-1}$ at the centers. Therefore, observations do suggest that mesoscale circulations are associated with closed MCC.

1.3 Theories concerning the role of cloud-top processes in driving convection

1.3.1 Cloud top radiative cooling

Lilly (1968) showed that radiative cooling is a driving force of the mixed layer. However, he assumed that the radiative cooling happens only in the inversion layer above cloud top. Kahn and Businger (1979) argued that the radiative cooling should occur inside the clouds. The radiative cooling in the inversion layer drives entrainment directly, while the radiative cooling in the STBL may drive convection first, which in turn enhances entrainment. Some theoretical results (Lilly and Schubert, 1980; Randall, 1980b; Schaller and Kraus, 1981) showed that the distribution of the cooling has some effect in driving convection. Later observational as well as numerical results show that more than 80% of the cooling occurs inside the clouds, and that the weak cooling above cloud top does not much affect the evolution of the STBL (Deardorff, 1981; Caughey et al., 1982; Slingo et al., 1982; Brost et al., 1982; Twomey, 1983; Nieuwstadt and Businger, 1984; Caughey and Kitchen, 1984; Curry, 1986). Therefore, radiative cooling mainly drives convection directly, and enhance entrainment indirectly through convection.

The efficiency of cloud-top radiative cooling in producing convection depends on how the local intense cooling is balanced by other heating effects, i.e., the sensible heat transported from below, latent heat release due to condensation, and sensible heat from entrainment warming. If the cooling is mainly balanced by sensible heat transported from below, it is mostly used to drive convection in the STBL. If it is mainly balanced by the local entrainment warming, the convection driven by the cooling would be weak. A balance with latent heat release can produce moderate convection.

There are two different mechanisms that drives entrainment which can generate sensible heat to balance the radiative cooling. One is entrainment that is driven by convection due to radiative cooling, as discussed above. In this case, the stronger the radiative cooling is, the stronger the entrainment is. However, once the entrainment becomes strong enough, it may evaporate the clouds so that the radiative cooling becomes weaker, and hence entrainment becomes weaker, until the clouds can return. This is a self-controlled process. The other is entrainment that is produced by wind shear near the inversion. The balance of the radiative cooling by this kind of entrainment is not self-controlling, and may result in the drying-out of clouds. Brost et al. (1982b) found that the longwave radiative heat loss was largely balanced by shear-driven entrainment so that the convection driven by radiative cooling was weak inside the clouds. Slingo et al. (1982) also found that the shear-produced entrainment is important in balancing the radiative cooling near cloud top.

Curry (1986) analyzed the flight data collected over the Beaufort Sea in the Arctic Stratus Experiment, conducted in June, 1980, and found that condensation balances part of the radiative cooling. She also found that the radiative cooling is closely related to the microphysics of clouds, and is associated with the change of liquid water content near cloud top.

Therefore, even though the radiative cooling rate near cloud top can be very strong, it does not necessarily drive strong convection in the STBL. Entrainment warming may largely offset the negative buoyancy produced by radiative cooling.

1.3.2 Cloud-top evaporative cooling

Entrainment produces not only mixing warming, but also evaporative cooling. Evaporation at cloud top occurs when the unsaturated entrained air is mixed with cloudy air. It leads to liquid water variations near cloud top, as shown earlier, and may in turn modify the intensity of radiative cooling. However, it is not clear yet how the detailed entrainment mixing processes evaporate cloud droplets when unsaturated entrained air is mixed with cloudy air. There are two proposed mixing processes: One is the *inhomogeneous mixing* first proposed by Baker and Latham (1979), the other is the *entity entrainment* proposed by Telford and Chai (1980). Inhomogeneous mixing reduces the liquid water content by removing some cloud drops of all sizes and results in changes in the total number density, but without affecting the drop-size spectrum. Entity entrainment, on the other hand, reduces the liquid water content by completely evaporating the smaller droplets, so that only larger drops survive, and therefore both the total number density and drop-size spectrum change. Inhomogeneous mixing is supported by the observational results analyzed by Slingo et al. (1982). Based on the observations she analyzed, Curry (1986) concluded that inhomogeneous mixing is applicable only to those portions of the clouds affected by entrainment near cloud top. Entity entrainment may be applied to the entrainment and mixing of parcels within clouds which are made inhomogeneous by processes other than cloud-top entrainment.

The way the evaporative cooling produces negative buoyancy is as follows: A parcel of the upper air is mixed into the cloudy air by entrainment. If the mixed parcel reaches saturation at a lower virtual temperature than that of its environment near the cloud top,

it is negatively buoyant and can then penetrate into the cloud. Lilly (1968) argued that if the penetration was not stopped by other processes, the evaporation and penetration processes would occur spontaneously and increase unstably until the cloud was evaporated. This is the so-called cloud top entrainment instability (CTEI). He concluded that the condition for the instability is that the jump of wet-bulb potential temperature at cloud top is negative ($\Delta\theta_w < 0$). Randall (1980) reconsidered the problem by including the effects of water loading on buoyancy, and derived a new criterion which is less strict than Lilly's for the CTEI. A similar criterion was also found by Deardorff (1980) from his numerical results. However, observational studies have not shown the breakup of clouds even when the criterion was met (Mahrt and Paumier, 1982; Hanson, 1984; Betts, 1985; Rogers and Telford, 1986; Kuo and Schubert, 1988; Albrecht, 1991). Based on the observational results, some attempts have been done to modify the criterion (McVean and Mason, 1990; Siems et al., 1991; Duynkerke, 1993). None of them has been solidly proved by observations yet. More recently, by using a fine-resolution linear eddy model, Krueger (1993) found that the entrained dry-air parcels cannot be completely mixed with cloudy air, and therefore the evaporative cooling is too weak to generate CTEI. By using a fine-resolution two-dimensional numerical model, MacVean (1993) found that CTEI can happen under the criterion derived by McVean and Mason (1990) which is more strict that Randall's (1980) criterion.

Even though cloud-top evaporative cooling is not strong enough to produce CTEI, it may help radiative cooling to generate convection by compensating part or even all of the mixing warming due to entrainment, so that the net heating effect with entrainment and cloud-top radiative cooling is a weaker warming, or even cooling. However, since

evaporation tends to reduce the liquid water content near cloud top, no matter whether it is inhomogeneous mixing or entity mixing, or even incomplete mixing (Krueger, 1993), the strength of the radiative cooling will also be reduced accordingly. A related question is then: Does radiative cooling contribute more to the cold downdrafts than evaporative cooling, or vice versa? This question has been studied case by case (Mahrt and Paumier, 1982; Nicholls, 1989; Khalsa, 1993; Wang and Albrecht, 1993; Shao et al., 1993), and there is not a universal answer for it yet.

All of the theories mentioned above are concerned with the local effects of the cloud-top processes, or how the small-scale convection is driven. There is still no theory which can explain whether mesoscale convection is related to cloud-top processes or not. Since the cloud-top processes do work locally, we could expect that some nonlinear processes might organize their local effects on the mesoscale.

1.4 Numerical studies

The idealized mixed layer models, which are represented by Lilly (1968), and followed by Arakawa (1975), Schubert (1976), Deardorff (1976), Randall (1980b), Kraus and Schaller (1978a, b), Kahn and Businger (1979), Schubert et al. (1979), Moeng (1979), Lilly and Schubert (1980), Fravalo et al. (1981), and Hanson (1984), have helped in understanding convection driven by cloud top radiative cooling as well as entrainment, and have provided guidance for experiments in the earlier stage of research on STBL (e.g., Wakefield and Schubert, 1976).

Higher-order closure models can relax some idealized assumptions in the mixed layer models, such as complete mixing, full cloud coverage, no drizzling, parameterized entrainment rate and prescribed radiative heating. These were developed later for a more detailed understanding of turbulent structures in the STBL, and allow a more realistic study of the effects of cloud-top processes (Oliver et al., 1978; Moeng and Arakawa, 1980; Chen and Cotton, 1983; Moeng and Randall, 1984; Bougeault, 1985; Shao and Randall, 1992; Wang and Wang, 1993).

The large-eddy simulation (LES) models, which were first used by Deardorff (1980), and later by Moeng (1986) to study the STBL, have been providing very useful three-dimensional solutions which can be considered as complementary data sources beside field experiments for the study of the complicated STBL. LES allows studies which may be impossible by observational methods. Based on the LES results, cloud-top processes have been extensively studied (e.g., Schumann and Moeng, 1991a, b; Moeng and Schumann, 1991; Randall et al., 1992; Moeng et al., 1992; Shen and Moeng, 1992; Shao et al., 1993). One of the drawbacks of LES is that it consumes a lot of computer time so that it is not feasible to study mesoscale convection at present. A mesoscale model which we have been using to study closed MCC with the cloud-top processes as driving forces, is the cloud ensemble model developed by Krueger (1985,1988). This model is a third-order closure model, and has subgrid condensation parameterization, as well as an upgraded interactive radiation parameterization (Krueger, personal communication). As far as we know, there is still no numerical study that investigates whether the local effects of the cloud-top processes can be organized to generate MCC or not, except some very idealized work such as that of Helfand and Kalnay (1983).

One of the practical reasons to study the STBL is to parameterize the planetary boundary layer (PBL) better in general circulation models (GCMs). Due to the computational expense of GCMs, only a very simple parameterization of the PBL is possible. We therefore need a model which is as simple as possible, but also includes crucial physical processes as accurately as possible. A mixed-layer model, in which only surface fluxes and STBL top entrainment processes are considered to determine the properties in PBL, has therefore been applied in the past (e.g., Suarez et al., 1983; Randall et al., 1985). However, as observational and numerical results have revealed (e.g., Deardorff, 1980; Nicholls and Leighton, 1986), decoupling between the cloud and subcloud layer may result in mean structures in the PBL that are far from being well mixed. This decoupling is closely related to the vertical transport of moisture and heat from the free atmosphere into the PBL. Therefore, we need at least a two-layer PBL model, which can distinguish the cloud and subcloud layers. Moreover, since the horizontal grid size of GCMs is very large, so that fractional cloudiness in grid cells practically always exists, the simple model should represent the effects of fractional cloudiness. Some efforts have been made to build a simple two-layer STBL model with enough physical processes included (e.g., Wang, 1993; Randall et al., 1993). However, this kind of two-layer model is not mature yet due to our limited understanding of the STBL, and has not been applied to a GCM so far.

1.5 Topics in this study

The observations have shown that, from a large scale point of view, the STBL is basically a two-layer structure: it consists of a cloud layer and a subcloud layer. The

properties of these two layers are determined by cloud-top processes and surface properties, as well as solar radiation, drizzle, and large-scale convergence. Therefore, like the bulk-flux model used for the surface layer, it should be possible to parameterize the processes in the layer near cloud top in which cloud-top processes are vigorous, (i.e., the so-called entrainment layer), by a similar bulk-flux model. The turbulent fluxes generally include contributions from all of the cloud-top processes as well as surface heating. This idea has actually already been used to estimate the entrainment rate, using the assumption that the entrainment layer is infinitesimally thin. Based on this idea, we develop an analytical second-order bulk PBL model, as shown in Chapter 2. This model is also capable of representing fractional cloudiness. A flow field from large-eddy simulation (Moeng, 1986) has been used to test the model.

In order to understand how surface heating and cloud-top processes generate fluxes in the surface and entrainment layers, respectively, we analyzed in detail, as reported in chapter 3, the same LES field used in Chapter 2. A method to calculate systematically the effects of radiative and evaporative cooling in the STBL is developed. This method is also applied to tethered balloon data observed during FIRE. The results are presented in Chapter 3.

So far, the studies are limited to the understanding of the effects of cloud-top processes on small-scale convection. As we mentioned earlier, although MCC is commonly observed in STBLs, the relation between closed MCC and cloud-top processes is still not clear. None of the observational, theoretical and numerical studies can give a definite conclusion on whether MCC is a result of the effects of cloud-top

processes or not. Therefore, we build an idealized 2-D dry-cloud model to study this problem both theoretically and numerically. This work is presented in Chapter 4. Chapter 5 gives concluding remarks and proposals for further research.

CHAPTER 2

Parameterization of Cloud-Top Processes in a Second-Order Bulk Boundary-Layer Model

2.1 Introduction

The "bulk" approach to parametric representation of boundary-layer processes in large-scale models, pioneered by Deardorff (1972) and further developed by Randall (1976), Benoit (1976), and Suarez *et al.* (1983) involves a simple planetary boundary layer (PBL) model in which some aspects of the vertical structure of the mean state are parameterized. Among the parameters introduced to represent the mean state are the PBL depth, which is prognostically determined, and "jumps" or discontinuities at the PBL top. The use of jumps amounts to a concession that, although the fine structure near the PBL top is important for the PBL physics, it is unresolvable by any grid that can be used in a large-scale model. Extensive results from a PBL parameterization based on a bulk model have been reported by Randall *et al.* (1985).

The key shortcomings of existing bulk models are their assumption of vertical homogeneity for conservative variables and their inability to predict fractional cloud

amounts. In attempts to address these deficiencies, a number of recent studies (cited below) have made use of a convective mass flux parameterization.

The mass flux concept was invented for use in a cumulus parameterization by Arakawa (1969). It was later adapted to the problem of boundary layer parameterization by Betts (1973, 1983), Albrecht, *et al.* (1979), Hanson (1981), Penc and Albrecht (1986), Wang and Albrecht (1986, 1990), Randall (1987), and Chatfield and Brost (1987). We refer to bulk boundary layer models that use the mass flux concept as "bulk mass flux models." In such models, the convective mass flux is assumed to be associated with convective circulations that have ascending and descending branches. Several of the modeling studies just cited allow the possibility that cloudiness can occur (or not) in either branch. The concept of "convective circulations" has also been used in observational studies (based on conditional sampling and/or joint distribution functions) by Lenschow and Stephens (1980, 1982), Greenhut and Khalsa (1982), Wilczak and Businger (1983), Mahrt and Paumier (1984), Grossman (1984), Khalsa and Greenhut (1985), Penc and Albrecht (1986), and Young (1988 a, b). Recently, it has been applied to analyze the results of large eddy simulations by Schmidt and Schumann (1989), Schumann and Moeng (1991 a,b) and Moeng and Schumann (1991).

The existing bulk mass flux models do not match the fluxes associated with the convective mass flux with those driven by ventilation at the surface and entrainment at the top. Also, no existing bulk mass flux model includes a physically based method to determine σ, the fractional area covered by rising motion. Finally, most of the existing bulk mass flux models have retained the "well mixed" assumption, with the notable exceptions of Betts (1973), Albrecht *et al.* (1979), and Wang and Albrecht (1990).

This chapter addresses all three of these problems.

2.2 Convective Mass Flux Model

The basic framework of our model is shown in Fig. 2.1. The level just above the PBL top is denoted by subscript B+, while the Earth's surface is denoted by S-. We define an infinitesimal "ventilation layer" just above the Earth's surface, and an infinitesimal "entrainment layer" just below the PBL top. These are indicated by stippling in Fig. 2.1. The ventilation layer is more conventionally known as the surface layer. The entrainment layer is the region within which the turbulent fluxes drop sharply from finite values to zero. Caughey *et al.* (1982) and Nicholls and Turton (1986) described the entrainment layer as a thin region of weak organized vertical motions and vigorous small-scale mixing. The top of the ventilation layer will be denoted by subscript S, and the base of the entrainment layer by subscript B. The depth of the PBL (in terms of pressure) is denoted by δp_M.

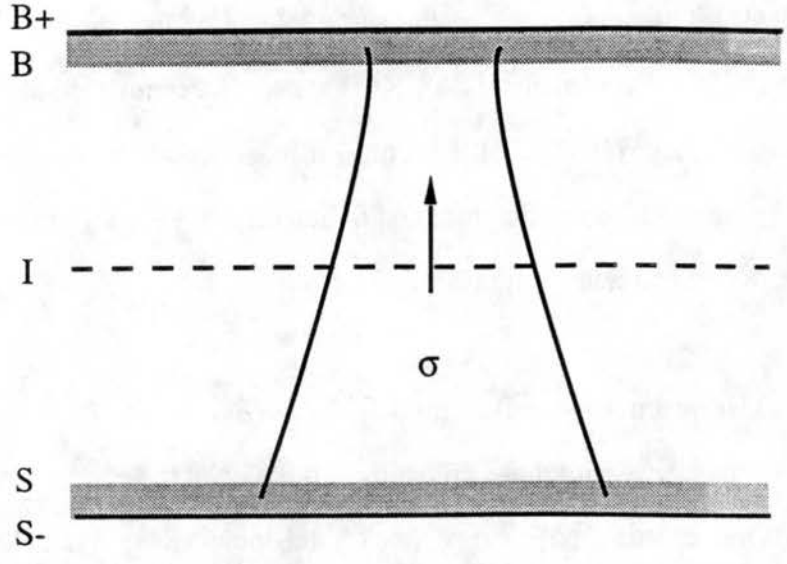

FIGURE 2.1: Diagram illustrating the assumed structure of the PBL. The interior, which is represented by two layers, is bounded above by a thin entrainment layer and below by a thin ventilation layer. Convective circulations occur, with rising branches occupying fractional area σ. The ascending and descending branches have different thermodynamic soundings and, therefore, different cloud base levels.

The generic variable ψ will be used to represent a prognostic intensive scalar such as the dry static energy, the mixing ratio of water, or a velocity component. Area-averaged values of ψ are denoted by $\overline{\psi}$. The upward turbulent flux of ψ is denoted by F_ψ. The mid-level of the PBL is indicated by the dashed line in Fig. 2.1; it is representative of the interior of the PBL, and will be denoted by subscript "I".

An entrainment mass flux, E, carries mass across the PBL top, and is closely related to the turbulent fluxes at the base of the entrainment layer. Correspondingly, a ventilation mass flux, V, is associated with the surface fluxes; in conventional parlance, V is the product of the surface air density, the surface wind speed, and a transfer coefficient. The fluxes at the top of the ventilation layer are assumed to be approximately equal to those at the surface. As explained later, the model incorporates diagnostic balances for mass, $\overline{\psi}$, and $\overline{\psi'^2}$, for both the entrainment and ventilation layers. These layers are assumed to be thin enough so that these approximations are applicable.

Within the ventilation layer, the turbulent fluxes have to be carried by small eddies, since the organized vertical motions associated with the convective circulations must vanish there. Within the entrainment layer the organized vertical motions associated with the convective circulations become negligible. Since the turbulent fluxes vanish above the PBL top, however, it is not necessary to hypothesize that small-eddy fluxes are important in the entrainment layer. Nevertheless, the existence of small eddies within the entrainment layer is well known from observations (e.g., Rayment and Readings, 1974).

As indicated in Fig. 2.1, we assume that the turbulent fluxes in the interior of the PBL are entirely due to the convective circulations, with rising branches covering fractional area σ, and sinking branches covering fractional area $1 - \sigma$. Some authors (e.g. Greenhut and Khalsa, 1982) have suggested a third, "environmental" domain in which the vertical

motion is nearly zero. We are not willing to accept such a complication without strong evidence that it is really necessary. The results of Schumann and Moeng (1991 a) suggest that it is not.

There have been numerous observations and numerical simulations yielding values of σ, based on various sampling methods. The methods used and results obtained are summarized in Table 2.1. Note that the various studies are based on data from several different PBL regimes, and employ several different definitions of σ. They have yielded a variety of numerical values for σ. For example, Manton (1977), Coulman (1978), and Lenschow and Stephens (1978) have adopted definitions involving not only the vertical velocity fluctuations but also the thermodynamic fluctuations. In these three studies, σ is found to be considerably less than 0.5. All of the remaining studies have adopted definitions based only on the sign of the vertical velocity. Greenhut and Khalsa (1982) and Schumann and Moeng (1991 a) defined three domains: updrafts, downdrafts, and an environment. The updrafts consisted of regions in which the vertical velocity exceeded a positive threshold. If we take the fractional area covered by updrafts to be σ, then Greenhut and Khalsa obtained $\sigma = 0.16$, by far the smallest value obtained in any of the studies, while Schumann and Moeng obtained $\sigma = 0.35$. We note, however, that Schumann and Moeng concluded that little is to be gained by defining an "environment" for the updrafts and downdrafts.

Table 2.1: Summary of observations and simulations of the fractional area covered by rising motion in several studies. Here $\langle\ \rangle$ denotes the expected value.

Author	Source of Data	Sampling Method Used to Define "Updraft"	Mean σ
Manton (1977)	Observations	$T > T_{th}$ such that $\langle w(T_{th})\rangle = 0$	0.38
Coulman (1978)	Observations	Similar to Manton (1977)	0.38
Lamb (1978)	LES results for clear PBL	Vertical velocity is positive	0.45
Greenhut and Khalsa (1982)	Observations	Vertical velocity exceeds a positive threshold. Three domains are defined: One for updrafts, one for downdrafts, and a third "environment."	0.16
Lenschow and Stephens (1982)	Observations	Moisture fluctuation is positive	0.25
Young (1988a)	Observations	Vertical velocity is positive	0.46
Nicholls (1989)	Observations of stratus-topped PBL over the North Sea	Vertical velocity is positive	0.70
Schumann and Moeng (1991a)	LES results	Vertical velocity exceeds a positive threshold. Three domains are defined: One for updrafts, one for downdrafts, and a third "environment."	0.35

The remaining three studies listed in Table 2.1 [i.e. those by Lamb (1978), Young (1988 a), and Nicholls (1989)] adopted definitions of σ that are essentially the same as ours, namely that σ is the fractional area covered by positive vertical velocity. The first two authors obtained values of σ equal to or slightly less than 0.5. Only the observations of Nicholls (1989), obtained by aircraft in stratocumulus clouds, show σ near 0.7. We conclude that σ is by no means an universal constant, but that with the definition we have

adopted here we should expect σ to be not too different from 1/2 under some conditions of interest.

Consider an arbitrary scalar ψ, satisfying a conservation equation of the form

$$\frac{\partial}{\partial t}(\rho\psi) = -\nabla\cdot(\rho V\psi) - \frac{\partial}{\partial z}(\rho w\psi) + S_\psi ,$$

(2.1)

where ρ is the density, which is quasi-constant in time and the horizontal, as in the usual anelastic approximation; V is the horizontal velocity vector; w is the vertical velocity; and S_ψ is the source of ψ per unit mass per unit time. The local time derivative and the ∇ operator are defined on constant height surfaces.

Area averages satisfy

$$\overline{\psi} = \psi_u\sigma + \psi_d(1-\sigma).$$

(2.2)

Here subscripts u and d denote upward and downward moving parcels, respectively. The fluxes associated with the convective circulations are given by

$$\begin{aligned} F_\psi = \rho\overline{w'\psi'} &= \rho\left[\left(w_u-\overline{w}\right)\left(\psi_u-\overline{\psi}\right)\sigma + \left(w_d-\overline{w}\right)\left(\psi_d-\overline{\psi}\right)(1-\sigma)\right] \\ &= M_c\left(\psi_u-\psi_d\right), \end{aligned}$$

(2.3)

where

$$M_c \equiv \rho\sigma(1-\sigma)\left(w_u-w_d\right)$$

(2.4)

is the convective mass flux.

For later use, we note that the variance of ψ is given by

$$\begin{aligned}\overline{\psi'^2} &= \sigma\left(\psi_u - \overline{\psi}\right)^2 + (1-\sigma)\left(\psi_d - \overline{\psi}\right)^2 \\ &= \sigma(1-\sigma)\left(\psi_u - \psi_d\right)^2 \\ &= \sigma(1-\sigma)\left(\frac{F_\psi}{M_c}\right)^2,\end{aligned} \tag{2.5}$$

while the plume-scale variance transport can be written as

$$\begin{aligned}\rho\overline{w'\psi'\psi'} &= \rho\left[\sigma\left(w_u - \overline{w}\right)\left(\psi_u - \overline{\psi}\right)^2 + (1-\sigma)\left(w_d - \overline{w}\right)\left(\psi_d - \overline{\psi}\right)^2\right] \\ &= \rho\sigma(1-\sigma)(1-2\sigma)\left(w_u - w_d\right)\left(\psi_u - \psi_d\right)^2 \\ &= (1-2\sigma)\frac{\left(F_\psi\right)^2}{M_c}.\end{aligned} \tag{2.6}$$

According to (2.6), $\rho\overline{w'\psi'\psi'}$ is positive (upward variance transport) if σ is less than 1/2, and negative (downward variance transport) if σ is greater than 1/2. For $\sigma = 1/2$, the variance transport vanishes. It follows that if the ventilation layer is exporting variance [production exceeds dissipation, and $\left(\rho\overline{w'\psi'\psi'}\right)_S$ is upward] then σ_S must be less than 1/2; this would normally be the case for a clear convective PBL driven by surface heating. Similarly, if the entrainment layer is exporting variance [production exceeds dissipation, and $\left(\rho\overline{w'\psi'\psi'}\right)_B$ is downward] then σ_B must be greater than 1/2.

Now and from time to time throughout the rest of this chapter, we investigate the consistency of our simple model with LES results obtained by C.-H. Moeng. These results are similar to the stratocumulus simulations of Moeng (1986), except that the

domain size was doubled to 5 km x 5 km x 1 km, and 80^3 grid points were used. The vertical resolution was 12.5 m. The horizontal resolution was 62.5 m. We have used six LES history records, spaced 250 simulated seconds apart. These same LES results were analyzed by Schumann and Moeng (1991 a; their "STBL" case).

Fig. 2.2 shows $\bar{h} / c_p$ and $\bar{q}_t$, plotted as functions of height. Here $h \equiv s_v - Lq_\ell$, c_p is the specific heat of air at constant pressure, and q_t is the total mixing ratio (vapor plus liquid). We use s_v to denote the virtual dry static energy, and q_ℓ to denote the liquid water mixing ratio. The figure shows averages over the six LES history records. The expected well mixed interior and near-discontinuities at the top and bottom of the PBL are readily apparent.

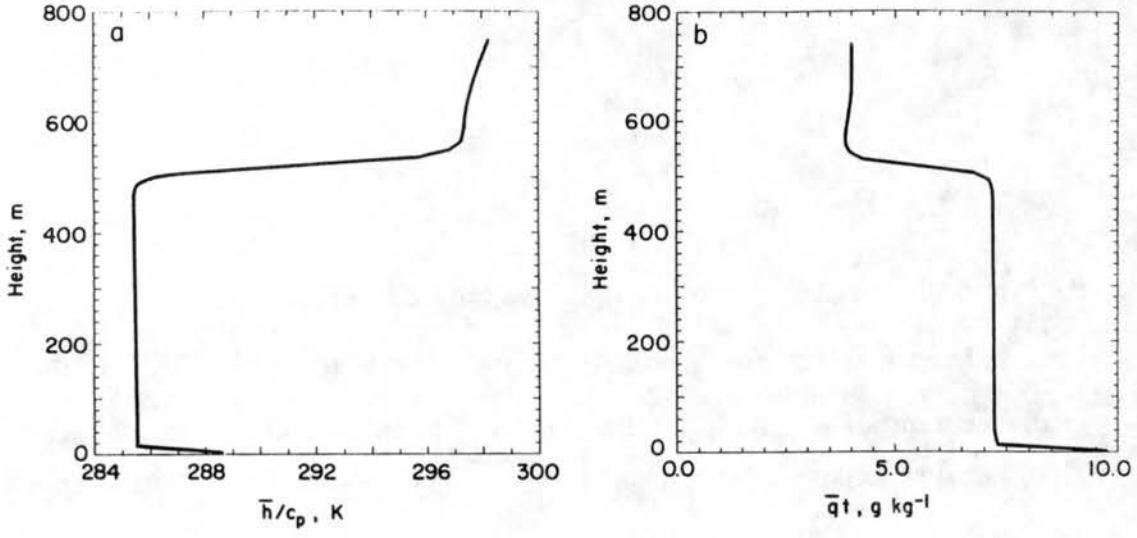

FIGURE 2.2: The vertical profiles of $\bar{h}$ and $\bar{q}_t$, plotted as functions of height.

We propose a new method to determine σ and M_c, based entirely on the vertical velocity statistics, and suggested by the analysis of Moeng and Rotunno (1990). The idea is to use (2.2), (2.5), and (2.6) with $\psi = w$, and to solve these three equations for the

three unknowns σ, w_u, and w_d. The convective mass flux can then be evaluated using (2.4). We find that

$$\sigma = \frac{1}{2} - \frac{S_w}{2\sqrt{4 + S_w^2}}, \tag{2.7}$$

where

$$S_w \equiv \frac{\overline{w'^3}}{\left(\overline{w'^2}\right)^{3/2}} \tag{2.8}$$

is the skewness of the vertical velocity. According to (2.7), σ is less than 1/2 when the skewness is positive, and greater than 1/2 when the skewness is negative. The form of (2.7) guarantees that $0 < \sigma < 1$. The convective mass flux satisfies

$$M_c = \frac{\rho\sqrt{\overline{w'^2}}}{\sqrt{4 + S_w^2}}. \tag{2.9}$$

One advantage of this approach is that it guarantees consistency among the mass flux and the variance of the vertical velocity, within the context of the mass flux model. A second advantage is that it can be used to determine σ and M_c in a higher-order closure model. Of course, we *cannot* use this method to determine σ and M_c in a bulk mass flux model, because such a model does not provide the needed input data, e.g. S_w is not available. Later, in Section 2.4, we present a method that can be used to determine σ and M_c in a bulk mass flux model.

Fig. 2.3 a shows the profiles of w_u and w_d obtained by the method described above, and also by directly sampling the LES results. The profiles are quite similar, but the method proposed here systematically overestimates the magnitudes of w_u and w_d. Fig. 2.3 b shows the profiles of σ and M_c, obtained from the LES results by the method described in the preceding paragraph. Although σ is close to 0.5 at all levels, it decreases noticeably upward through most of the PBL's depth, from about 0.6 near the surface to about 0.4 slightly below the PBL top. This is consistent with the analysis of Moeng and Rotunno (1990). The convective mass flux has a roughly parabolic profile, with a maximum slightly above the mid-level of the PBL, and much smaller values near the surface and the PBL top. The maximum value of M_c is about 0.45 kg m^{-2} s^{-1}.

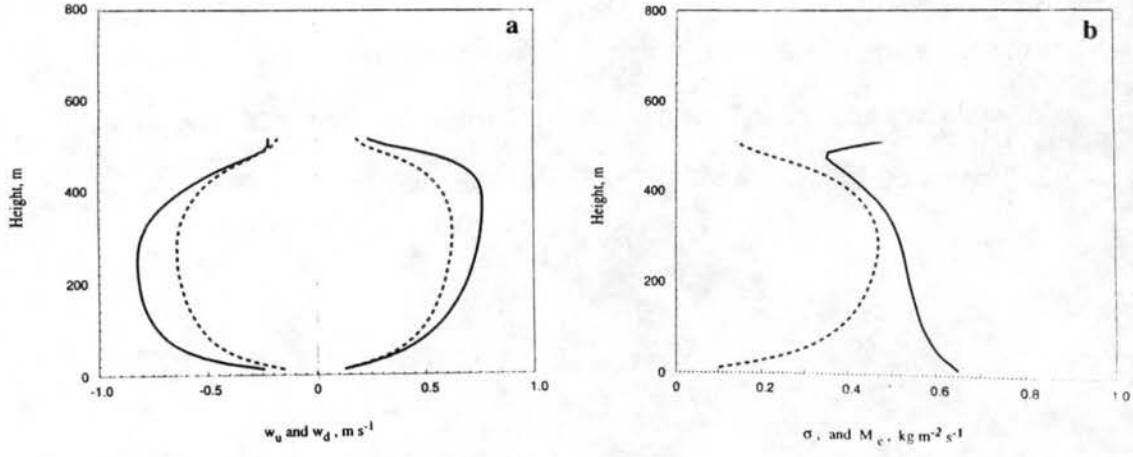

Figure 2.3: a) The vertical profiles of w_u and w_d obtained by the method described in Section 2.2 (solid curves), and also by directly sampling the LES results (dashed curves). b) The vertical profiles of σ (solid curve) and M_c (dashed curve), plotted as functions of height normalized by the PBL depth. Values are not plotted above the PBL top, since σ and M_c have little meaning there.

Using (2.2) and (2.3), we can evaluate ψ_u and ψ_d as follows:

$$\psi_u = \overline{\psi} + \frac{1-\sigma}{M_c} F_\psi \,, \tag{2.10}$$

$$\psi_d = \overline{\psi} - \frac{\sigma}{M_c} F_\psi \,.$$

(2.11)

The values of ψ_u and ψ_d obtained directly by conditional sampling (based on the sign of the vertical velocity) are slightly different from those obtained from the fluxes using (2.10 - 11). This is shown in Fig. 2.4 a for h/c_p and in Fig. 2.4 b for q_t. In these figures, the solid lines show the updraft and downdraft properties obtained from (2.10 - 11), and the dashed lines show the corresponding values based on conditional sampling. The updrafts are "warm" and "wet," and the downdrafts are "cold" and "dry." To give the correct fluxes, (2.10 - 11) make the updrafts warmer and wetter, and the downdrafts colder and drier, than the corresponding updraft and downdraft properties obtained by conditional sampling (c.f. Young, 1988 a; Wang and Albrecht, 1990; Schumann and Moeng, 1991 a). The discrepancies are fairly small, however, compared to the differences between the updraft and downdraft properties. These discrepancies are due to the "top hat" profiles assumed in the convective mass flux model. In a sense, the mass circulation of the convective mass flux model produces fluxes less efficiently than the more realistic simulation produced through LES. In the remainder of this chapter, we use ψ_u and ψ_d as determined from (2.10 - 11).

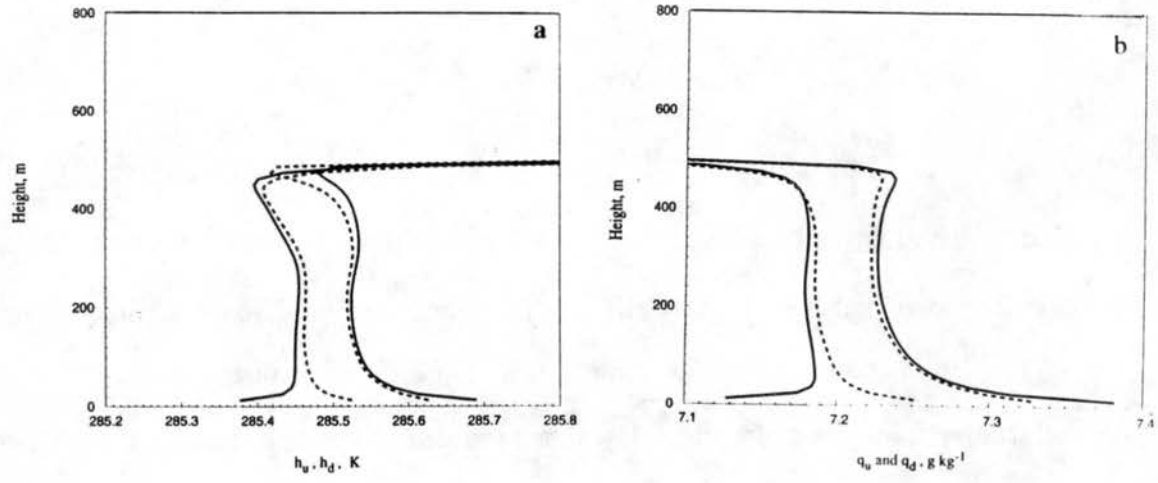

Figure 2.4: Profiles of ψ_u and ψ_d calculated directly by conditional sampling (based on the sign of the vertical velocity) and from the fluxes using (2.10 - 11). a) for h / c_p; and b) for q_t. The solid lines show the updraft and downdraft properties obtained from (2.10 - 11), and the dashed lines show the corresponding values based on conditional sampling.

2.3 Matching the fluxes

The surface fluxes are assumed to satisfy the usual bulk aerodynamic formula,

$$(F_\psi)_S = V(\overline{\psi}_{S-} - \overline{\psi}_S)\,, \tag{2.12}$$

where V is the "ventilation mass flux," which is usually written as the product of surface wind speed, a transfer coefficient, and the surface air density.

We assume that the fluxes at the top of the ventilation layer are entirely due to the convective circulations, and that the small-eddy fluxes are negligible there. Using this assumption with (2.3), (2.12), and also using our assumption that the ventilation layer is thin, we can write

$$V(\overline{\psi}_{S-} - \overline{\psi}_S) = M_{c,S}(\psi_u - \psi_d)_S.$$

(2.13)

This condition implies a consistency between the fluxes obtained from the bulk formula and those determined from the mass flux model. Wang and Albrecht (1990) did not impose (2.13) or the corresponding condition at the PBL top (discussed later).

At level S, the parcels rising away from the lower boundary must be "charged" with the properties of the boundary. We cannot assume, however, that the properties of the updrafts at level S are *the same* as those of the boundary, because there can be very strong gradients across the ventilation layer. The small eddies of the ventilation layer rapidly dilute air that has been in contact with the boundary, by mixing it with air that has recently descended from the interior of the PBL. As a result, $|\overline{\psi}_{S-} - \overline{\psi}_S| >> |(\psi_u - \psi_d)_S|$; from (2.13), this implies that $M_{c,S} >> V$. In order to take this into account, we introduce a nondimensional parameter, χ_V, such that

$$(\psi_u)_S - \overline{\psi}_S = \chi_V(\overline{\psi}_{S-} - \overline{\psi}_S);$$

(2.14)

in case $\chi_V = 1$, we get $(\psi_u)_S = \psi_{S-}$. Smaller values of χ_V indicate stronger mixing by the small eddies of the ventilation layer. We expect $0 < \chi_V << 1$. By combining (2.2), (2.13), and (2.14), we find that

$$\chi_V G_V = 1 - \sigma_S,$$

(2.15)

where $G_V \equiv M_{c,S} / V$. This is a "continuity equation" for the eddies, expressing a relationship between the convective mass flux and the ventilation mass flux.

In the preceding discussion, it has been tacitly assumed that χ_V is independent of ψ, i. e., that a single "mixing" parameter χ_V satisfies (2.14) whether ψ is moist static energy, total water mixing ratio, or some other intensive scalar. This assumption is supported by (2.15); if $M_{c,S}$, V, and σ_S are all independent of ψ, then χ_V must also be independent of ψ. Such independence suggests that χ_V is a useful concept.

We now apply a similar analysis to the entrainment layer. The assumption that it is thin yields the familiar "jump" relation between $(F_\psi)_B$ and the entrainment rate:

$$(F_\psi)_B = -E(\overline{\psi}_{B+} - \overline{\psi}_B) - \int_{z_B}^{z_{B+}} \overline{S_\psi}\, dz. \tag{2.16}$$

Here E is the rate at which mass is entrained across the PBL top. In (2.16), we follow Lilly (1968) by keeping the S_ψ term, which represents a possible concentrated entrainment-layer "source" of ψ, (e.g., due to radiation). We now assume that the fluxes at the base of the entrainment layer are entirely due to the convective circulations, and that the "small-eddy" fluxes are negligible. Then, by comparing (2.3) and (2.16), and using (2.2), we obtain

$$M_{c,B}(\psi_d - \overline{\psi})_B = E\sigma_B(\overline{\psi}_{B+} - \overline{\psi}_B) + \sigma_B \int_{z_B}^{z_{B+}} \overline{S_\psi}\, dz. \tag{2.17}$$

At this point, we introduce a mixing parameter χ_E, by analogy with (2.14). To allow for the effects of the concentrated source, however, we include an additional term:

$$(\psi_d - \overline{\psi})_B = \chi_E(\overline{\psi}_{B+} - \overline{\psi}_B) + \lambda \int_{z_B}^{z_{B+}} \overline{S_\psi}\, dz\,. \tag{2.18}$$

Here λ is a coefficient that is determined below. According to (2.18), the properties of the descending air at level B are related to those of the free atmosphere just above the PBL top, as modified by small-eddy mixing and the effects of any concentrated source within the entrainment zone. Since there is a sharp gradient of ψ across the entrainment layer, we expect $0 < \chi_E << 1$.

The mixing parameter χ_E is closely related to the parameter χ discussed by Siems *et al.* [1989; see also Albrecht *et al.* (1985) and Nicholls and Turton (1986)]. We can interpret χ_E as the value of χ associated with the downdraft air at level B. Further discussion is given later in this Section.

Comparing (2.17) with (2.18), we find that

$$(-M_{c,B}\chi_E + E\sigma_B)(\overline{\psi}_{B+} - \overline{\psi_B}) + (-M_{c,B}\lambda + \sigma_B)\int_{z_B}^{z_{B+}} \overline{S_\psi}\, dz = 0. \tag{2.19}$$

In case the source term of (2.19) vanishes, we obtain

$$\chi_E G_E = \sigma_B, \tag{2.20}$$

where $G_E \equiv M_{c,B} / E$. This relationship does not involve ψ; it must, therefore, apply for *all* ψ. To ensure that (2.20) will be satisfied even when the source term of (2.198) is not zero, we must choose

$$\lambda = \sigma_B / M_{c,B}. \tag{2.21}$$

We can interpret (2.20) as another "continuity equation", analogous to (2.15). Again, we have tacitly assumed that χ_E is independent of the species under consideration. This assumption is consistent with (2.20), since $M_{c,B}$, E, and σ_B are independent of species. We can use (2.20) to eliminate $M_{c,B}$ in (2.17), or, alternatively, use (2.21) to eliminate λ in (2.18); either way, the result is:

$$(\psi_d)_B = \chi_E \overline{\psi_{B+}} + (1-\chi_E)\overline{\psi}_B + \frac{\chi_E}{E}\int_{z_B}^{z_{B+}} \overline{S_\psi}\, dz. \tag{2.22}$$

According to (2.22), the descending air at level B has the properties of the free atmosphere, except as modified by mixing (when $\chi_E < 1$) and by the concentrated source. Caughey *et al.* (1982) and Nicholls (1989) have reported observations of cool downdrafts in the upper portions of stratocumulus cloud sheets. They concluded that the sinking air had been radiatively cooled near the cloud top. Such effects are represented by the S_ψ term of (2.22).

This term is inversely proportional to E, which means that radiative cooling in the entrainment layer can produce negatively buoyant parcels most effectively if the entrainment rate is slow. This suggests that entrainment driven by radiative cooling near cloud-top tends to be self-limiting.

According to (2.15), ventilation-layer dilution becomes more effective (in other words, χ_V decreases) as the convective mass flux increases relative to $V\,(1 - \sigma_S)$. The ventilation mass flux times the fractional area covered by the incoming downdrafts is a measure of the rate at which the updrafts leaving the ventilation layer can be supplied with air that has been charged with surface properties, and the convective mass flux is a measure of the rate at which this air is removed from the surface layer. The stronger the convective mass flux

becomes, the less effectively ventilation-layer air can be charged with surface properties before it is carried away into the interior of the PBL. A similar interpretation can be given for (2.20).

If we combine (2.15) and (2.20), and assume that σ is independent of height through the depth of the PBL, so that $\sigma_S = \sigma_B$, we find that

$$\sigma = \frac{1}{1 + \dfrac{\chi_V G_V}{\chi_E G_E}}. \tag{2.23}$$

Suppose that M_c is also independent of height, so that $M_{c,S} = M_{c,B}$. If we substitute (2.23) back into either (2.15) or (2.20), and use the definitions of G_V and G_E, we obtain

$$M_c = \frac{(E/\chi_E)(V/\chi_V)}{(E/\chi_E)+(V/\chi_V)}. \tag{2.24}$$

With the assumption that M_c is independent of height, (2.23) can be rewritten as

$$\sigma = \frac{1}{1 + \dfrac{E}{V}\dfrac{\chi_V}{\chi_E}}. \tag{2.25}$$

Of course, bulk PBL models normally include parameterizations for V and E. If we have a parameterization for χ_V / χ_E, then (2.25) can be used to determine σ. Note that the *forms* of (2.23) and (2.25) ensure that $0 < \sigma < 1$. We use both (2.24) and (2.25) later in this chapter.

The profiles of σ and M_c shown in Fig. 2.3 are not independent of height. Nevertheless, the assumption that these two parameters are vertically uniform is of interest as a particularly simple special case.

Now we test the main conclusions of this Section, using the LES results.

First we have to identify levels S-, S, B and B+ based on the LES output. In this we are guided not only by the mean structures but also by the turbulence results, since we have defined the ventilation and entrainment layers in terms of the relative importance of small-eddy fluxes. Fig. 2.5 shows the mean structure of the total moisture q_t (g kg^{-1}, solid line) and the ratio of the subgrid moisture flux to the total moisture flux. The ratio becomes appreciable only near the top and bottom of the PBL. We identify the entrainment and ventilation layers as those regions within which the ratio exceeds 0.1. We have also taken into account the mean structure. The entrainment and ventilation layers that we have identified are indicated in Fig. 2.5. The height of level S- is zero (the surface), while level S is at 62.5 m, level B is at 475 m, and level B+ is at 537.5 m. The average cloud top is near 504 m. Since the vertical grid spacing of the LES model is 12.5 m, there are four model layers inside the ventilation layer, and four more inside the entrainment layer.

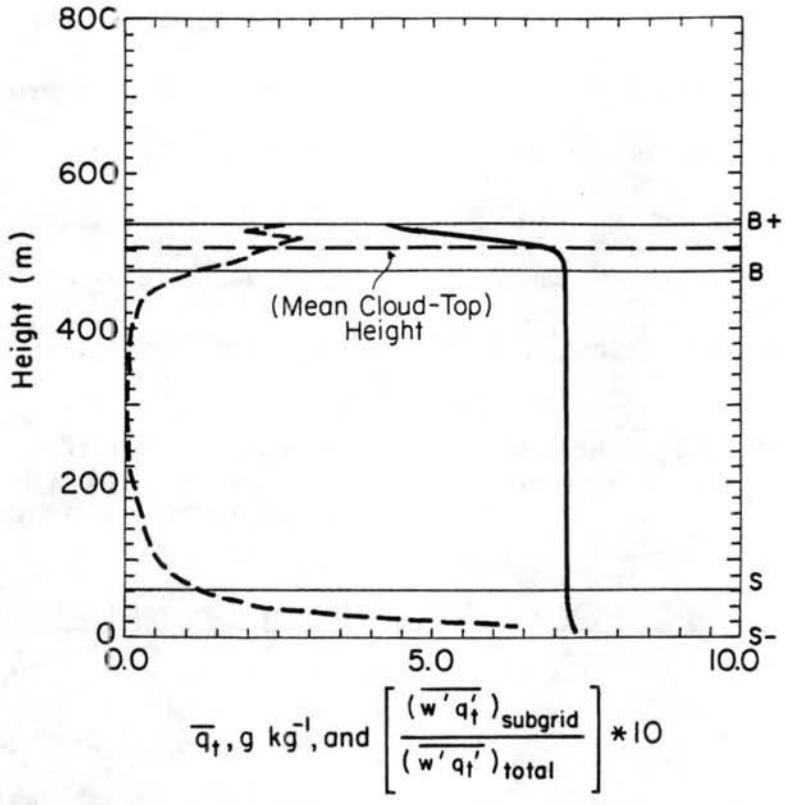

Figure 2.5: For the LES results, the ratio of the subgrid-scale flux moisture flux to the total flux. The ventilation and entrainment layers are indicated by stippling.

Averaging over six LES history records, we obtain the following numerical values for the mean-state variables:

$$\overline{h_{B+}} / c_p = 295.73\ K,$$
$$\overline{h_B} / c_p = 285.45\ K,$$
$$\overline{(q_t)}_{B+} = 4.22\ g\ kg^{-1},$$
$$\overline{(q_t)}_{B} = 7.18\ g\ kg^{-1},$$
$$\overline{h_S} / c_p = 285.51\ K,$$
$$\overline{h_{S-}} / c_p = 288.67\ K,$$
$$\overline{(q_t)}_{S} = 7.23\ g\ kg^{-1},$$
$$\overline{(q_t)}_{S-} = 9.80\ g\ kg^{-1}.$$

These values are indicated in Fig. 2.2.

We have evaluated the ventilation mass flux from the LES results, as the ratio of the surface flux of h or q_t to the surface-air difference in the same quantity, as indicated in (2.12). Averaging over six LES history records, the ventilation mass flux based on h is 1.04×10^{-2} kg m^{-2} s^{-1}, while that based on q_t is 0.965×10^{-2} kg m^{-2} s^{-1}. We estimate, therefore, that the correct value of V is about 1.0×10^{-2} kg m^{-2} s^{-1}.

Table 2.2: The LES entrainment mass flux in 10^{-2} kg m^{-2} s^{-1}, as determined by methods HA, HB, QA, QB, and Z. See text for explanation of the methods.

	History Record Number						
	1	2	3	4	5	6	Average
HA	0.803	0.768	0.816	0.814	0.797	0.841	0.806
HB	0.660	0.639	0.666	0.691	0.741	0.767	0.694
QA	0.819	0.786	0.859	0.835	0.853	0.833	0.831
QB	0.633	0.625	0.670	0.671	0.760	0.733	0.682
Z							0.656

Table 2.2 gives the entrainment mass flux, E, as evaluated from the LES data by the following methods:

Method HA:

$$E_h = \frac{\Delta R + (F_h)_{B+} - (F_h)_B}{\overline{\Delta h}}$$

Method HB:

$$E_h = \frac{\Delta R - (F_h)_B}{\overline{\Delta h}}$$

Method QA:

$$E_q = \frac{\left(F_{qt}\right)_{B+} - \left(F_{qt}\right)_B}{\overline{\Delta q_t}}$$

Method QB:

$$E_q = \frac{-\left(F_q\right)_B}{\overline{\Delta q_t}}$$

Method Z:

$$E = \rho \frac{dz_T}{dt} - \rho \overline{w}_B$$

Here z_T is the cloud top height. Methods HA and QA include the small contributions from the fluxes at level B+, and so are *a priori* more reliable than methods HB and QB. Our results indicate that the effect of fluxes at level B+ on the estimated entrainment rate amounts to about 20%. Method Z does not give a reliable value for the entrainment rate because of uncertainties in determining the values of z_T and especially its time change; we have shown only the average value based on the total length of the record available to us. From the results given in Table 2.2, we conclude that the correct value of E is about 0.82 x 10^{-2} kg m^{-2} s^{-1}. This corresponds to an "entrainment velocity" of about 25 m hr^{-1} or about 600 m day^{-1}, which is in line with observations (e.g., Nicholls and Turton, 1986). Note that E and V are quite comparable in magnitude.

We have argued that χ_V and χ_E are independent of species. Do the LES results support this? Substituting (2.10) and (2.11) into (2.14) and (2.17), and using (2.21), we obtain expressions for χ_V and χ_E :

$$\chi_V = \left(\frac{1-\sigma_S}{M_{cS}}\right)\left[\frac{(F_\psi)_S}{\overline{\psi}_{S-} - \overline{\psi}_S}\right], \tag{2.26}$$

$$\chi_E = -\left(\frac{\sigma_B}{M_{c,B}}\right)\left[\frac{(F_\psi)_B + \int_{z_B}^{z_{B+}} \overline{S}_\psi dz}{\overline{\psi}_{B+} - \overline{\psi}_B}\right]. \tag{2.27}$$

For $\psi = q_t$, we have $S_\psi = 0$, while for $\psi = h$ we have

$$-\int_{z_B}^{z_{B+}} \overline{S}_\psi \, dz = \Delta\overline{R} = -\int_{z_B}^{z_{B+}} \overline{\rho c_p \left(\frac{\partial T}{\partial t}\right)_{RAD}} \, dz \,, \tag{2.28}$$

where $\left(\frac{\partial T}{\partial t}\right)_{RAD}$ is the heating rate due to longwave radiation.

Using the methods of Section 2.2, we have evaluated σ and the convective mass fluxes at levels B and S. The results, averaged over the six history records, are σ_S = 0.595, σ_B = 0.352, $M_{c,S}$ = 0.316 kg m^{-2} s^{-1}, and $M_{c,B}$ = 0.235 kg m^{-2} s^{-1}. From the mass fluxes, we obtain G_V = 31.56, and G_E = 28.66. We have also evaluated $\overline{\Delta R}$, by using (3.17). The result is $\overline{\Delta R}$ = 82.1 W m^{-2}. In a similar way, we have determined that the radiative flux "jump" across the ventilation layer is a warming, of 2.2 W m^{-2}.

We have also determined χ_V and χ_E using each of the six LES history records. For this purpose, we used (3.3) and (3.7), with the numerical values of ψ_u, ψ_d, and $\overline{\psi}$ given earlier. The results are given in Table 2.3. The χ_E's obtained for $\psi = h$ and $\psi = q_t$ agree very well. Note that $\chi_{V,h}$ is generally a little bit larger than $\chi_{V,q}$. If we include the small

radiative flux jump across the ventilation layer, we find that the two χ_V's agree as well as the two χ_E's do. On the basis of these results, we conclude that $\chi_V = 1.22 \times 10^{-2}$, and that $\chi_E = 1.02 \times 10^{-2}$. The good agreement between the values of χ obtained with h and q_t supports our assertion that χ_V and χ_E are independent of species. As expected, both χ_V and χ_E are small compared to one. Their numerical values are quite similar.

Table 2.3: Values of χ_V and χ_E determined from the LES results by various methods. Subscript q indicates that we have used $\psi = q_t$, while subscript h indicates that we have used $\psi = h$. In the case of $\chi'_{V,h}$ we have taken into account the weak radiative forcing of the ventilation layer. This slightly reduces the values of $\chi_{V,h}$, bringing them into better overall agreement with those of $\chi_{V,q}$.

	History Record Number						
	1	2	3	4	5	6	Average
$\chi_{V,q}$	0.0124	0.0124	0.0130	0.0121	0.0125	0.0119	0.0124
$\chi_{V,h}$	0.0126	0.0137	0.0140	0.0130	0.0140	0.0127	0.0133
$\chi_{E,q}$	0.0097	0.0104	0.0101	0.0094	0.0109	0.0106	0.0101
$\chi_{E,h}$	0.0101	0.0106	0.0101	0.0097	0.0107	0.0110	0.0104
$\chi'_{V,q}$	0.0113	0.0124	0.0128	0.0117	0.0127	0.0114	0.0121

Since we have chosen V and E so that (2.12) and (2.16) are satisfied, the good results presented above for χ_V and χ_E ensure that (2.15) and (2.20) will be satisfied. Substituting our "best estimates" f E, V, χ_V and χ_E into (2.25), we find that the effective height-independent value of σ is 0.505, in reasonably good agreement with the LES results shown in Fig. 2.3.

Using the numerical values given above for E, V, χ_E, and χ_V, we find from (2.24) that the effective height-independent value of M_c is 0.406 kg m^{-2} s^{-1}. This is slightly larger than the value of $M_{c,S}$ obtained directly from the LES results, and is substantially larger than the value of $M_{c,B}$. It is fairly close to the maximum value of M_c shown in Fig. 2.3.

Before leaving this Section, we offer an alternative interpretation of χ_E. The air descending at level B is a mixture of updraft air that has passed through the entrainment layer, and newly entrained air from level B+. Let f be the fraction of air from level B+, i.e.

$$(\psi_d)_B = (\psi_u)_B(1-f) + f\overline{\psi_{B+}}. \tag{2.29}$$

For simplicity we have assumed no concentrated sources or sinks; note, however, that this assumption does not alter the result below. Comparing (2.29) with (2.187), we find that

$$f = \frac{\chi_E}{\chi_E + \sigma_B(1-\chi_E)}. \tag{2.30}$$

Substituting the numerical values of σ and χ_E from above, we obtain $f \equiv 0.028$. This means that, for the case studied here, about 3 % of the air descending at level B has just been entrained; the remainder is "recycled" updraft air.

Appendix A presents an analysis of the budgets of $\overline{\psi'^2}$ for the entrainment and ventilation layers.

2.4 The convective mass flux and the turbulence kinetic energy

In this Section, we present methods to determine σ and M_c inside the convective mass flux model, using the turbulence kinetic energy (TKE) and the entrainment and ventilation mass fluxes as inputs.

Obviously, there has to be a close connection between the convective mass flux and the turbulence kinetic energy (TKE). Let a_3 be the fraction of the vertically integrated TKE that resides in the vertical component of the motion. We can write

$$a_3 e_M \int_{z_{S-}}^{z_{B+}} \rho \, dz = \frac{1}{2} \int_{z_{S-}}^{z_{B+}} \rho \overline{w'^2} \, dz \, . \tag{2.31}$$

Here e_M is the vertically averaged TKE per unit mass. If the TKE is equipartitioned among the three convective velocity components, then $a_3 = 1/3$. Using the LES results, and considering only the resolved-scale motions in the region $z_{S-} \le z \le z_{B+}$, we find that $e_M = 0.712$ m^2 s^{-2}, and $a_3 = 0.281$.

Using (2.3), we can express $\overline{w'^2}$ in terms of the difference in vertical velocity between the updrafts and the downdrafts. Next, (2.4) can be used to rewrite this difference in terms of the convective mass flux, giving

$$\overline{w'^2} = \frac{M_c^2}{\rho^2 \sigma (1-\sigma)} . \tag{2.32}$$

Because of the way we have determined σ and M_c from the LES results (see Section 2.2), (2.32) has to be exactly satisfied when $\overline{w'^2}$ is evaluated from the LES. By substitution from (2.32), (2.31) can be rewritten as

$$a_3 e_M \int_{z_{s-}}^{z_{B+}} \rho \, dz = \frac{1}{2} \int_{z_{s-}}^{z_{B+}} \frac{M_c^2}{\rho \sigma (1-\sigma)} \, dz \, . \tag{2.33}$$

If σ and M_c are independent of height, then (2.33) reduces to

$$M_c = \sqrt{\frac{2a_3 \sigma (1-\sigma) e_M \int_{z_{s-}}^{z_{B+}} \rho \, dz}{\int_{z_{s-}}^{z_{B+}} \frac{1}{\rho} \, dz}} \, . \tag{2.34}$$

The integrals in (2.34) are easily evaluated for a given sounding. If we consider the density of the air to be approximately constant with height in the PBL, then (2.34) can be simplified to

$$M_c = \rho_M \sqrt{2a_3 \sigma (1-\sigma) e_M} \, . \tag{2.35}$$

Appendix B gives a method to predict e_M in a bulk boundary layer model. Then (2.35) can be used to evaluate M_c, provided that σ is known.

From the LES results, we have already found, in Section 2.3, that the effective height-independent values of M_c and σ are 0.406 kg m^{-2} s^{-1} and 0.505, respectively. Substituting numerical values into the rhs of (2.35), we obtain M_c = 0.383 kg m^{-2} s^{-1}. This is in fair agreement with the value just mentioned, and seems reasonable in view of the LES results shown in Fig. 2.3.

By equating (2.35) and (2.24), and using (2.25), we can derive a constraint on the product $\chi_V \chi_E$, i.e.

$$\chi_V \chi_E = \frac{EV}{2a_3 \rho_M^2 e_M}. \tag{2.36}$$

Substituting numerical values on the rhs of (2.36) gives $\chi_V \chi_E = 1.40 \times 10^{-4}$, which should be compared with the value inferred in Section 2.3, i.e. $\chi_V \chi_E = (1.22 \times 10^{-2}) \times (1.02 \times 10^{-2}) = 1.24 \times 10^{-4}$.

Alternatively, we can set the lhs of (2.35) to 0.406 kg m^{-2} s^{-1}, which is the value obtained in Section 2.3, and solve (2.35) for a_3. This gives $a_3 = 0.316$, which is slightly larger than the value obtained directly from the LES results, mentioned above. This small discrepancy in a_3 comes from our assumption that both σ and M_c are independent of height. If $a_3 = 0.316$ is used in (2.36), we are guaranteed to obtain the same value of $\chi_V \chi_E$ that we reported in Section 2.3. Of course, given a method to determine χ_E and χ_V , we could use (2.36) to solve for a_3.

Our plan is to parameterize χ_E and χ_V. The parameterization must be consistent with (2.36). Note that the denominator on the rhs of (2.36) contains only quantities that characterize the PBL *as a whole*, rather than the entrainment or ventilation layers. We expect E and V to appear symmetrically in the expressions for χ_E and χ_V . The form of (2.36) thus suggests the following two alternative possibilities for χ_E and χ_V :

$$\chi_V = \frac{V}{\rho_M \sqrt{2a_3 e_M}}, \quad \chi_E = \frac{E}{\rho_M \sqrt{2a_3 e_M}}; \tag{2.37 a}$$

or

$$\chi_V = \chi_E = \sqrt{\frac{EV}{2a_3\rho_M^2 e_M}}\,.$$

(2.37 b)

Obviously, neither (2.37 a) nor (2.37 b) follows rigorously from (2.36); these are just two particularly plausible possibilities. A possible motivation for (2.37 a) is that it pairs V with χ_V and E with χ_E, thus keeping ventilation-layer quantities together and entrainment layer quantities together. A motivation for (2.37 b) is that the product EV is, in a sense, characteristic of the PBL as a whole, so that it can plausibly appear symmetrically in the expressions for χ_E and χ_V.

Substituting the previously mentioned numerical values for the quantities on the right-hand-sides of (2.37 a), we obtain $\chi_V = 1.31 \times 10^{-2}$ and $\chi_E = 1.07 \times 10^{-2}$. Similarly, (2.37 b) gives $\chi_V = \chi_E = 1.18 \times 10^{-2}$. These values are reasonably close to those deduced from the LES results in Section 2.2, i.e. $\chi_V = 1.22 \times 10^{-2}$ and $\chi_E = 1.02 \times 10^{-2}$.

We can now substitute (2.37 a) or (2.37 b) back into (2.25), to obtain an expression for σ. From (4.7 a) we obtain:

$$\sigma = \tfrac{1}{2}\,;$$

(2.38 a)

and from (2.37 b):

$$\sigma = \frac{1}{1+\frac{E}{V}}\,.$$

(2.38 b)

Since E and V are practically equal in the LES results under discussion here, (2.38 a) and (2.38 b) give essentially the same numerical value for σ, and both are reasonably

consistent with the LES results presented in Section 2.3, which gave σ close to *1/2*. It would be useful to have observations or LES results for which E and V differed appreciably; if σ was also known, this would allow us to choose between (2.38 a) and (2.38 b).

2.5 Interiors

Up to this point we have discussed only the ventilation and entrainment layers. Now it is time to consider the interior of the PBL. The purpose of this Section is to show how the "well mixed" assumption can be relaxed by using a simple second-order closure, within the context of our bulk mass flux model.

We assume that the variance budget of the PBL's interior satisfies

$$\frac{\partial}{\partial t}\overline{\psi'^2} = -2\frac{F_\psi}{\rho}\frac{\partial \overline{\psi}}{\partial z} - \frac{1}{\rho}\frac{\partial}{\partial z}(\rho\overline{w'\psi'\psi'}) - 2\varepsilon_\psi .$$

(2.39)

Advection by the mean flow has been neglected, and we have assumed for simplicity that ψ is a conservative variable. (This assumption is not necessary and can easily be relaxed.) We now model each term of (2.39), following the methods introduced earlier. The variance itself is replaced by (2.5). The triple correlation in the transport term is replaced by (2.6). The dissipation is modeled by

$$\varepsilon_\psi = \frac{\overline{\psi'^2}}{\tau_{dis}} = \frac{\sigma(1-\sigma)}{\tau_{dis}}\left(\frac{F_\psi}{M_c}\right)^2 ,$$

(2.40)

where τ_{dis} is a dissipation time scale whose functional dependence on σ will be discussed later. With the assumptions that σ and M_c are independent of height, we find that

$$\frac{\partial}{\partial t}\left[\sigma(1-\sigma)\left(\frac{F_\psi}{M_c}\right)^2\right] = -2\frac{F_\psi}{\rho}\frac{\partial\overline{\psi}}{\partial z} - \frac{M_c(1-2\sigma)}{\sigma(1-\sigma)}\frac{1}{\rho}\frac{\partial}{\partial z}\left[\sigma(1-\sigma)\left(\frac{F_\psi}{M_c}\right)^2\right] - \frac{2\sigma(1-\sigma)}{\tau_{dis}}\left(\frac{F_\psi}{M_c}\right)^2 .$$

(2.41)

It is interesting to consider the equilibrium ($\partial / \partial t = 0$) solutions of (2.41) for two limiting cases. First, suppose that $\sigma = 1/2$, so that the middle term (the transport term) of (2.41) drops out. Then we get

$$F_\psi = -\frac{M_c^2\tau_{dis}}{\sigma(1-\sigma)}\frac{1}{\rho}\frac{\partial\overline{\psi}}{\partial z} .$$

(2.42)

This is a down-gradient diffusion formula.

Next, suppose that $\sigma << 1$, as in the case of cumulus convection. Then (2.41) reduces to

$$\frac{\partial F_\psi}{\partial z} = -M_c\frac{\partial\overline{\psi}}{\partial z} .$$

(2.43)

This is the "compensating subsidence" formula that has become familiar in cumulus parameterization theories. (The "detrainment" terms that appear in cumulus parameterizations can be included here too by relaxing our simplifying assumption that M_C is independent of height.)

In short, (2.41) includes both downgradient mixing and "compensating subsidence" as special cases.

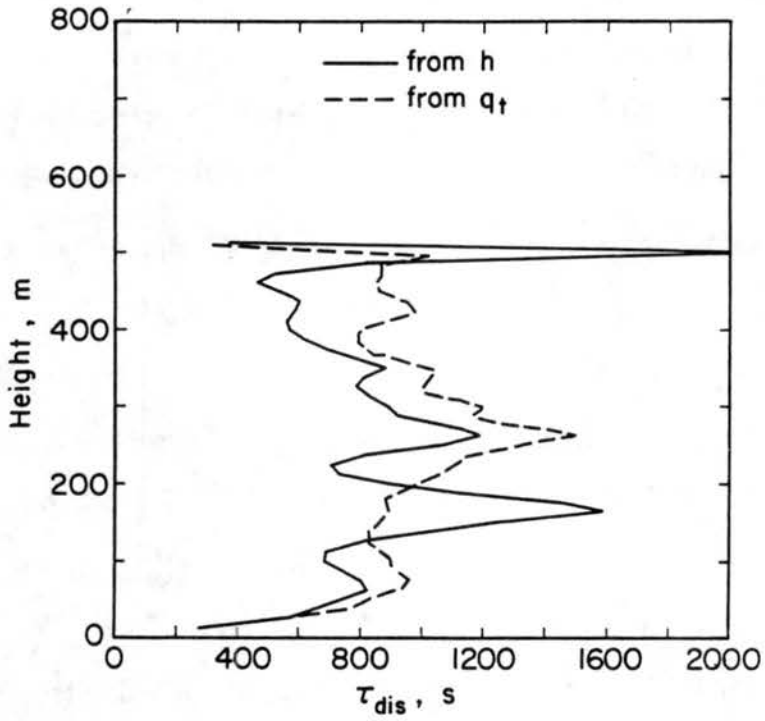

Figure 2.6: Vertical profiles of τ_{dis}, as determined from the LES results for dissipation of h (solid line) and q_t (dashed line).

Fig. 2.6 shows the dissipation time scale obtained from the LES results, as a function of height, determined by using

$$\tau_{dis} = \frac{\overline{\psi'^2}}{\varepsilon_\psi}, \tag{2.44}$$

for both h (solid line) and q_t (dashed line). Near the mid-level of the PBL, τ_{dis} is on the order of a thousand seconds. It is considerably shorter near the surface and the PBL top. This might be because the resolved-scale variances are small near the edges of the PBL, or it might be because dissipation is actually more effective in those regions where small eddies are dominant. We use a single, height-independent value of τ_{dis} in our model. Further discussion of τ_{dis} is given later.

We can use these results in either of two ways, both of which allow us to relax the "well mixed" assumption. On the one hand, the equilibrium solution of (2.41) gives a constraint on $\partial\overline{\psi}/\partial z$ similar to that proposed by Wyngaard and Brost (1984). In fact, one way to proceed from here would be to adopt the formulae for $\partial\overline{\psi}/\partial z$ and F_ψ proposed by Wyngaard and Brost (e.g., their Eq. 46), and to force consistency with our model. This approach would yield constraints on σ and M_c.

The other possible application of (2.41) is as follows. Note that (2.41) is hyperbolic; only the first derivative with respect to z of $\sigma(1-\sigma)\left(F_\psi / M_c\right)^2$ appears, and it is multiplied by the "velocity" $M_c(1-2\sigma)/[\rho\sigma(1-\sigma)]$. This "velocity" is upward (positive) if $\sigma < 1/2$, and downward (negative) if $\sigma > 1/2$. It follows that the single boundary condition on $\sigma(1-\sigma)\left(F_\psi / M_c\right)^2$ must be applied at level S if $\sigma < 1/2$, and at level B if $\sigma > 1/2$. We cannot force the surface flux to satisfy the bulk aerodynamic formula and the flux at level B to satisfy (2.16) simultaneously, unless some additional freedom is introduced.

The needed freedom lies in the choice of $\partial\overline{\psi}/\partial z$, which is unknown at this point anyway. We now assume that $\partial\overline{\psi}/\partial z$ is constant with height, and drop the time-derivative term of (2.42). This leads to an ordinary differential equation for F_ψ, which, using hydrostatics, can be written as

$$\frac{(1-2\sigma)}{M_c}\left(\frac{\partial F_\psi}{\partial p}-\frac{F_\psi}{\delta p_*}\right)=-\frac{\partial\overline{\psi}}{\partial p}, \tag{2.45}$$

where

$$\delta p_* \equiv \frac{gM_c\hat{\tau}}{\sigma(1-\sigma)(1-2\sigma)},$$

(2.46)

and

$$\hat{\tau} \equiv (1-2\sigma)^2 \tau_{dis}.$$

(2.47)

We assume that $\hat{\tau}$ is independent of σ. The motivation for this assumption is explained in Appendix C.

The solution of (2.45) is

$$F_\psi = M_c\left[\frac{\delta p_*}{(1-2\sigma)}\frac{\partial\overline{\psi}}{\partial p} + A\exp\left(\frac{p-p_B}{\delta p_*}\right)\right],$$

(2.48)

where A is an arbitrary constant. In order to maintain consistency of (2.48) with the imposed fluxes at the top and bottom of the PBL, we must choose appropriate values of $\partial\overline{\psi}/\partial p$ and A.

In this way, we find that

$$\frac{\partial\overline{\psi}}{\partial p} = \frac{(1-2\sigma)}{M_c\delta p_*}\left[\frac{\left(F_\psi\right)_S - \left(F_\psi\right)_B\exp\left(\frac{\delta p_M}{\delta p_*}\right)}{1-\exp\left(\frac{\delta p_M}{\delta p_*}\right)}\right],$$

(2.49)

and

$$F_\psi = \frac{\left(F_\psi\right)_S\left[1-\exp\left(\frac{p-p_B}{\delta p_*}\right)\right] + \left(F_\psi\right)_B\left[\exp\left(\frac{p-p_B}{\delta p_*}\right) - \exp\left(\frac{\delta p_M}{\delta p_*}\right)\right]}{1-\exp\left(\frac{\delta p_M}{\delta p_*}\right)}.$$

(2.50)

These results show how the mean gradient and the flux profile are determined for given values of the fluxes at levels S and B and the other parameters. Note from (2.49) that $\partial\overline{\psi}/\partial p$ vanishes for σ = 1/2. Inspection of (2.50) confirms that F_ψ satisfies the appropriate boundary conditions at levels S and B.

Obviously, $\delta p_M / \delta p_*$ is a key parameter in (2.49 - 2.50). It can be written as

$$\frac{\delta p_M}{\delta p_*} = \frac{\sigma(1-\sigma)(1-2\sigma)\delta p_M}{gM_c\hat{\tau}} .$$

(2.51)

As an example, Fig. 2.7 shows how $\delta p_M / \delta p_*$ varies with σ, for the particular case M_c = 0.4 kg m^{-2} s^{-1}, δp_M = 50 mb. The solid line is for $\hat{\tau}$ = 1 second, and the dashed line is for $\hat{\tau}$ = 10 seconds (see Appendix C for a discussion of $\hat{\tau}$). Note that $\delta p_M / \delta p_*$ passes through zero for σ = 1/2. As is apparent from (2.51), $\delta p_M / \delta p_*$ decreases as $\hat{\tau}$ increases. In this example, for $\hat{\tau}$ = 1 second $\delta p_M / \delta p_*$ can be of order $\pm 10^2$ for σ moderately different from 1/2. Smaller values of $\delta p_M / \delta p_*$ are favored by a stronger convective mass flux and larger values of $\hat{\tau}$.

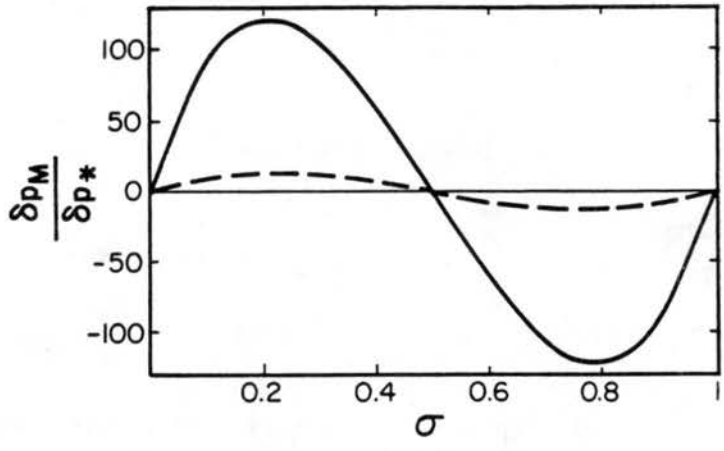

Figure 2.7: The variation of $\delta p_M / \delta p_*$ with σ, for the particular case M_c = 0.4 kg m^{-2} s^{-1}, δp_M = 50 mb. The solid line is for $\hat{\tau}$ = 1 second, and the dashed line is for $\hat{\tau}$ = 10 seconds.

Extending this example, Fig. 2.8 shows how $\partial\overline{\psi}/\partial p$ varies with σ. Again, the solid line is for $\hat{\tau}$ = 1 second, and the dashed line is for $\hat{\tau}$ = 10 seconds. Here we consider potential temperature, θ (Fig. 2.8 a), and the mixing ratio of water vapor, q (Fig. 2.8 b). The "edge" fluxes are assumed to be $(F_\theta)_S$ = 0.1 kg K m^{-2} s^{-1}, $(F_\theta)_B$ = -0.02 kg K m^{-2} s^{-1}, and $(F_q)_S$ = 3 x 10^{-5} kg m^{-2} s^{-1} and $(F_q)_B$ = 2.5 x 10^{-5} kg m^{-2} s^{-1}. For potential temperature, the results are plotted as K (50 mb)$^{-1}$, and for moisture they are plotted as g kg^{-1} (50 mb)$^{-1}$. The figure shows that the sign of $\partial\overline{\theta}/\partial p$ depends on σ; positive values (upward decrease) occur for $\sigma > 1/2$, and negative values (upward increase) for $\sigma < 1/2$. In contrast, the sign of $\partial\overline{q}/\partial p$ is positive (upward decrease) for all values of σ. The different behaviors of $\partial\overline{\theta}/\partial p$ and $\partial\overline{q}/\partial p$ arise from the differences in their respective presecribed fluxes at levels S and B. With the values of these fluxes that we have prescribed for this example, observations suggest (e.g., Wyngaard and Brost, 1984) that potential temperature should increase upward and water vapor mixing ratio should decrease upward. Our model predicts such a result for σ less than 1/2. The numerical values of the vertical gradients are qualitatively reasonable. The gradients become stronger as $\hat{\tau}$ decreases, for a given value of σ.

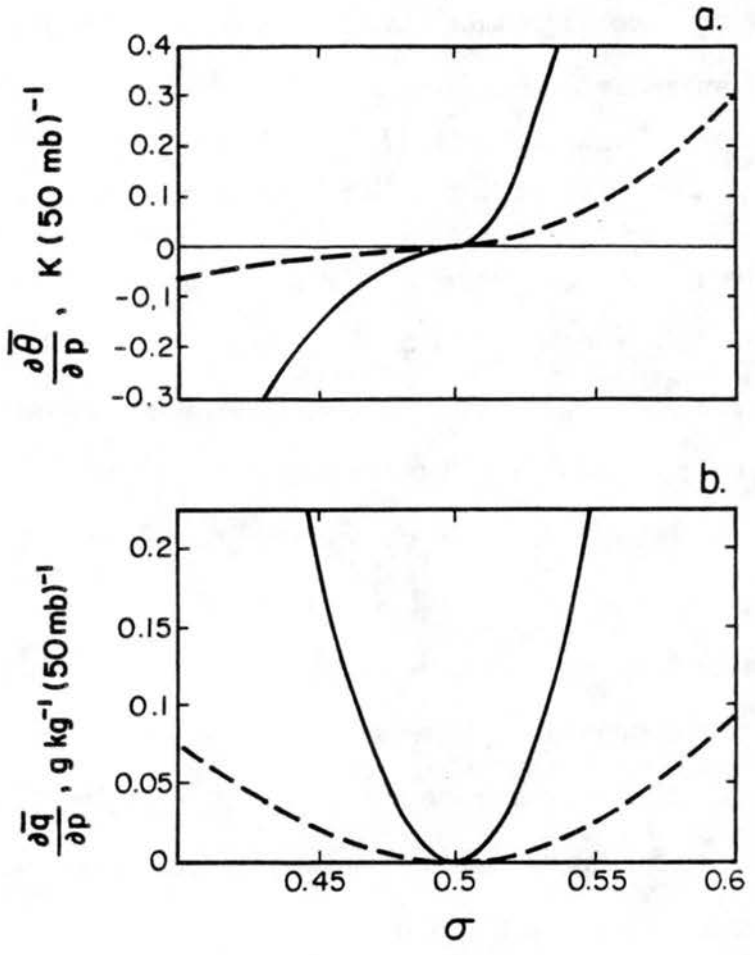

Figure 2.8: As in Fig. 2.7, but for the variation of $\partial \overline{\psi} / \partial p$ with σ: a) potential temperature, in units of K (50 mb)$^{-1}$; b) the mixing ratio of water vapor, in units of g kg^{-1} (50 mb)$^{-1}$.

Fig. 2.9 shows the variations of the fluxes of potential temperature and moisture with height, from the surface to the PBL top. As before, the solid line is for $\hat{\tau} = 1$ second, and the dashed line is for $\hat{\tau} = 10$ seconds. Larger $\hat{\tau}$ favors more linear flux profiles.

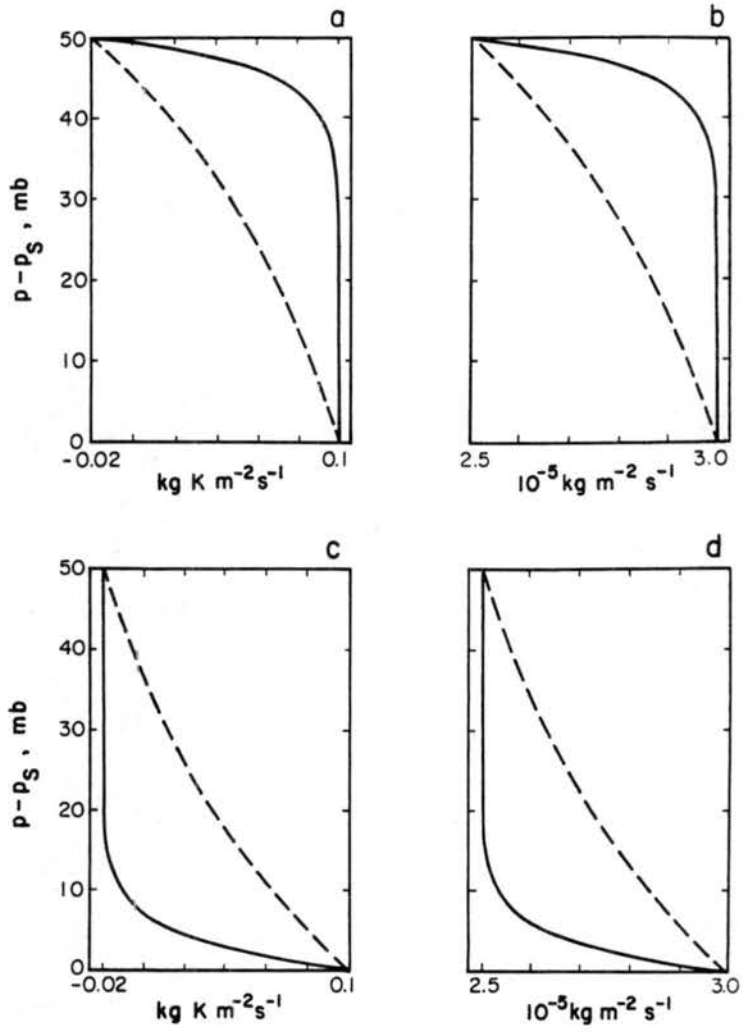

Figure 2.9: As in Fig. 2.7, but for the variations of the fluxes of potential temperature and moisture with height, from the surface to the PBL top: a) Potential temperature flux for $\sigma = 0.52$; b) moisture flux for $\sigma = 0.52$; c) potential temperature flux for $\sigma = 0.48$; d) moisture flux for $\sigma = 0.48$.

As discussed earlier, there is reason to believe that σ is often close to 1/2. For $\delta p_M / \delta p_* << 1$, which can be interpreted [see (2.46) or Fig. 2.7] as σ close to 1/2, (2.50) and (2.49) can be approximated by

$$F_\psi \equiv \left(F_\psi\right)_B\left(\frac{p_S - p}{\delta p_M}\right) + \left(F_\psi\right)_S\left(\frac{p - p_B}{\delta p_M}\right)$$
$$+\tfrac{1}{2}\left(\frac{\delta p_M}{\delta p_*}\right)\left(\frac{p - p_B}{\delta p_M}\right)\left(\frac{p_S - p}{\delta p_M}\right)\left[\left(F_\psi\right)_B - \left(F_\psi\right)_S\right],$$

(2.52)

and

$$\frac{\partial \overline{\psi}}{\partial p} \equiv \frac{g\hat{\tau}}{\sigma(1-\sigma)(\delta p_M)^2}\left(\frac{\delta p_M}{\delta p_*}\right)\left\{\left[\left(F_\psi\right)_B - \left(F_\psi\right)_S\right] + \tfrac{1}{2}\frac{\delta p_M}{\delta p_*}\left[\left(F_\psi\right)_B + \left(F_\psi\right)_S\right]\right\},$$

(2.53)

respectively. To obtain (2.53) from (2.49), we have used (2.46). In (2.52) we have kept terms of first order in $\delta p_M / \delta p_*$, while in (2.53) we have kept terms of second order. Since (2.52) is quadratic in p, differentiating it twice with respect to p gives a constant, which is compatible with our assumed constant value of $\partial \overline{\psi} / \partial p$.

According to (2.53), $\partial \overline{\psi} / \partial p$ vanishes for σ = 1/2, since this is the limit $\delta p_M / \delta p_* \to 0$. In this same limit, (2.52) reduces to the familiar linear flux profile. We conclude that our model reduces to the classical well mixed layer for $\sigma = 1/2$.

Suppose that F_ψ is independent of height, as in the water-vapor example given above. Then (2.53) reduces to

$$\frac{\partial \overline{\psi}}{\partial p} \equiv \frac{g\hat{\tau}}{\sigma(1-\sigma)(\delta p_M)^2}\left(\frac{\delta p_M}{\delta p_*}\right)^2 F_\psi.$$

(2.54)

For $F_\psi > 0$, as in the case of an upward moisture flux, (2.54) predicts that $\overline{\psi}$ decreases upward. This is consistent with observations showing that the mixing ratio of water vapor typically decreases upward in strongly entraining boundary layers (e.g., Wyngaard and

Brost, 1984). As a second special case, suppose that $\left|\left(F_\psi\right)_B\right| << \left|\left(F_\psi\right)_S\right|$, which is typically true for the potential temperature flux in convective PBLs. Then (2.53) reduces to

$$\frac{\partial\overline{\psi}}{\partial p} \cong \frac{-g\hat{\tau}}{\sigma(1-\sigma)(\delta p_M)^2}\left(\frac{\delta p_M}{\delta p_*}\right)\left[1-\tfrac{1}{2}\left(\frac{\delta p_M}{\delta p_*}\right)\right]\left(F_\psi\right)_S$$
$$\cong \frac{-g\hat{\tau}}{\sigma(1-\sigma)(\delta p_M)^2}\left(\frac{\delta p_M}{\delta p_*}\right)\left(F_\psi\right)_S. \tag{2.55}$$

For the case of an upward surface potential temperature flux, with $\sigma < \frac{1}{2}$ (i.e., $\delta p_m/\delta p^* > 0$), (2.55) predicts that the potential temperature increases upward, i.e. the flux is countergradient; again, this is consistent with observations (e.g., Wyngaard and Brost, 1984).

If we truncate (2.53) at first order in $\delta p_M / \delta p_*$, substitute into (2.54), and use (2.47), we obtain

$$F_\psi \cong \left(F_\psi\right)_B\left(\frac{p_S - p}{\delta p_M}\right) + \left(F_\psi\right)_S\left(\frac{p - p_B}{\delta p_M}\right)$$
$$+\tfrac{1}{2}\frac{(p-p_B)(p_S-p)\sigma(1-\sigma)}{g\hat{\tau}}\frac{\partial\overline{\psi}}{\partial p}. \tag{2.56}$$

The first line on the rhs of (2.56) is the linear flux profile characteristic of a well mixed layer, and the second represents a downgradient diffusion. According to (2.56), when the PBL fluctuates away from a well mixed structure, the flux profile changes in such a way as to damp the fluctuation. This seems quite plausible.

2.6 Summary and conclusions

We have presented what we believe to be an internally consistent PBL model that has a parameterized vertical structure but also includes a simple second-order closure.

In Section 2.2, we proposed a new way to determine the updraft and downdraft properties applicable to a mass flux model by using vertical motion statistics obtained from observations, LES, or even higher-order closure. This method cannot be used to determine σ and M_c in a bulk mass flux model, however, because the needed inputs are not available in such a model.

In Section 2.3, we used imposed consistency conditions among the various fluxes, and applied suitable "boundary conditions" on the updraft properties at the top of the ventilation layer and the downdraft properties at the base of the entrainment layer, to develop simple relationships among mass fluxes, fractional areas, and mixing parameters.

In Section 2.4, we presented methods, applicable to the bulk mass flux model, to determine the convective mass flux and σ. So far as we are aware, the results obtained in Section 4 represent the first physically based method to determine σ.

By applying the mass flux model to the interior of the PBL, we obtained, in Section 2.5, an idealized but physically based approach to relaxing the "well mixed" assumption that has been such a mainstay of bulk boundary layer models over the past 25 years or so. In particular, the variance budget equation determines the turbulent fluxes and the gradients of the mean state in the interior of the PBL. These vertical profiles are solved for analytically. Under appropriate conditions, the variance budget equation can reduce to downgradient diffusion, or to a "compensating subsidence" formula similar to that used in

cumulus parameterizations. This represents a first attempt to marry the approaches of higher-order closure and convective mass flux closure. Appendix A extends this higher-order closure approach to the entrainment and ventilation layers.

In the future, we hope to generalize the model to allow σ and M_c to vary with height, possibly by following the approach sketched in Appendix A.

The variance balance equation presented in Section 2.5, together with the TKE-prediction equation given in Appendix B, comprise what amounts to a simple "second order closure," formulated in terms of the mass flux model, and applicable to the bulk boundary layer model. This approach can be put into perspective, as follows.

In recent years, two new approaches have emerged for including the effects of the planetary boundary layer (PBL) in large-scale models. The first involves coupling the large-scale model with a "bulk" PBL model. Advantages of the bulk approach are its simplicity and computational economy. A disadvantage, up to now, is its inability to represent the internal structure of the PBL.

A second approach is to make use of a higher-order-closure model in which one or more turbulence variables are prognostically determined. This idea has aroused widespread interest, but has been adopted in practice only by K. Miyakoda's group at the Geophysical Fluid Dynamics Laboratory (Miyakoda and Sirutis, 1977; Miyakoda *et al.*, 1983). Advantages of this approach are its relatively high degree of physical sophistication and its ability to predict the internal structure of the PBL. Disadvantages are its requirement for high vertical resolution, and its relative complexity. Both of these lead to considerable computational expense.

The present model can be viewed as an attempt to merge these two approaches, retaining the advantages of each, and giving rise to what we call a "second-order bulk model", or S.O.B. Our model also makes use of a convective mass flux, a concept which has been important in the development of cumulus parameterizations. Fig. 2.10 summarizes the conceptual pedigree of our model, relative to earlier models used in boundary-layer and cumulus parameterizations.

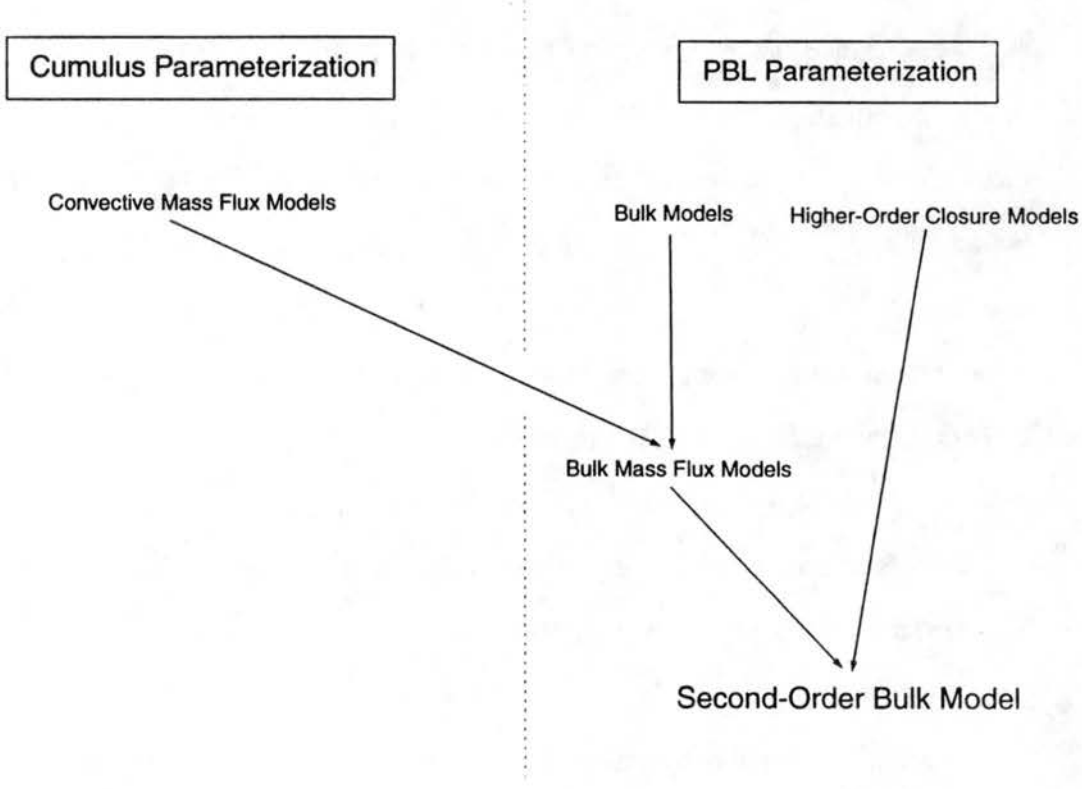

Figure 2.10: Diagram summarizing the relationship of the present model to earlier models used in boundary-layer and cumulus parameterizations.

Although the approach presented here is highly idealized, it is potentially useful for parameterization and also for physical understanding of the results of more complex models.

Q. Shao

CHAPTER 3

Plume Generation in the Entrainment Layer by the Cloud-Top Processes

3.1 Introduction

As discussed by Randall et al. (1992; hereafter referred to as RSM), the convective PBL consists of a relatively deep interior region bounded above by a thin entrainment layer and below by a thin ventilation† layer. The interior has modest or even negligible gradients of the conservative mean fields (e.g., liquid water static energy and total mixing ratio), and is dominated by "plumes" with length scales comparable to the PBL depth. The entrainment and ventilation layers are typically marked by sharp gradients of the mean fields, and are dominated by smaller eddies. The plumes and small eddies produce mixing, which results in turbulent fluxes of various physical properties.

Since the ventilation and entrainment layers serve as the boundaries of the interior of the PBL, the plumes in the interior must originate in these two layers. It is the updrafts in

†. We use the term "ventilation layer" to refer to what is usually called the surface layer. Our motivation for this non-standard terminology is as follows: The "entrainment layer" is named for the process associated with it, namely entrainment. A key process associated with the surface layer is ventilation, i.e. modification of the surface properties by the action of the air moving over it, e.g. advecting away sensible heat and moisture. We therefore introduce "ventilation layer" as a construct in parallel with "entrainment layer."

the ventilation layer (Wilczak, 1984) and downdrafts in the entrainment layer (Nicholls, 1989) that transfer the properties of these two layers into the interior, and produce the plumes there (Moeng and Schumann, 1991). Of course, the outer boundaries of the PBL are the Earth's surface at the bottom and the free atmosphere just above the entrainment layer. The parcels inside the ventilation layer are continually being "charged" with surface properties. The properties of a steady surface layer can be represented statistically using the flux-profile relationships given by Businger et al., (1971), which involve surface properties such as roughness length and temperature. The updrafts emerging from the ventilation layer typically have properties very different from those of the surface itself (Wilczak, 1984; Schols et al., 1985). Similarly, entrainment constantly introduces free-atmospheric (FA) parcels into the entrainment layer (Caughey et al., 1982), but the downdrafts emerging from the entrainment layer typically have properties radically different from those of the free atmosphere (Nicholls, 1989; Khalsa, 1993).

These observations raise questions regarding how parcels are assembled and/or selected in the ventilation and entrainment layers for incorporation into the updrafts and downdrafts, respectively. How much information is brought by updrafts from the surface into the ventilation layer, and by downdrafts from the free atmosphere into the entrainment layer? How is this information carried into the interior of the PBL?

Organized updrafts from the unstably stratified ventilation layer have been studied extensively over several decades (Taylor, 1958; Priestly, 1959; Kaimal and Businger, 1970; Frisch and Businger, 1973; Kaimal, 1974; Antonia and Chambers, 1978; Antonia et al., 1979, 1983; Phong-Anant et al., 1980; Khalsa, 1980; Wilczak, 1984; Wilczak and

Businger, 1984; Schols et al., 1985). As described by many authors, thermals are widely observed in field experiments as ramp structures. They tilt in the direction of the mean wind and move as entities. The height of their base is, on average, 1.2 m above the ground in the Kansas data (Kaimal, 1974). The fractional area covered by thermals is about 0.42 (e.g., Frisch and Businger, 1973; Antonia et al., 1983). The correlation between vertical velocity and temperature is positive inside thermals (Kaimal and Businger, 1970; Kaimal, 1974; and Wilczak, 1984), and contributes about 25% to 40% of the average local heat flux (Antonia and Chambers, 1978; Phong-Anant et al., 1980; Schols et al., 1985). Since thermals contribute little (<10%) to the mean local fluxes for neutrally or stably stratified ventilation layers (Phong-Anant et al., 1980), we discuss only the unstably stratified ventilation layer, which is buoyantly driven.

In contrast, downdrafts from the entrainment layer of the cloud-topped PBL have attracted attention only in more recent years (Mahrt and Paumier, 1982; Caughey et al., 1982; Nicholls and Turton, 1986; Nicholls, 1989; Moeng and Schumann, 1991; RSM; Moeng et al, 1992; Khalsa, 1993; and Wang and Albrecht, 1993). It has been suggested that they play an important role in the breakup of stratocumulus cloud decks through cloud-top entrainment instability (CTEI) (Randall, 1980 a; Deardorff, 1980; Kuo and Schubert, 1988; Siems et al, 1992), which in turn may be important for climate dynamics (Randall et al., 1984). As discussed in the studies mentioned above, the downdrafts are relatively cold and dry on average, compared with their surroundings, and have negative buoyancy (corresponding to upward heat flux). By analyzing the variances of the mean quantities, however, Nicholls (1989) also found some warmer and wetter regions in the downdrafts. The negative buoyancy of the downdrafts is largely due to evaporative and

radiative cooling (Nicholls and Turton, 1986; Nicholls, 1989; Moeng and Schumann, 1991; Khalsa, 1993; and Wang and Albrecht, 1993). Evaporative cooling is strongest when a mixed parcel consisting of cold-moist cloudy air and warm-dry FA air is marginally saturated (Nicholls and Turton, 1986; Siems et al., 1991). The relative humidity of a mixed parcel depends on the amount of FA air involved. The average fraction of FA air in downdrafts varies between 0.7% and 3% (Nicholls, 1989; Khalsa, 1993). On the other hand, the strength of the radiative cooling is related to the cloud liquid water concentration near cloud top (e.g., Slingo et al., 1982). Today there is no doubt that radiative cooling enhances entrainment near cloud top, although earlier there was a protracted debate about the mechanism through which radiative cooling drives turbulence (Oliver et al., 1978; Kahn and Businger, 1979; Deardorff, 1981; Caughey et al., 1982; Slingo et al., 1982; Brost et al., 1982; Twomey, 1983; Nieuwstadt and Businger, 1984; Randall, 1980 b; Caughey and Kitchen, 1984; Curry, 1986).

The relative importance of evaporative and radiative cooling in driving turbulent mixing near cloud top remains an unsolved problem. By comparing theoretical calculations of the evaporative cooling with observations of the radiative cooling, Nicholls and Turton (1986) concluded that the evaporative cooling is generally stronger than the radiative cooling, except when the mixing fraction of FA air is very large (~100%) or very small (~0%). In the downdrafts, where the fraction of the FA air is small, radiative cooling dominates. Nicholls (1989) studied data collected during five missions of the Meteorological Research Flight Hercules aircraft in horizontally uniform, unbroken sheets of stratocumulus over the sea near the United Kingdom. By a detailed analysis of the data collected on a flight leg slightly below cloud top, Nicholls concluded

that entrainment mixing combined with evaporative cooling could produce only positive buoyancy fluctuations in almost all cases, and that the corresponding mean virtual temperature excess in the downdrafts ranged from -0.002 K to 0.05 K. Since the actual observed values of the mean virtual temperature perturbations in the downdrafts ranged from -0.04 K to -0.07 K, he concluded that the incorporation of radiatively cooled, cloudy air into downdrafts must be the primary mechanism for producing negative buoyancy near cloud top. He also found that a parcel typically remained in the radiatively cooled layer for a "residence time" of about 150 seconds, which was long enough to acquire the observed cooling before sinking into a downdraft. Using flight data gathered on 7 July 1987 during FIRE, Khalsa (1993) showed that at cloud top the maximum evaporative cooling for θ_v due to mixing was about -0.026 K, while the total cooling for θ_v observed was -0.068 K. He therefore attributed -0.042 K to radiative cooling. By analyzing flight data collected on 3 July during FIRE, Wang and Albrecht (1993) found that near cloud top evaporative cooling dominated the radiative cooling for their case, with an average of -0.08 K to -0.034 K for $\delta\theta_v$. The above studies show that the relative importance of evaporative versus radiative cooling varies from case to case, and that evaporative cooling can be either stronger or weaker than radiative cooling.

In the aforementioned studies, the updrafts in the ventilation layer were treated as entities, and their properties were studied using surface-layer similarity theory. These studies do not clearly show how the updrafts acquired their surface-like properties. Similarly, the downdrafts in the entrainment layer were conditionally sampled, and the ensemble properties of the downdrafts were analyzed by taking the average of the properties in all the downdrafts sampled, except in the study of Wang and Albrecht

(1993). Such compositing does not reveal how the downdrafts in the entrainment layer are formed. We ma ask, for example, why are some parcels in the downdrafts even wetter and warmer than their environment, as found by Nicholls (1989)? How do evaporation and radiation produce the cooling? How do these kinds of cooling depend on the amount of FA air mixed into a parcel?

To approach these problems, we first study the properties of individual parcels. The rising and sinking parcels are then grouped together to obtain the composite properties of the updrafts or downdrafts. The purpose of this paper is to quantitatively explore, from a "large-scale," statistical point of view, the process(es) governing the properties of the updrafts that emerge from the ventilation layer and the downdrafts that emerge from the entrainment layer. For the parcel-by-parcel-analysis, a statistical analysis is applied to LES results and to a tethered balloon dataset, as described in Section 2. Our results are given in Section 3, and concluding remarks in Section 4.

3.2 Data and methodology

The ventilation and entrainment layers are defined as follows. In a typical stratus-topped PBL, the vertical structure is as shown in Fig.3.1, where the solid line represents schematically the vertical profile of the total mixing ratio (vapor plus liquid), q_t. In the absence of drizzle, q_t is conservative. We define the ventilation layer as the shaded region between levels S and S-, and the entrainment layer as the shaded region between levels B and B+. Levels S, S-, B and B+ are defined in such a way so that in these layers

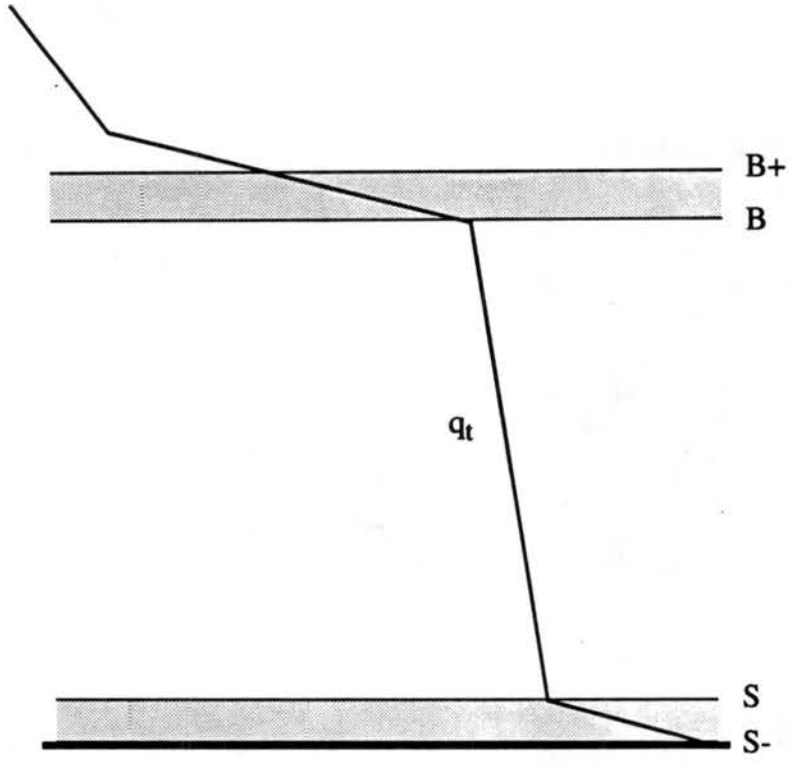

FIGURE 3.1: Diagram illustrating the mean profile of total water content for a convective boundary layer, and identifying the ventilation and entrainment layers.

typically the structures of the mean properties have sharp gradients, and the small- scale turbulent mixing is strong.

Our first dataset is a large eddy simulation (LES) field of a cloud-topped boundary layer generated by Moeng (1984, 1986) and reported by RSM. In the latter study, we identified the ventilation and entrainment layers in the LES results by analyzing the simulated moisture field. In RSM, we used four LES levels between *S*- and *S*, and another four between *B* and *B*+. Since each grid level consists of 80^2 cells, there are 25600 grid cells between *S*- and *S*, and a further 25600 cells between *B* and *B*+. In these study, we include only the cloudy air in the entrainment layer for the χ-space analysis.

Therefore there are less than 25600 cells between B and $B+$. The numbers of cloudy grid cells at each level in the entrainment layer, including levels B and $B+$, are shown in Table 1.

Table 3.1: The numbers of cloudy grid cells (n) and their percentage (%) of the total (6400) at each level in the entrainment layer.

Level		B	B+1	B+2	B+3	B+4	B+
Total cloudy cells	n	6376	6242	5638	3169	61	0
	%	99.6	97.5	88.1	49.5	0.95	0
Cloudy cells with w>0	n	2831	2870	2775	1740	42	0
	%	44.2	44.8	43.4	27.2	0.65	0
Cloudy cells with w<0	n	3545	3372	2863	1429	19	0
	%	55.4	52.7	44.7	22.3	0.30	0

The LES flow has deficiencies near the surface and the entrainment layer due to the numerical resolution. However, it provides us with detailed three-dimensional flow fields and is the only dataset that can be used for the detailed analysis given in this paper. A sounding or a flight dataset can only provide us with a one- or two-dimensional view of the atmospheric structure, and difficulties appear during the analysis of data since often the moisture can not be measured accurately, as is the case in the second data set we used.

This second dataset was obtained using a tethered balloon operated on San Nicolas Island during FIRE (Albrecht et al., 1988; Higgnett, 1991; Schubert et al., 1987; Hein et al., 1988). Data from 10 July 1987 are used here. Fig.3.2 shows the mean structure of the dry bulb temperature from the tethered balloon data. We have not attempted to evaluate the turbulent fluxes, so only mean structures were used to identify the entrainment layer, which is also shown in Fig.3.2. Level $B+$ (with 79 data points) is at 889.2 mb, and B

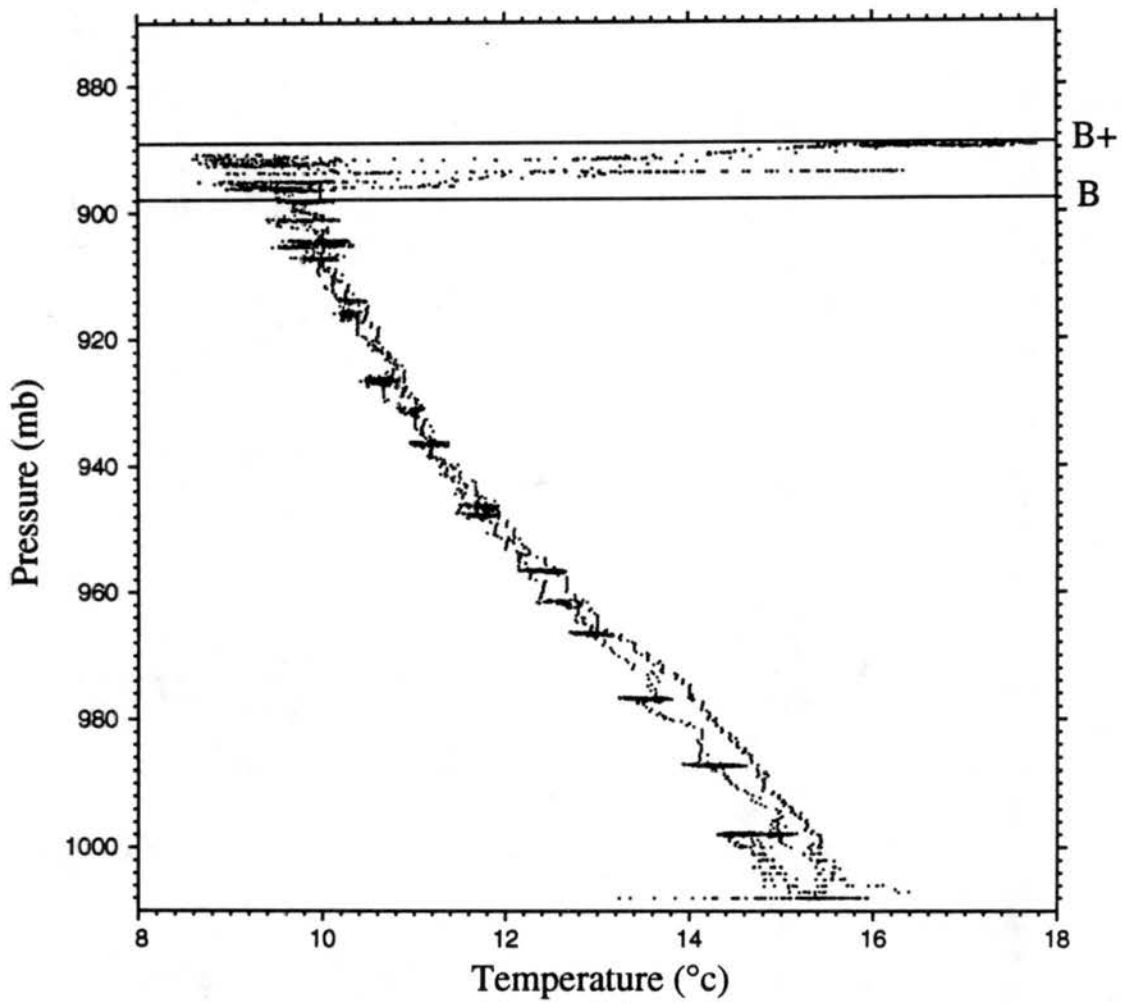

FIGURE 3.2: The mean structure of dry bulb temperature from the tethered balloon data. Levels B and B+ are indicated.

(with 77 data points) at is 898.2 mb. The 230 cloudy data points in between these levels are used as "parcels." We compared the tethered balloon data with rawinsonde data obtained at the same time and place (Schubert et al., 1987), shown in Fig.3.3, in order to investigate the sounding above the highest level reached by the tethered balloon. The maximum temperatures observed from the rawinsonde and the tethered balloon are about the same. Fig.3.4 shows the pressure at which the tethered balloon data was collected, as

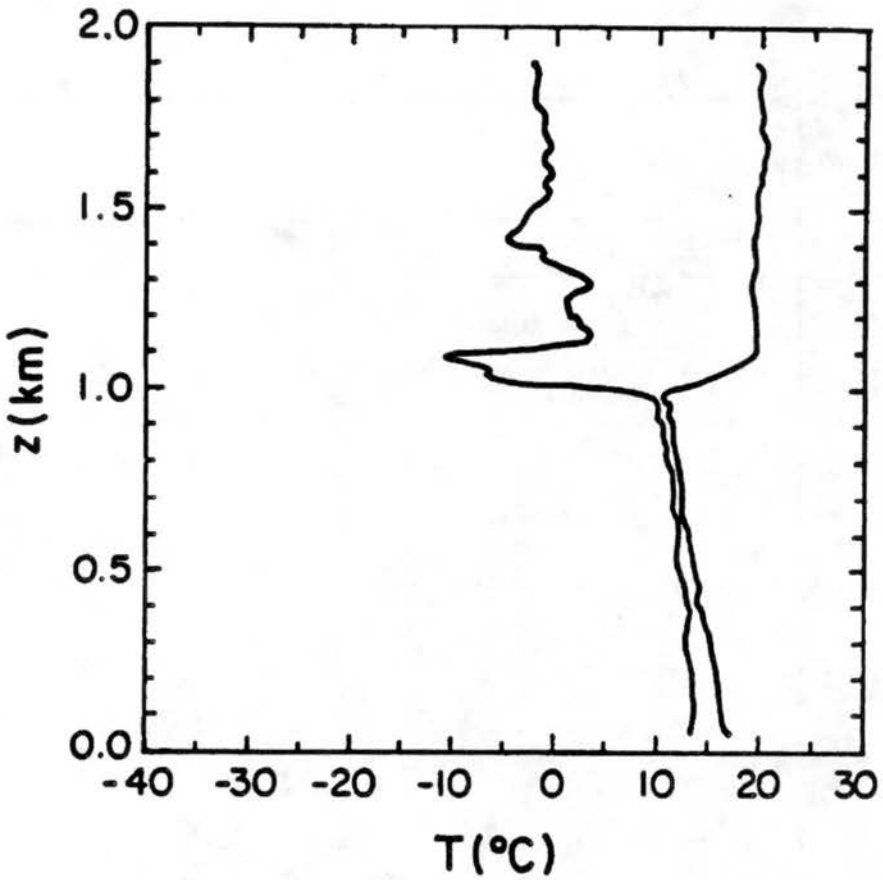

FIGURE 3.3: The rawinsonde sounding obtained at the same time and place as the tethered balloon sounding of Fig.3.2.

a function of time; the time interval used in the study is also indicated in the figure. The methods used to evaluate the total water content and the equivalent potential temperature from the balloon data are explained in Appendix D.

A conditional sampling method is needed to define the updrafts and downdrafts. Some previously used methods were surveyed in Table 1 of RSM; this survey will not be repeated here. For the ventilation layer only, vertical velocity (Priestly, 1959), temperature (Frisch and Businger, 1973) and high-frequency wind variance of the longitudinal velocity (Khalsa and Businger, 1977; Khalsa, 1980) have been used as

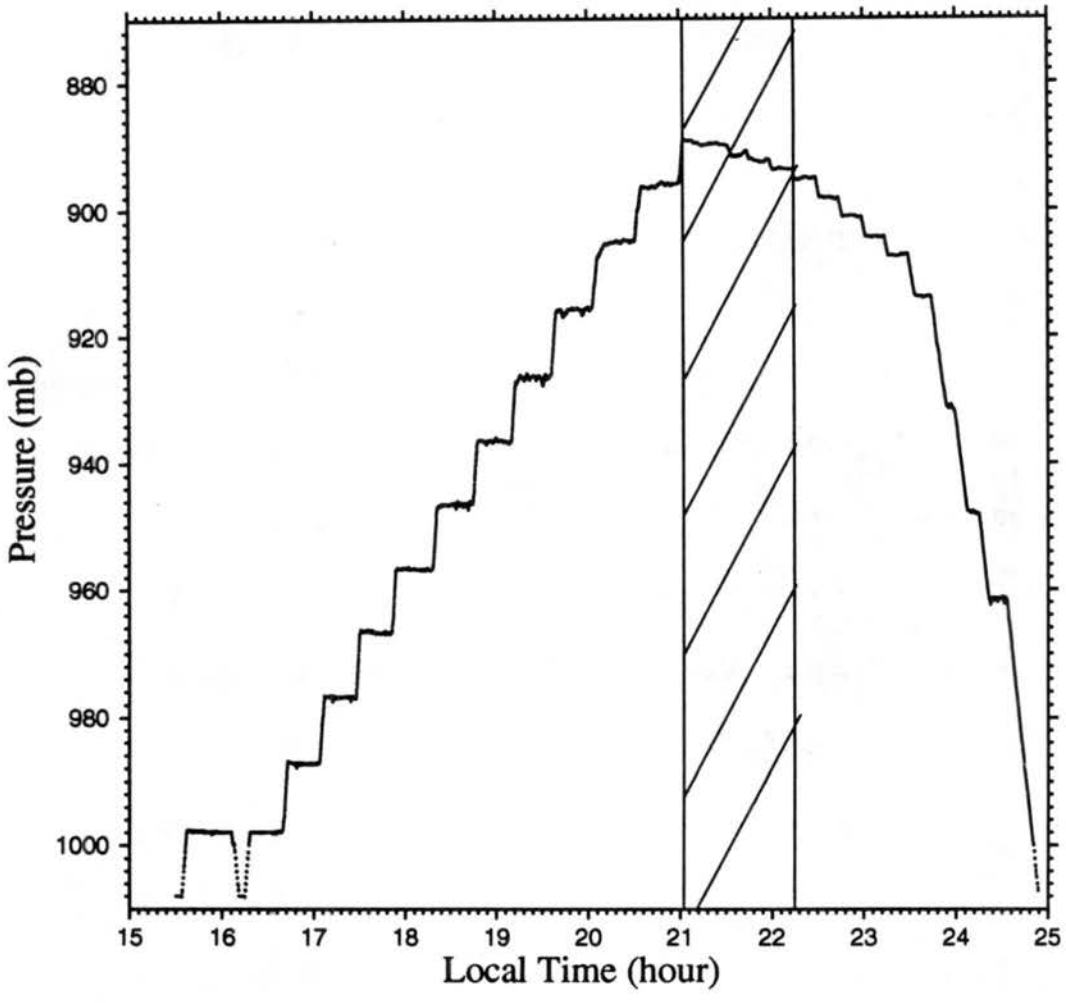

FIGURE 3.4: The pressure at which data was collected. The hatched area indicates the time period for this study.

indicators of the updrafts. Since, as stated above, in the updrafts of the ventilation layer vertical velocity and temperature are always positively correlated, the updrafts defined by vertical velocity and temperature should be very similar. As for the wind variance, Antonia et al. (1983) compared two conditional sampling techniques: one used both longitudinal velocity and temperature, and the other used temperature only. They found that the fraction occupied by and frequency of occurrence of the updrafts obtained with

these two methods were essentially the same. Hence any one of the methods mentioned above can be used to define the updrafts in the ventilation layer. In this study we use positive vertical velocity to indicate updrafts and negative vertical velocity to downdrafts for both ventilation and entrainment layers, as did RSM.

3.2.1 The ventilation layer

Within the ventilation layer, there exist parcels with various total mixing ratios, produced by mixing, in various proportions, the air from the interior of the PBL (represented by the mean properties at level *S*), with the air that has been charged with surface properties (represented by the mean properties at level *S*-). For the ventilation layer, we define the mixing fraction χ as follows: For each ventilation-layer parcel, χ is the mixing fraction of the air with surface properties, so that the total mixing ratio q_t is

$$q_t(\chi) = \chi\,(\overline{q_t})_{S-} + (1-\chi)\,(\overline{q_t})_S, \tag{3.1}$$

where the overbar denotes a horizontal average. With the known $q_t(\chi)$, χ can be evaluated from (2.1), as follows:

$$\chi = \frac{q_t - (\overline{q_t})_S}{(\overline{q_t})_{S-} - (\overline{q_t})_S}. \tag{3.2}$$

From (3.2) we can see that the mean properties at levels *S*- and *S* are crucial for determining χ. However, it is not easy to choose the level *S* objectively. In Appendix E we discuss the method by which we have chosen level *S* (and levels *B* and *B*+ as discussed in Section 2.2) in the present study. This method can be generalized for use in other similar

studies.

An implicit assumption used in (3.1) is that parcels which enter the ventilation layer through level S are characterized by the mean properties at S, while those from the lowest level, S-, are characterized by the mean properties at S-. Hence S and S- act as "pools" of two kinds of parcels. When the time scale for the change of the mean properties is much longer than that for the small scale mixing, these two pools can be regarded as independent. If this statement is exactly true, then according to (3.1) the q_t for each parcel inside the ventilation layer would be in the range between $(\overline{q_t})_{S-}$ and $(\overline{q_t})_S$, and so we would find $0 \le \chi \le 1$ in all cases. However, because of horizontal inhomogenities, the properties of parcels from level S and S- are variable, and in fact there are some parcels for which $\chi < 0$.

Parcels with $\chi < 0$ (or $\chi > 1$) can never be produced by mixing the mean properties at S and S-. We assume that no mixing has affected such parcels since they entered the ventilation layer, and refer to them as "unmixed" parcels.

Let the probability density function (pdf) for χ in the ventilation layer be denoted by $\Pi_V(\chi)$. Then $\Pi_V(\chi)\,d\chi$ gives the probability of encountering a parcel whose properties correspond to a value of χ in the range $(\chi, \chi + d\chi)$. The calculation of $\Pi_V(\chi)$ is as follows: For every parcel we can find χ from (3.2), using the known q_t. A range of χ will then be obtained for all of the parcels considered. We divide the range $-0.1 \le \chi \le 1.1$ into 120 groups so that $\Delta\chi = 0.01$ for each group. The parcels are then grouped according to their χ-values. Those data with $\chi < -0.1$ are grouped into $\chi = -0.11$ and those with $\chi > 1.1$ into $\chi = 1.11$. There are, therefore, altogether 122

groups of χ. By counting the number of parcels in each χ-bin, and dividing this number by the total parcel count, we obtain $\Pi_V(\chi)$. The total number of parcels considered depends on what $\Pi_V(\chi)$ represents. For example, when the LES dataset is used, if $\Pi_V(\chi)$ is for the whole ventilation layer, the total number is 25600, and if it is for one level of grid points, the total number is 6400.

After the parcels are grouped into different χ-bins, their properties are averaged in each group separately so that the results shown later in the χ-space represent the mean properties in that group, or the properties each parcel would have if all the properties of the parcels in that χ-bin were the same. We denote this mean for each χ-bin by "$\langle\ \rangle$."

The percentage of rising parcels at level S can be obtained from $\int_{\text{rising parcels}} \Pi_V(\chi)|_S d\chi$. Let us denote an arbitrary intensive scalar property of a parcel by ψ. Then the average of $\psi(\chi)$ for rising parcels at level S is

$$(\overline{\psi_u})_S = \frac{\int_{\text{rising parcels}} \psi(\chi)\,\Pi_V(\chi)|_S d\chi}{\int_{\text{rising parcels}} \Pi_V(\chi)|_S d\chi}. \tag{3.3}$$

This χ-analysis can be used to interpreted the physical meaning of the mixing parameter, χ_V, defined by RSM using

$$(\overline{\psi_u})_S - \overline{\psi}_S = \chi_V(\overline{\psi}_{S-} - \overline{\psi}_S). \tag{3.4}$$

Substituting (3.1) into (3.3) for $\psi(\chi)$, and (3.4) into (3.3) for $(\overline{\psi_u})_S$, we get

$$\overline{\psi_S}(1-\chi_V)+\overline{\psi_{S\text{-}}}\chi_V=\overline{\psi_S}\left(1-\frac{\int_{\text{rising parcels}}\chi\Pi_V(\chi)|_S d\chi}{\int_{\text{rising parcels}}\Pi_V(\chi)|_S d\chi}\right)+\overline{\psi_{S\text{-}}}\frac{\int_{\text{rising parcels}}\chi\Pi_V(\chi)|_S d\chi}{\int_{\text{rising parcels}}\Pi_V(\chi)|_S d\chi} \tag{3.5}$$

Under the assumption that $\overline{\psi_S}$ and $\overline{\psi_{S\text{-}}}$ are statistically independent, (3.5) gives

$$\chi_V=\frac{\int_{\text{rising parcels}}\chi\Pi_V(\chi)|_S d\chi}{\int_{\text{rising parcels}}\Pi_V(\chi)|_S d\chi}. \tag{3.6}$$

This shows that χ_V is a bulk value of χ characteristic of the updrafts as they emerge from the ventilation layer.

3.2.2 The entrainment layer

We now apply a similar analysis to the entrainment layer. The various parcels found in the entrainment layer are produced by mixing, in various proportions, air from the interior of the PBL with air that has recently been entrained. Of course, radiation and phase changes are also important. For the entrainment layer we define χ as follows: For each entrainment-layer parcel, χ is the mixing fraction of the air with free-atmospheric properties, so that the total mixing ratio q_t is

$$q_t(\chi)=\chi(\overline{q_t})_{B+}+(1-\chi)(\overline{q_t})_B. \tag{3.7}$$

From the known q_t of a parcel, χ can be evaluated from (3.1) as

$$\chi = \frac{q_t - (\overline{q_t})_B}{(\overline{q_t})_{B+} - (\overline{q_t})_B}. \tag{3.8}$$

A discussion similar to that given for (3.1) can be applied to (3.8). Again, when we find that $\chi < 0$ or $\chi > 1$, we assume that the parcels have not recently undergone mixing. From (3.8), parcels with $\chi < 0$ are wetter than $(\overline{q_t})_B$, and therefore are likely to be air from the PBL interior. We again denote these as "unmixed" parcels.

Eq. (3.8) has been used by many authors (Mahrt and Paumier, 1982; Nicholls and Turton, 1986; Kuo and Schubert, 1988; Siems et al., 1991; Duynkerke, 1993) to study theoretically the effect of entrainment mixing and evaporative cooling on buoyancy in the entrainment layer. A similar formula has also been used to calculate the mixing fraction of FA air in the downdrafts from the observations (Nicholls, 1989; Khalsa, 1993; and Wang and Albrecht, 1993):

$$\chi' = \frac{q'_t}{(\overline{q_t})_{B+} - (\overline{q_t})_B}, \tag{3.9}$$

Here $q'_t = q_t - (\overline{q_t})_{\text{obs}}$ is the departure of q_t from its horizontal average *at the observational level*. The quantity q_t is often replaced by the ozone mixing ratio, O_3, which is also conserved during mixing.

As far as we know, no one has discussed the difference between (3.8) and (3.9). It is easy to see that $(\overline{q_t})_B$ in (3.8) is replaced by $(\overline{q_t})_{\text{obs}}$ in (3.9). Only when the observational level used is level B itself are (3.8) and (3.9) the same. Generally, however, $(\overline{q_t})_{\text{obs}}$ is located at a level in between levels B and B+. Actually, χ' is the departure of

χ from its horizontal average at the observation level. Since the horizontal mean of χ at the observational level is

$$\bar{\chi} = \frac{(\bar{q}_t)_{\text{obs}} - (\bar{q}_t)_B}{(\bar{q}_t)_{B+} - (\bar{q}_t)_B}, \tag{3.10}$$

we see that

$$\begin{aligned} \chi - \bar{\chi} &= \frac{q_t - (\bar{q}_t)_B}{(\bar{q}_t)_{B+} - (\bar{q}_t)_B} - \frac{(\bar{q}_t)_{\text{obs}} - (\bar{q}_t)_B}{(\bar{q}_t)_{B+} - (\bar{q}_t)_B} \\ &= \frac{q_t - (\bar{q}_t)_{\text{obs}}}{(\bar{q}_t)_{B+} - (\bar{q}_t)_B} = \chi'. \end{aligned} \tag{3.11}$$

In other words, $\chi = \bar{\chi} + \chi'$, as would be expected. The actual mixing fraction is represented by χ, as given by (3.8). However, the effects of mixing on the local buoyancy of a parcel should be calculated using χ'. These effects will be described below, after evaporative and radiative cooling have been discussed.

For any non-conservative scalar field, say ψ, we can write

$$\psi(\chi) = \chi\overline{\psi_{B+}} + (1-\chi)\overline{\psi_B} + \delta\psi(\chi). \tag{3.12}$$

The $\delta\psi$ term of (3.12) represents the effects of sources and sinks. We can rewrite (3.12) as

$$\delta\psi(\chi) = \psi(\chi) - \overline{\psi_B} - \chi(\overline{\psi_{B+}} - \overline{\psi_B}). \tag{3.13}$$

By appropriate choice of ψ, we can use (3.13) to calculate the radiative and evaporative cooling of each parcel in the entrainment layer, as explained below. Of course, $\delta\psi$ is an

amount rather than a **rate**. This means that it represents the accumulated net change in ψ, due to sources and sinks, since some "initial condition." We consider the "initial time" for a parcel in the entrainment layer to be the moment at which it most recently entered the entrainment layer. The "initial value" of ψ at this time is taken as $\overline{\psi}_B$. Of course, in reality parcels generally have ψ different from $\overline{\psi}_B$ as they enter the entrainment layer, and this will lead to errors in $\delta\psi$. These limitations of our method should be kept in mind as our results are presented later.

The virtual liquid water static energy h can be defined, following Moeng (1986), as

$$h = c_p T_V + gz - Lq_l, \tag{3.14}$$

where T_V is virtual temperature, and q_l is the liquid water mixing ratio. The virtual liquid water static energy is approximately conserved under both moist adiabatic and dry adiabatic processes, So that only radiative cooling and mixing can change it. Let $\psi = h$ in (3.13). Then

$$\delta h_R(\chi) = h(\chi) - \overline{h_B} - \chi(\overline{h_{B+}} - \overline{h_B}) \tag{3.15}$$

represents the radiative cooling experienced by a parcel.

When (3.15) has been applied to observations in the past (e.g. Wang and Albrecht, 1993), it has been used in the form:

$$\delta h'_R(\chi') = h' - \chi'(\overline{h_{B+}} - \overline{h_B}), \tag{3.16}$$

where χ' is obtained from (3.9), and $h' = h - (\bar{h})_{\text{obs}}$. We can show by an analysis

similar to that given above that $\delta h'_R(\chi')$ represents the departure of $\delta h_R(\chi)$ from its horizontal average at the observation level. From (3.15) the average of $\delta h_R(\chi)$ at the observation level is

$$\overline{\delta h_R} = (\bar{h})_{\text{obs}} - \overline{h_B} - \bar{\chi}(\overline{h_{B+}} - \overline{h_B}) \tag{3.17}$$

where $\bar{\chi}$ is defined by (3.10). Hence,

$$\begin{aligned} \delta h_R(\chi) - \overline{\delta h_R} &= h - \overline{h_B} - \chi(\overline{h_{B+}} - \overline{h_B}) - [(\bar{h})_{\text{obs}} - \overline{h_B} - \bar{\chi}(\overline{h_{B+}} - \overline{h_B})] \\ &= h - (\bar{h})_{\text{obs}} - (\chi - \bar{\chi})(\overline{h_{B+}} - \overline{h_B}) \\ &= h' - \chi'(\overline{h_{B+}} - \overline{h_B}) = \delta h'_R(\chi'). \end{aligned} \tag{3.18}$$

Therefore, $\delta h'_R(\chi')$ is the departure of $\delta h_R(\chi)$ from its horizontal mean, $\overline{\delta h_R}$. In other words, $\delta h_R(\chi)$ represents the departure of the h of a parcel from $\overline{h_B}$, due to radiative cooling.

The mean state at level B has itself been affected by radiative cooling, as can be seen in Fig.3.5. This figure shows the vertical profiles of $\frac{h}{c_p}$ and $\frac{s_v}{c_p}$, derived from the LES results, for the updrafts, downdrafts, and mean state. Although s_v increases strongly upward in the cloud layer, h decreases upward there. This cannot be due to entrainment, since $\bar{h}_{B+}$ is larger than any value of h in the cloud layer. Our interpretation is that radiative cooling reduces the h of parcels in a shallow layer near cloud top. These radiatively cooled parcels sink in downdrafts. As they sink, they mix laterally with air in the adjacent updrafts. This causes the downdraft's h to increase downward, and the updraft's h to decrease upward.

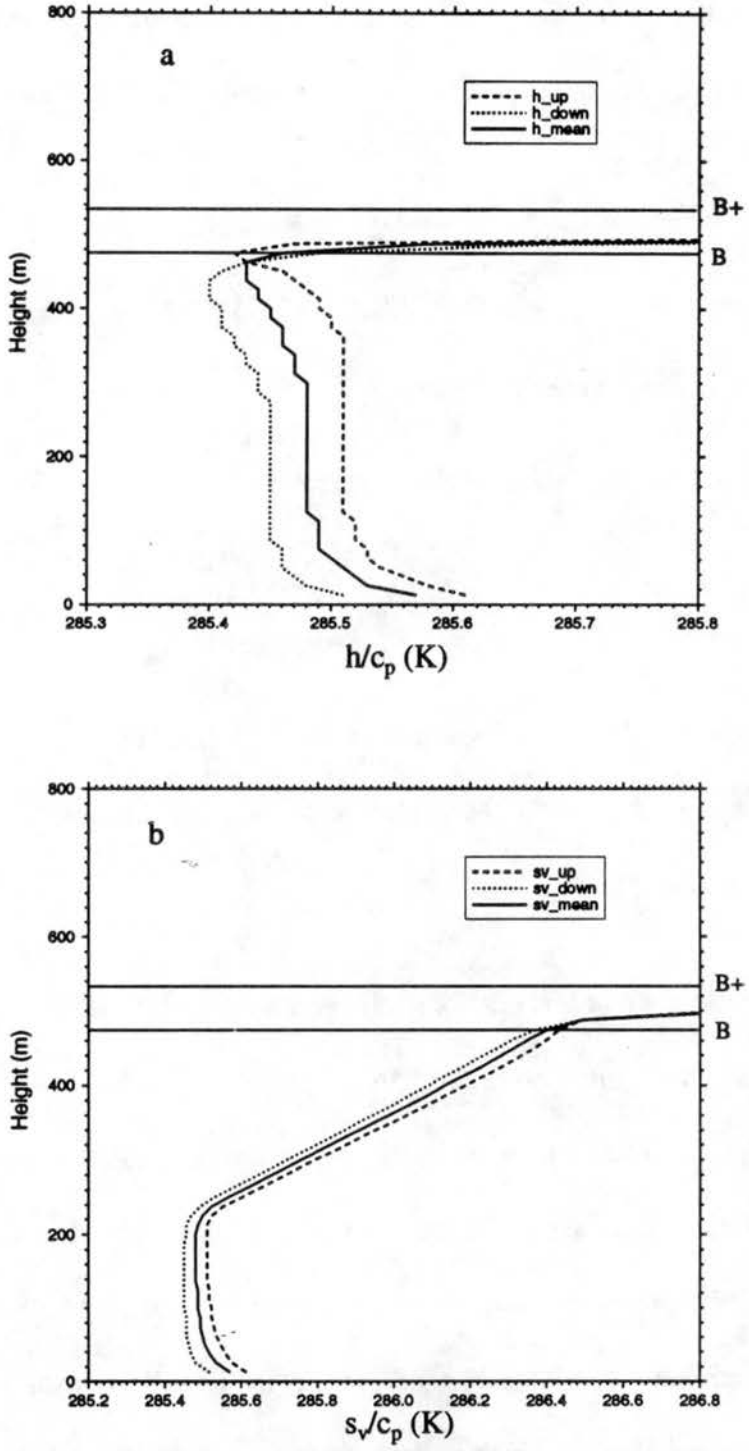

FIGURE 3.5: The conditionally sampled horizontal means of h (a) and s_v (b) for the updrafts, downdrafts and the total.

A similar process is occurring near the surface. Parcels emerging from the ventilation layer have large values of h, since they have been in contact with the warm ocean. As

they rise, they mix laterally with the adjacent downdrafts. This causes the h of the updrafts to decrease upward, and the h of the downdrafts to increase downward.

The h of the updrafts and downdrafts is uniform with height near the mid-level of the PBL. This suggests that lateral mixing is weak there, which is reasonable since we know that the horizontal components of the turbulence energy are weak near the mid-level.

The point is that parcels rising into the entrainment layer have already "felt" the radiative cooling at the cloud top, to some extent, because they have been cooled by lateral mixing with radiatively cooled downdrafts. We should, therefore, interpret $\delta h_R(\chi)$ as the radiative cooling that parcels experience while they are inside the entrainment layer, i.e. after their most recent entry into the entrainment layer.

Once the radiative cooling of each parcel has been obtained, the evaporative cooling can be inferred from the virtual dry static energy s_v, which is defined as

$$s_v = c_p T_V + gz = h + Lq_l. \tag{3.19}$$

The virtual dry static energy is conserved only under dry adiabatic process. Therefore when $\psi = s_v$,

$$\delta s_v(\chi) = s_v(\chi) - \overline{s_{vB}} - \chi(\overline{s_{vB+}} - \overline{s_{vB}}) \tag{3.20}$$

includes the effects of both radiative and evaporative cooling. However, since the radiative cooling is the same for both h and s_v, and is already known, the evaporative cooling can be extracted from $\delta s_v(\chi)$ by using

$$(\delta s_v)_{evp}(\chi) = \delta s_v(\chi) - \delta h_R(\chi). \tag{3.21}$$

We note that $\delta s_v(\chi)$ represents the cooling inside the entrainment layer, or the deviation of the s_v of a parcel from $\overline{s_{vB}}$ due to radiative and evaporative cooling, while

$$\delta s'_v(\chi') = s'_v - \chi'(\overline{s_{vB+}} - \overline{s_{vB}}) \tag{3.22}$$

is the perturbation of $\delta s_v(\chi)$ from its horizontal mean at the observational level:

$$\overline{\delta s_v} = (\overline{s_v})_{\text{obs}} - \overline{s_{vB}} - \overline{\chi}(\overline{s_{vB+}} - \overline{s_{vB}}). \tag{3.23}$$

Here $s'_v = s_v - (\overline{s_v})_{\text{obs}}$. The $(\delta s_v)_{evp}(\chi)$ in (3.21) represents the evaporative cooling that has occurred inside the entrainment layer. The horizontal perturbation of $(\delta s_v)_{evp}(\chi)$ is then

$$(\delta s'_v)_{evp}(\chi') = \delta s'_v(\chi') - \delta h'_R(\chi'). \tag{3.24}$$

Nicholls (1989) and Khalsa (1993) used (3.22) and (3.24) to estimate the radiative cooling of the downdrafts. They estimated the maximum possible value of $(\delta s'_v)_{evp}(\chi')/c_p + \chi'(\overline{s_{vB+}} - \overline{s_{vB}})/c_p$ first, by using the mean χ' in downdrafts calculated from (3.9). The horizontal deviation of virtual temperature (T_V) or virtual potential temperature (θ_V) in the downdrafts was calculated from the observations. This is equivalent to s'_v/c_p. The radiative cooling, $\delta h'_R(\chi')/c_p$, was then obtained by subtracting $(\delta s'_v)_{evp}(\chi')/c_p + \chi'(\overline{s_{vB+}} - \overline{s_{vB}})/c_p$ from s'_v/c_p.

The differences between χ and χ', $\delta h_R(\chi)$ and $\delta h'_R(\chi')$, and $(\delta s_v)_{evp}(\chi)$ and $(\delta s'_v)_{evp}(\chi')$ remind us that we have to be cautious when we compare the theoretical

and observational results, as well as the results between different experiments. For example, Nicholls and Turton (1986) estimated the radiative cooling by using the horizontal perturbation of T_V, and the evaporative cooling by using (3.8) and (3.20). As discussed above, these two sets of results are not comparable. Instead, (3.9) and (3.22) should be used to calculate evaporative cooling for the comparison with the radiative cooling obtained. The difference, which is shown by (2.23), can be about -0.1 K at the cloud top in the LES data we analyzed. This is on the same order as the horizontal perturbation of T_V obtained in previous studies mentioned above. In other words, the error can be serious.

In the following discussion, $\delta s_v(\chi)$ will be used to represent the total cooling inside the entrainment layer. Its horizontal perturbation, $\delta s'_v(\chi')$, will be used when buoyancy due to the coolings is considered. From (3.22), together with the horizontal perturbation of the entrainment mixing effect, we see that $\delta s'_v(\chi')$ is equivalent to the horizontal perturbation of s_v. Theoretically, (3.8) and (3.9) are equivalent when the entrainment layer, or the depth between level B and level B+, is infinitesimally thin. This assumption can be unrealistic, however, especially when level B is defined far below the observational level, such as in the study of Kuo and Schubert (1988).

From $(\delta s_v)_{evp}(\chi)$, we can determine how much liquid water must have been evaporated into the parcel. Defining $l(\chi)$ as the liquid water (mixing-ratio) evaporated into the parcel with mixing fraction χ, we have

$$l(\chi) = -(\delta s_v)_{evp}(\chi)/L. \tag{3.25}$$

Note that $l(\chi)$ is different from q_l. The former is the liquid water that has already been evaporated. The latter is the liquid water currently in the parcel, i.e., the liquid water we can observe directly.

The quantities $(\delta s_v)_{evp}(\chi)$ and $l(\chi)$ can actually be related directly to the liquid water content q_l, in place of (3.21). We substitute

$$h = s_v - Lq_l \tag{3.26}$$

into (3.15), and solve for s_v:

$$s_v(\chi) = \chi (s_v)_{B+} + (1-\chi)(s_v)_B + \delta h_R(\chi) + L[q_l(\chi) - \chi (q_l)_{B+} - (1-\chi)(q_l)_B] \tag{3.27}$$

Comparing (3.27) with (3.20) and (3.21), and assuming that $(q_l)_{B+} = 0$, we find that

$$(\delta s_v)_{evp} = L[q_l(\chi) - (1-\chi)(\overline{q_l})_B], \tag{3.28}$$

Then, using (3.25), we get

$$l(\chi) = (1-\chi)(\overline{q_l})_B - q_l(\chi). \tag{3.29}$$

The horizontal perturbations of $(\delta s_v)_{evp}$ and $l(\chi)$ can be expressed as

$$(\delta s'_v)_{evp} = L[q'_l(\chi') + \chi'(\overline{q_l})_B] \tag{3.30}$$

and

$$l'(\chi') = -[q'_l(\chi') + \chi'(\overline{q_l})_B], \tag{3.31}$$

respectively.

Eq. (3.28) is equivalent to (3.21), and can give some physical insight to the meaning of $(\delta s_v)_{evp}(\chi)$ and $l(\chi)$. A mixed parcel contains a fraction $(1-\chi)$ of cloudy air, and so it had a liquid amount of $(1-\chi)(q_l)_B$ before mixing. After mixing and evaporation (or condensation) happens, the final liquid content of the parcel is $q_l(\chi)$. The difference, $q_l(\chi) - (1-\chi)(\overline{q_l})_B$, is the liquid water evaporated (or condensed), as given by (3.29). The parcel will be cooled (or warmed) by evaporating (or condensing) $l(\chi)$, as described by (3.28). Note from (3.28) and (3.29) that if $q_l(\chi) = 0$, both $(\delta s_v)_{evp}$ and $l(\chi)$ will vary linearly with χ.

According to (3.28), the evaporative cooling is weaker when χ is larger. This conflicts with our general sense that a larger value of χ would result in more evaporative cooling. The paradox is not hard to understand. In (3.28), χ not only represents the mixing fraction of FA air, but also the initial amount of the liquid water in a parcel, i.e. $(1-\chi)(q_l)_B$. A parcel with a larger χ has a smaller initial liquid water content. If the final liquid water content $q_l(\chi)$ is the same, a parcel with a larger χ must, therefore, experience less evaporative cooling than one with a smaller χ.

Of course, we do not expect that $q_l(\chi)$ is actually constant with χ. As shown in Fig. 12a, discussed later, $q_l(\chi)$ decreases with χ much faster than $(1-\chi)(q_l)_B$ does, so that the total effect of the mixing is to enhance the evaporative cooling. For the LES data analyzed in the next section, the decrease of $q_l(\chi)$ with χ is about eight times faster than that of $(1-\chi)(q_l)_B$.

Eq. (3.28), which is equivalent to (3.24), is easier to apply to observations than (3.24) is. The liquid water content q_l in clouds can be measured, although sometimes the

accuracy is questionable; but it is impossible to observe δh_R directly in an experiment. That is why the radiative cooling was calculated from (3.24), after evaporative cooling was evaluated, by Nicholls (1989) and Khalsa (1993). In their studies, however, $(\delta s'_v)_{evp}$ was evaluated very crudely. An advantage of (3.28) is that it provides an accurate way to determine $(\delta s'_v)_{evp}$. Note that it is $(\overline{q_l})_B$, rather than $(\overline{q_l})_{\text{obs}}$, that contributes to $(\delta s'_v)_{evp}$.

Let the pdf for χ in the entrainment layer be denoted by $\Pi_E(\chi)$. The physical meaning and the calculation method for $\Pi_E(\chi)$ are analogous to those for $\Pi_V(\chi)$, except that the parcels are now in the entrainment layer and χ is calculated from (3.8). Only cloudy air is considered here. The total numbers of parcels at each level are shown in Table 1.

The fraction of the parcels at level B that are sinking is $\int_{\text{sinking parcels}} \Pi_E(\chi)|_B d\chi$. The ψ of the sinking air emerging from the entrainment layer at level B is

$$(\overline{\psi_d})_B = \frac{\int_{\text{sinking parcels}} \psi(\chi)\,\Pi_E(\chi)|_B d\chi}{\int_{\text{sinking parcels}} \Pi_E(\chi)|_B d\chi}, \tag{3.32}$$

whether ψ is conservative or not.

We can interpret the physical meaning of the mixing parameter χ_E defined by RSM as

$$(\overline{\psi_d})_B = \chi_E \overline{\psi_{B+}} + (1-\chi_E)\overline{\psi}_B + \frac{\chi_E}{E}\int_{z_B}^{z_{B+}} \overline{S_\psi} dz. \tag{3.33}$$

Here S_ψ is a source or sink of the generic variable ψ. Substituting (3.12) into (3.32) for $\psi(\chi)$, and (3.33) into (3.32) for $(\overline{\psi_d})_B$, we obtain

$$\begin{aligned}\chi_E \overline{\psi_{B+}} + (1-\chi_E)\overline{\psi}_B + \frac{\chi_E}{E}\int_{z_B}^{z_{B+}} \overline{S_\psi} dz = \overline{\psi_{B+}} \frac{\int_{\text{sinking parcels}} \chi \Pi_E(\chi)|_B d\chi}{\int_{\text{sinking parcels}} \Pi_E(\chi)|_B d\chi} \\ + \overline{\psi_B}\left(1 - \frac{\int_{\text{sinking parcels}} \chi \Pi_E(\chi)|_B d\chi}{\int_{\text{sinking parcels}} \Pi_E(\chi)|_B d\chi}\right) + \frac{\int_{\text{sinking parcels}} \delta\psi(\chi)\Pi_E(\chi)|_B d\chi}{\int_{\text{sinking parcels}} \Pi_E(\chi)|_B d\chi}.\end{aligned} \tag{3.34}$$

In case ψ is conservative, we find that

$$\chi_E = \frac{\int_{\text{sinking parcels}} \chi \Pi_E(\chi)|_B d\chi}{\int_{\text{sinking parcels}} \Pi_E(\chi)|_B d\chi}, \tag{3.35}$$

and hence χ_E is a bulk value of χ characteristic of the downdrafts as they emerge from the entrainment layer.

If ψ is not conservative, since (3.35) still holds, we find that

$$\frac{\int_{\text{sinking parcels}} \delta\psi(\chi)\Pi_E(\chi)|_B d\chi}{\int_{\text{sinking parcels}} \Pi_E(\chi)|_B d\chi} = \frac{\chi_E}{E}\int_{z_B}^{z_{B+}} \overline{S_\psi} dz. \tag{3.36}$$

In case $\psi = h$, we have $\int_{z_B}^{z_{B+}} \overline{S_\psi} dz = -\overline{\Delta R}$, where $\overline{\Delta R}$ is the jump of the radiation flux

across the entrainment layer, and so

$$\frac{\int_{\text{sinking parcels}} \delta h_R(\chi)\,\Pi_E(\chi)|_B\,d\chi}{\int_{\text{sinking parcels}} \Pi_E(\chi)|_B\,d\chi} = \frac{\chi_E}{E}\overline{\Delta R}. \tag{3.37}$$

Tests of (3.6), (3.35) and (3.37), using the LES data, are given in next section. In the following analysis, the units of s_v and h are K, because we have divided by c_p.

3.3 Results

3.3.1 Mixing and selection processes in the ventilation layer

Fig.3.6 shows $\Pi_v(\chi)$ for each level in the ventilation layer, as well as its components for updrafts and downdrafts. When $\chi < 0$, the parcel is drier than $(\bar{q}_t)_S$, and so as mentioned earlier we assume that no mixing has affected the parcel since it entered the ventilation layer. Parcels with properties very close to those of the surface itself (χ near one) do not occur, so that $\Pi_V(\chi)$ becomes appreciable only for χ less than about 0.1. This is not surprising because there are no parcels that actually originate at level S-. The *only* source of air for the ventilation layer is the downdrafts that enter from the interior of the PBL. For the cases considered here, the downdrafts are relatively cold and dry. The pdf in Fig.3.6 shows that the downdrafts in the ventilation layer contain more unmixed dry parcels ($\chi < 0$) than the updrafts do, while the updrafts contain more mixed moist parcels ($\chi > 0$) than downdrafts do, at each level. The fraction of the mixed parcels in the downdrafts becomes larger as we approach level S-. At levels S-3 and S-4, most of

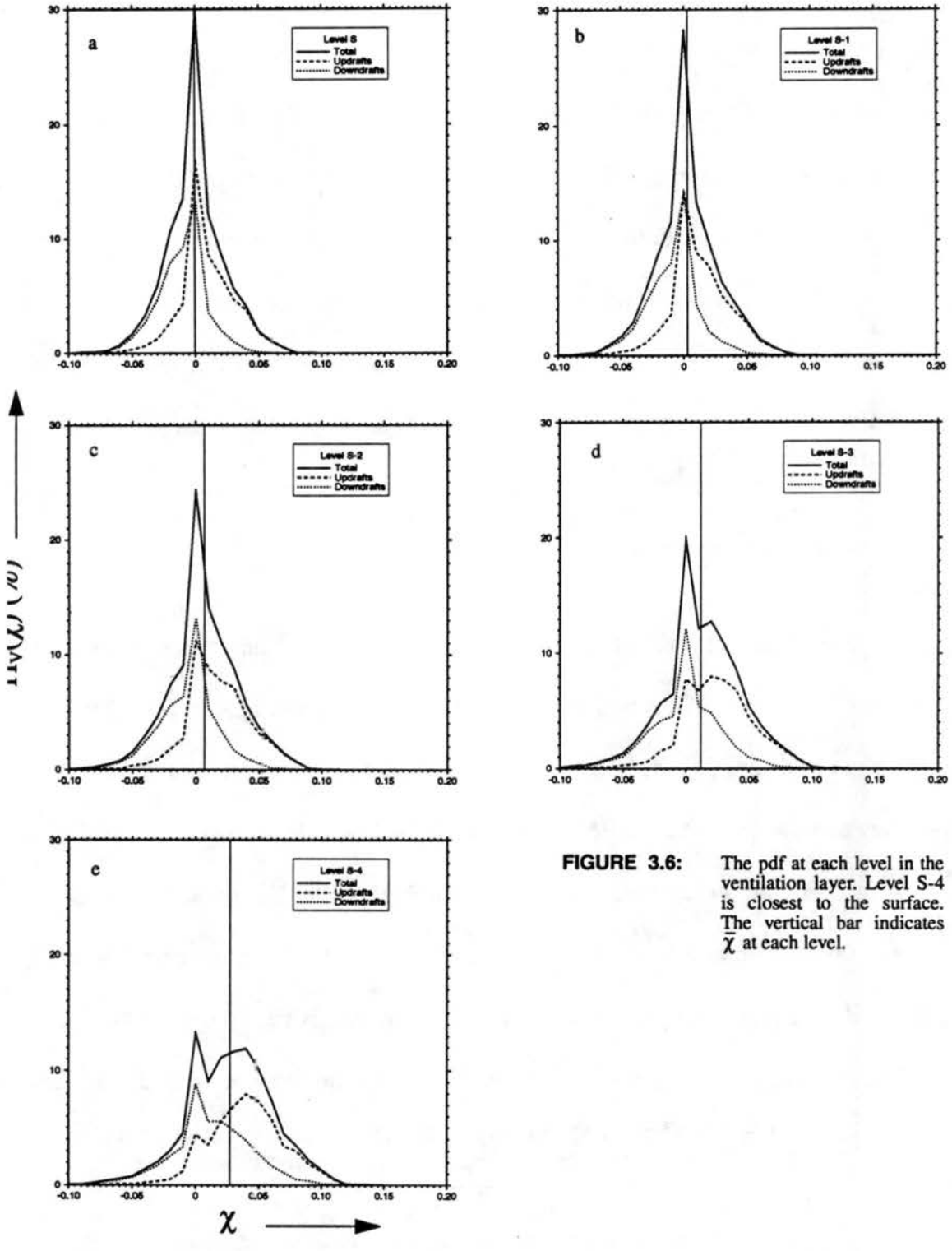

FIGURE 3.6: The pdf at each level in the ventilation layer. Level S-4 is closest to the surface. The vertical bar indicates $\bar{\chi}$ at each level.

the parcels are mixed. The pdf is bimodal at these lower levels (Fig.3.6d, e) and

unimodal at the higher levels (Fig.3.6a, b, c), due to different contributions from updrafts and downdrafts.

These results suggest that the parcels acquire properties characteristic of level *S-* only by contact. We mean that, by following the downdrafts from level *S*, some parcels touch level *S-* itself and acquire properties relatively similar to those of level *S-*. When these parcels gain enough buoyancy, they join the updrafts. However, there are no parcels for which χ is close to one. The properties of the parces are determined by the lower boundary conditions used in the LES model. The properties of the parcels at the lowest level are forced to satisfy similarity theory (Moeng, 1984), so that they cannot have properties very close to those of the surface.

The results shown in Fig.3.6 also suggest that lateral mixing between updrafts and downdrafts occurs. This was also shown by Schumann and Moeng (1991) in their plume budget analysis of the same LES dataset. The parcels in the downdrafts become wetter as they approach the surface. Before they reach the lowest level, the only source of moisture is mixing with the updrafts, which results in both wetter downdrafts towards the bottom and drier updrafts towards level S. Consequently, the average mixing fraction $\bar{\chi}$ in the ventilation layer decreases with height. This decrease is nearly exponential, as shown in Table 2. The average $\bar{\chi}$ at each level is listed in the first row of Table 2, and indicated in

Table 3.2: The average mixing fraction (%) and the fraction of the area covered by updrafts at each level in the ventilation layer.

Level	S-4	S-3	S-2	S-1	S
$\bar{\chi}$ (%)	2.7	1.3	0.7	0.3	0
Area covered by updrafts (%)	54.1	54.0	53.7	53.0	53.0

Fig.3.6. At level S the $\bar{\chi}$-line is also the $\chi = 0$ line from (3.2). This is guaranteed by (3.11). Also listed in Table 2 is the area covered by the updrafts at each level. This area is almost constant with height throughout the ventilation layer.

The buoyancy of the updrafts and downdrafts is shown in Fig.3.7, and $\bar{\chi}$ for each level is also indicated. The buoyancy is represented by $\langle s'_v \rangle$, the horizontal perturbation of s_v, averaged for each χ-bin. For a given χ, the s_v in the updrafts is generally a little bit larger than that in the downdrafts. This may indicate that s_v is not quite conservative in the ventilation layer, due to a weak radiative warming (RSM). If this effect is ignored, then $\langle s'_v \rangle$ is positive for $\chi > \bar{\chi}$ and negative for $\chi < \bar{\chi}$ (i.e., moist parcels are warm and dry parcels are cold), regardless of whether the parcel is in an updraft or a downdraft. This means that the properties of a parcel inside the ventilation layer are mainly controlled by mixing. The mean mixing fraction χ in the updrafts can therefore represent how much information the updrafts bring into the interior of the PBL from the surface, S- . This is why χ_V, which is related to χ through (3.6), can be an important parameter in the parameterization of the bulk PBL model (RSM). Stronger turbulence due to an unstable stratification can result in a stronger lateral mixing between updrafts and downdrafts, and hence a smaller χ in updrafts.

When all of the parcels in the updrafts and downdrafts are grouped together, as shown in Fig.3.8, we have $\langle w \rangle > 0$, $\langle s'_v \rangle > 0$ when $\chi > \bar{\chi}$, and $\langle w \rangle < 0$, $\langle s'_v \rangle < 0$ when $\chi < \bar{\chi}$. Therefore, cold-dry ($\langle s'_v \rangle < 0$, $\chi < \bar{\chi}$) parcels dominate the downdrafts ($\langle w \rangle < 0$), and warm-moist ($\langle s'_v \rangle > 0$, $\chi > \bar{\chi}$) parcels dominate the updrafts ($\langle w \rangle > 0$). In this way, moisture and sensible heat are transported upward.

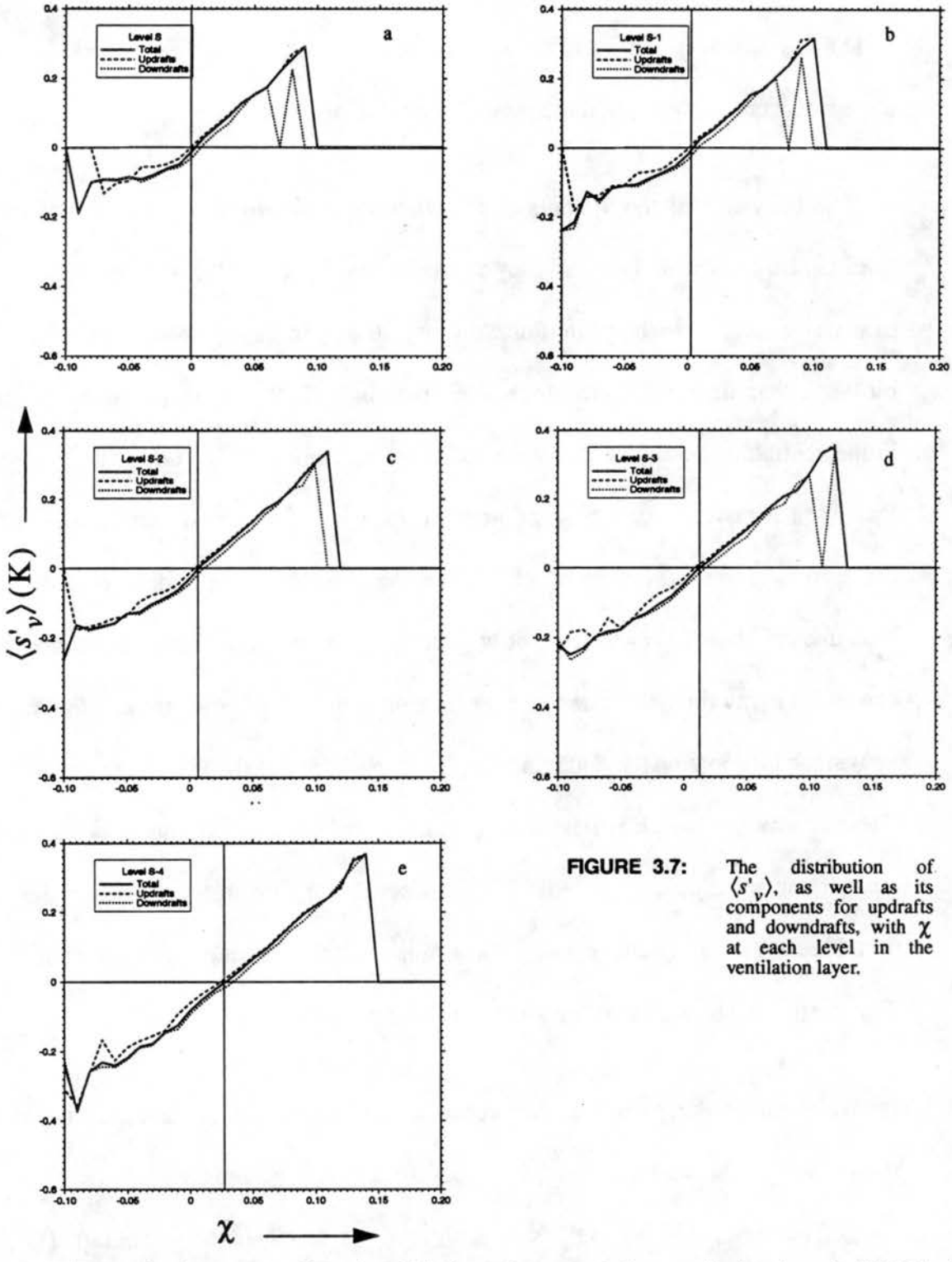

FIGURE 3.7: The distribution of $\langle s'_v \rangle$, as well as its components for updrafts and downdrafts, with χ at each level in the ventilation layer.

When updrafts emerge from level S (i.e., the top of the ventilation layer), 82.3% of the parcels there are warm-moist, and 17.7% are cold-dry, by integrating the pdf at level

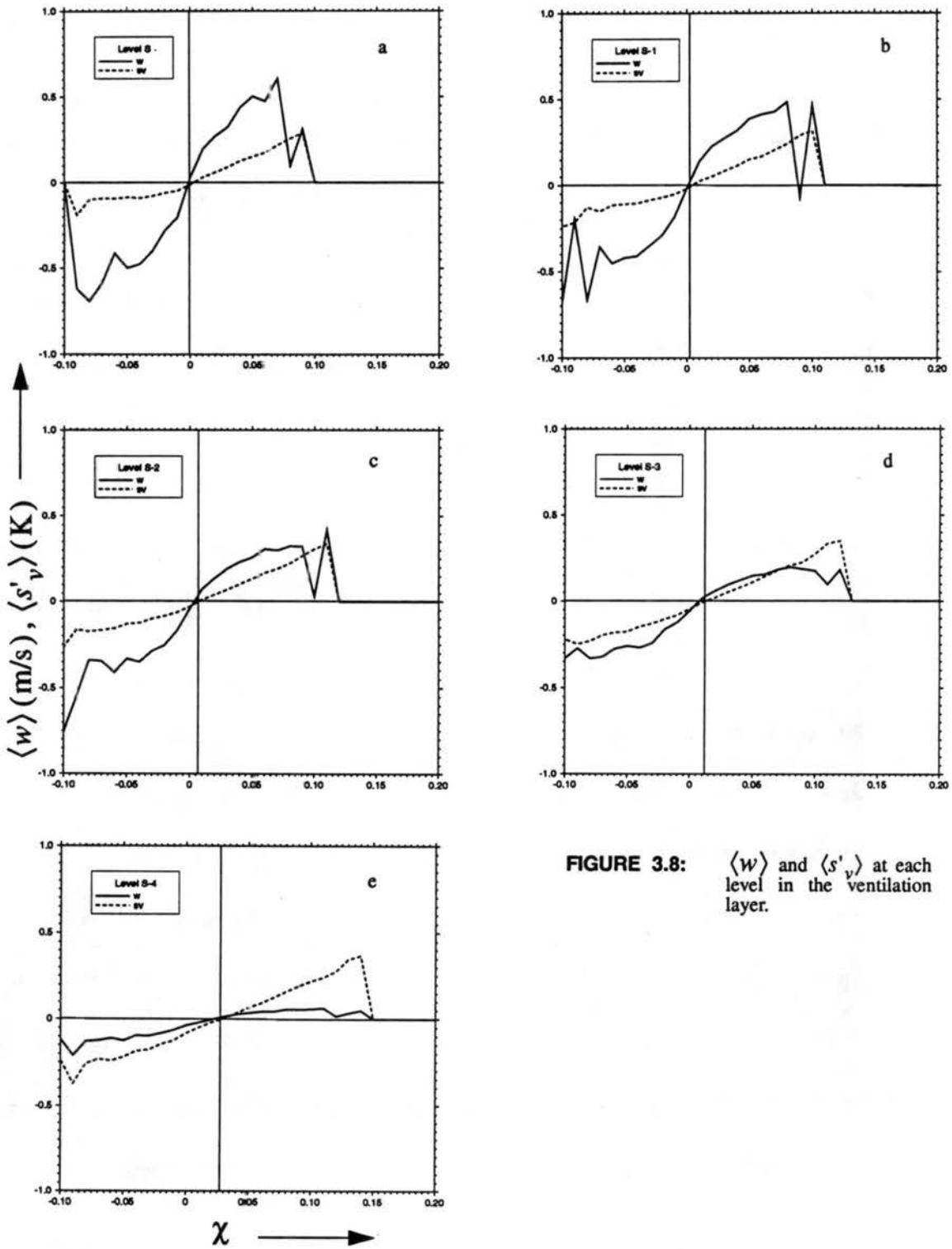

FIGURE 3.8: $\langle w \rangle$ and $\langle s'_v \rangle$ at each level in the ventilation layer.

S for updrafts. The average χ in the updrafts is

$$\chi_V = \frac{\int_{\text{rising parcels}} \chi \Pi_V(\chi)|_S d\chi}{\int_{\text{rising parcels}} \Pi_V(\chi)|_S d\chi} = 0.96 \times 10^{-2}. \tag{3.1}$$

This results agrees reasonably well with $\chi_V = 1.22 \times 10^{-2}$, as obtained by RSM through different methods. At level S, the average buoyancy of the updrafts is 0.04 K.

The above results can be summarized to give a description of the mixing and selection processes in the ventilation layer: Parcels enter the ventilation layer by descending through level *S*. If a parcel is warmer and wetter than the mean state at level *S*, it is likely to return to the interior of the PBL due to its positive buoyancy ($\langle w \rangle > 0$, $\langle s'_v \rangle > 0$ when $\chi > 0$). Otherwise, it is likely to sink further into the ventilation layer. As it sinks, it may mix with other parcels, changing its mixing fraction, χ. If the χ of the parcel becomes larger than $\bar{\chi}$ at its current level, it is likely to join the updrafts. Otherwise it keeps sinking until it reaches the surface. There, it acquires properties closer to those of *S*-, gains buoyancy, and increases its χ. When $\chi > \bar{\chi}$ and the buoyancy is large enough, the parcel joins an updraft. Whether or not the parcel will continue to rise depends on how it much it mixes with cold-dry parcels, and whether it keeps $\chi > \bar{\chi}$. The warm-moist parcels which finally rise through level S in the updrafts effectively have 0.96% [i.e., χ_V in (3.1)] of their properties "from the boundary," S-, and 99.04% from re-cycled downdraft air. The number of such parcels entering the interior per unit time and per unit area determines the rate at which information about the properties of the surface is carried into the interior. This "parcel injection rate" is closely related to the convective mass flux discussed by RSM.

3.3.2 Mixing and selection processes in the entrainment layer

3.3.2.1 LES data

In this paper, only cloudy parcels are considered to be inside the entrainment layer, because the radiative cooling and evaporative cooling mainly happen in cloudy parcels, and because turbulent mixing occurs only inside the cloud. The total number of total cloudy parcels at each level, as well as the fractional area covered by updrafts and downdrafts, is shown in Table 1. Almost all of the parcels at level B are cloudy, and no cloudy parcels exist at level B+. The number of cloudy parcels decreases with height, which indicates the existence of cloud turrets. These results suggest that the parcels between levels B and B+ are very representative of the air at cloud top, where mixing, radiative cooling and evaporative cooling are all vigorous. These processes, as well as their combined effects on buoyancy, are discussed separately in the following subsections.

3.3.2.1.1 Turbulent mixing

The pdf for the χ of the cloudy parcels at each level in the entrainment layer is shown in Fig.3.9. By definition [(3.8)] parcels with $\chi < 0$ have mixing ratios wetter than the average at level B, and are considered unmixed. Compared with the pdf for the ventilation layer in Fig.3.6, the range of χ is larger in the entrainment layer, but the values of χ are still clustered near zero. No parcels have χ close to one (i.e., no parcels consist entirely of FA air), even though the free atmosphere serves as source of air in addition to the updrafts that enter from the interior of the PBL.

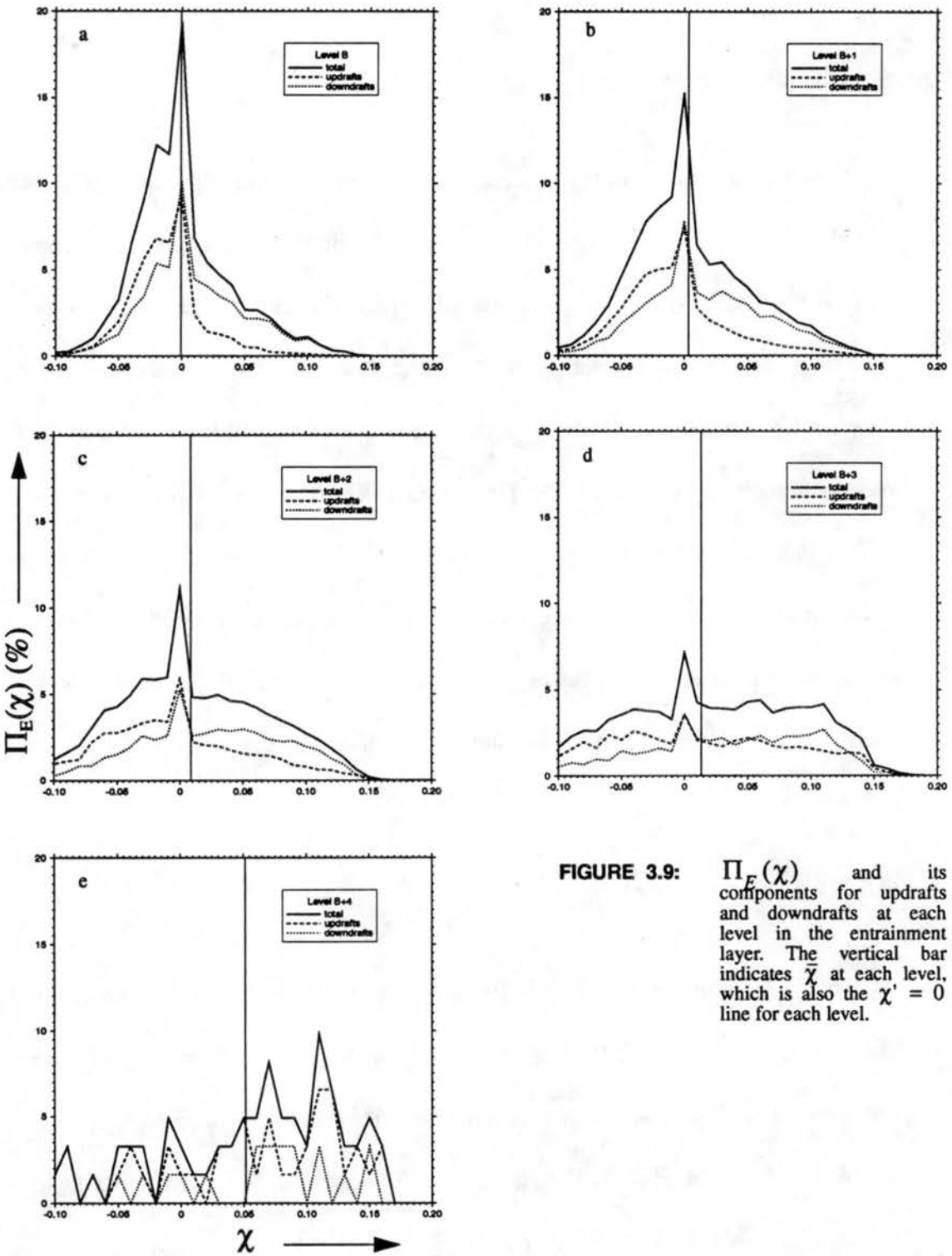

FIGURE 3.9: $\Pi_E(\chi)$ and its components for updrafts and downdrafts at each level in the entrainment layer. The vertical bar indicates $\overline{\chi}$ at each level, which is also the $\chi' = 0$ line for each level.

The absence of parcels with $\chi \cong 1$ can be explained by our data sampling method. When the χ of a parcel is large enough (i.e., mixed with large enough amount of FA air),

its liquid water is completely evaporated, so that it is not included in the data analyzed. This indicates that the maximum χ obtained corresponds to the maximum evaporative cooling at each level, if parcels are well mixed. This maximum χ of cloudy parcels is about 14% at level B, and increases slightly with height.

Fig.3.9 also shows the pdfs for updrafts and downdrafts. Moist parcels ($\chi < 0$, i.e., unmixed parcels) dominate the updrafts at all levels. The decrease of $\Pi_E(\chi)$ with height in this range shows that some of these moist parcels were mixed during their stay in the entrainment layer, and became dry mixed parcels.

The dry mixed parcels ($\chi > 0$) dominate the downdrafts at level B, and make the area covered by downdrafts there larger than that covered by updrafts (as shown in Table 1). With increasing height, however, the fraction of dry mixed parcels in the downdrafts decreases, until more dry parcels appear in updrafts than in downdrafts at level B+4 (i.e., the heavy dashed curve, for $w > 0$, lies the thin dashed curve, for $w < 0$, when $\chi > 0$ in Fig.3.9e).

The greater number of dry parcels in updrafts than in downdrafts, at the upper levels, can not be explained by lateral mixing. Such lateral mixing may make the updrafts drier, but it never makes them drier than the downdrafts at the same level. Instead, it can be explained as a result of entrainment and mixing at cloud top. Moist parcels reach cloud top in updrafts and mix with the dry entrained air there. The dry mixed parcels may still go upward inertially, until negative buoyancy stops them. Hence more dry parcels may be expected to occur in the updrafts near cloud top. Entrainment also affects the pdf at level B+3 (Fig.3.9d), where only about half of the area is covered by clouds (Table 1),

and entrained air can come from both top and the sides. At lower levels where the cloudy cells occupy more than 88% of the layer, the increase in the number of mixed parcels in the updrafts is more likely due to lateral mixing.

Both entrainment and lateral mixing occur in the entrainment layer. As a result of these processes, the average mixing fraction, $\bar{\chi}$, decreases downward, as listed in Table 3. The value of $\bar{\chi}$ at level B+4 is much larger than that at other levels, which simply

Table 3.3: The average χ at each level for cloudy parcels in the entrainment layer.

Level	B	B+1	B+2	B+3	B+4
$\bar{\chi}$ (%)	0.00	0.44	0.93	1.39	5.20

means that entrainment has a strong effect on the properties of the air very close to the cloud tops. The mixing fraction in the downdrafts at level B, just before they emerge into the interior, is

$$\chi_E = \bar{\chi}|_{\text{downdrafts}} = \frac{\int_{\text{sinking parcels}} \chi \Pi_E(\chi)|_B d\chi}{\int_{\text{sinking parcels}} \Pi_E(\chi)|_B d\chi} = 1.03 \times 10^{-2}, \tag{3.38}$$

which is in very good agreement with $\chi_E = 1.02 \times 10^{-2}$, as obtained by RSM using a different method. The warming of the downdrafts due to mixing, obtained by using $\overline{s_{v_{B+}}} - \overline{s_{v_B}} = 9.5\text{K}$, is

$$\bar{\chi}|_{\text{downdrafts}} \left(\overline{s_{v_{B+}}} - \overline{s_{v_B}}\right) = 0.098\text{K}. \tag{3.39}$$

3.3.2.1.2 Radiative cooling

The radiative cooling at all levels in the entrainment layer, relative to the average cooling at level B, has been calculated by using (3.15), and is shown in Fig.3.10a. At level B, this relative cooling is equivalent to the perturbation of δh_R about the horizontal mean there. The radiative cooling amounts for updrafts and downdrafts are also calculated separately at each level. These results are shown as the difference from the total, $\delta h_R(\chi)$ (Fig.3.10a), at each level, i.e. we have plotted $\langle \delta h_R \rangle_{\text{updrafts}}(\chi) - \langle \delta h_R \rangle(\chi)$ and $\langle \delta h_R \rangle_{\text{downdrafts}}(\chi) - \langle \delta h_R \rangle(\chi)$, respectively, as in Fig.3.10b-f. Recall here that "$\langle\ \rangle$" denotes an average over a $\chi-$bin. Note the scale difference for the ordinates of the different panels.

For $\chi > 0$, Fig.3.10a shows evidence of radiative cooling, except at level B+4. Generally the cooling increases towards level B, and increases with χ at each level. For $0 < \chi < 0.06$, the cooling is mainly apparent in downdrafts, as shown in Figs.3.10b, c, and d, since the parcels in the downdrafts are colder than those in the updrafts and the number of parcels in the downdrafts is more than that in the updrafts (Figs.3.9a-c). This stronger cooling in the downdrafts may be due to the longer residence time in the entrainment layer of the parcels in downdrafts, compared to those in updrafts. A parcel that stays longer in the entrainment layer can be radiatively cooled more strongly. Since the residence time is, on average, largest in the downdrafts at level B, the cooling is also strongest at level B.

The cooling for parcels with $\chi > 0.06$ can still be interpreted in terms of the time over which the parcels stay near the cloud top, although there is no systematic difference

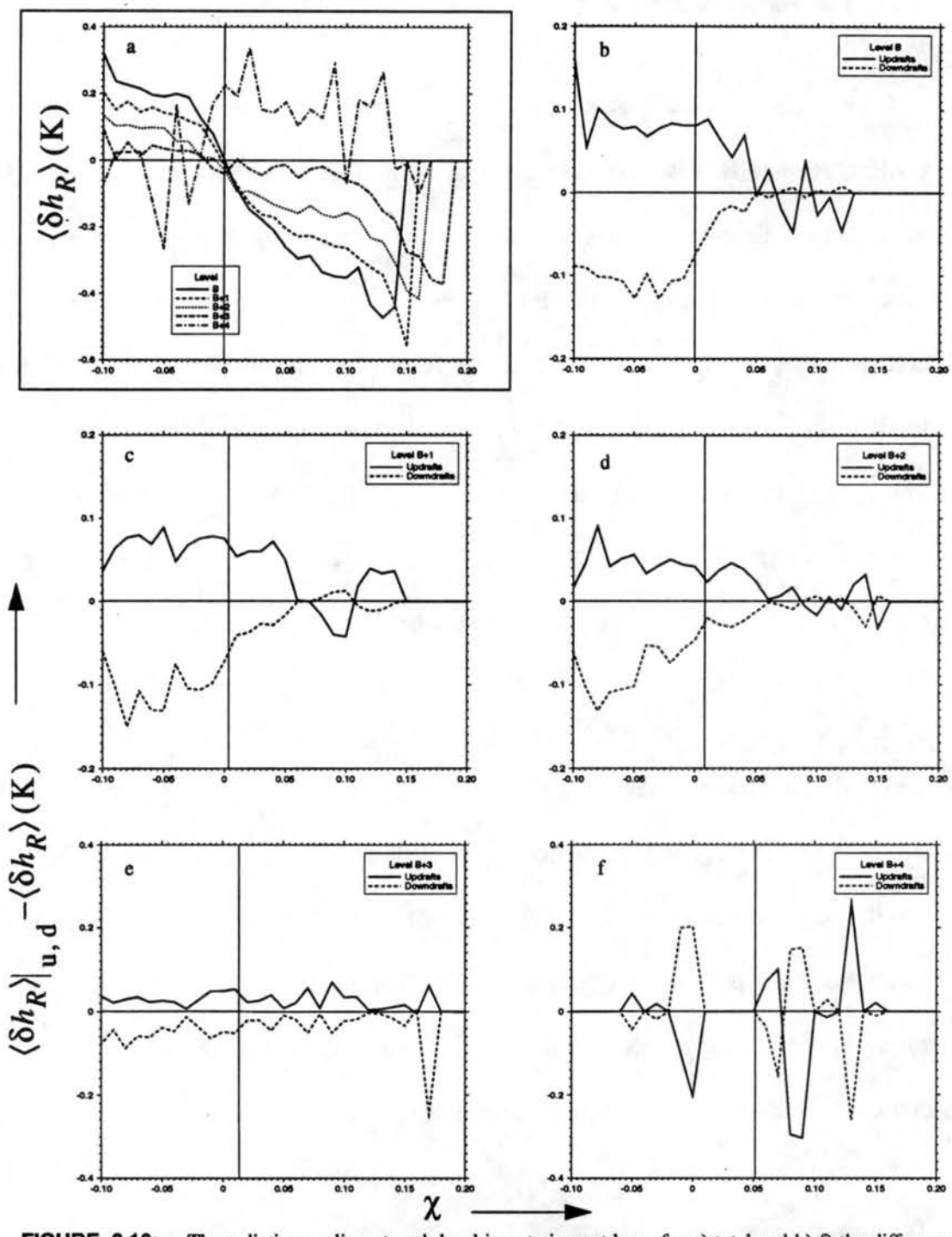

FIGURE 3.10: The radiative cooling at each level in entrainment layer for a) total and b)-f) the difference of updrafts and downdrafts from the total. Note the scale difference between different panels.

between the cooling amounts in the updrafts and downdrafts (Figs.3.10b-d). Parcels in this χ range are all strongly cooled, regardless of whether they are in updrafts or

downdrafts. This suggests that lateral mixing may strongly affect these parcels. A mixed parcel in a downdraft may be brought back into an updraft by lateral mixing, and will then experience additional radiative cooling, so that its cooling is even stronger than other parcels with $0 < \chi < 0.06$. This kind of parcel generally undergoes multiple mixing episodes, and so has a relatively large value of χ. Since these parcels circulate between updrafts and downdrafts, and have large values of χ, we refer to them here as "well mixed" parcels. It is interesting to note that $\chi = 0.06$ is very close to the average mixing fraction at level B+4 (Table 3). A parcel may need a longer residence time to acquire a larger χ, which would also explain why the radiative cooling increases sharply with χ.

Cloudy parcels that can make it all the way to level B+4 without being forced down first by negative buoyancy must have very large "initial" values of h upon entering the entrainment layer, and cannot have been significantly affected by dilution or radiative cooling. From this perspective, it is not surprising that most of the cloudy parcels at level B+4 have $h(\chi) > \bar{h}_B$, and so imply $\delta h_R(\chi) > 0$ through (3.15). Figs.3.10b-e show that parcels in updrafts contribute more positive values to $\langle \delta h_R \rangle$ than those in downdrafts. Fig.3.9 also shows that at these levels updrafts dominate the cloudy parcels. These results imply that the parcels with large h come from the interior of the PBL in updrafts, and this explains why they are moist ($\chi < 0$). As they rise, these moist parcels tend to experience strong radiative cooling, due to their large liquid water contents (see Fig.3.12), so that their positive $\langle \delta h_R \rangle$ values decrease upward. The cooling for each parcel in the downdrafts is stronger than that in the updrafts (Figs.3.10b-e), as discussed above.

Although updrafts still dominate at level B+4, it is the relatively dry parcels ($\chi > 0$) that have positive δh_R. The reason may be related to the entrainment at cloud top. A few parcels may undergo little mixing with dry parcels before reaching cloud top, but still experience some radiative cooling. Once they reach cloud top, they mix with dry parcels quickly by entrainment, with a very large average mixing fraction (Table 3). Hence the parcels become dry ($\chi > 0$). During the brief mixing process, radiative cooling is unable to make $\langle h \rangle - \bar{h}_B$ smaller than $\chi\,(\overline{h_{B+}} - \overline{h_B})$. Therefore, the dry parcels at cloud top also have positive $\langle \delta h_R \rangle$. Since parcels in updrafts can be shifted into downdrafts very quickly at cloud top, we expect little systematic difference of $\langle \delta h_R \rangle$ between updrafts and downdrafts there. In Fig.3.10f, this difference appears to be random.

In summary, the amount radiative cooling experienced by a parcel is related to the length of time that the parcel stays in the entrainment layer. With a longer residence time, the accumulated radiative cooling is greater, so that generally the parcels in downdrafts (exiting the entrainment layer) have been cooled more than those in updrafts (entering the entrainment layer). The longer residence time also allows parcels to undergo more mixing, and hence to acquire a larger χ. Therefore, in χ-space, the radiative cooling increases with χ. Positive $\langle \delta h_R \rangle$ is obtained for the warm-moist parcels that the updrafts bring into the entrainment layer. These parcels also are radiatively cooled, regardless of whether they are mixed with other parcels later.

The average radiative cooling introduced into the interior of PBL by the downdrafts emerging through level B can be calculated by using the left-hand-side of (3.37):

$$\overline{\delta h_R}\Big|_{\text{downdrafts}} = \frac{\int_{\text{sinking parcels}} \langle \delta h_R(\chi) \rangle \Pi_E(\chi)\big|_B d\chi}{\int_{\text{sinking parcels}} \Pi_E(\chi)\big|_B d\chi} = -0.108\text{K}. \tag{3.40}$$

By using $\chi_E = 1.02 \times 10^{-2}$, $\overline{\Delta R} = 82.1\,\text{W m}^{-2}$, and $E = 0.82 \times 10^{-2}\text{kg m}^{-2}\text{s}^{-1}$ from RSM, we find that the right-hand-side of (3.37) becomes

$$\overline{\delta h_R}\Big|_{\text{downdrafts}} = \frac{\chi_E}{E}\overline{\Delta R} = -0.102\text{K}. \tag{3.41}$$

This represents a satisfactory test of (3.37).

3.3.2.1.3Evaporative cooling

The title of this subsection, "Evaporative cooling," and the notation introduced in (3.21), "$(\delta s_v)_{evp}(\chi)$," suggest that $(\delta s_v)_{evp}(\chi)$ can only be different from zero if cloud droplets evaporate, and that it can never be positive. The reality is more complicated. Three physical processes can influence $(\delta s_v)_{evp}(\chi)$:

1) Evaporation of cloud droplets due to mixing with unsaturated air, favoring $(\delta s_v)_{evp}(\chi) < 0$;

2) Condensation or evaporation due to moist adiabatic vertical motions inside the entrainment layer, which can either increase or decrease $(\delta s_v)_{evp}(\chi)$;

3) Radiative cooling, which will tend to drive condensation, favoring positive $(\delta s_v)_{evp}(\chi)$. This can be seen from (3.21).

In general, all three processes can effect $(\delta s_v)_{evp}$, so that it can be either positive or negative, depending on which processes dominate.

Obviously, the effects of mixing on the evaporative cooling should vary systematically with the mixing fraction χ, as shown by (3.28). Note that $q_l(\chi)$ is also a function of χ. Radiative cooling may promote the growth of cloud droplets, and hence increase the cloud water amount in the downdrafts (Caughey et al., 1982; Curry, 1986). By comparing the growth time of a droplet in clouds with the time an individual droplet is exposed to the radiative cooling, Caughey et al. (1982) concluded that there is sufficient time for creation of significant liquid water content fluctuations near cloud top by radiative cooling.

Fig.3.11 shows the evaporative cooling relative to the mean evaporative cooling at level B, $\langle (\delta s_v)_{evp} \rangle$, calculated from (3.28). As seen from (3.29), this is proportional to the amount of liquid water evaporated, $\langle -l(\chi) \rangle$. Of course, a positive value of $\langle -l(\chi) \rangle$ means net condensation. The total liquid water amount at each level, $\langle q_l(\chi) \rangle$, is given in Fig.3.12 for comparison. Fig.3.11a shows $\langle (\delta s_v)_{evp} \rangle$ at each level, and Figs.3.11b-f show the deviations of the evaporative cooling in updrafts and downdrafts from the total, i.e., $\langle (\delta s_v)_{evp} \rangle_{\text{updrafts}} - \langle (\delta s_v)_{evp} \rangle$, and $\langle (\delta s_v)_{evp} \rangle_{\text{downdrafts}} - \langle (\delta s_v)_{evp} \rangle$, respectively. Fig.3.12 is similar to Fig.3.11 except for q_l. Note the scale difference between the first panel and the rest of the panels in both figures. This is necessary since the perturbations are only a small portion of the total. It is apparent that Fig.3.11 looks similar to Fig.3.12.

The value of $\langle (\delta s_v)_{evp} \rangle$ is positive when $\chi < 0$. These moist, unmixed parcels are from the interior of the PBL, and undergo condensation warming inside the entrainment layer. The condensation is primarily due to radiative cooling, which increases with height for the parcels with $\chi < 0$ (see Fig.3.10).

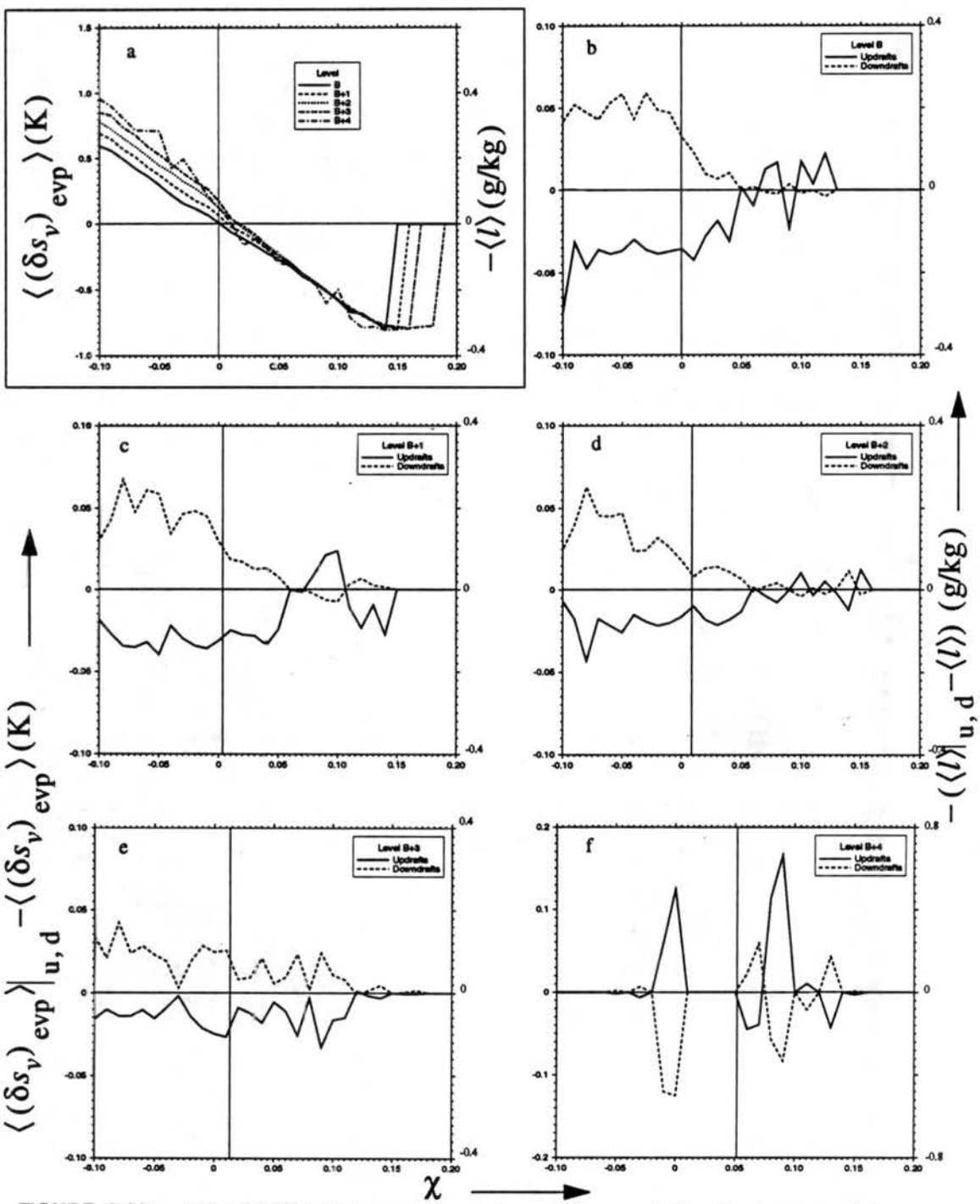

FIGURE 3.11: As in Fig.3.10 but for evaporative cooling and the amount of liquid water evaporated.

For $\chi > 0$, evaporative cooling is found, and it increases with χ, i.e. with the strength of the mixing. For $0 < \chi < 0.06$, evaporative cooling is largest at level B, and decreases

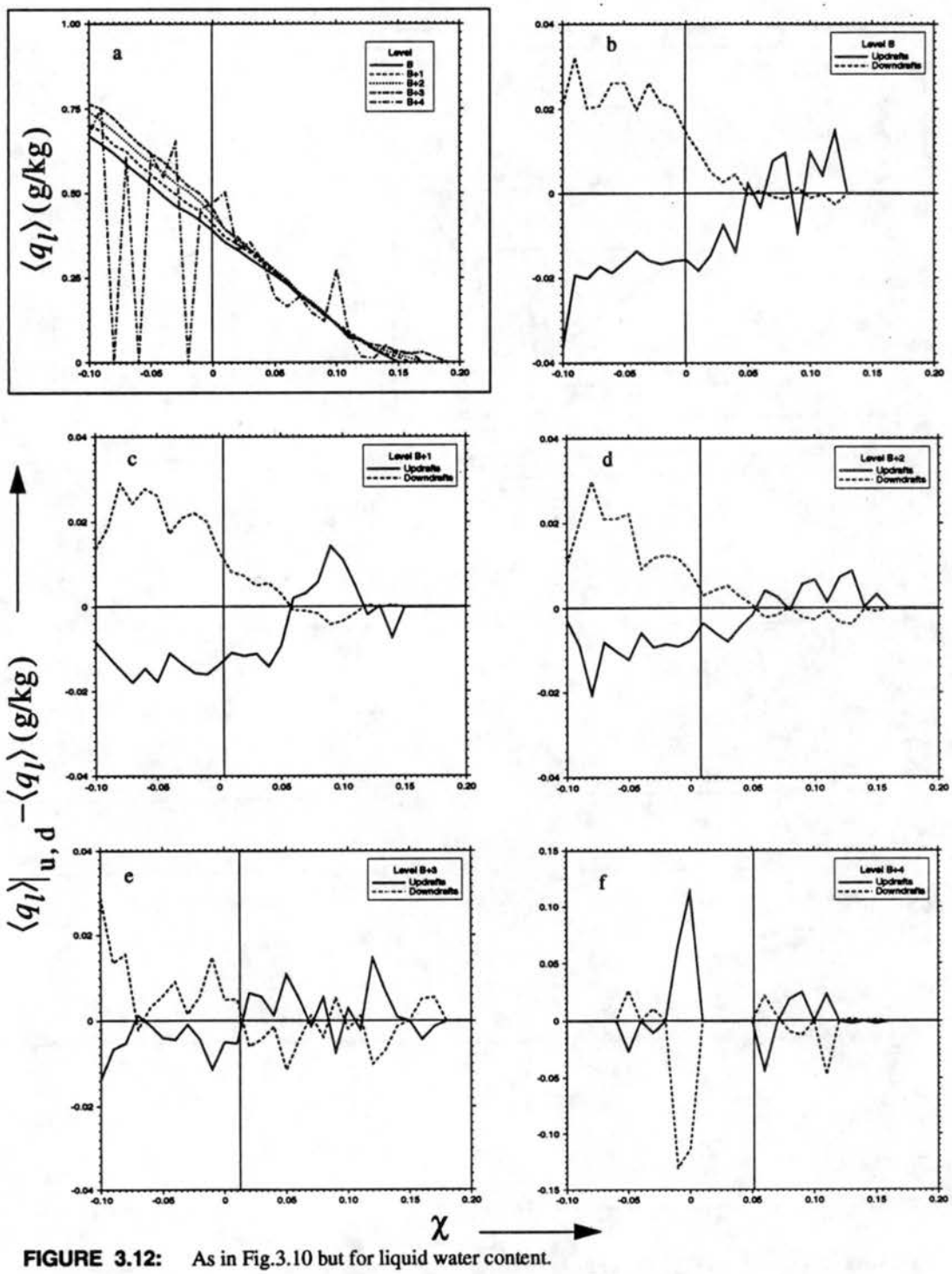

FIGURE 3.12: As in Fig.3.10 but for liquid water content.

with height. This is opposite to the effect to be expected from radiative cooling, which should result in the largest condensation warming at level B, and hence the smallest

evaporative cooling there. Adiabatic condensation, which is shown in Fig.3.12a by q_l increasing upward, can reduce the evaporative cooling at higher levels. Therefore, for $0 < \chi < 0.06$, evaporative cooling dominates over condensation warming, while the adiabatic condensation dominates over condensation due to radiative cooling. For $\chi > 0.06$, the parcels are "well mixed" due to multiple mixing episodes, as discussed earlier, so that only the effect of χ is discernible. With a larger mixing fraction, the evaporative cooling is stronger.

Comparison of Figs.3.10b-f, Figs.3.11b-f and Figs.3.12b-f shows that, relative to the updrafts with the same χ, the downdrafts have experienced stronger radiative cooling, weaker evaporative cooling, and a larger liquid water content.

In summary, for mixed parcels, the evaporative cooling which is driven by mixing with dry air, as analyzed in last section, dominates over condensation warming. For unmixed parcels ($\chi < 0$), the condensation warming due to radiative cooling and adiabatic cooling is obvious.

The average evaporative cooling in the downdrafts at level B, before they emerge into the interior, is

$$(\overline{\delta s_v})_{\text{evp}}\Big|_{\text{downdrafts}} = \frac{\int_{\text{sinking parcels}} \langle (\delta s_v)_{\text{evp}}(\chi) \rangle \Pi_E(\chi)\, d\chi}{\int_{\text{sinking parcels}} \Pi_E(\chi)\, d\chi} = -0.027\text{K}. \qquad (3.42)$$

This is smaller than the mean radiative cooling in the downdrafts [(3.37)], although the evaporative cooling of a parcel with $\chi > 0$ is stronger than its radiative cooling (Figs.3.10

and 3.11). This is because downdrafts also include some condensation-warmed moist parcels (Figs.3.9 and 3.12), which reduce the average evaporative cooling in the downdrafts by about 74%. Therefore, in an average sense, the radiative cooling dominates in the downdrafts near cloud top for this simulated CTBL. The cooling amounts determined here are comparable with results obtained in previous studies.

3.3.2.1.4Buoyancy

An analytical expression for the buoyancy can be obtained by rearranging (3.27):

$$\begin{aligned} \langle s'_v \rangle &= \langle s_v \rangle - (\overline{s_v})_{\text{obs}} \\ &= \chi\,[(\overline{s_v})_{\text{B+}} - (\overline{s_v})_{\text{B}}] + \langle \delta h_R(\chi) \rangle + \langle (\delta s_v)_{\text{evp}}(\chi) \rangle + [(\overline{s_v})_{\text{B}} - (\overline{s_v})_{\text{obs}}]. \end{aligned} \tag{3.43}$$

The first three terms represent mixing warming, radiative cooling and evaporative cooling, respectively. From (3.43) we can see how the various processes discussed above determine the buoyancy of parcels. The fourth term is the difference between the buoyancy defined by $s_v - (\overline{s_v})_{\text{obs}}$ and by $s_v - (\overline{s_v})_B$. It is about -0.1 K at level B+2 for cloudy parcels only. This difference is of the same magnitude as $\langle s'_v \rangle$ (see Fig.3.13). If the fourth term of (3.43) is ignored, or if the buoyancy is (incorrectly) determined from $s_v - (\overline{s_v})_B$, then most of the parcels will appear to be positively buoyant, although in reality their buoyancy may be negative. Therefore, we do not think that the expression $s_v - (\overline{s_v})_B$ is accurate enough to be used to determine the buoyancy.

The term $(\overline{s_v})_{\text{B}} - (\overline{s_v})_{\text{obs}}$ can be eliminated if other terms in (3.43) are expressed as perturbations from the horizontal mean. We can obtain $(\overline{s_v})_{\text{obs}}$ by averaging (3.27), and then substitute it into (3.43). This gives

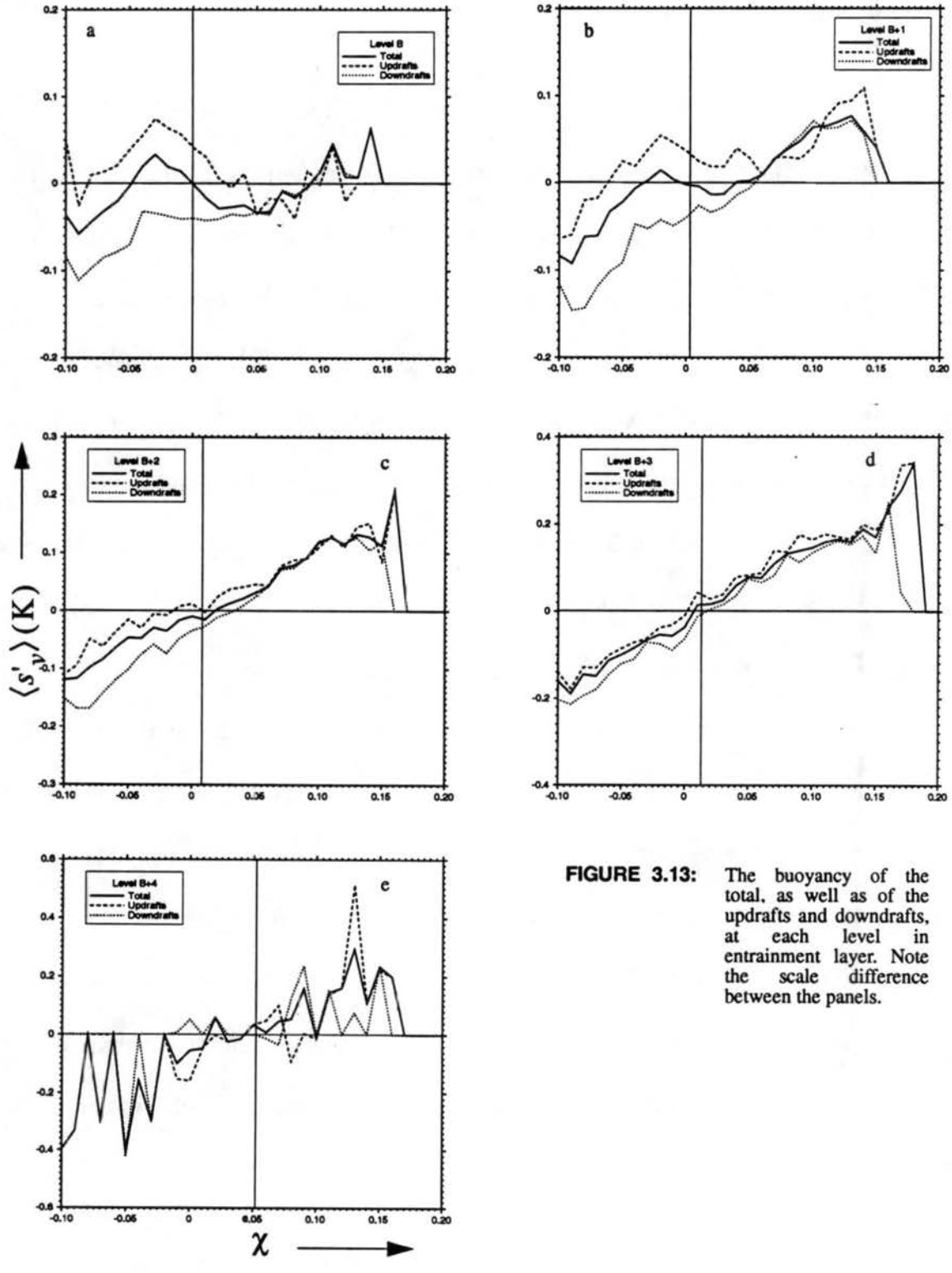

FIGURE 3.13: The buoyancy of the total, as well as of the updrafts and downdrafts, at each level in entrainment layer. Note the scale difference between the panels.

$$\langle s'_\nu \rangle = \langle s_\nu \rangle - (\overline{s_\nu})_{\text{obs}}$$
$$= \chi' [(\overline{s_\nu})_{B+} - (\overline{s_\nu})_{B}] + \langle \delta h'_R(\chi') \rangle + \langle (\delta s'_\nu)_{\text{evp}}(\chi') \rangle, \tag{3.44}$$

which clearly shows that the buoyancy is influenced by the horizontal perturbations of heating and cooling, as well as mixing.

The buoyancy at each level is shown in Fig.3.13. Its components for updrafts and downdrafts are also indicated. The horizontal average mixing fraction is shown for each level; this is actually the zero line for χ'. At higher levels (Figs.3.13c-e) the buoyancy is mainly controlled by mixing, so that essentially the dry parcels ($\chi > \bar{\chi}$) are warm ($\langle s'_v \rangle > 0$) and the moist parcels ($\chi < \bar{\chi}$) are cold ($\langle s'_v \rangle < 0$), regardless of whether they are in updrafts or in downdrafts. At lower levels B and B+1 (Figs.3.13a, b), the average mixing fraction is relatively small, and the effects of radiative and evaporative cooling are appreciable. At level B, when $\chi < 0$, condensation warming is dominant in updrafts, while radiative cooling is dominant in downdrafts, so that downdrafts contain cold-moist parcels. The negative buoyancy of the moist parcels in the downdrafts implies that, at level B, these downdrafts are buoyantly driven, rather than being forced down by the large-eddy circulations. When $0 < \chi < 0.06$, mixing warming compensates part of the evaporative and radiative cooling, but still the parcels in the downdrafts are colder than average. Hence cold-dry parcels appear in the downdrafts as well. When $\chi > 0.06$, the parcels are "well mixed" by small eddies, and distributed randomly between updrafts and downdrafts. When χ is large enough ($\chi > 0.1$), mixing-warming dominates. Parcels in this range can be either cold-dry or warm-dry. The results for level B+1 can be analyzed similarly.

In summary, the downdrafts at level B include three kinds of parcels: cold-moist, cold-dry, and warm-dry. They are presented very clearly in the χ-space, and can be

denoted as unmixed ($\chi < 0$), mixed ($0 < \chi < 0.1$), and well mixed ($\chi > 0.1$), respectively. Their percentages in downdrafts are 35.7%, 60.5%, and 3.8%, respectively. Therefore, cold-dry parcels dominate in the downdrafts, as might be expected and as has been observed in previous studies. The average buoyancy, s'_v, in downdrafts is

$$\overline{s'_v}\Big|_{\text{downdrafts}} = \frac{\int_{\text{sinking parcels}} \langle s'_v \rangle \Pi_E(\chi)\big|_B d\chi}{\int_{\text{sinking parcels}} \Pi_E(\chi)\big|_B d\chi} = -0.037\text{K}. \tag{3.45}$$

This negative buoyancy is a combined result of mixing warming [(3.39)], radiative cooling [(3.37)], and evaporative cooling [(3.37)]. The mixing warming compensates about 70% of the various coolings.

3.3.2.1.5Mixing and selection processes

The above analysis reveals the mixing and selection processes at work in the entrainment layer: After moist parcels enter entrainment layer through level B, they may remain unmixed ($\chi < 0$), or become mixed ($\chi > 0$) either with drier parcels introduced by entrainment at cloud top or with their neighbors in the entrainment layer. Some parcels ($\chi > 0.06$) are well mixed by repeated encounters. The unmixed parcels ($\chi < 0$) experience radiative cooling due to their large liquid water contents, and experience condensation warming due to radiative and adiabatic cooling. If they stay long enough in the entrainment layer, so that their buoyancy becomes negative due to radiative cooling, they sink into downdrafts. Hence the unmixed parcels in downdrafts are cold and moist. Mixed parcels ($\chi < 0$) experience mixing warming, radiative cooling, and evaporative cooling, which all increase with χ, and are of the same order of magnitude. When the

parcels are mixed only with a relatively small amount of warm-dry inversion air ($0 < \chi < 0.06$), the radiative and evaporative cooling dominate, so that these parcels sink to form cold and dry parcels in downdrafts. When parcels are well mixed ($\chi > 0.06$), their properties are essentially the same regardless of whether they are in updrafts or downdrafts. Mixing warming dominates for $\chi > 0.06$ at higher levels, and for $\chi > 0.1$ at level B. The well mixed parcels may follow the flow into downdrafts, and contribute both cold-dry and warm-dry parcels to them.

When the downdrafts emerge from the entrainment layer into the interior of the PBL through level B, they contain 35.7% cold-moist parcels, 60.5% cold-dry parcels, and 3.8% warm-dry parcels. Hence the downdrafts are on average cold and dry at level B. The average radiative cooling (-0.108 K) is four times stronger than the average evaporative cooling (-0.027 K), while the sum of both coolings dominate over the warming due to entrainment mixing (0.098 K), so that the buoyancy of the downdrafts is negative (-0.037 K). On average, these parcels bring 1.03% [see (3.35)] of the mass of the downdrafts consists of air from level B+.

3.3.2.2 Tethered balloon data

We now perform a similar but necessarily less complete analysis of the tethered balloon data collected on San Nicolas Island during FIRE. Fig.3.14 shows the results for cloudy air only, with a total of 230 cloudy parcels. These parcels are analyzed together, rather than level-by-level, because the balloon could not stay exactly at the same level for a long enough time. Consequently, the buoyancy of the parcels can only be expressed as $\langle s_v - (\overline{s_v})_B \rangle$, rather than $\langle s_v - (\overline{s_v})_{obs} \rangle$, since $(\overline{s_v})_B$ can not be obtained.

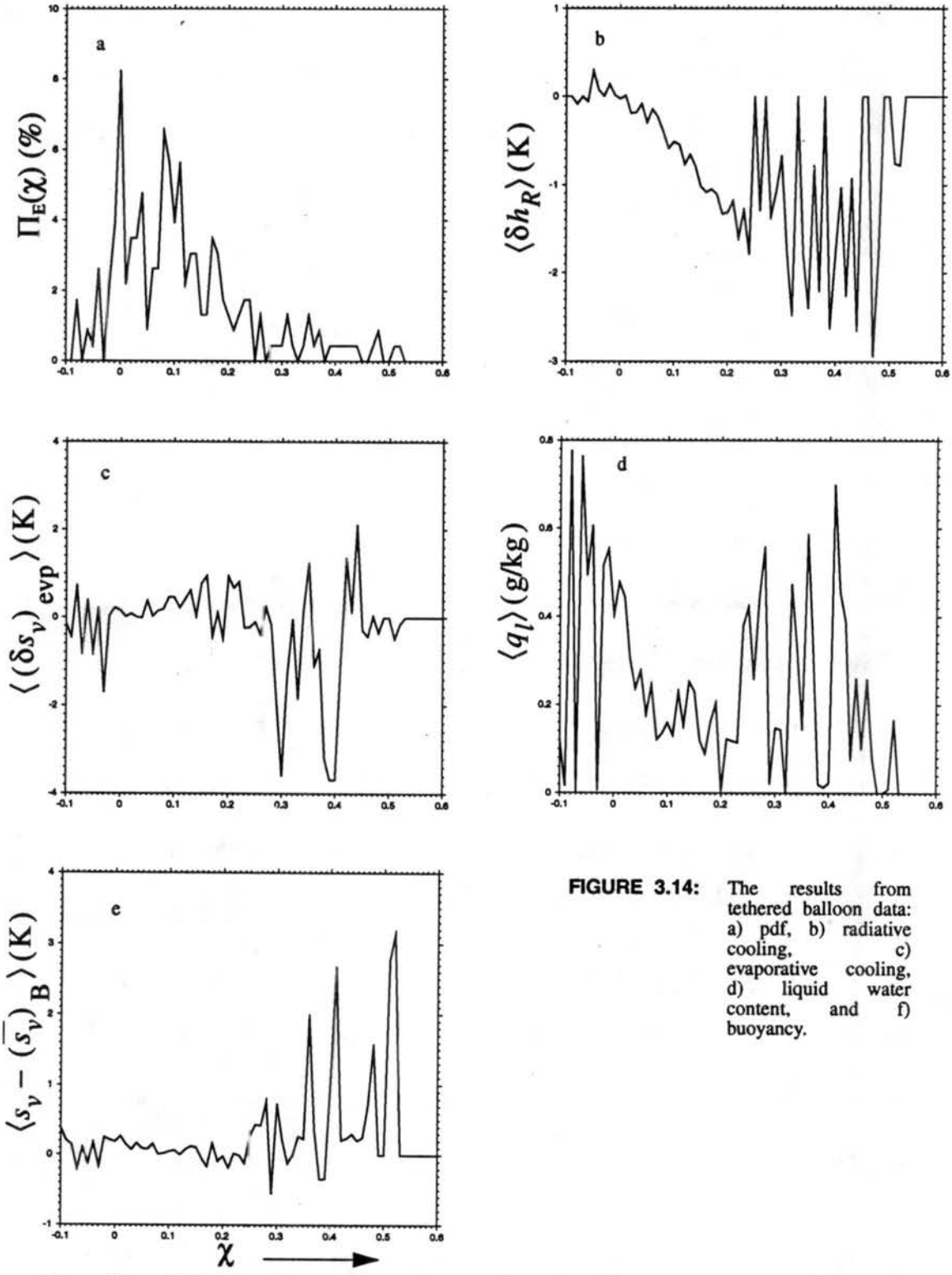

FIGURE 3.14: The results from tethered balloon data: a) pdf, b) radiative cooling, c) evaporative cooling, d) liquid water content, and f) buoyancy.

The pdf, radiative cooling, evaporative cooling, liquid water content, and perturbation of s_v relative to $(\overline{s_v})_B$ are shown in Figs.3.14 a, b, c, d, and e, respectively. It is seen

that the parcels are much drier than those from the LES data, with an average mixing fraction of 11.8%. The magnitude of $\langle \delta h_R \rangle$ is also about ten times larger than that from the LES data, with an average of -0.634 K. The maximum cooling occurs, on average, for χ near 0.4. There is an average condensation warming of 0.077 K, although some parcels show strong evaporative cooling (Fig.3.14 c). The liquid water content has two peaks. The peak near $\chi = 0.4$ may be due to the strong radiative cooling and resulting condensation. The buoyancy, defined by $\langle s_v - (\overline{s_v})_B \rangle$, is positive for almost all χ. This is not surprising but is probably misleading, since $(\overline{s_v})_B$, rather than $(\overline{s_v})_{obs}$, is used. The effects of mixing warming are larger for larger χ, as would be expected.

There are two possible reasons for the strong δh_R observed from the balloon. One is related to problems associated with the instruments used, especially the output of the FSSP (Forward Scattering Spectrometer Probe), which was shifted to lower bins, so that the resolution was reduced. As a result, q_l and q_t were underestimated. With the underestimated q_t, χ can be overestimated, which in turn leads to an overestimation of the radiative cooling. To illustrate this point, let us assume that the real values of q_t, $(\overline{q_t})_B$, and $(\overline{q_t})_{B+}$ are 6.92 g kg^{-1}, 7.2 g kg^{-1} and 4.3 g kg^{-1}, respectively. From (3.8), $\chi = 0.1$. Suppose that the observed q_t was 6.62 g kg^{-1}, with the -0.3 g kg^{-1} difference coming from the underestimation of q_l. Then χ would be doubled, from 0.1 to 0.2. For $(\overline{h_{B+}} - \overline{h_B}) \sim 10$ K, a $\Delta\chi$ of 0.1 could result in -1.0 K of "extra" cooling. We conclude that our results are very sensitive to the observed total water contents.

Another possible reason for the difference between the San Nicolas Island results and other observations, as well as our LES results, is that the residence times of parcels in the

radiatively cooled layer in this case could have been significantly longer than in the other cases. This idea is partly supported by the large χ observed for the cloudy parcels. Longer residence times might be associated with mesoscale circulationss that advect parcels through the radiatively cooled layer for an extended period of time. Such mesoscale cells cannot occur in the LES since the domain size is too small.

3.4 Concluding remarks

We have demonstrated a method that can be used to investigate the effects of mixing, evaporative cooling and radiative cooling in the ventilation and entrainment layers. By applying this method to an LES-simulated flow and to tethered balloon data, the physical processes in the ventilation and entrainment layers have been quantified. The results show how the parcel properties depend on the mixing fraction.

A particular LES flow field was analyzed to study the mixing and selection processes that generate updrafts in the convective ventilation layer, and downdrafts in the cloudy entrainment layer, with the hope that the results would shed some light on what happens in stratus-topped boundary layer flow. We know, however, that the LES has some weaknesses near the top and bottom of the PBL, due to the numerical resolution and the assumed lower boundary conditions.

Turbulent mixing is the main arbiter of the properties of the updrafts emerging from the ventilation layer. The updrafts are warm and moist, and have been modified by "contact" with the surface. It is this modified air that advects surface-like properties (e.g.

temperature and moisture) into the interior of the PBL. The effect of the surface is represented by the mixing fraction χ_V in the updrafts, which is determined by turbulent mixing. Stronger lateral mixing between the dry downdrafts and the moist updrafts leads to a reduction in χ_V. This suggests that χ_V can be used as an external parameter in a bulk surface-layer model. The total effect of the surface on the interior is also partially determined by the convective mass flux.

In a cloudy entrainment layer, the relative importance of turbulent mixing, evaporative cooling and radiative cooling in generating downdrafts depends on χ. These processes are comparable in magnitude, but their dependencies on χ are different. For $\chi < 0$ (unmixed parcels) the radiative cooling, and condensation warming driven by radiative and adiabatic cooling are the main processes that determine the buoyancy of the parcels. For the case studied here, radiative cooling dominates in downdrafts, which results in negative buoyancy, so that some parcels in downdrafts are cold and moist.

For $\chi > 0$, mixing warming, evaporative cooling and radiative cooling all increase with χ at each level, and mixing warming increases most rapidly. Hence mixing warming dominates for relative large χ. At level B (i.e., the bottom of the entrainment layer), the radiative cooling and evaporative cooling are dominant for $\chi < 0.1$, so that cold-dry parcels appear in the downdrafts. In fact, most of the parcels in the downdrafts are cold and dry. Mixing warming is dominant for $\chi > 0.1$. These parcels are in the range we defined as "well mixed." As discussed in last section, parcels with $\chi > 0.06$ show no systematic differences between updrafts and downdrafts. The strong radiative cooling and relatively large mixing fraction in this range of χ indicate that these parcels have

experienced multiple mixing events, and have stayed in the entrainment layer for a relatively long time.

The efficiency with which free atmospheric air can be introduced into the interior is measured by χ_E. This mixing fraction determines the mixing warming, and partly determines the evaporative cooling. The net effect of the mixing warming and evaporative cooling is a warming of 0.071 K for the downdrafts at level B, which is close to the value obtained in Nicholls' (1989) study of aircraft measurements. The radiative cooling is stronger than this warming, so that the downdrafts are negatively buoyant.

When we talk about entrainment-mixing effects near cloud top, radiative cooling can not be ignored. The radiative cooling not only enhances the entrainment rate, but also suppresses the evaporative cooling. The radiative cooling itself is independent of the mixing fraction. It is indirectly related to χ_E, however, through the change of q_l. A positive feedback exists between the radiative cooling and the liquid water content near cloud top. A larger q_l favors stronger radiative cooling. The radiative cooling in turn reduces the temperature of the air, and hence suppresses the decrease of q_l from evaporatin, as was shown in our LES results. This effect of radiative cooling on evaporative cooling was generally not included in the theoretical studies mentioned above (e.g., Kuo and Schubert, 1988; Duynkerke, 1993), which calculated the buoyancy of parcels due only to mixing warming and evaporative cooling. The liquid water amount evaporated and the negative buoyancy of the mixed parcels could be overestimated by ignoring this effect.

Tethered balloon data from San Nicolas Island was also used to study the properties of the entrainment layer. The average mixing fraction is very large in this case. The radiative cooling also appears to be very strong. Further study of this data is needed to find convincing explanations for these results.

CHAPTER 4

Effects of Cloud-top Cooling on Mesoscale Shallow Convection

4.1 Introduction

Mesoscale shallow convection is often observed together with small-scale convection, as reviewed in Chapter 1. This includes mesoscale cellular convection (MCC). Small-scale cumuli are organized to form mesoscale cloud patterns, as was reported by Krueger and Fritz (1961), and Hubert (1966). The basic characteristics of MCC are its large aspect ratio (diameter/depth), which is about 15 to 30, and direction of circulation, which includes both closed cells (i.e., wide upward motion at the cell centers and thin downward motion at the cell edges) and open cells (i.e., the direction of circulation is opposite to that of closed cells). However, it is not clear yet how the radiative and evaporative cooling are related to these basic features of MCC. Can the cooling, which is strongest near cloud top, produce a large-aspect-ratio convection as well as control the direction of the circulation so that closed MCC develops in a stratus topped PBL?

To understand this problem, it is useful to look back to see what mechanisms have been proposed in the past for the formation of MCC. Since the pattern of MCC resembles the pattern of classical Rayleigh-Benard (RB) convection, considerable work has been performed to modify the RB theory to explain the formation of MCC, although the aspect ratio of RB convection is about an order of magnitude smaller than that of MCC. The previous work can be basically grouped into two broad approaches: One is to modify the classical RB theory by additional physical processes which are unique to the atmosphere. These processes include turbulent diffusion, synoptic-scale forcing, the internal distributions of heating and cooling associated with clouds, the interactions between gravity waves and convection, the interactions between the PBL and the free atmosphere, and various boundary conditions. The second approach is based on the idea that mesoscale organization exists in the PBL due to the inherent nonlinearity of convection when the Rayleigh number is large enough. These mechanisms are discussed below one by one.

The spatial inhomogenity and anisotropy of turbulent diffusion have been used to try to explain the direction of circulation and flatness of MCC. Stommel (1947) postulated that convective motions originate in a low viscosity region, and move towards a high viscosity region. Based on this assumption, Hubert (1966) proposed that vertical variations of the eddy diffusion coefficient determines the direction of circulation of MCC. An increase (decrease) of eddy diffusion coefficient with height will result in open (closed) cells. This idea was further elaborated by Agee and Chen (1973) by using a mathematical model. They concluded that the vertical variation of the eddy diffusive coefficient has little effect on the flatness of cells. Rather, as first suggested by Priestley

(1962), and later demonstrated by Ray (1965) by using a linear model, they concluded that the degree of cell flatness is principally controlled by the degree of anisotropy of the eddy coefficients. The larger the horizontal diffusion coefficient is relative to the vertical one, the wider the cells are. However, to reach an aspect ratio of 30:1, the horizontal diffusion coefficient has to be about 100 times larger than the vertical diffusion coefficient (Ray, 1965), which is not plausible for the convective PBL.

MCC is often associated with some synoptic weather systems, such as cold-air outbreaks and subtropical highs (e.g., Agee, 1987). Krishnamurti (1975a, b, c) showed, by using both mathematical and laboratory models, that large scale vertical motion can control the direction of circulation of MCC. Large scale rising (sinking) motion prefers closed (open) cells. However, based on the observational data, Sheu and Agee (1977) found that this is not always true in the atmosphere. For reasonable values of the parameters, the models give an aspect ratio of about 3. Therefore, this mechanism cannot be used to explain the flatness and the direction of MCC.

The appearance of clouds is a distinctive feature of MCC, although some mesoscale shallow convection may still be observed in clear sky condition (e.g., Hardy and Ottersten, 1969; Konrad, 1970). Clouds may produce vertically inhomogeneous internal heating and cooling in the PBL due to radiation and phase changes. That latent heat release can produce open MCC in a conditionally unstable atmosphere has been commonly accepted (Bjerknes, 1938; Lilly, 1960; Kuo, 1961, 1965; Asai, 1967; Yamasaki, 1972; Rosmond, 1973; Asai and Nakasuji, 1977, 1982; Sheu et al., 1980; Van Delden, 1985a; Brugge and Moncrieff, 1985; Oerlemans, 1986; Bretherton, 1987, 1988;

Chlond, 1988; Huang, 1990). The basic idea of this mechanism for open MCC is that a conditionally unstable atmosphere is unstable for ascending pseudoadiabatic motions and stable for dry descending motions. Therefore two kinds of scales can be involved in the motions: One is the small scale related to the cumulus updrafts; the other is the mesoscale associated with the wide downdrafts. The degree of cell flatness depends on the basic state stability of the cloudy layer, or the rate of latent heat release. In this case surface heating must be provided to generate convection. Due to the small amount of cloudness, radiative and evaporative cooling are not dominant effects.

Closed cells have a direction of circulation opposite to that of open cells, and large cloud amount of about 90%. They happen more frequently over stable surface layers (Hubert, 1966; Agee et al., 1973), although they have also been observed over warm ocean currents (e.g., Agee and Lomax, 1978). Radiative and evaporative cooling at cloud top are therefore at least part of the driving force of convection for closed MCC. There is no single, commonly accepted theory for how the cooling is related to MCC, however. Helfand and Kalnay (1983) studied the effects of asymmetric internal heating by using a RB-type model, but with a zero heat-flux boundary conditions at high Rayleigh number. They concluded that strong cooling in the upper part of the layer can generate circulations of a closed type, and that strong warming in the lower part of the layer can generate circulations of an open type. This result suggests that radiative and evaporative cooling at cloud top may be the driving force for closed MCC. However, their results cannot explain the observations of closed MCC over warm water and open cells over cold water. Moreover, the aspect ratio of their domain size was 3, which means that no conclusion about the cell flatness could be obtained. They mentioned that when the

aspect ratio of their domain size increased to 4, the one-cell pattern bifurcated into a two cell pattern.

Clark et al. (1986) and Huang (1990) suggested that interactions between gravity waves and convection may be important for MCC. Convection can generate vertically and horizontally propagating gravity waves. The gravity waves can feed back on the convection, and organize small scale convection into mesoscale structures. The effect of vertically propagating gravity waves on the convection inside the PBL represents an interaction of the free atmosphere and the PBL (Clark et al., 1986).

Sasaki (1970) first noticed that the top and bottom boundaries of a PBL in which MCC happens are not necessarily at constant temperature. It is the constant temperature (or perfectly conductive) boundary condition that gives the small aspect ratio to the most unstable mode in the classical RB theory (see Chandrasekhar, 1961). From a linear analysis of the RB problem with imperfectly conducting boundaries, Sparrow et al. (1964) and Hurle et al. (1967) found that, in the extreme case of non-conductive (or constant heat flux) boundary conditions, the critical horizontal wavenumber for the onset of convection approaches zero, in sharp contrast with the constant temperature case. Sasaki (1970) did a thorough linear analysis for MCC for different dynamic boundary conditions, and obtained similar results. Following this direction, Fiedler (1985) developed a linear theoretical model based on the imperfectly conducting boundary conditions. He also did some numerical simulations with small Rayleigh numbers (R_a) (Fiedler, 1989, 1990, 1993): $R_a/R_{ac} \sim 1$, where R_{ac} is the critical Rayleigh number.

Based on the results derived from his linear model (Fiedler, 1985), Fiedler argued that mesoscale entrainment instability (MEI) (proposed by Fiedler, 1984) is a plausible mechanism for the formation of closed MCC. MEI requires that at a cloud top with a positive height anormaly ($h' > 0$), the entrainment rate is weaker, and the entrainment mixing warming due to buoyancy is stronger, than at other places with $h' < 0$. Therefore, where $h' > 0$ the cloud-top buoyancy is more positive, and cloud-top turbulence is enhanced; while where $h' < 0$ the cloud-top turbulence is suppressed due to less warming, and the clouds tend to disappear due to stronger entrainment. The requirement of weaker entrainment at cloud top in this mechanism is very hard to understand. Through numerical simulations, Rand and Bretherton (1991) found that an extremely weak inversion and a very strong stable stratification above the inversion are required, to be consistent with MEI, which is unrealistic. van Delden (1985b) commented that for MEI to happen, a turbulent transfer coefficient of 1000 $m^2 s^{-1}$ would be required, which is unreasonable for the PBL.

Based on his numerical results, Fiedler (1989, 1990, 1993) concluded that MCC could not appear in a two-dimensional model. He argued that, besides the imperfectly conducting boundary conditions, a three-dimensional model is needed to generate MCC (Fiedler, 1993). Later in this chapter, we will show evidence that this argument may not be true.

In contrast to approaches based on adding physical mechanisms, Rothermel and Agee (1986) studied the classical RB model, which has constant-temperature boundary conditions. They ran the model for different Rayleigh numbers and found that when

$R_a/R_{ac} \sim 1-10$ the aspect ratio of the cells cannot be greater than the critical value of about 2 predicted by linear theory. When $R_a/R_{ac} \sim 10^2-10^3$, however, the initial smaller cells gradually merged into larger cells. At R_a/R_{ac} = 600 and 800, the model predicts an aspect ratio of 9.43, which is well within the range for MCC. They then concluded that the nonlinearity inherent in the model is crucial to produce the cell flatness. However, Sykes and Henn (1988) could not find mesoscale circulations by using the same model as used by Rothermel and Agee (1986), except that the numerical methods used to solve the equations were different between these two studies. Therefore Sykes and Henn (1988) argued that the conclusions in Rothermel and Agee (1986) were strongly influenced by numerical methods.

Our main purpose in this chapter is to see what role cloud-top cooling plays in the formation of closed MCC. This is a very complicated problem, since it involves the microphysics of clouds as well as radiative transfer. The simplest way to approach the problem is to prescribe a heating/cooling profile with the strongest cooling near cloud top. We expect that the advection of the strongly cooled cloud-top air could produce or enhance MCC. Therefore, nonlinear effects should be important. For this purpose, a two dimensional nonlinear model with constant-flux boundary conditions and internal heating/cooling is developed. Large-scale divergence is not considered. The effects of moisture on buoyancy are also ignored at this stage, except that the heating/cooling due to the presence of clouds is included in the idealized, prescribed heating/cooling profile. The interactions between the PBL and the free atmosphere are also omitted here so that the domain height represents the height of the PBL. A derivation of the equations is given in Section 2. Finite-amplitude weakly nonlinear analytical solutions are derived

and discussed in Section 3, and fully nonlinear numerical solutions are discussed in Section 4. Concluding remarks are given in Section 5.

4.2 The model

4.2.1 The equations

Since closed MCC is shallow, and density fluctuations result primarily from thermal effects, the Boussinesq equations without the Coriolis effect are used in the present study:

$$\frac{\partial u_j}{\partial x_j} = 0,$$

$$\frac{\partial u_i}{\partial t} + \frac{\partial}{\partial x}(u_i u_j) = -\frac{1}{\rho_0}\frac{\partial p}{\partial x_i} + \frac{\theta}{\Theta_0} g\delta_{i3} + K_M \frac{\partial^2 u_i}{\partial x_j}, \tag{4.1}$$

$$\frac{\partial \theta}{\partial t} + \frac{\partial}{\partial x_j}(u_j \theta) = \dot{Q} + \beta w + K_H \frac{\partial^2 \theta}{\partial x_j}.$$

Here $u_i\,(i=1,3)$, p, θ are fluctuations of wind, pressure and potential temperature from their basic state values, respectively. The basic-state wind is zero and the basic state pressure is hydrostatic. The initial basic-state stratification is represented by $\beta = -d\Theta_0/dz$. We have also assumed that the turbulent diffusion coefficients are constants, and are the same both horizontally and vertically. Molecular terms are absorbed into the turbulent diffusion terms. The quantity $\dot{Q}$ represents the prescribed internal heating/cooling profile. In this study it only changes with height.

By defining a stream function, ψ, and setting $u = -\frac{\partial \psi}{\partial z}$, $w = \frac{\partial \psi}{\partial x}$, and introducing the vertical vorticity component $\zeta = \frac{\partial w}{\partial x} - \frac{\partial u}{\partial z}$, the system (4.1) can be rewritten in the "vorticity form" as

$$\begin{aligned} \zeta &= \frac{\partial^2 \psi}{\partial x^2} + \frac{\partial^2 \psi}{\partial z^2}, \\ \frac{\partial \zeta}{\partial t} - \frac{\partial \psi}{\partial z}\frac{\partial \zeta}{\partial x} + \frac{\partial \psi}{\partial x}\frac{\partial \zeta}{\partial z} &= \frac{g}{\Theta_0}\frac{\partial \theta}{\partial x} + K_M\left(\frac{\partial^2 \zeta}{\partial x^2} + \frac{\partial^2 \zeta}{\partial z^2}\right), \\ \frac{\partial \theta}{\partial t} - \frac{\partial \psi}{\partial z}\frac{\partial \theta}{\partial x} + \frac{\partial \psi}{\partial x}\frac{\partial \theta}{\partial z} &= \dot{Q} + \beta\frac{\partial \psi}{\partial x} + K_H\left(\frac{\partial^2 \theta}{\partial x^2} + \frac{\partial^2 \theta}{\partial z^2}\right). \end{aligned} \tag{4.2}$$

The heat fluxes at the upper and lower boundaries are prescribed constants. The lower boundary is rigid and non-slip, and the upper boundary is rigid and free-slip. The upper and lower boundary conditions can be expressed as

$$u = 0,\ w = 0\ \left(\text{or } \frac{\partial \psi}{\partial z} = 0,\ \psi = 0\right), \text{ and } \frac{\partial \theta}{\partial z} = c_b \text{ at } z = 0; \tag{4.3}$$

$$\frac{\partial u}{\partial z} = 0,\ w = 0\ \left(\text{or } \frac{\partial^2 \psi}{\partial z^2} = 0,\ \psi = 0\right), \text{ and } \frac{\partial \theta}{\partial z} = c_t \text{ at } z = d. \tag{4.4}$$

The interpretation of c_b and c_t are explained later. The lateral boundaries are assumed to be periodic.

4.2.2 The internal forcing, $\dot{Q}$

In order to allow a steady state, the total internal forcing $\dot{Q}$ has to be balanced by the heating at the boundaries. Taking the horizontal average, denoted by $\langle\ \rangle$, of the thermodynamic equation in (4.2), and integrating it vertically, we obtain

$$\int_0^d \langle \dot{Q} \rangle dz = K_H (c_b - c_t) . \tag{4.5}$$

Here we have used the condition that the resolvable heat fluxes at the top and bottom are zero, since the vertical velocities are zero there. Eq. (4.5) gives a constraint between the internal forcing and boundary conditions that must be satisfied if a final steady state is desired. If we take $\int_0^d \langle \dot{Q} \rangle dz = 0$, as in this study, then we should have $c_b = c_t$. This condition will again be obtained naturally in the next section.

The heating profile used is similar to that of Helfand and Kalnay (1983):

$$\langle \dot{Q} \rangle = \dot{Q} = a [(z_0/d)^n - (z/d)^n] , \tag{4.6}$$

where a represents the magnitude of $\dot{Q}$, and $n \geq 1$. We choose z_0 as

$$z_0 = d \left(\frac{1}{n+1} \right)^{1/n} , \tag{4.7}$$

which guarantees that (1.6) is satisfied. Note that $n = 1$ gives a linear profile of $\dot{Q}$, with $z_0/d = 1/2$. For $a > 0$, $\dot{Q}$ is positive when $z < z_0$, and negative when $z > z_0$. Therefore, there are two key quantities in (4.6): One is a, which represents the strength of the heating/cooling; and the other is z_0, which represents the asymmetry of the profile. When $a > 0$, Eq. (4.6) gives cooling in the upper part of the fluid and warming in the lower part. When z_0 (or n) increases, the cooling becomes more concentrated at the top of the layer.

From (4.5), the flux "generated by" the positive part of $\dot{Q}$ equals that generated by the negative part:

$$F \equiv \int_0^{z_0} \langle \dot{Q} \rangle dz = -\int_{z_0}^{d} \langle \dot{Q} \rangle dz > 0. \tag{4.8}$$

When the fluxes at the boundaries are zero ($c_b = c_t = 0$), the flux F is the only heat source that can drive motions. Substituting (4.6) into (4.8), we obtain

$$F = dan \left(\frac{1}{n+1}\right)^{(2n+1)/n}. \tag{4.9}$$

It is easy to prove that $\lim_{n \to \infty} F = 0$.

The change of $F/(da)$ and z_0/d with n, and that of $\dot{Q}/a$ with z/d for $n = 5$, are shown in Fig. 4.1. With a larger n, z_0 is larger, while F is smaller. The strong cooling is concentrated in the layer $z > z_0$, while the mild warming is spread out in the deep layer where $z < z_0$.

In order to facilitate intercomparison of the results shown in the following sections, it is useful to keep the total heat input [see (4.12) below] from both internal forcing [i.e., F in (4.8)] and boundary forcing [i.e., c_b] the same for all cases. In this study we use $F_0 = F(n = 5)$ as a reference. The parameters used for the reference solution are

$$d = 1500\text{m}, \tag{4.10}$$

$$n = 5,\ a = \frac{1}{600}\text{Ks}^{-1},\ c_b = c_t = 0; \tag{4.11}$$

so that the total heating is

$$-K_H c_b + F(n) = F_0 = F(n = 5) = 0.23\text{K ms}^{-1}. \tag{4.12}$$

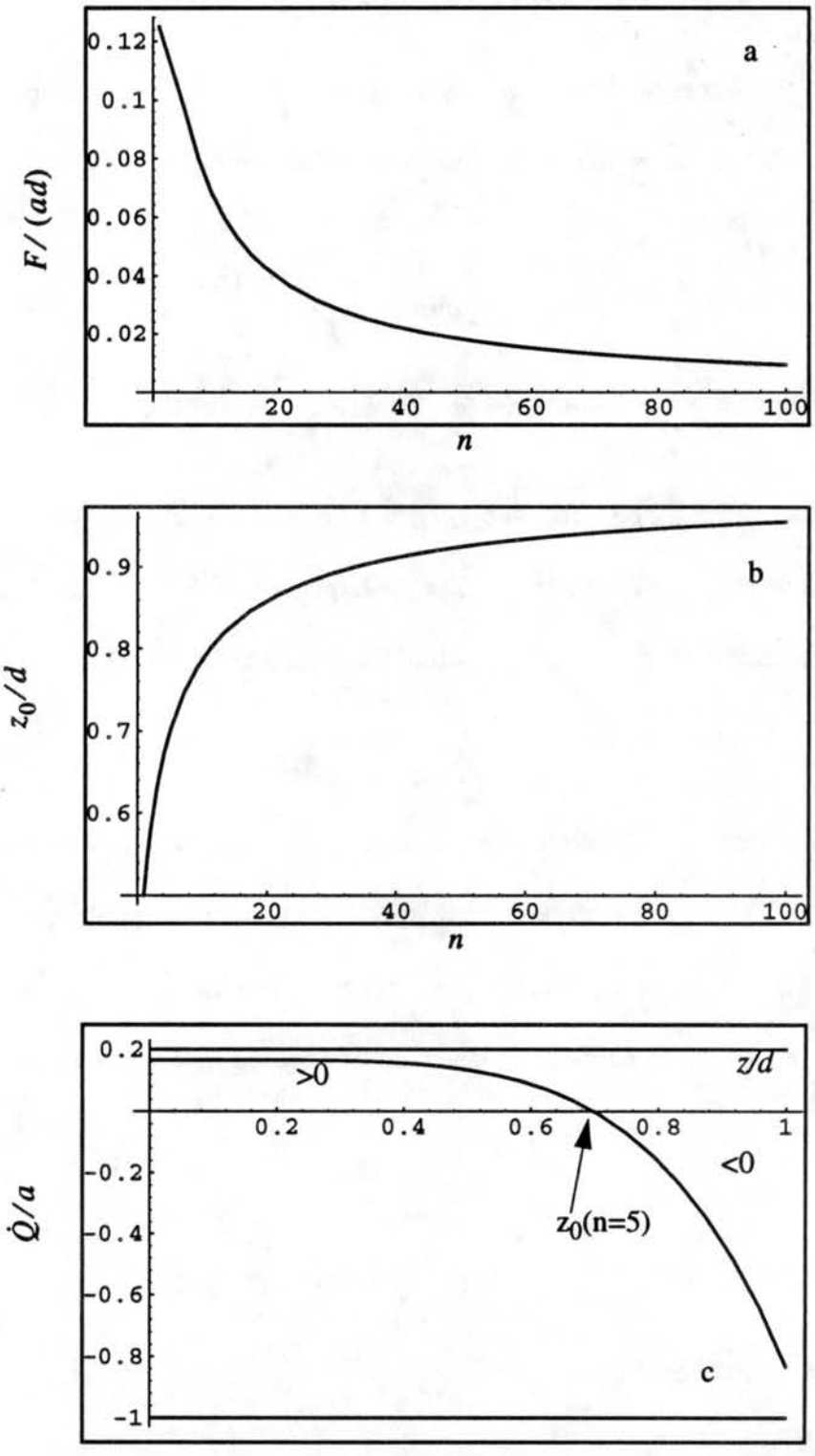

FIGURE 4.1: The change of (a) $F/(da)$, and (b) z_0/d with n, and (c) $\dot{Q}/a$ with z/d at $n = 5$.

Based on (4.12), the parameters in (4.11) are subject to change with different profiles of internal forcing. The five different profiles used in our experiments are listed in Table 1, and plotted in Fig. 4.2. They are designed to show how the cell structure is affected

Table 4.1: The parameters for the internal and boundary forcings

Case	n	a (10^{-3}K s^{-1})	z_0/d	F (K m s^{-1})	c_b (K m^{-1})
1 (n5)	5	1.667	0.7	0.23	0
2 (n35)	35	6.636	0.9	0.23	0
3 (n1)	1	1.294	0.5	0.23	0
4 (cb)	--	0	--	0	$-0.23/K_H$
5 (n35cb)	35	3.318	0.9	0.115	$-0.115/K_H$

when:

(1) only the internal heating/cooling exists (i.e., the heat fluxes at the boundaries are zero), and the asymmetry of their profiles changes (cases 1 to 3). Since the change of asymmetry is represented by n, we also denote these cases by n5, n35, and n1, respectively.

(2) the heating/cooling happens only at the top and bottom boundaries of the layer (case 4). This case is also denoted by cb.

(3) the combination of (1) and (2), i.e., both internal and boundary heating/cooling exist (case 5). This case is denoted as n35cb.

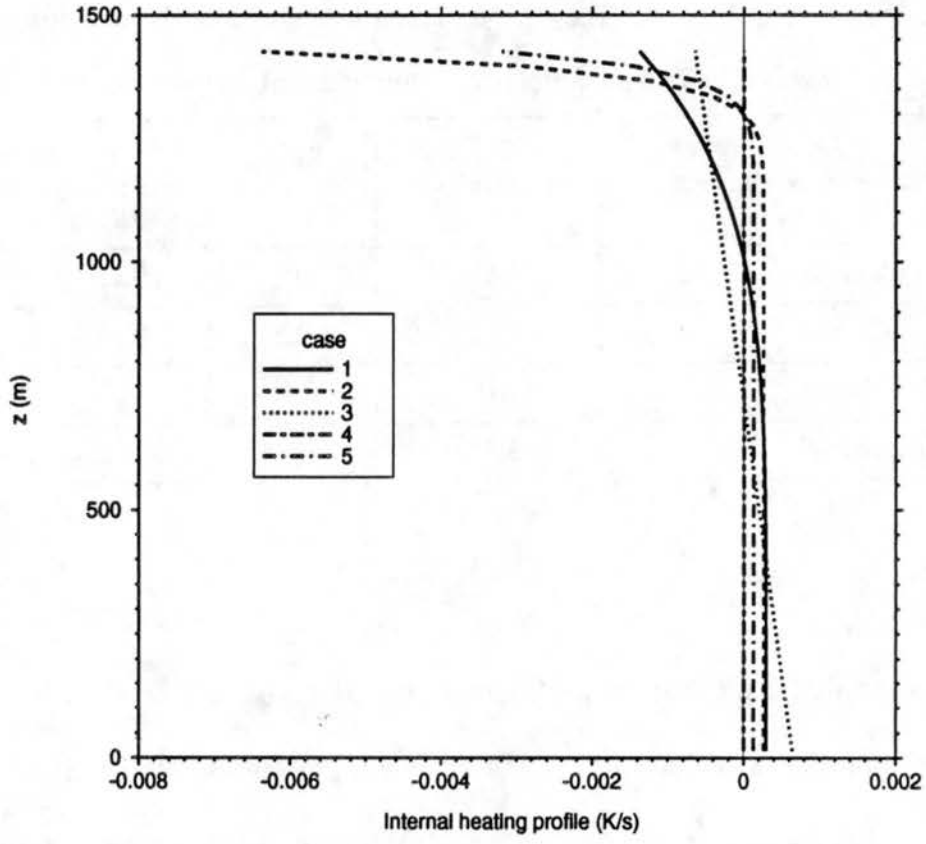

FIGURE 4.2: The internal heating/cooling profiles based on values listed in Table 1. Fluxes from boundaries (c_b and c_t) are not indicated here. Since $F = F_0$ is the same for all cases, the larger the n (or the more asymmetric the profile), the stronger the cooling near the top.

4.3 The weak nonlinear analytical solution to the effect of coolings at the top

4.3.1 The nondimensional equations

A nondimensional form of (4.2) is used in this section. The scaling parameters are chosen as follows:

- the depth of the domain: $[d] = \mathrm{m}$;
- the heat diffusion coefficient: $[K_H] = \mathrm{m^2 s^{-1}}$;
- the total forcing $[F_0] = \mathrm{K\,m\ s^{-1}}$, which is the same for all of the cases studied.

The variables can then be expressed in nondimensional form as

$$\begin{aligned} \psi &= \hat{\psi} K_H \ , \\ \theta &= \hat{\theta} F_0 d / K_H \ , \\ t &= \hat{t} d^2 / K_H \ , \\ (x, z) &= d\,(\hat{x}, \hat{z}) \, . \end{aligned} \tag{4.13}$$

Here "^" denotes a nondimensional variable. By substituting (4.13) into (4.2), we obtain the nondimensional form of the equations:

$$\begin{aligned} \hat{\zeta} &= \frac{\partial^2 \hat{\psi}}{\partial \hat{x}^2} + \frac{\partial^2 \hat{\psi}}{\partial \hat{z}^2} \ , \\ \frac{1}{P_r}\left(\frac{\partial \hat{\zeta}}{\partial \hat{t}} - \frac{\partial \hat{\psi}}{\partial \hat{z}}\frac{\partial \hat{\zeta}}{\partial \hat{x}} + \frac{\partial \hat{\psi}}{\partial \hat{x}}\frac{\partial \hat{\zeta}}{\partial \hat{z}}\right) &= R_a \frac{\partial \hat{\theta}}{\partial \hat{x}} + \frac{\partial^2 \hat{\zeta}}{\partial \hat{x}^2} + \frac{\partial^2 \hat{\zeta}}{\partial \hat{z}^2} \ , \\ \frac{\partial \hat{\theta}}{\partial \hat{t}} - \frac{\partial \hat{\psi}}{\partial \hat{z}}\frac{\partial \hat{\theta}}{\partial \hat{x}} + \frac{\partial \hat{\psi}}{\partial \hat{x}}\frac{\partial \hat{\theta}}{\partial \hat{z}} &= A_Q + q\frac{\partial \hat{\psi}}{\partial \hat{x}} + \frac{\partial^2 \hat{\theta}}{\partial \hat{x}^2} + \frac{\partial^2 \hat{\theta}}{\partial \hat{z}^2} \ , \end{aligned} \tag{4.14}$$

where $Pr = K_M / K_H$ is the turbulent Prandtl number, $R_a = (g F_0 d^4) / (\Theta_0 K_H^2 K_M)$ is the Rayleigh number, $q \equiv (\beta K_H) / F_0$ is the nondimensionalized initial basic state stratification, and $A_Q = \dot{Q}\,(d / F_0)$ is the nondimensionalized internal forcing, which changes only with height. The boundary conditions (4.3) and (4.4) become

$$\frac{\partial \hat{\psi}}{\partial \hat{z}} = 0,\ \hat{\psi} = 0, \text{and } \frac{\partial \hat{\theta}}{\partial \hat{z}} = (c_b K_H)/F_0 \text{ at } \hat{z} = 0; \tag{4.15}$$

$$\frac{\partial^2 \hat{\psi}}{\partial \hat{z}^2} = 0,\ \hat{\psi} = 0, \text{and } \frac{\partial \hat{\theta}}{\partial \hat{z}} = (c_t K_H)/F_0 \text{ at } \hat{z} = 1. \tag{4.16}$$

4.3.2 A perturbation method

As was discussed in the first section, the linear theory shows that the most unstable wave number is zero when the boundaries of the fluid are insulating (e.g., Hurle et al., 1967; Sasaki, 1970). This is illustrated in Fig. 4.3. The linear theory requires that the

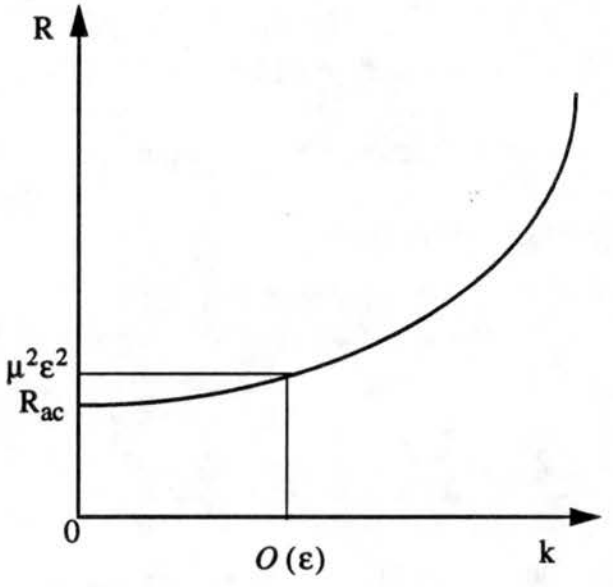

FIGURE 4.3: A schematic illustration of the relation between critical Rayleigh number and wave number obtained from linear theory. The minimum R_{ac} happens at k=0. (Chapman and Proctor, 1980)

amplitude of perturbations be infinitesimal. In the case we are studying, however, nonlinear effects are expected to be important due to advection. To relax the infinitesimal

amplitude requirement, a perturbation method or small-parameter is applied to solve (4.14).

The approach followed here is to identify the inversion of the aspect ratio of the cell, $\varepsilon = H/L$, as a small parameter, and to expand the variables in (4.14) in terms of ε. Here H represents the height of the cell, and L represents the width of the cell. The H is at the same order of the scaling parameter, d, as used in Eq. (4.13). This means that the wave number of the cells which will be obtained must be $k = O(\varepsilon)$ for consistency. Since the minimum R_{ac} shown in Fig. 4.3 is obtained for even powers of k (Hurle et al., 1967; Sasaki, 1970), the Rayleigh number related to this wave number is $R_a = R_{ac} + \mu^2\varepsilon^2$, where $0 < \mu^2 \leq 1$. With $\mu^2 = 1$, we have $\varepsilon^2 = R_a - R_{ac}$. Therefore, the solution is slightly supercritical. This is also indicated in Fig. 4.3. This small-parameter method has been used by Childress et al. (1975) to solve the problem of convection due to swimming micro-organisms, and by Chapman and Proctor (1980) to solve mantle-convection problems. No limit is imposed on the amplitude of the motion.

Following Chapman and Proctor (1980), the magnitudes of other variables in (4.14) can be expressed as

$$
\begin{aligned}
(\hat{x}, \hat{z}) &= (X, \varepsilon Z) \quad , \\
(-\frac{\partial \hat{\psi}}{\partial \hat{z}}, \frac{\partial \hat{\psi}}{\partial \hat{x}}) &= (-\varepsilon \frac{\partial \varphi}{\partial Z}, \varepsilon^2 \frac{\partial \varphi}{\partial X}) \quad , \\
\hat{\theta} &= \theta \quad , \\
\frac{\partial}{\partial \hat{t}} &= \varepsilon^4 \frac{\partial}{\partial \tau} \quad , \\
R_a &= R_{ac} + \mu^2 \varepsilon^2 \quad ,
\end{aligned}
\tag{4.17}
$$

where $X, Z, -\frac{\partial\varphi}{\partial Z}, \frac{\partial\varphi}{\partial X}, \theta, \tau, R_c$ and μ are $O(\varepsilon^0)$. By substituting (4.17) into (4.14), we have

$$\frac{1}{P_r}\{\varepsilon^6\frac{\partial}{\partial\tau}\left(\frac{\partial^2\varphi}{\partial X^2}\right)+\varepsilon^4\frac{\partial}{\partial\tau}\left(\frac{\partial^2\varphi}{\partial Z^2}\right)+\varepsilon^4\left[(\frac{\partial\varphi}{\partial X})\frac{\partial}{\partial Z}\left(\frac{\partial^2\varphi}{\partial X^2}\right)-(\frac{\partial\varphi}{\partial Z})\frac{\partial}{\partial X}\left(\frac{\partial^2\varphi}{\partial X^2}\right)\right]$$
$$+\varepsilon^2\left[-(\frac{\partial\varphi}{\partial Z})\frac{\partial}{\partial X}\left(\frac{\partial^2\varphi}{\partial Z^2}\right)+(\frac{\partial\varphi}{\partial X})\frac{\partial}{\partial Z}\left(\frac{\partial^2\varphi}{\partial Z^2}\right)\right]\} \tag{4.18}$$
$$=(R_{ac}+\mu^2\varepsilon^2)\frac{\partial\theta}{\partial X}+\varepsilon^4\frac{\partial^4\varphi}{\partial X^4}+2\varepsilon^2\frac{\partial^2}{\partial X^2}\left(\frac{\partial^2\varphi}{\partial Z^2}\right)+\frac{\partial^4\varphi}{\partial Z^4},$$

$$\varepsilon^4\frac{\partial\theta}{\partial\tau}+\varepsilon^2(\frac{\partial\varphi}{\partial X}\frac{\partial\theta}{\partial Z}-\frac{\partial\varphi}{\partial Z}\frac{\partial\theta}{\partial X})=A_Q+\varepsilon^2 q\frac{\partial\varphi}{\partial X}+\varepsilon^2\frac{\partial^2\theta}{\partial X^2}+\frac{\partial^2\theta}{\partial Z^2}, \tag{4.19}$$

where the nondimensional radiative forcing A_Q is $O(\varepsilon^0)$. The boundary conditions are

$$\frac{\partial\varphi}{\partial Z}=0,\ \varphi=0, \text{ and } \frac{\partial\theta}{\partial Z}=(c_bK_H)/F_0 \text{ at } Z=0; \tag{4.20}$$

$$\frac{\partial^2\varphi}{\partial Z^2}=0,\ \varphi=0, \text{ and } \frac{\partial\theta}{\partial Z}=(c_tK_H)/F_0 \text{ at } Z=1. \tag{4.21}$$

By inspection of (4.18) and (4.19) we can see that only even powers of ε appear in the equations. Therefore we can expand θ and φ with respect to ε as

$$\begin{aligned}\theta&=\theta_0+\varepsilon^2\theta_2+\varepsilon^4\theta_4+\dots\\ \varphi&=\varphi_0+\varepsilon^2\varphi_2+\varepsilon^4\varphi_4+\dots\ .\end{aligned} \tag{4.22}$$

The boundary conditions for each component of φ are

$$\frac{\partial\varphi_i}{\partial Z}=0 \text{ and } \varphi_i=0,\ i=0,1,2,\dots \text{ at } Z=0; \tag{4.23}$$

and

$$\frac{\partial^2 \varphi_i}{\partial Z^2} = 0, \text{ and } \varphi_i = 0,\ i = 0, 1, 2, \ldots \text{ at } Z = 1. \tag{4.24}$$

The boundary conditions for each component of θ are

$$\frac{\partial \theta_0}{\partial Z} = (c_b K_H)/F_0 \text{ and } \frac{\partial \theta_i}{\partial Z} = 0,\ i = 1, 2, \ldots \text{ at } Z = 0; \tag{4.25}$$

and

$$\frac{\partial \theta_0}{\partial Z} = (c_t K_H)/F_0 \text{ and } \frac{\partial \theta_i}{\partial Z} = 0,\ i = 1, 2, \ldots \text{ at } Z = 1. \tag{4.26}$$

In (4.25) and (4.26) non-zero boundary conditions are applied to θ_0 because these non-zero constants are of $O(\varepsilon^0)$.

4.3.3 Solution

4.3.3.1 Derivation of the prognostic equation for potential temperature at the leading order

The logic for solving Eqs. (4.18) and (4.19) with boundary conditions (4.25) and (4.26) is that, by matching the coefficients of the terms at the same order of ε, relations between different variables can be revealed, and we expect that the components at the leading order can be solved for analytically. This is the basic idea of the perturbation method.

Substitute (4.22) into (4.18) and (4.19). The terms of $O(\varepsilon^0)$ in (4.19), (4.25) and (4.26) give

$$\begin{aligned} \frac{\partial^2 \theta_0}{\partial Z^2} &= -A_Q \ , \\ \left.\frac{\partial \theta_0}{\partial Z}\right|_{Z=0} &= (c_b K_H)/F_0 \ , \\ \left.\frac{\partial \theta_0}{\partial Z}\right|_{Z=1} &= (c_t K_H)/F_0 \ . \end{aligned} \tag{4.27}$$

Integrating the first line of (4.27) once, we get

$$\left.\frac{\partial \theta_0}{\partial Z}\right|_{Z=1} - \left.\frac{\partial \theta_0}{\partial Z}\right|_{Z=0} = -\int_0^1 A_Q dZ. \tag{4.28}$$

By applying the boundary conditions in (4.27) to (4.28), we have

$$c_t - c_0 = -\frac{F_0}{K_H}\int_0^1 A_Q dZ. \tag{4.29}$$

Eq. (4.29) is identical to (4.5), except that it is in nondimensional form here. Since in this study we let $\int_0^1 A_Q dZ = 0$, we have $c_t = c_b$.

Integrating the first of (4.27) twice gives

$$\theta_0 = f(X,\tau) - \int\left[\int_0^Z A_Q(Z')\,dZ' - (c_b K_H)/F_0\right]dZ \equiv f(X,\tau) + \Theta(Z)\,, \tag{4.30}$$

where $f(X,\tau)$ is an integration constant, and

$$\Theta(Z) \equiv -\int\left[\int_0^Z A_Q(Z')\,dZ' - (c_b K_H)/F_0\right]dZ \tag{4.31}$$

is the vertical distribution of potential temperature generated by the motion field. We will see that only its gradient,

$$-d\Theta(Z)/dZ = \int_0^Z A_Q(Z')\,dZ' - (c_b K_H)/F_0, \tag{4.32}$$

appears in the final results, modifying the initial basic state stratification, q. The integration constant $f(X,\tau)$, which represents the horizontal distribution of θ at leading order, is what we want to solve for.

From $O(\varepsilon^0)$ of (4.18), (4.23) and (4.24) we have

$$\begin{aligned} 0 &= R_{ac}\frac{\partial\theta_0}{\partial X} + \frac{\partial^4\varphi_0}{\partial Z^4}\ , \\ \varphi_0\big|_{Z=0,1} &= 0\ , \\ \left.\frac{\partial\varphi_0}{\partial Z}\right|_{Z=0} = 0, &\quad \left.\frac{\partial^2\varphi_0}{\partial Z^2}\right|_{Z=1} = 0\ . \end{aligned} \tag{4.33}$$

Substituting θ_0 from (4.30) into (4.33), and solving for φ_0, we obtain

$$\varphi_0 = R_{ac}P(Z)f', \tag{4.34}$$

where f' and $P(Z)$ are defined by

$$f' = \frac{\partial f}{\partial X}\ ,\ \frac{\partial^4 P}{\partial Z^4} = -1. \tag{4.35}$$

Eq. (4.34) simply means that the leading-order stream function is related to the horizontal gradient of the leading-order potential temperature.

From $O(\varepsilon^2)$ of (4.19), we get

$$-\frac{\partial\varphi_0}{\partial Z}\frac{\partial\theta_0}{\partial X}+\frac{\partial\varphi_0}{\partial X}\frac{\partial\theta_0}{\partial Z}=q\frac{\partial\varphi_0}{\partial X}+\frac{\partial^2\theta_0}{\partial X^2}+\frac{\partial^2\theta_2}{\partial Z^2}. \tag{4.36}$$

Substituting (4.30) and (4.34) into (4.36), we find that

$$\begin{aligned}\frac{\partial^2\theta_2}{\partial Z^2}&=-R_{ac}\frac{\partial P}{\partial Z}f'^2-f'\{R_cP[q-d\Theta(Z)/dZ]+1\}\ ,\\ \left.\frac{\partial\theta_2}{\partial Z}\right|_{Z=0,1}&=0\ .\end{aligned} \tag{4.37}$$

Integrating (4.37) vertically from $Z = 0$ to $Z = 1$, we can obtain

$$f'\int_0^1\{R_{ac}P[q-d\Theta(Z)/dZ]+1\}\,dZ=0, \tag{4.38}$$

so that for $f' \neq 0$ the critical Rayleigh number must satisfy

$$R_{ac}=-1/\int_0^1\{P[q-d\Theta(Z)/dZ]\}\,dZ. \tag{4.39}$$

This result clearly shows that $-d\Theta(Z)/dZ$ modifies the initial stratification, q. Solving for θ_2 from (4.37) gives

$$\theta_2=f_2(X,\tau)+f'^2W(Z)+f'H(Z) \tag{4.40}$$

where $f_2(X,\tau)$ is an integration constant, and $W(Z)$ and $H(Z)$ are defined by

$$\begin{aligned}\frac{\partial^2H}{\partial Z^2}&=-R_{ac}P[q-d\Theta(Z)/dZ]+1\ ,\\ \frac{\partial^2W}{\partial Z^2}&=-R_c\frac{\partial P}{\partial Z}\ .\end{aligned} \tag{4.41}$$

From $O(\varepsilon^2)$ of (4.18), we have

$$\begin{aligned}&\frac{1}{P_r}\left[-\frac{\partial\varphi_0}{\partial Z}\frac{\partial}{\partial X}\left(\frac{\partial^2\varphi_0}{\partial Z^2}\right)+\frac{\partial\varphi_0}{\partial X}\frac{\partial}{\partial Z}\left(\frac{\partial^2\varphi_0}{\partial Z^2}\right)\right]\\&=R_{ac}\frac{\partial\theta_2}{\partial X}+\mu^2\frac{\partial\theta_0}{\partial X}+2\frac{\partial^2}{\partial X^2}\left(\frac{\partial^2\varphi_0}{\partial Z^2}\right)+\frac{\partial^4\varphi_2}{\partial Z^4}\ .\end{aligned}\tag{4.42}$$

Substituting (4.30), (4.34) and (4.40) into (4.42), and using (4.23) and (4.24), we can solve for φ_2:

$$\varphi_2 = R_{ac}f_2'P+\mu^2f'P+f'''U+f'f'S,\tag{4.43}$$

where $U(Z)$ and $S(Z)$ satisfy

$$\begin{aligned}\frac{\partial^4 S}{\partial Z^4}&=-2R_{ac}W+P_r^{-1}R_{ac}^2\left(P\frac{\partial^3 P}{\partial Z^3}-\frac{\partial P\partial^2 P}{\partial Z\partial Z^2}\right)\ ,\\\frac{\partial^4 U}{\partial Z^4}&=-R_{ac}H-2R_{ac}\frac{\partial^2 P}{\partial Z^2}\ .\end{aligned}\tag{4.44}$$

From $O(\varepsilon^4)$ of (4.19), we can get

$$\begin{aligned}&\frac{\partial\theta_0}{\partial\tau}+\frac{\partial\varphi_2\partial\theta_0}{\partial X\,\partial Z}-\frac{\partial\varphi_2\partial\theta_0}{\partial Z\,\partial X}+\frac{\partial\varphi_0\partial\theta_2}{\partial X\,\partial Z}-\frac{\partial\varphi_0\partial\theta_2}{\partial Z\,\partial X}\\&=q\frac{\partial\varphi_2}{\partial X}+\frac{\partial^2\theta_2}{\partial X^2}+\frac{\partial^2\theta_4}{\partial Z^2}\ .\end{aligned}\tag{4.45}$$

Substituting (4.30), (4.34), (4.40) and (4.43) into (4.45), integrating it between $Z = 0$ and $Z = 1$ by using (4.25) and (4.26), and using (4.39), we finally obtain a nonlinear prognostic equation for the horizontal temperature distribution at the leading order:

$$\frac{\partial f}{\partial \tau} = -A\mu^2 f' - Bf''' + C(f^3)' - D(f'f'')'. \tag{4.46}$$

Here A, B, C and D are defined by

$$\begin{aligned} A &\equiv 1/R_{ac} \ , \\ B &\equiv -\int_0^1 \{U[q - d\Theta(Z)/dZ] + H\}\, dZ \ , \\ C &\equiv R_{ac}^2 \int_0^1 P^2 dZ \ , \\ D &\equiv R_{ac} \int_0^1 P \frac{\partial H}{\partial Z} dZ - \int_0^1 \{S[q - d\Theta(Z)/dZ] + 2W\}\, dZ \ . \end{aligned} \tag{4.47}$$

For given $-d\Theta(Z)/dZ$, we see that A, B, C and D are constants. Remember that (4.46) is only valid for motions with large aspect ratios, since it is derived on that basis, as discussed at the beginning of this section.

Eq. (4.46) looks exactly the same as that obtained by Chapman and Proctor (1980), except that the coefficients given in (4.47) are different from theirs. Eq. (4.46) can be reduced to a canonical form by defining

$$\xi = \sqrt{\frac{A}{B}} X, \quad T = \frac{A^2}{B}\tau, \quad F = \sqrt{\frac{C}{B}} f, \tag{4.48}$$

so that (4.46) becomes

$$F_T = -\mu^2 F_{\xi\xi} - F_{\xi\xi\xi\xi} + (F_\xi^3)_\xi - \alpha (F_\xi F_{\xi\xi})_\xi \tag{4.49}$$

where

$$\alpha = D/(\sqrt{BC}) . \tag{4.50}$$

From (4.48), the variable F corresponds to the horizontal distribution of potential temperature, since B and C are determined constants for a given forcing.

The dependencies of the solution for F to be obtained from (4.49), on the imposed upper and lower boundary conditions, as well as the heating profile ($\dot{Q}$), are represented by the nonlinear α-term. This is because the vertical coordinate Z does not appear explicitly in (4.49), and therefore the effects of the vertical structure on F can only enter through the constants in (4.47), which are in turn represented by α in (4.49). We can determine α by a method described below.

4.3.3.2 Steady state solution

For $F_T = 0$, i.e. a steady state, we can integrate (4.49) respect to ξ once, and get

$$G_{\xi\xi} + \mu^2 G - G^3 + \alpha G G_{\xi} + \beta = 0, \tag{4.51}$$

where $G \equiv F_{\xi}$ corresponds to the horizontal distribution of stream function according to (4.34) and (4.48). To have a periodic solution for F, we need $\beta = 0$.

An example of the change of G and F with α for $\mu^2 = 1$ is shown in Fig. 4.4, which is obtained from (4.51) by using iteration and Gaussian elimination. We can see that the cell is symmetric with $\alpha = 0$, and asymmetric with $\alpha > 0$. A larger α represents a broader and warmer updraft and a narrower and colder downdraft. This dependence of the cell asymmetry on α was also demonstrated by Chapman and Proctor (1980). It indicates that in our case only boundary conditions and imposed heating can

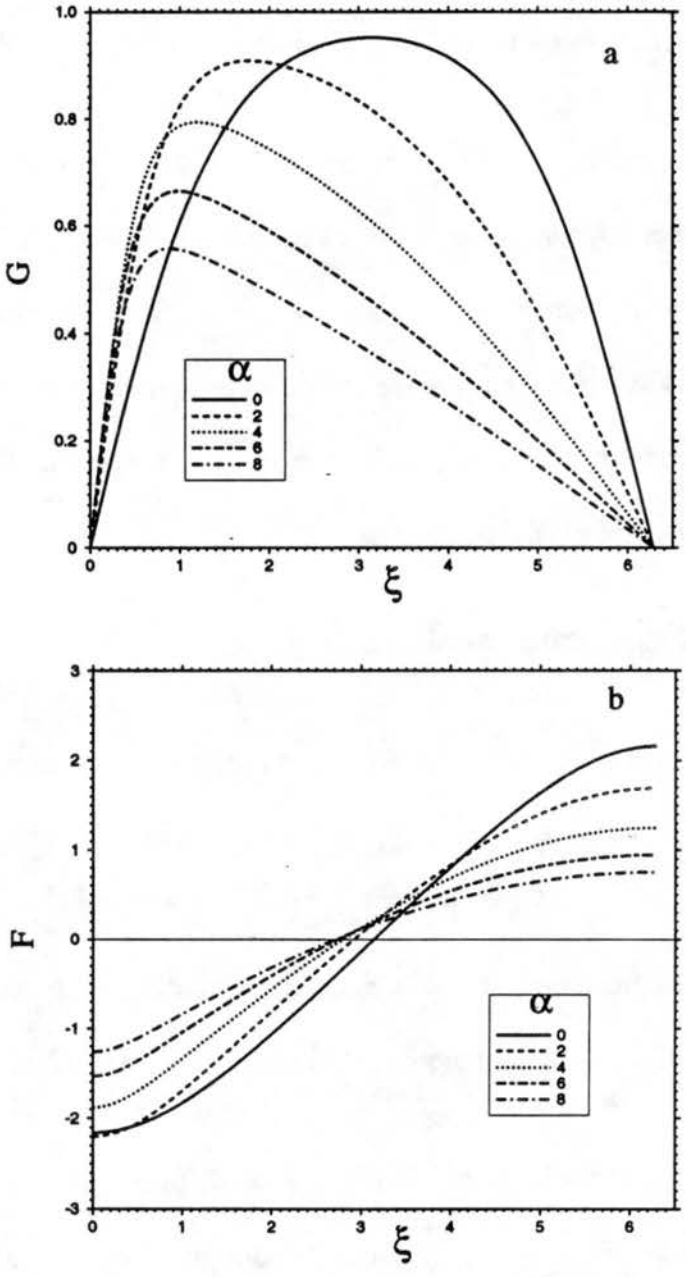

FIGURE 4.4: The solution of (a) stream function G and (b) potential temperature F as a function of α.

affect the asymmetric structure of the cell. We expect that when the imposed forcing is more asymmetric, or n in (4.6) is larger, α is larger, and the cells are more asymmetric.

4.3.3.3 The dependence of R_{ac} and α on the forcing

In order to find the appropriate values of α for our cases, we need to determine the functions $P(Z)$, $H(Z)$, $W(Z)$, $S(Z)$ and $U(Z)$ first. Then the coefficients in (4.47) can be calculated, and α can be obtained from (4.50).

The nondimensional form of Eq. (4.6) is used as the imposed heating profile to calculate $-d\Theta(Z)/dZ$ by (4.32), which results in

$$-\frac{d\Theta(Z)}{dZ} = \frac{daZ(1-Z^n)}{F_0(n+1)} - \frac{c_b K_H}{F_0}. \tag{4.52}$$

Since $-d\Theta(Z)/dZ$ can not change sign with height as long as $a \geq 0$ and $c_b \leq 0$, as listed in Table 1, $\Theta(Z)$ always decreases monotonically with height, corresponding to an unstable basic state stratification produced by the motion field. The initial basic-state stratification, q, is taken to be zero. The Prandtl number, P_r, is assumed to be 1.

The boundary conditions for $P(Z)$, $H(Z)$, $W(Z)$, $S(Z)$ and $U(Z)$ can be derived from Eqs. (4.23) to (4.26):

$$
\begin{aligned}
&P|_{Z=0,1} = 0, \quad \left.\frac{\partial P}{\partial Z}\right|_{Z=0} = 0, \quad \left.\frac{\partial^2 P}{\partial z^2}\right|_{Z=1} = 0 \ , \\
&\left.\frac{\partial H}{\partial Z}\right|_{Z=0,1} = 0 \ , \\
&\left.\frac{\partial W}{\partial Z}\right|_{Z=0,1} = 0 \ , \\
&S|_{Z=0,1} = 0, \quad \left.\frac{\partial S}{\partial Z}\right|_{Z=0} = 0, \quad \left.\frac{\partial^2 S}{\partial Z^2}\right|_{Z=1} = 0 \ , \\
&U|_{Z=0,1} = 0, \quad \left.\frac{\partial U}{\partial Z}\right|_{Z=0} = 0, \quad \left.\frac{\partial^2 U}{\partial Z^2}\right|_{Z=1} = 0 \ .
\end{aligned}
\tag{4.53}
$$

From (4.35) and (4.53),

$$
P(Z) = -\frac{1}{48}(2Z^4 - 5Z^3 + 3Z^2) \, . \tag{4.54}
$$

The distribution of P with height is shown in Fig. 4.5.

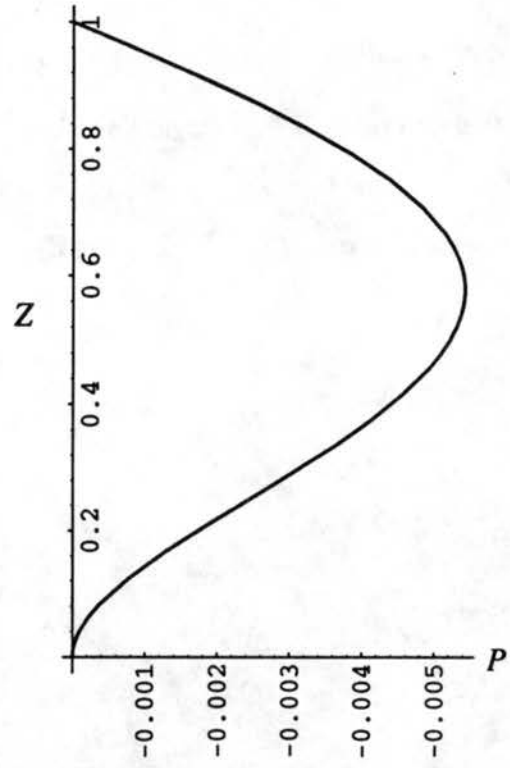

FIGURE 4.5: The distribution of P(Z) with height.

Substituting (4.52) and (4.54) into (4.39), we obtain an expression for the critical Rayleigh number

$$R_{ac} = -\frac{2880\,(1+n)\,(4+n)\,(5+n)\,(6+n)}{\frac{c_b K_H}{F_0}\,(1080+1746n+801n^2+144n^3+9n^4)-\frac{ad}{F_0}\,(310n+75n^2+5n^3)} \quad (4.55)$$

The functions $H(Z)$, $W(Z)$, $S(Z)$ and $U(Z)$ and α have been evaluated using Mathematica (Wolfram, 1993). An example is shown in Appendix F.

The procedure for obtaining R_{ac} and α above can be summarized as follows: First, the imposed heating profile is determined by (4.6), which is substituted into (4.32) to obtain the basic state stratification, as given by (4.52). The functions $P(Z)$, $H(Z)$, $W(Z)$, $S(Z)$ and $U(Z)$ defined in (4.35), (4.41) and (4.44) are then solved for by using the boundary conditions given in (4.53), respectively. This is the only place that the boundary conditions enter into the solution. The solution for $P(Z)$ given by (4.54) and the basic state stratification given by (4.52) are substituted into (4.39) to obtain R_{ac} in (4.55). The functions are used to calculate the constants in (4.53), which are used to calculate α from (4.50).

Based on the three classes of cases listed in Table 1, the solutions can be correspondingly classified into three kinds, respectively.

(1) $c_b = 0$, $F(n) = F_0$, so that $\frac{ad}{F_0} = (n+1)^{(2n+1)/n}/n$ [from (4.9)] as is represented by cases n5, n35 and n1.

In this situation the heat flux from the boundaries is zero. Only internal forcing drives convection. The c_b-term in (4.55) is zero. The dependence of R_{ac} and α on n is shown in Fig. 4.6 (solid lines). With increasing n, as the imposed forcing becomes more asymmetric, α increases, and the cell becomes more asymmetric, as expected. However, α approaches an asymptotic value of 1.3, which gives a cell pattern in between those for $\alpha = 0$ and $\alpha = 2$, shown in Fig. 4.4. It does not make the updraft as wide as observed.

(2) $c_b K_H = -F_0$, $F(n) = 0$, so that $a = 0$ (no imposed heating), as is represented by case cb.

It is obvious that in this situation convection is driven by surface forcing only. Since there is no internal forcing, R_{ac} and α are constants. Their values are 320 and 0.853, respectively.

It is interesting to note that, even when there is no internal heating, the value of α is still greater than zero, which means that a factor other than the asymmetric heating affects the cell geometry. By reviewing the derivation, we can see that the only possible explanation is the asymmetric dynamical boundary conditions at the top and bottom of the layer. The free-slip upper boundary allows horizontal advection to be stronger than that at the non-slip lower boundary, and hence makes it easier to for cold air to sink in narrower but stronger downdrafts.

From (4.52) we have $-d\Theta(Z)/dZ = 1$ for this case. Since only $q - d\Theta(Z)/dZ$ appears in the solution, as pointed out earlier, this case is equivalent to the case with $q = 1$ and $-dT(Z)/dZ = 0$.

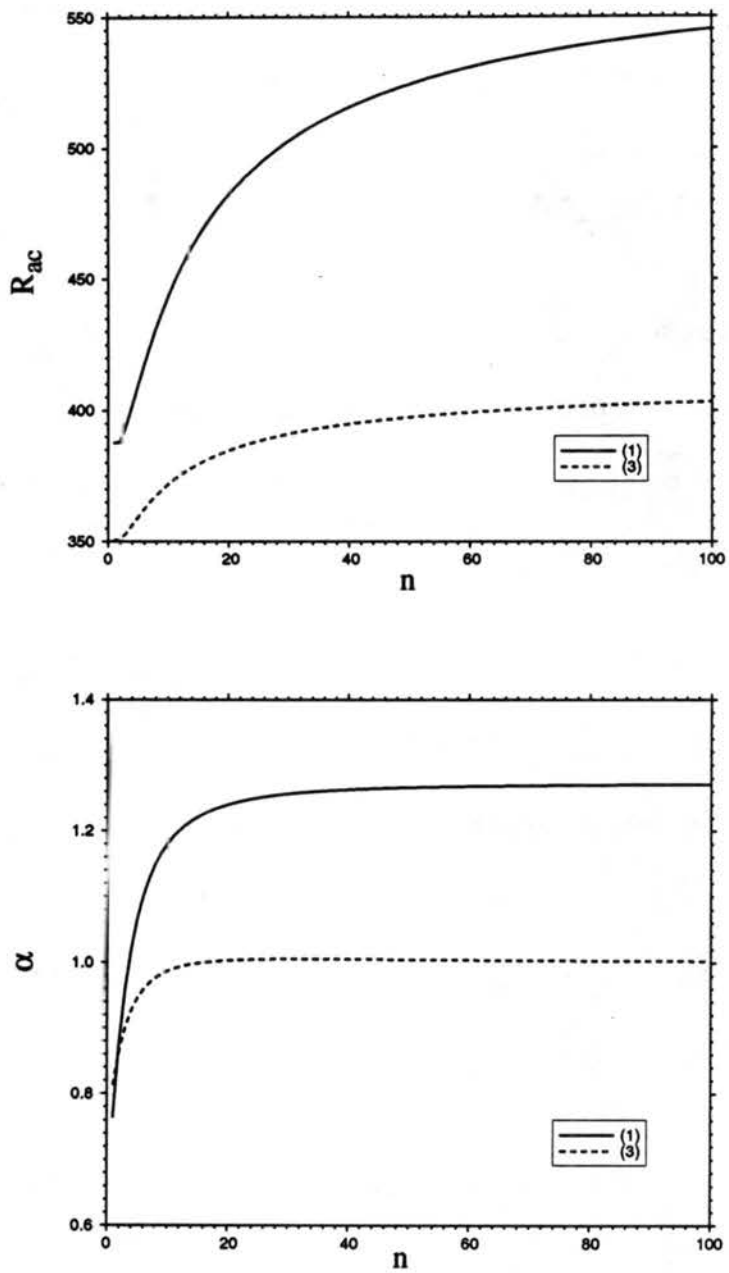

FIGURE 4.6: The change of R_{ac} and α with n for class (1) on page 29 (solid line) and class (3) on page 31 (dashed line).

(3) $c_b K_H = -0.5F_0$, $F(n) = 0.5F_0$, so that $\frac{ad}{F_0} = 0.5\,(n+1)^{(2n+1)/n}/n$, as is represented by case n35cb.

This situation is a combination of (1) and (2) above. The values of R_{ac} and α are also intermediate, as shown in Fig. 4.6 (dashed lines). The asymptotic value of α is 1 in this case, which still gives a slightly asymmetric cell.

4.3.4 Discussion

Our results show that vertically asymmetric internal heating can enhance the closed-MCC type structure through nonlinear advection. The effect shown is not as large as we think it should be, however, due to the limitations of the *weakly nonlinear* assumption, as discussed below.

The main deficiency of the weakly nonlinear assumption is that it requires large diffusion. As discussed earlier, under this assumption the motions are slightly supercritical, and R_a is slightly larger than R_{ac}. For the cases we are studying, the range of R_{ac} is about 320 to 510. For a given heating profile (or F_0) and layer depth, the only mechanism that can force R_a to be close to R_{ac} is diffusion. This can be seen from the definition of R_a:

$$R_a = (gF_0 d^4) / (\Theta_0 K_H^2 K_M) . \tag{4.56}$$

Let us use the parameters listed in Table 1: $F_0 = 0.23\mathrm{K\,ms^{-1}}$, $d = 1500\mathrm{m}$, and take $g = 9.8\mathrm{ms^{-2}}$, $\Theta_0 = 300\mathrm{K}$, $R_a = 500$, then (4.56) gives $K_H = K_M = 424\mathrm{m^2 s^{-1}}$ if $P_r = 1$. This strong diffusion balances out the forcing at leading order, while the nonlinear effects are of second order, as was shown in (4.18) and (4.19). If we take $K_H = K_M = 30\mathrm{m^2 s^{-1}}$, for example, as is true for the atmosphere in an oceanic

convective PBL, then R_a will be 1.5×10^6, which is much larger than R_{ac}, and this would allow nonlinear processes to be fully expressed by the model.

In next section, we will use a fully nonlinear numerical model to see these effects.

4.4 The fully nonlinear numerical solution to the effect of coolings at the top

The results of the weakly nonlinear analysis in last section showed that the cells in all cases have asymmetric structures, i.e., wide warm updrafts and narrow cold downdrafts, although this asymmetry is not as dominant as we expect due to the limitations of the theory. In this section we will see the nonlinear effects more completely by using numerical methods. The dimensional form of the Eqs. (4.2), (4.3), (4.4), and (4.6) is used for the numerical study.

4.4.1 Numerical method

The distribution of variables on the grid is shown in Fig. 4.7. The variables ψ, w, and u are staggered in such a way that w and u can be calculated from the horizontal and vertical gradients of ψ, respectively, using just one grid interval. Similarly, θ, w and u are staggered so that the advection of θ can be calculated by Takacs' (1985) advection scheme. Finally, ζ, w, and u are staggered since ζ is calculated from the gradients of w and u.

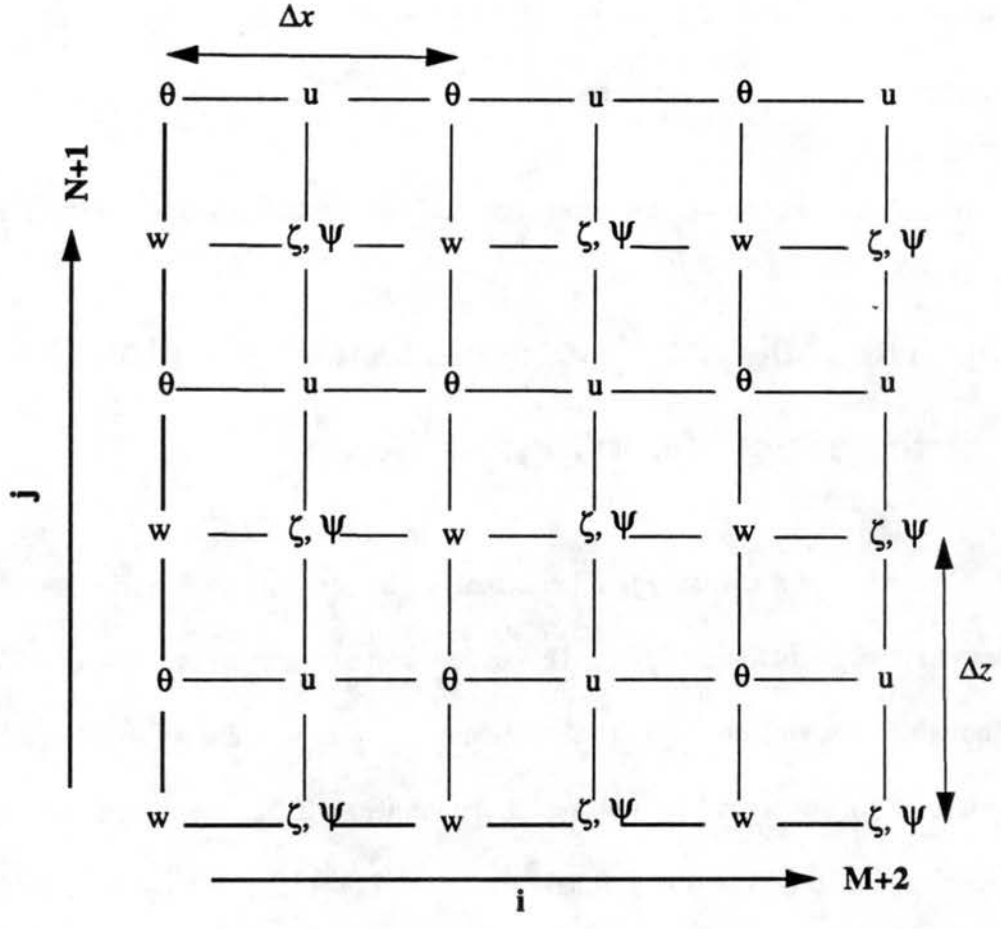

FIGURE 4.7: The grid for the 2-D model.

Given vorticity ζ, the stream function is obtained by solving the Poisson equation in (4.2) by using a multi-grid method (e.g., Brandt, 1977; Fulton et al., 1986). The prognostic equations are then solved by the third-order Adams-Bashforth scheme (Durran, 1991).

4.4.1.1 Poisson equation

The Poisson equation is solved by a multi-grid method. This method was comprehensively studied first by Brandt (1977). A concise review of the method is given by Fulton et al. (1986). The multi-grid method differs from the traditional Gauss-Seidel

relaxation by using multi-level grids G_l (l=1,...,m), i.e., m grids overlapped with resolutions from fine to coarse, or $h_{l-1} = 2h_l$, on which the equation is solved. The lower-wave number components are relaxed on the coarser grid. Only the highest wave number components are relaxed on the finest grid. In this way, the total number of grid points in relaxation sweeps is reduced, and hence computer time is saved.

The centered second-order finite-difference approximation for the Poisson equation is

$$\frac{1}{\Delta x^2}(\psi_{i-1,j} - 2\psi_{i,j} + \psi_{i+1,j}) + \frac{1}{\Delta z^2}(\psi_{i,j-1} - 2\psi_{i,j} + \psi_{i,j+1}) = \zeta_{i,j}, \qquad (4.57)$$

where $i = 2, \ldots, M+1$, $j = 2, \ldots, N$. Let $\gamma^2 = (\Delta x^2)/(\Delta z^2)$. Then (4.57) becomes

$$\psi_{i-1,j} - 2\psi_{i,j} + \psi_{i+1,j} + \gamma^2(\psi_{i,j-1} - 2\psi_{i,j} + \psi_{i,j+1}) = \Delta x^2 \zeta_{i,j}, \qquad (4.58)$$

which can be compactly written as

$$L\psi = f. \qquad (4.59)$$

On each grid level l, Eq. (4.58) is solved by a z-line† Gauss-Seidel relaxation method, which converges very quickly when $\gamma^2 \gg 1$, as for our case. This convergence rate has been fully demonstrated by Fulton et al. (1986), and will not be proved here. If we use $\psi^k_{i,j}$ to represent the kth estimate of $\psi_{i,j}$, the relaxation gives the (k+1)th estimate as

$$\psi^{k+1}_{i-1,j} - 2\psi^{k+1}_{i,j} + \psi^{k}_{i+1,j} + \gamma^2(\psi^{k+1}_{i,j-1} - 2\psi^{k+1}_{i,j} + \psi^{k+1}_{i,j+1}) = \Delta x^2 \zeta_{i,j}, \qquad (4.60)$$

†. A z-line relaxation is to relax the discrete equation column by column, rather than points by points.

or

$$\gamma^2\psi_{i,j-1}^{k+1} - 2(1+\gamma^2)\psi_{i,j}^{k+1} + \gamma^2\psi_{i,j+1}^{k+1} = \Delta x^2\zeta_{i,j} - \psi_{i-1,j}^{k+1} - \psi_{i+1,j}^{k} \tag{4.61}$$

The rhs of (4.61) is known. Therefore, Eq. (4.61) is a tridiagonal linear system, and can be solved directly. Here we use the Crout-reduction method to solve (4.61) (Burden and Faires, 1985, p.353). All the j-points on the ith-column are solved simultaneously. The error is transferred to the lower grid level (l to $l-1$) if the convergence is slow, i.e. if

$$(\psi_{i,j}^{k+2} - \psi_{i,j}^{k+1})^2 / (\psi_{i,j}^{k+1} - \psi_{i,j}^{k})^2 \le 0.6. \tag{4.62}$$

The relaxation is either transferred to a higher grid level (l to $l+1$) or stopped (see Fig. 4.8 below) if the convergence criterion

$$(\psi_{i,j}^{k+1} - \psi_{i,j}^{k})^2 / (\psi_{i,j}^{k})^2 \le 10^{-4} \tag{4.63}$$

is met.

The transfer between the grid levels (l) is determined by the C-Cycle discussed by Brandt (1977), and diagramed in Fig. 4.8. The transfer of error from the finer to the coarser grid I_{l+1}^{l} is through bi-linear interpolation. The transfer of the solution from coarser to finer grid I_{l-1}^{l} is through full weighting, i.e.,

$$I_{l-1}^{l} = \frac{1}{16}\begin{bmatrix} 1 & 2 & 1 \\ 2 & 4 & 2 \\ 1 & 2 & 1 \end{bmatrix} \tag{4.64}$$

for interior points and

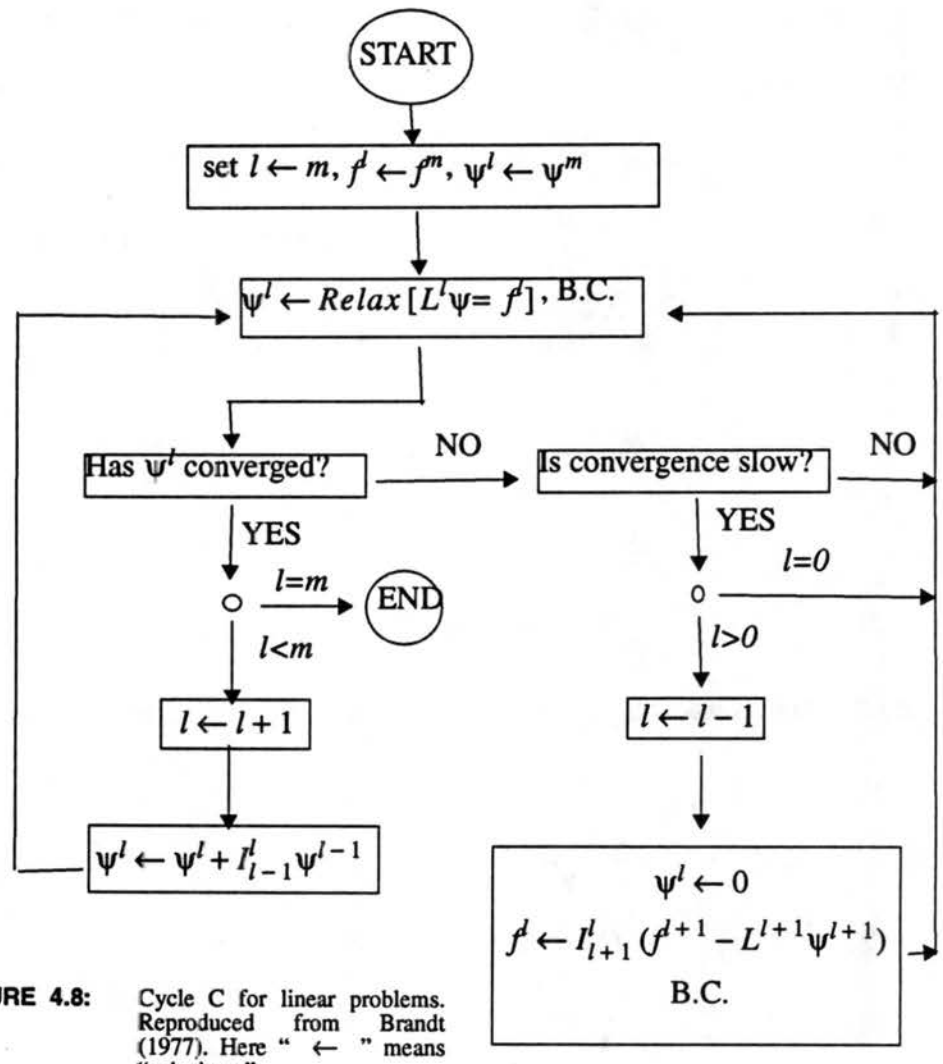

FIGURE 4.8: Cycle C for linear problems. Reproduced from Brandt (1977). Here " $\leftarrow$ " means "substitute."

$$I^l_{l-1} = \frac{1}{16}\begin{bmatrix} 0 & 0 & 0 \\ 2 & 4 & 2 \\ 1 & 2 & 1 \end{bmatrix} \quad \text{and} \quad \frac{1}{16}\begin{bmatrix} 1 & 2 & 1 \\ 2 & 4 & 2 \\ 0 & 0 & 0 \end{bmatrix} \tag{4.65}$$

for the upper and lower boundaries, respectively.

4.4.1.2 Prognostic equations

The prognostic equations are solved using the third-order Adams-Bashforth scheme (Durran, 1991):

$$y^{n+1} - y^n = \frac{\Delta t}{12}\left[23F(y^n) - 16F(y^{n-1}) + 5F(y^{n-2})\right], \tag{4.66}$$

where y represents the prognostic quantities. When $y = \zeta$,

$$\begin{aligned} F(\zeta_{i,j}) &= J_{i,j}(\zeta, \psi) \\ &+ \frac{g}{\Theta_0}\left(\frac{\theta_{i+1,j} - \theta_{i-1,j}}{2\Delta x}\right) + K_M\left(\frac{\zeta_{i+1,j} - 2\zeta_{i,j} + \zeta_{i-1,j}}{\Delta x^2} + \frac{\zeta_{i,j+1} - 2\zeta_{i,j} + \zeta_{i,j-1}}{\Delta z^2}\right), \\ & i = 2, \ldots, M+1, \quad j = 2, \ldots, N \end{aligned} \tag{4.67}$$

and the Arakawa Jacobian advection scheme is used for vorticity (Arakawa, 1966):

$$\begin{aligned} J_{i,j}(\zeta, \psi) = -\frac{1}{12\Delta x \Delta z}\,[& \zeta_{i+1,j}(\psi_{i,j-1} + \psi_{i+1,j-1} - \psi_{i,j+1} - \psi_{i+1,j+1}) \\ & -\zeta_{i-1,j}(\psi_{i-1,j-1} + \psi_{i,j-1} - \psi_{i-1,j+1} - \psi_{i,j+1}) \\ & +\zeta_{i,j+1}(\psi_{i+1,j} + \psi_{i+1,j+1} - \psi_{i-1,j} - \psi_{i-1,j+1}) \\ & -\zeta_{i,j-1}(\psi_{i+1,j-1} + \psi_{i+1,j} - \psi_{i-1,j-1} - \psi_{i-1,j}) \\ & +\zeta_{i+1,j+1}(\psi_{i+1,j} - \psi_{i,j+1}) - \zeta_{i-1,j-1}(\psi_{i,j-1} - \psi_{i-1,j}) \\ & +\zeta_{i-1,j+1}(\psi_{i,j+1} - \psi_{i-1,j}) - \zeta_{i+1,j-1}(\psi_{i+1,j} - \psi_{i,j-1})\,] \end{aligned} \tag{4.68}$$

This advection scheme conserves both enstrophy and kinetic energy.

When $y = \theta$,

$$F(\theta_{i,j}) = F_{Takacsadv} + (\dot{Q})_{i,j}$$
$$+\beta\left(\frac{\Psi_{i+1,j}-\Psi_{i-1,j}}{2\Delta x}\right) + K_H\left(\frac{\theta_{i+1,j}-2\theta_{i,j}+\theta_{i-1,j}}{\Delta x^2} + \frac{\theta_{i,j+1}-2\theta_{i,j}+\theta_{i,j-1}}{\Delta z^2}\right) \quad (4.69)$$
$$i = 2, \ldots, M+1, \quad j = 2, \ldots, N$$

and $F_{Takacsadv}$ is the advection calculated by the second-order-accurate Takacs' scheme [Takacs, 1985, Eqs. (9.1), (9.2)]. This advection scheme behaves well for quantities with steep gradients.

4.4.1.3 Boundary conditions

The bottom and top boundary conditions are

$$\Psi_{i,1} = 0 \ ,$$
$$\zeta_{i,1} = \left.\frac{\partial u}{\partial z}\right|_s = \frac{u_1 - u_s}{\frac{1}{2}\Delta z} = \frac{2u_1}{\Delta z} = \frac{2}{\Delta z}\left(\frac{\Psi_{i,2}-\Psi_{i,1}}{\Delta z}\right) = \frac{2\Psi_{i,2}}{\Delta z^2} \ , \quad (4.70)$$
$$\theta_{i,1} = \theta_{i,2} - \left.\frac{\partial \theta}{\partial z}\right|_s \Delta z = \theta_{i,2} - c_b \Delta z \ ,$$

and

$$\Psi_{i,N+1} = 0 \ ,$$
$$\zeta_{i,N+1} = 0 \ , \quad (4.71)$$
$$\theta_{i,N+1} = \theta_{i,N} + \left.\frac{\partial \theta}{\partial z}\right|_t \Delta z = \theta_{i,N} + c_t \Delta z \ .$$

The horizontal periodicity conditions are

$$
\begin{aligned}
\Psi_{1,j} &= \Psi_{M+1,j} \ , \\
\Psi_{M+2,j} &= \Psi_{2,j} \ , \\
\zeta_{1,j} &= \zeta_{M+1,j} \ , \\
\zeta_{M+2,j} &= \zeta_{2,j} \ , \\
\theta_{1,j} &= \theta_{M+1,j} \ , \\
\theta_{M+2,j} &= \theta_{2,j} \ .
\end{aligned}
\tag{4.72}
$$

4.4.2 Parameters

The horizontal domain size is 32 km, unless otherwise noted. The domain height is 1.5 km. The diffusion coefficients are $K_H = K_M = 30\mathrm{m}^2\mathrm{s}^{-1}$ so that $P_r = 1$. These parameters give $R_a = 1.44 \times 10^6$, which corresponds to $R_a/R_{ac} \sim 10^3$ based on the R_{ac} (~ 500) obtained in the last section. The five cases listed in Table 1 are run with $\Delta x = 250$ m, $\Delta z = 30$ m, or 130×50 grid points, and $\Delta t = 0.5$ s. The number of grid levels used to solve the Poisson equation is $m = 4$. Each case is disturbed initially by the same random perturbation on potential temperature, with an amplitude 0.05 K, and is run for 24 simulated hours.

4.4.3 Results

4.4.3.1 A general description of the steady state results

We do not intend to explain how the cell patterns evolve with time. Only the results of the final steady state are analyzed. The domain averages of resolvable turbulent kinetic energy and enstrophy shown in Fig. 4.9 indicate that the solutions are close to a steady state in the last three hours (time step $> 1.5 \times 10^5$). Later results will also show that the solutions are steady at least in the last hour.

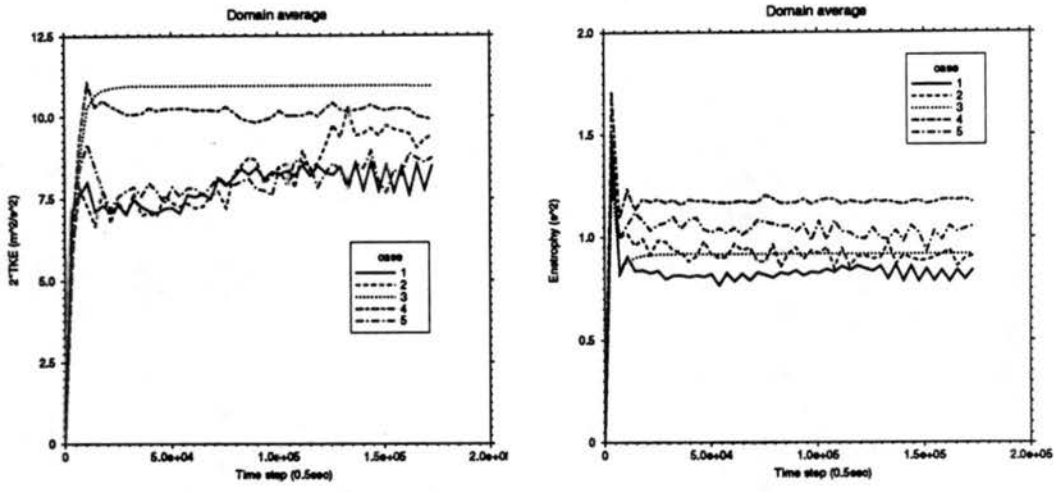

FIGURE 4.9: The change of domain averaged TKE and enstrophy with time.

The potential temperatures and stream functions are shown in Figs. 4.10 to 4.14 for cases 1 to 5 (i.e., cases n5, n35, n1, cb, and n35cb, see Table 1), respectively. There are two panels for each variable in these figures. The upper one shows the structure at the end of the 24th hour, and the lower one shows the structure averaged over the last hour. We can see that the patterns of the two panels are almost identical, which implies that the cell patterns are very steady in the last hour. The horizontal and vertical velocities at the end of the 24th hour are shown in Figs. 4.15 to 4.19 for each case.

The results from cases 1 to 3 are intended to show the sensitivity of the cell patterns to the different internal heating/cooling profiles. They differ drastically (Figs. 4.10 to 4.12). Two-cell, four-cell and ten-cell patterns appear for $n = 35$, $n = 5$, and $n = 1$, respectively, corresponding to average aspect ratios of 10.7, 5.3, and 2.1, respectively. Although large differences of the aspect ratio exist, Figs. 4.15 to 4.17 show that the widths of the downdrafts (indicated by the dashed lines in the lower panel of each figure)

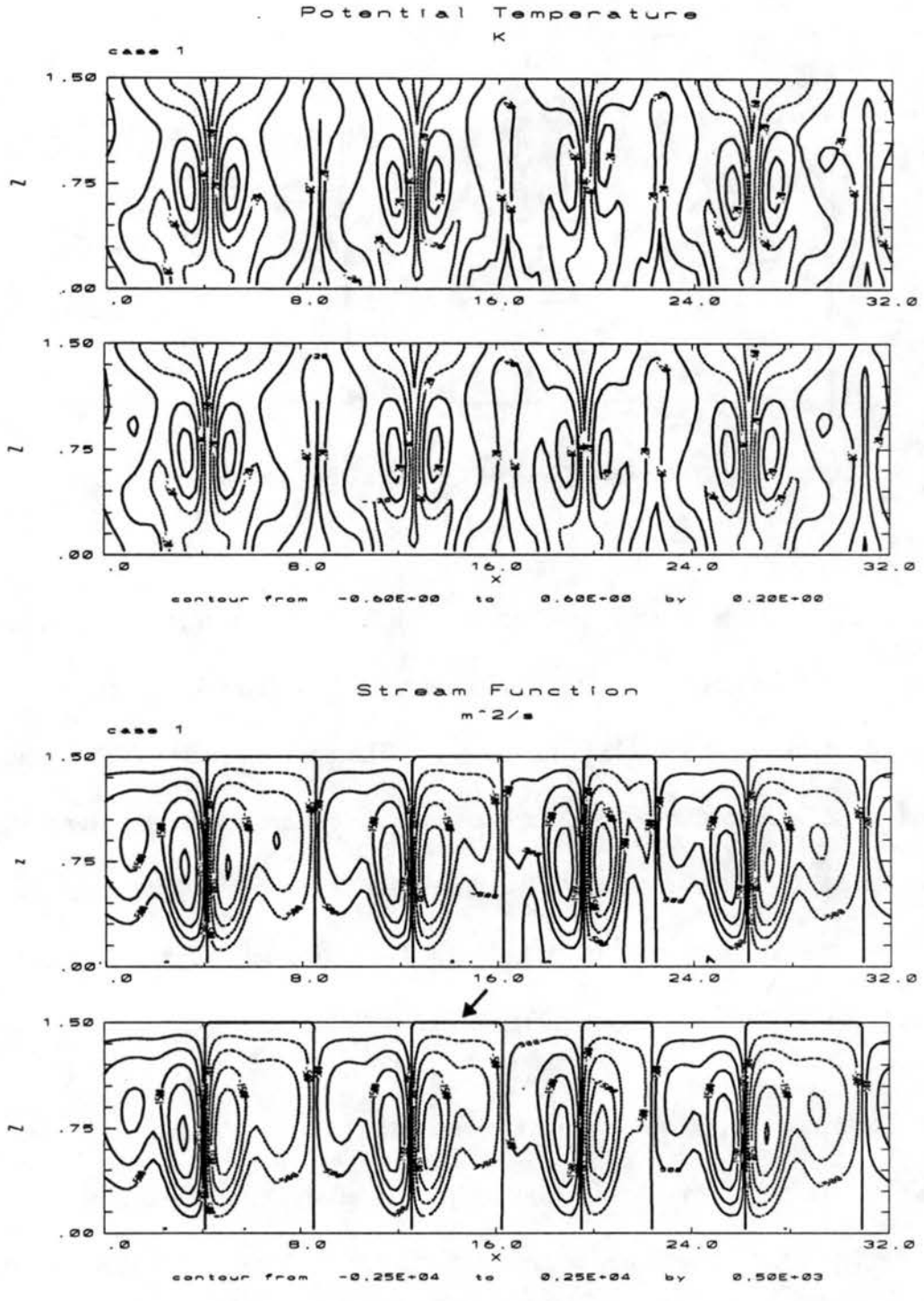

FIGURE 4.10: The temperature (K) and stream function (m^2/s) for case 1 (n5). The top and bottom panels for each variable are the value at the 24th hour and 1 hour average value over the 24 hour, respectively. The arrow indicates the cell appeared in the trajectory analysis in section 4.4.3.3.

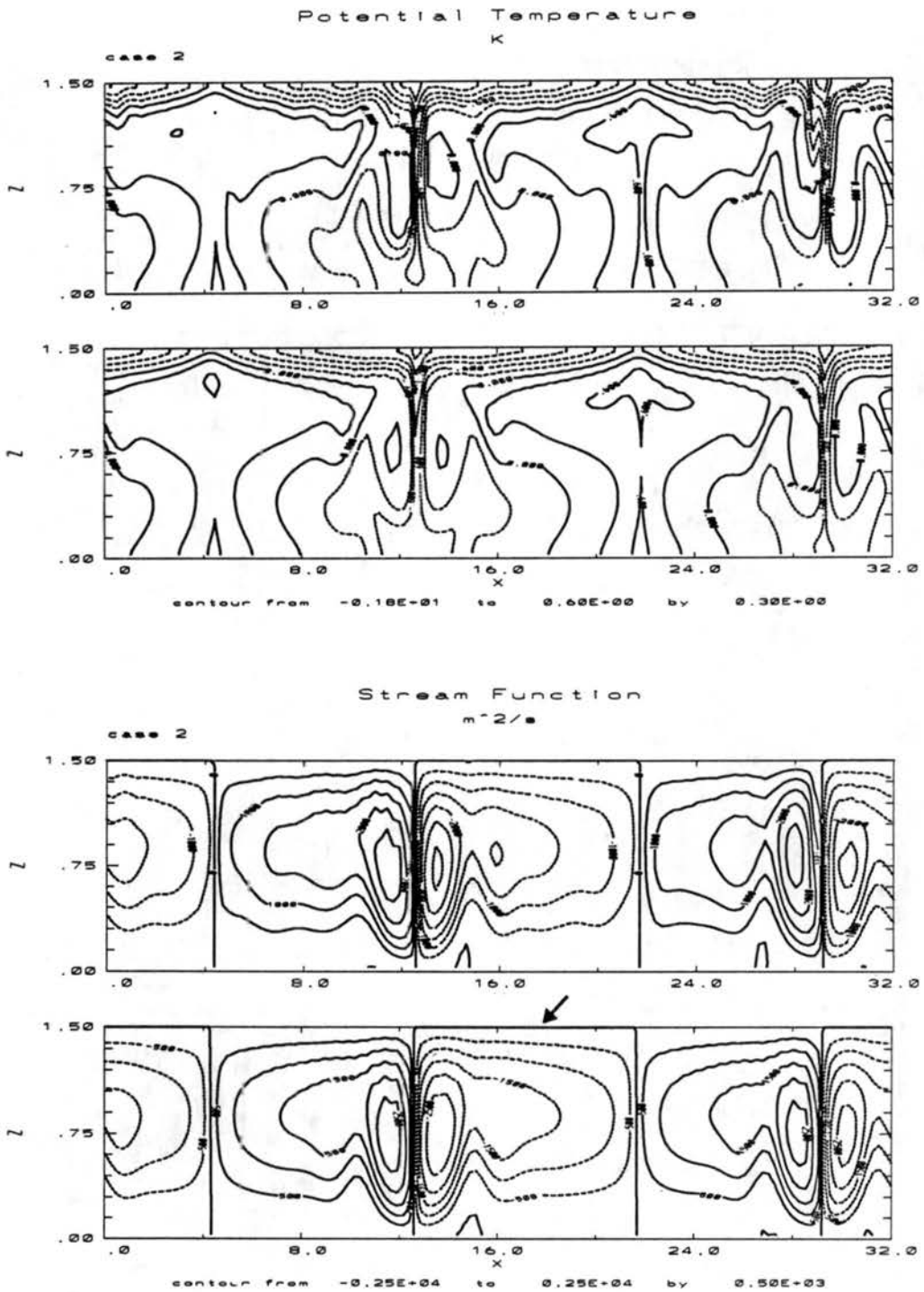

FIGURE 4.11: Same as in Fig.4.10 except for case 2 (n35).

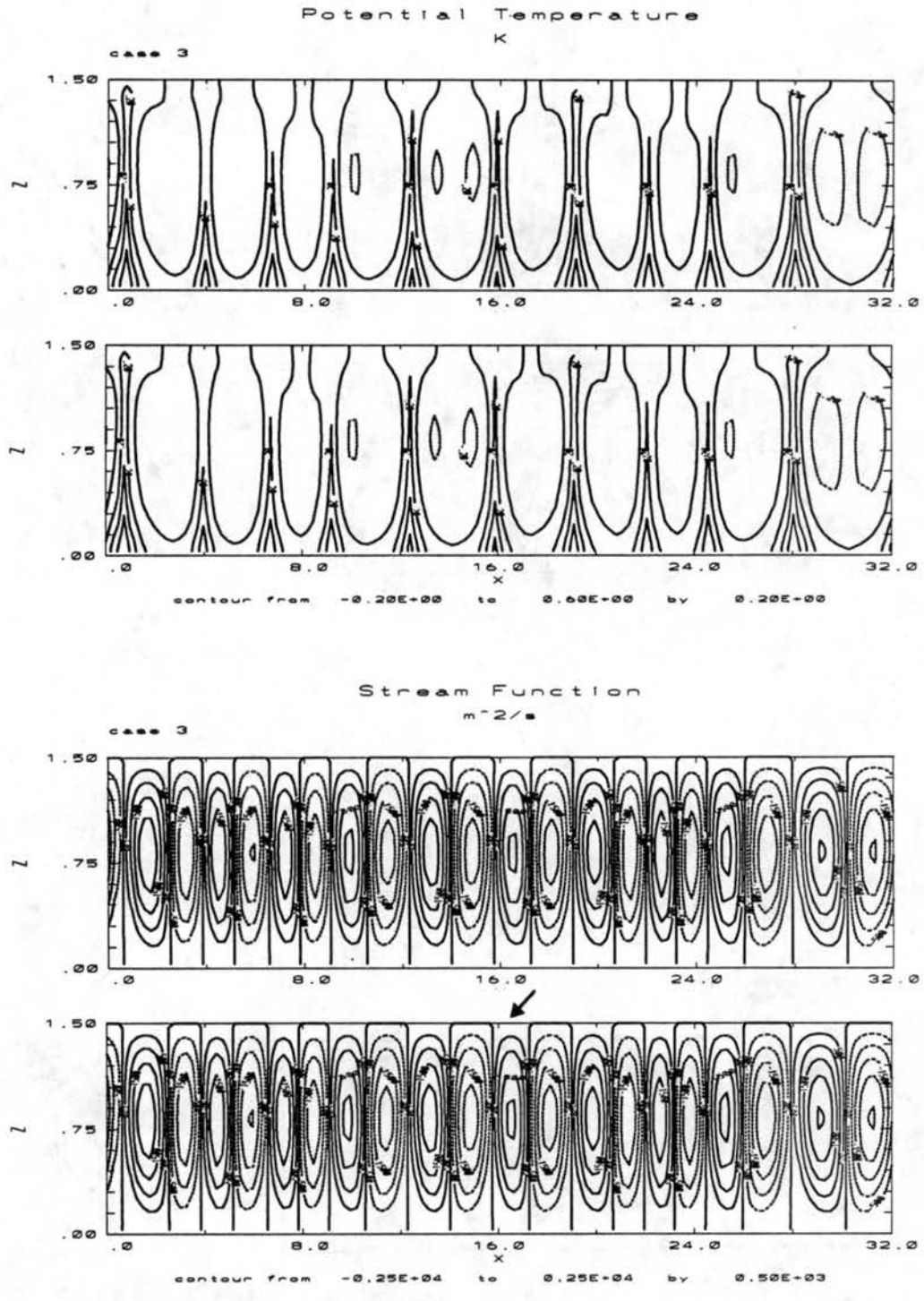

FIGURE 4.12: Same as in Fig.4.10 except for case 3 (n1).

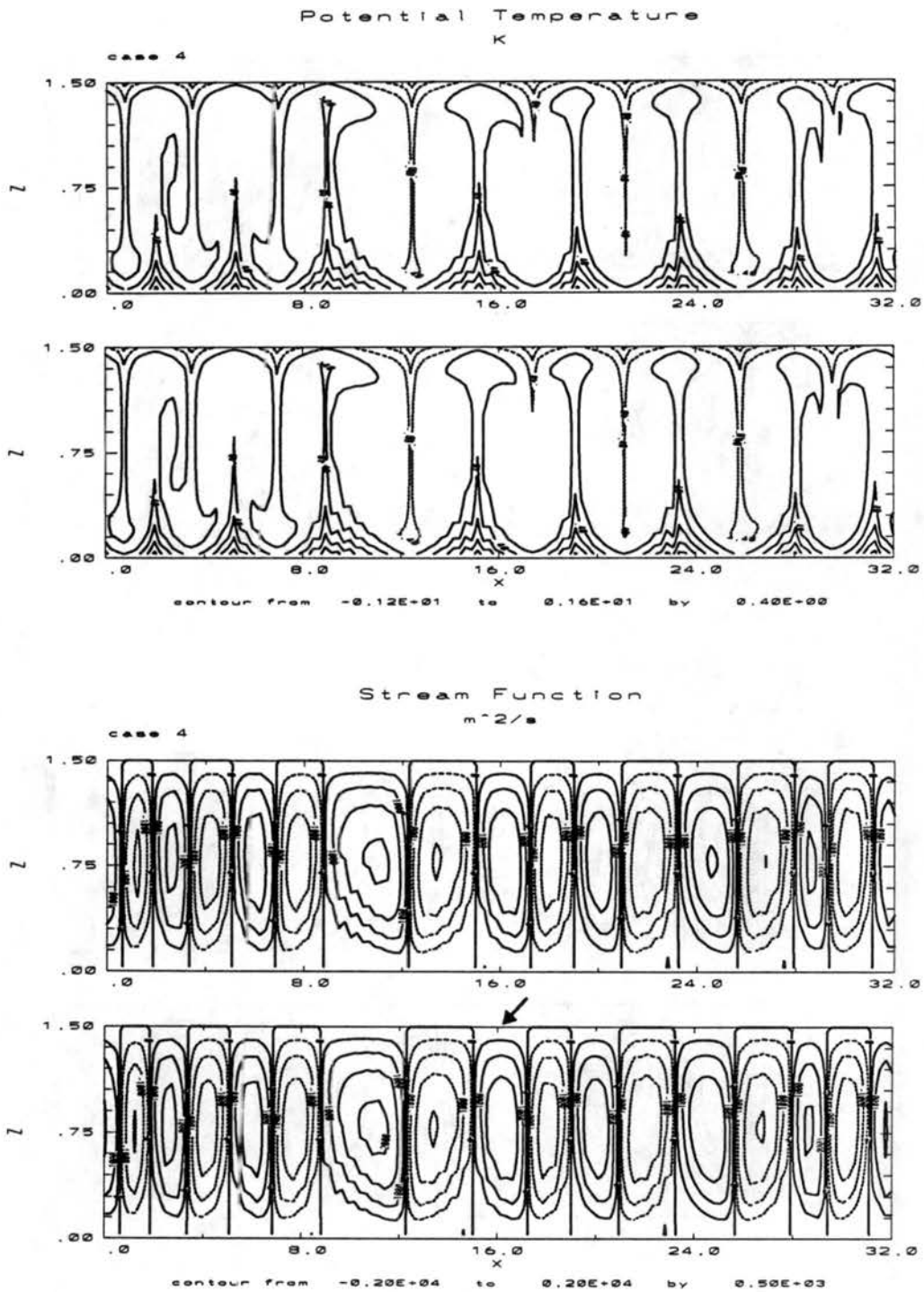

FIGURE 4.13: Same as in Fig.4.10 except for case 4 (cb).

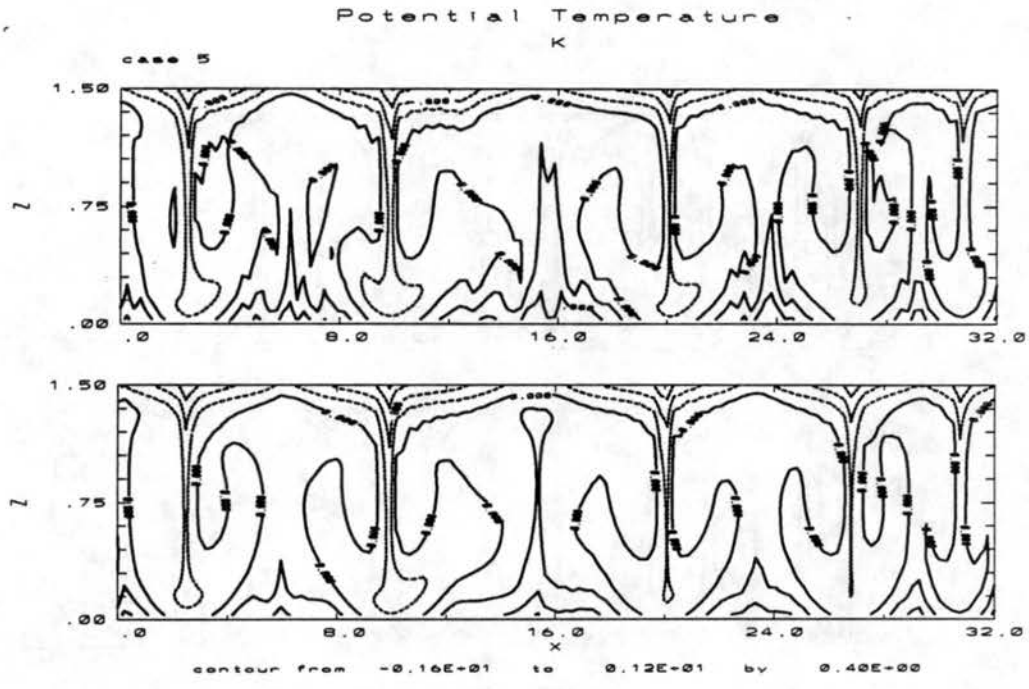

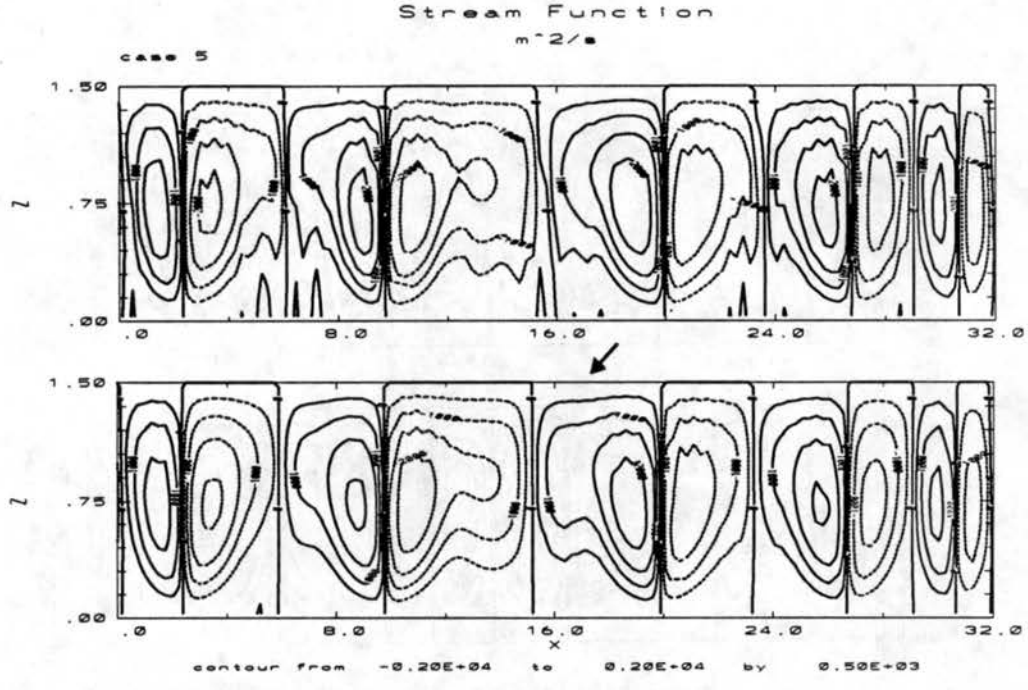

FIGURE 4.14: Same as in Fig.4.10 except for case 5 (n35cb).

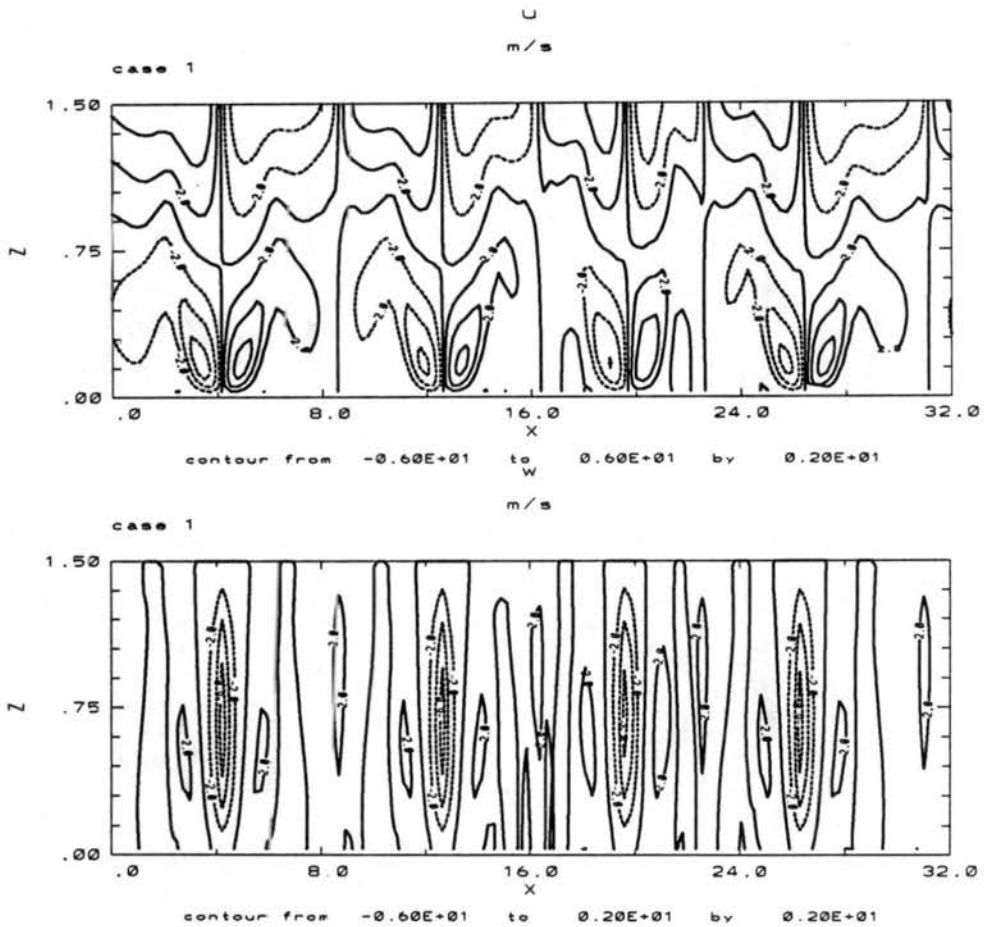

FIGURE 4.15: The horizontal and vertical velocities (m/s) at the end of 24th hour for case 1 (n5).

are almost the same for all three cases. The increase of the aspect ratio is due to an increase of the width of the updrafts. These results suggest that the asymmetric internal heating with concentrated cooling at the top of the layer is a strong mechanism to select cells with broad updrafts, or "closed" mesoscale circulations. This was also noticed by Helfand and Kalnay (1983), although they used a much smaller domain size (their domain aspect ratio was 3). The failure of symmetric heating to produce broad cells (case 3) is obvious. Even so, however, we can still see that the updrafts tend to be wider and weaker than the downdrafts in this case (Figs. 4.12 and 4.17). This is due to the non-

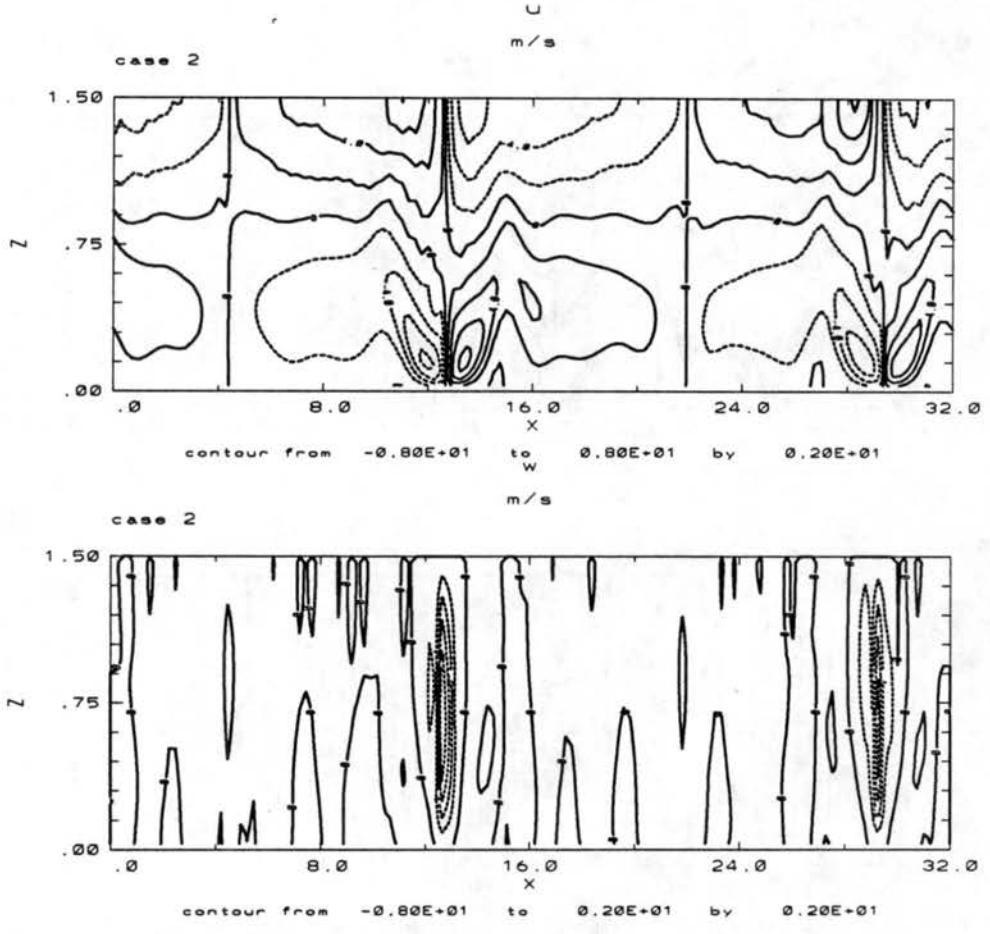

FIGURE 4.16: As in Fig. 4.15 except for case 2 (n35).

slip lower boundary condition, as was also found by the weakly nonlinear analytical solution in the last section. This effect of the dynamical boundary condition is also shown by the asymmetric profile of horizontal velocity in Fig. 4.17.

A common feature of the temperature field for these three cases is that a cold core is located in downdrafts, or at the edge of each cell, and a warm core is associated with each updraft at the cell center, except near very top and bottom where motions are essentially horizontal. However, in cases 1 and 2 the horizontal potential temperature

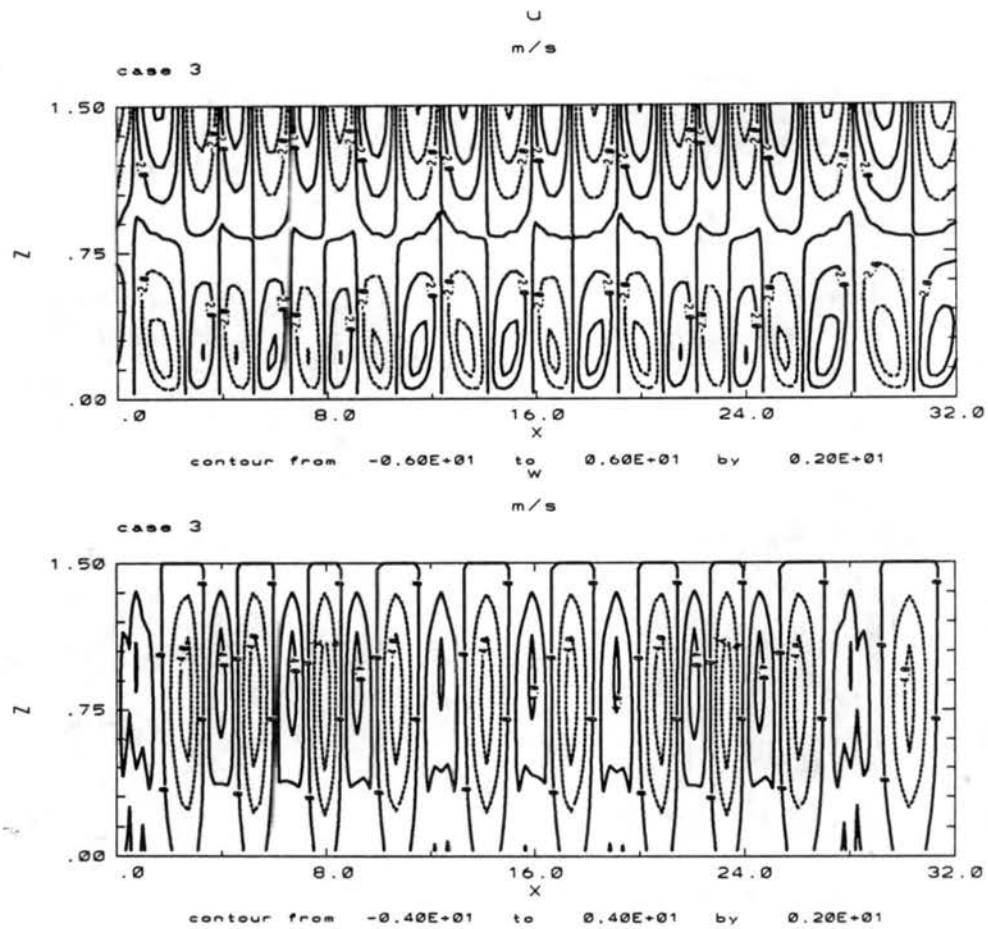

FIGURE 4.17: As in Fig. 4.15 except for case 3 (n1).

gradient is strong in downdrafts (Figs. 4.10 and 4.11), while in case 3 this gradient is very flat (Fig. 4.12). Moreover, two small-scale warm cores appear beside each downdraft in cases 1 and 2, but not in case 3. These warm cores seem to be formed by the cold air splashing back from the lower boundary. The circulations are obviously related to the warm cores in these cases, as shown by their stream functions (Figs. 4.10, 4.11 and 13). For cases 1 and 2, mesoscale circulations are associated with the mesoscale warm cores, while small-scale circulations are associated with the small-scale warm cores. This "two-scale" structure does not appear in case 3. It is interesting to see,

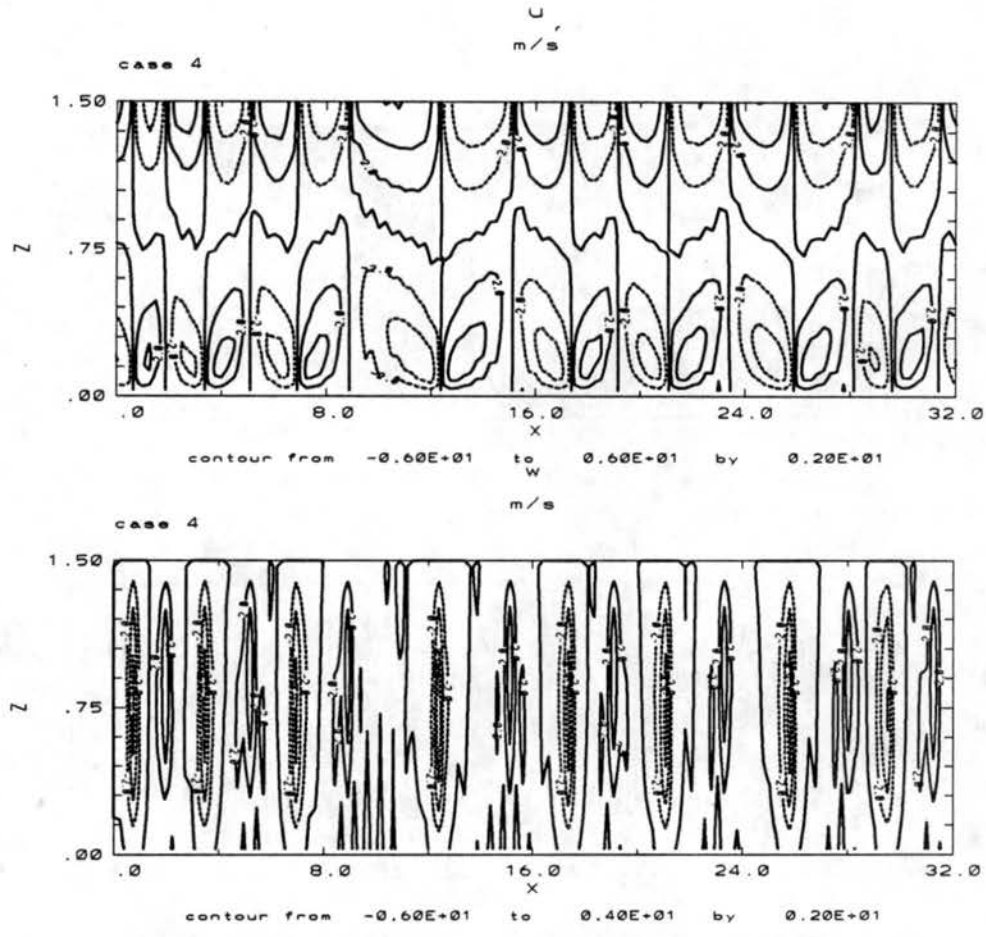

FIGURE 4.18: As in Fig. 4.15 except for case 4 (cb).

however, that the scale of the circulations in case 3 is close to that of the smaller-scale circulations in cases 1 and 2. Moreover, when the internal heating is more asymmetric (or n is larger), the small-scale circulations are weaker. This difference in the scales of the circulations may indicate that asymmetric internal heating helps parcels to "escape" from the small-scale circulations to join in mesoscale circulations. This idea will be further discussed below by trajectory analysis.

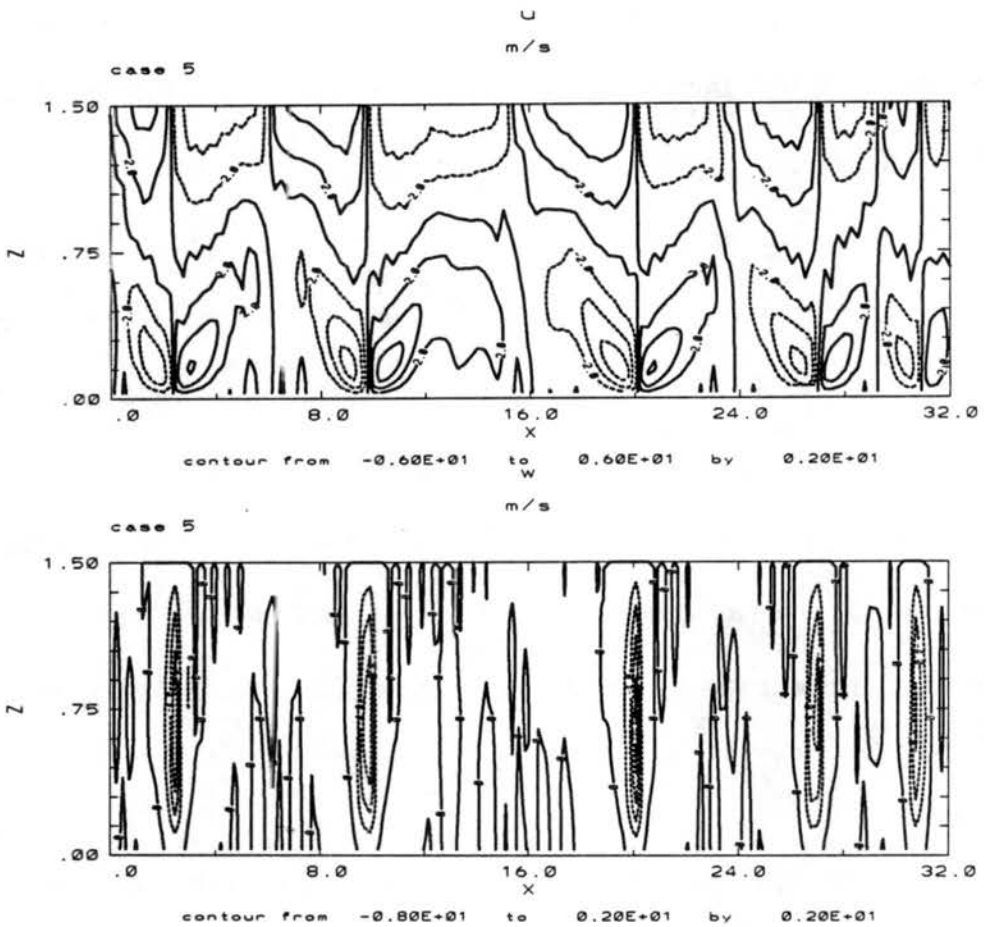

FIGURE 4.19: As in Fig. 4.15 except for case 5 (n35cb).

Case 4 (cb) is designed to see the effects of heat fluxes from the boundaries. In this case there is no internal heating, so that only diffusion and advection determine the distribution of potential temperature. As in case 3, the only reason for the cell asymmetry is the asymmetry of the dynamical boundary conditions. Figs. 4.13 and 4.18 show a lot of small cells. However, unlike case 3, a large cell with aspect ratio of 4 does appear between 8 km and 16 km. The cell pattern is of the closed type (i.e., wider updrafts and narrower downdrafts), although strong surface warming exists. The potential temperature distribution is different not only from that of case 3, but also from those of cases 1 and 2.

This case is actually equivalent (for linear dynamics) to a case with two overlapped heating profiles: One is the profile with $n \to \infty$ in (4.6). Since when $n \to \infty$ we have $z_0 \to 1$ and $F(n) \to 0$, from (4.12) all of the flux F_0 has to go to the top boundary. This profile should give a temperature pattern like that for cases 1 and 2. The second is an upside-down version of the first, but with the opposite sign. It therefore gives a temperature pattern like that in cases 1 and 2 but upside-down, and with the effects of the no-slip lower boundary condition. The superposition (not exact, however, due to nonlinearity) of these two patterns results in the potential temperature distribution in Fig. 4.13. The two strong asymmetric heatings tend to cancel each other. It seems that the free-slip upper boundary condition allows the top cooling to be somewhat dominant, however, so that cells still have some chance to expand, and to evolve to the closed cell pattern.

The two-scale circulations found in cases 1 and 2 do not exist in this case, although some cells may dominate over others. This indicates that without internal heating, constant boundary fluxes can not efficiently generate mesoscale circulations.

Case 5 (n35cb) is a combination of cases 2 (n35) and case 4 (cb) (Figs. 4.14 and 4.19). The asymmetric internal heating strongly enhances the mesoscale circulations. The two best developed mesoscale cells (located between 6 km and 24 km) show again the two-scale circulations. Also, like case 4, this case again demonstrates that closed cells can occur even when strong heating exists at the lower boundary, consistent with the observations reviewed earlier (e.g., Burt and Agee, 1977; Rothermel and Agee, 1980).

The above qualitative analysis has shown that, for the five cases studied, mesoscale circulations appear only when asymmetric internal heating exists. Also, the increase of cell sizes is due to the increase of the widths of updrafts. The widths of downdrafts are essentially unchanged no matter whether mesoscale structures appear or not. We conclude that asymmetric internal heating can generate "closed" MCC. Accompanying the appearance of MCC, a small-scale circulation associated with downdrafts also appears. These phenomena need further investigation since they may reveal how MCC is related to small-scale structures, which we believe may be more directly generated by local cooling than mesoscale structures. We want to understand how the asymmetric internal heating produces scale selection in the nonlinear problem. The weakly nonlinear theory does show that the asymmetry of internal heating enhances the asymmetry of the cells, but it cannot explain the effects of asymmetric heating on scale selection, since it is based on the *assumption* that the aspect ratio of the cells is large.

4.4.3.2 Spectral analysis

The power spectra of the convective kinetic energy (CKE) and enstrophy at the mid-level have been analyzed to show quantitatively the convection scales present in the cases studied, as shown in Figs. 4.20 and 4.21, respectively. The three lines in each panel represent the spectrum at the end of 22nd, 23rd and 24th hours, respectively. The consistency between these lines indicates that the spectrum represents the scales of motion realistically. A scale separation exists for all cases: One group contains mesoscale cells with wave numbers in the range one to four (aspect ratios 32 to 5.3), and the other contains small-scale cells with wave numbers greater than ten (aspect ratio 2.1

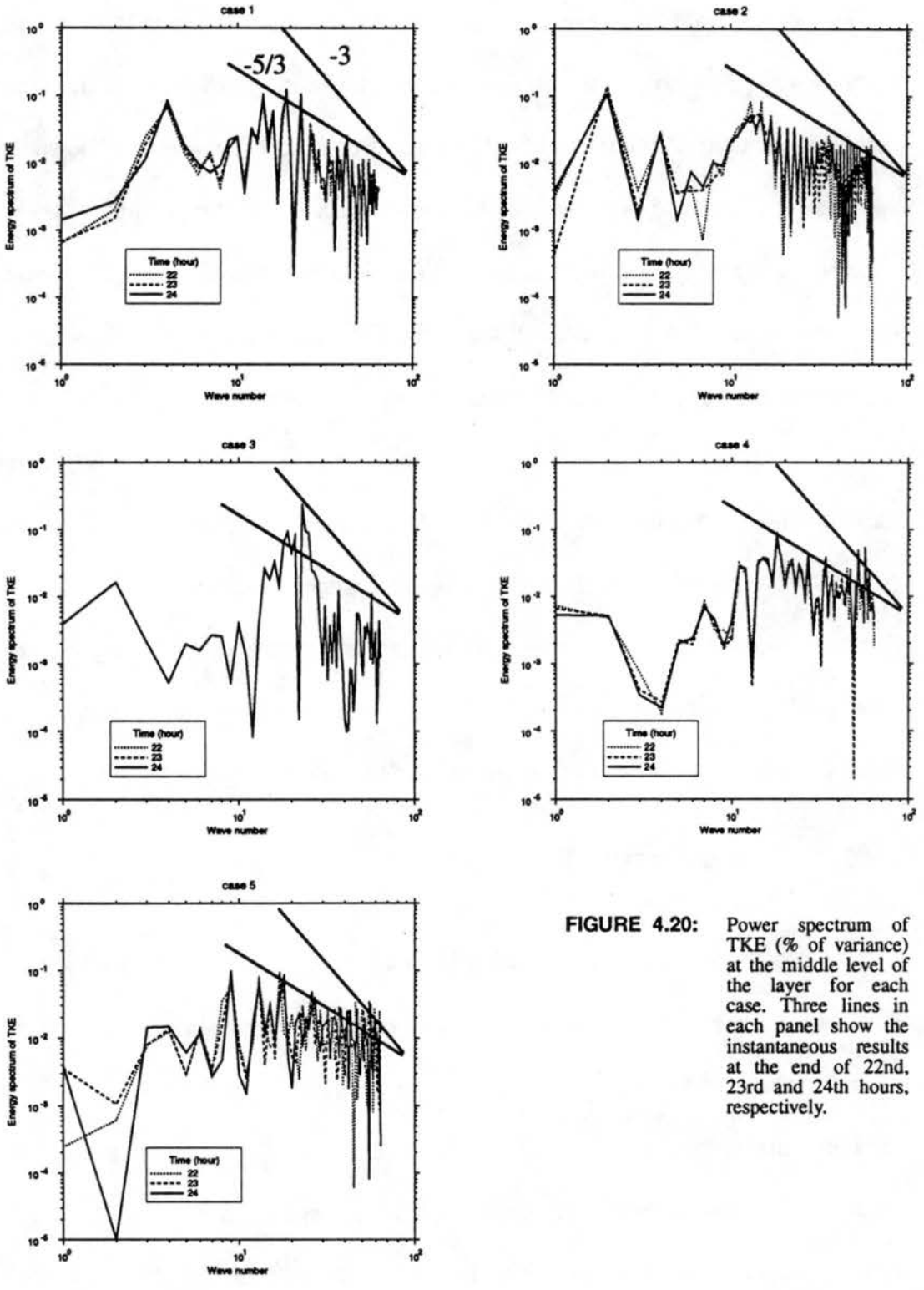

FIGURE 4.20: Power spectrum of TKE (% of variance) at the middle level of the layer for each case. Three lines in each panel show the instantaneous results at the end of 22nd, 23rd and 24th hours, respectively.

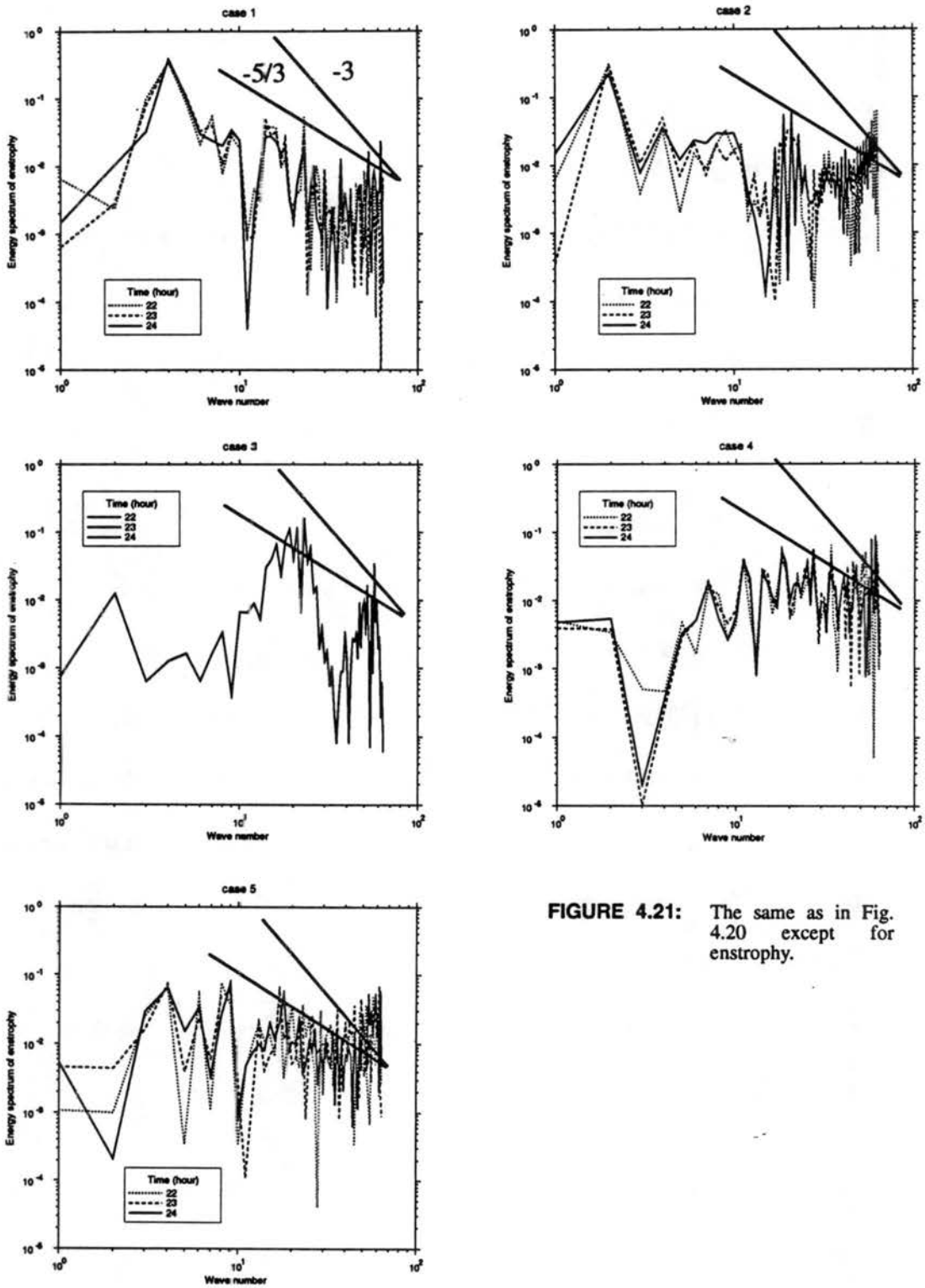

FIGURE 4.21: The same as in Fig. 4.20 except for enstrophy.

or smaller). Mesoscale cells dominate in cases 1 (n5), 2 (n35) and 5 (n35cb), as also shown by their stream functions (Figs. 4.10, 4.11 and 15). The CKE of a mesoscale cell is comparable to that of a small-scale cell, while the enstrophy of the mesoscale cells is an order of magnitude larger than that of small-scale cells for these cases. This large CKE at small scale and large enstrophy at the mesoscale indicate that the anti-cascade mechanism inherent in a 2-D model is not a dominant factor for the cell broadening shown in our model results. Since the slope of the spectra in Figs. 4.20 and 4.21 are not definite, it is hard to say exactly to what extent a 2-D upscale energy anti-cascade exists.

The dominance of small-scale cells in cases 3 and 4 (or cases n1 and cb) tells us that although the longest wave ($k \to 0$) is most unstable from the linear theory of constant boundary fluxes, it is not necessarily dominant in a fully developed nonlinear system. The linear theory can tell us what wave number appears most easily at the *onset* of convection, but not what wave number will dominate when convection is fully developed. When the Rayleigh number is very large ($R_a / R_{ac} \gg 1$), so that motions with almost all scales can happen, as is true for the PBL, there is no obvious reason to believe that mesoscale motion should appear and dominate, even though the existence of a mesoscale mode is possible in the model. Some mechanisms must be there to "select" the mesoscale cells. The asymmetric internal heating is such a mechanism.

The existence of small-scale convection in all cases may be related to the scale of the downdrafts which does not change much from case to case. To illustrate this point, we take case 1 (n5) as an example and analyze the one-hour averaged field shown in Figs. 4.10 to see whether the mesoscale convection contributes to the CKE of downdrafts. To

isolate the mesoscale contribution, we use a 19-point horizontal running average to select the scales with wave numbers less than 6. The profile of the filter is shown in Appendix G. The 2-D distributions obtained for the total and mesoscale components of the CKE are shown in Fig. 4.22. It is obvious that most of the total CKE is associated with

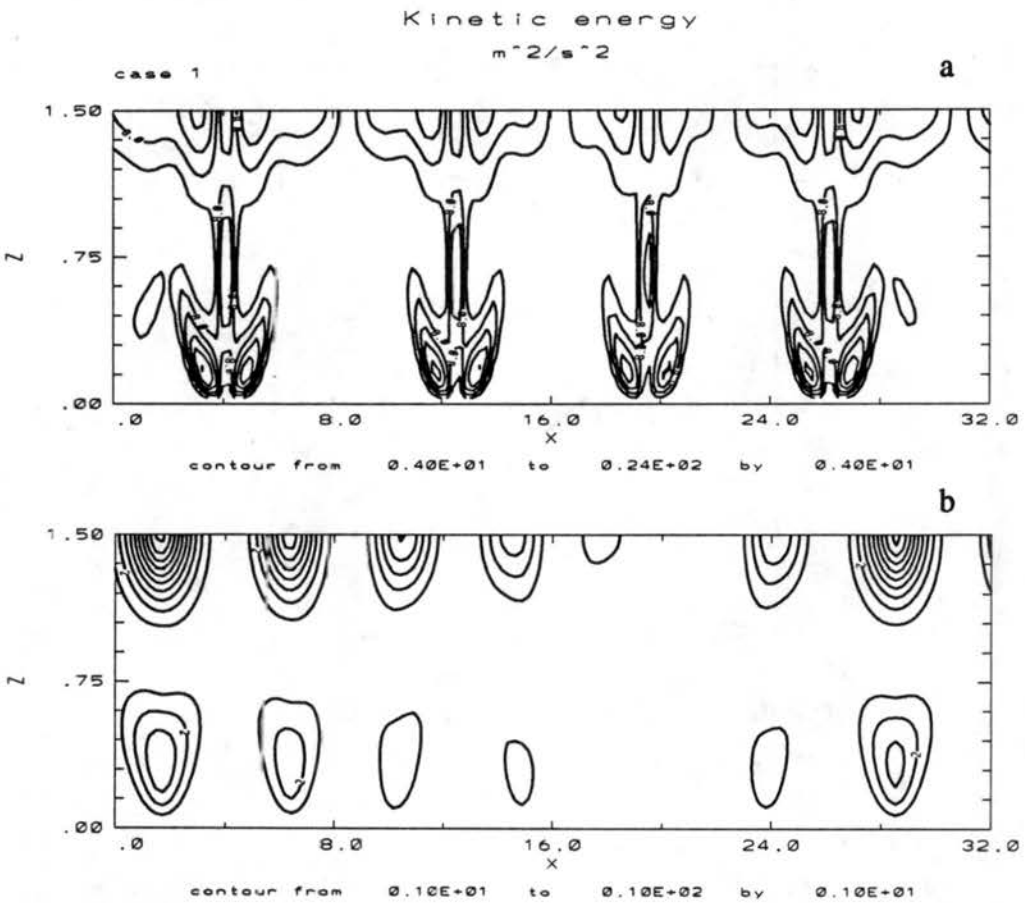

FIGURE 4.22: The distribution of (a) total and (b) mesoscale component of TKE for case 1.

downdrafts (Fig. 4.22a). The local maxima of the total CKE are related to the local maxima and minima of u and w (Fig. 4.15), so that u contributes more to CKE at the upper and lower levels, while w contributes more at the mid-level. After filtering, however, the downdrafts are completely gone (Fig. 4.22b). The mesoscale component of

the CKE only appears in the region between downdrafts, or in updrafts, with maximum values located at the top (Fig. 4.23), where inflow and outflow are the strongest (Fig. 4.15). Therefore, we can conclude that in the CKE spectrum, the small-scale group is associated with downdrafts. The horizontally averaged vertical distribution of CKE and its mesoscale component are shown in Fig. 4.23. Figs. 4.22b and 4.23 together show that

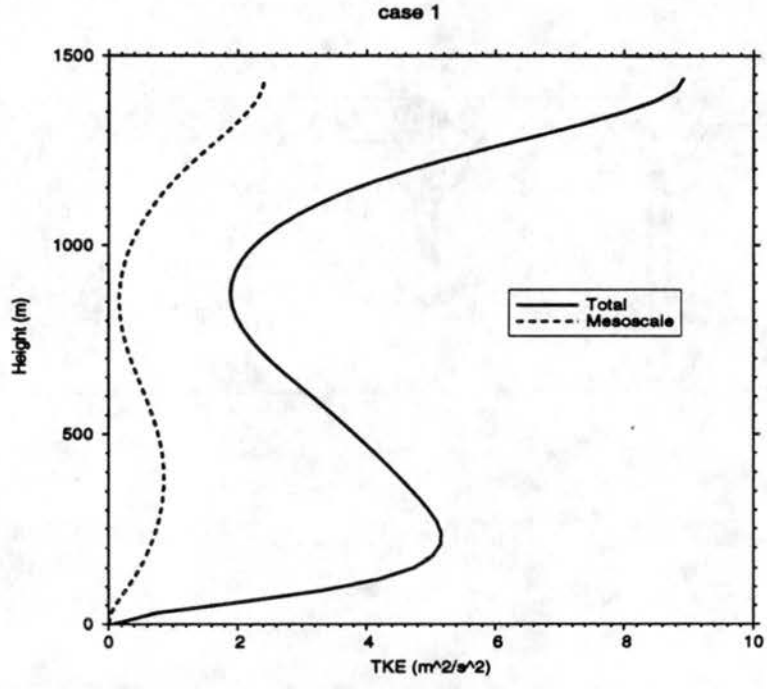

FIGURE 4.23: The vertical distribution of TKE.

the mesoscale contribution is mainly related to the horizontal motion near top and bottom. This indicates that mesoscale horizontal advection is an important nonlinear process in the model.

4.4.3.3 Vertical distributions of potential temperature and heat flux

The development of convection must be closely related to the temperature stratification in the layer. Convection is suppressed by stable stratification, and generated

by unstable stratification. As shown in Figs. 4.10 to 4.14, although the convection in these cases is fully developed, and reaches a steady state, the air in the layer is far from well mixed. This is again shown by the horizontally averaged vertical distribution of potential temperature for each case in Fig. 25. The vertical distribution of potential temperature averaged for updrafts and downdrafts, respectively, are also shown. Unlike the monotonic decrease of potential temperature with height from the weakly nonlinear theory [Eq.(4.52)], a non-monotonic distribution of potential temperature, including a statically stable layer (indicated by the bars in Fig. 4.24), exists for these fully nonlinear cases. Stable layers exist in both updrafts and downdrafts, but their heights and depths differ between updrafts and downdrafts, as well as from case to case. The stable layer is the deepest and strongest in updrafts in case 2 where the internal heating is the most asymmetric, and is the shallowest and weakest in downdrafts in case 4 where there is no internal heating. Unstable layers exist both above and below the stable layer, except in case 3 where the stable layer extends to the top. Downdrafts are more unstable than updrafts in these unstable layers.

Our analyses show that nonlinear processes are responsible for generating the stable layer. The two processes which determine the vertical distribution of potential temperature are the internal and/or boundary heating, and the vertical transport of heat by motion, including turbulence diffusion. The heating profiles for all of the cases have cooling in the upper part (and/or at the top) and warming in the lower part (and/or at the bottom). This heating by itself would tend to produce a monotonic decrease of temperature with height, and can thus account for the unstable layers near the top and bottom, where convection is generated. The vertical transport of heat, therefore, is the

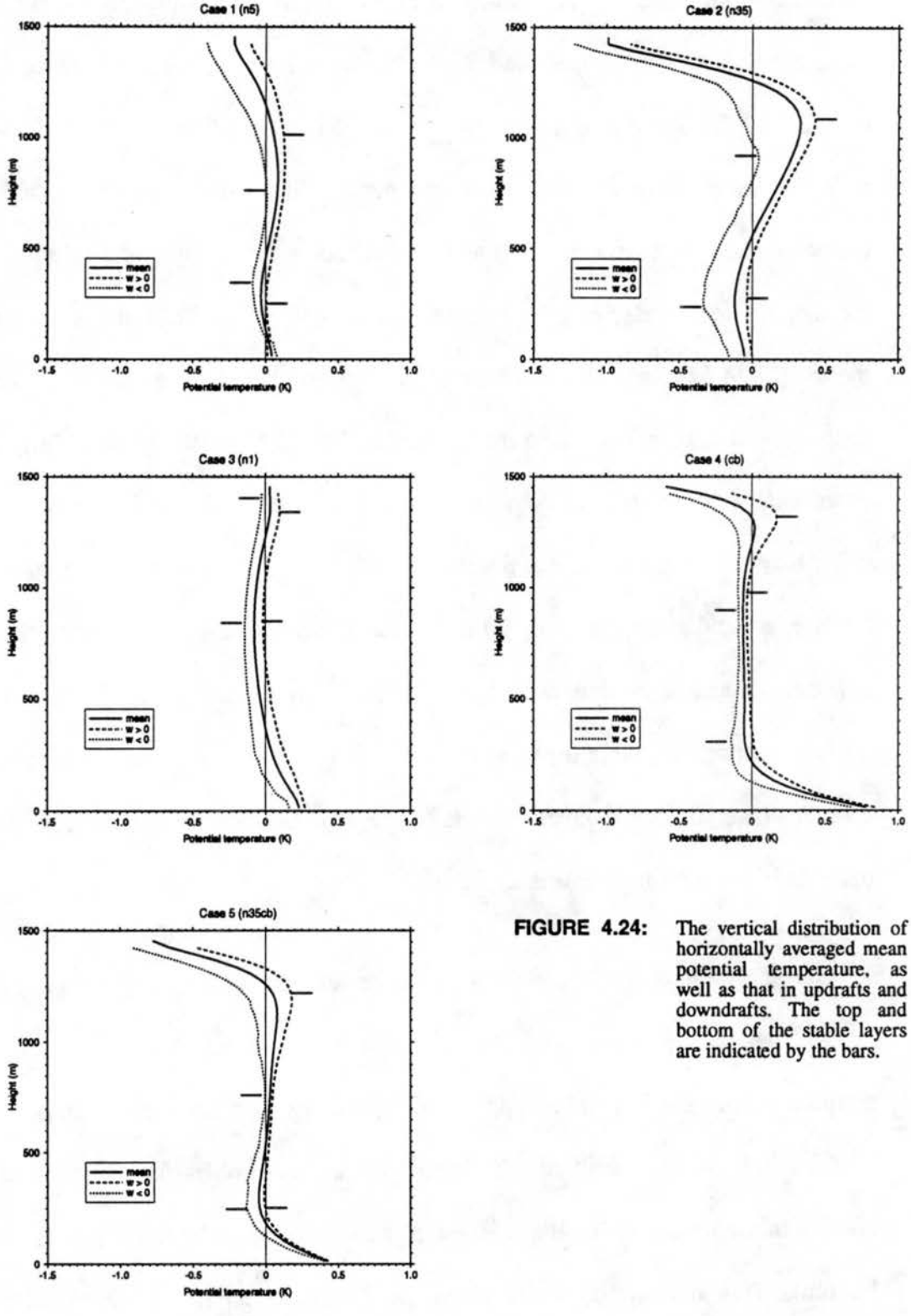

FIGURE 4.24: The vertical distribution of horizontally averaged mean potential temperature, as well as that in updrafts and downdrafts. The top and bottom of the stable layers are indicated by the bars.

process that must generate and maintain the stable layer. The vertical transport of heat, includes the parameterized subgrid flux, the small-scale flux, and the mesoscale flux calculated from the filtered vertical velocity and potential temperature, as shown in Fig. 4.25. The subgrid flux is parameterized as a linear down-gradient transport, and hence tends to smooth out the temperature. It can not build up a stable layer. The resolved heat flux, in contrast, produces counter-gradient transports in the stable layer (positive when the subgrid flux is negative), which enhances the stratification of the stable layer. This resolved heat flux is positive throughout the layer, and dominates the total flux in all cases, except near the boundaries where it is limited by the boundary conditions on the vertical velocity. Therefore, this resolved heat transport, which is a nonlinear process, maintains the stable stratification. Note that mesoscale component of the heat flux is also counter-gradient transport. The stronger the stable layer is, the larger the mesoscale heat flux.

The correlation between temperature and vertical velocity can further demonstrate how small-scale cells are suppressed by the stable stratification in cases 1 and 2. Fig. 4.26 shows an example for the mid-level from case 1. Although at this level the mean stratification is stable for both updrafts and downdrafts, the strong spikes in the centers of the updrafts (noted by 1) and downdrafts (noted by 3) contribute to the positive heat flux. These two spikes represent mesoscale circulations, as seen by comparison with the stream function in Fig. 4.10. The two small-scale warm cores beside each downdraft, discussed earlier, contribute negatively to the heat flux in area 2. This correlation pattern shows that mesoscale convection is allowed to develop (positive heat flux in areas 1 and

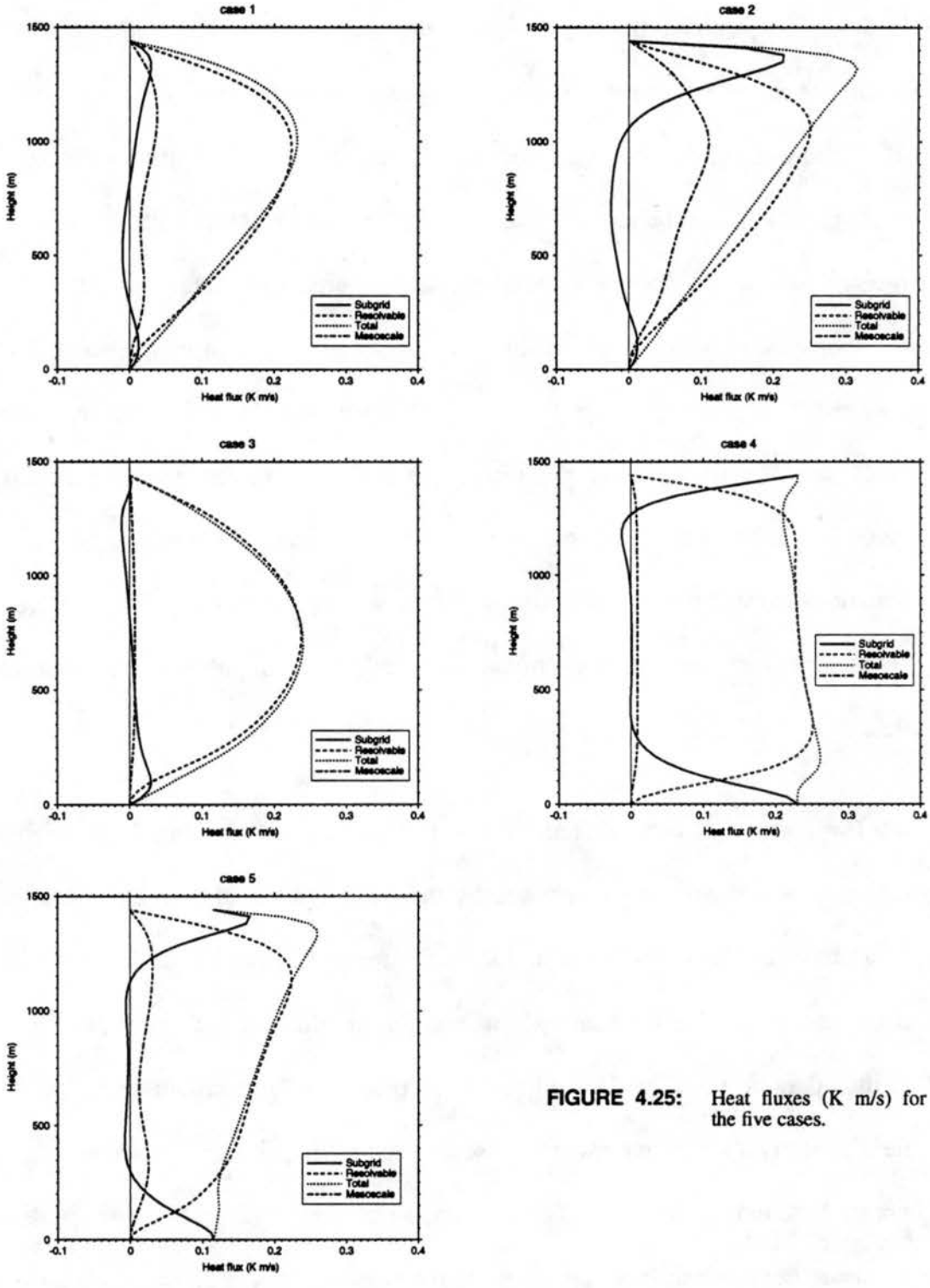

FIGURE 4.25: Heat fluxes (K m/s) for the five cases.

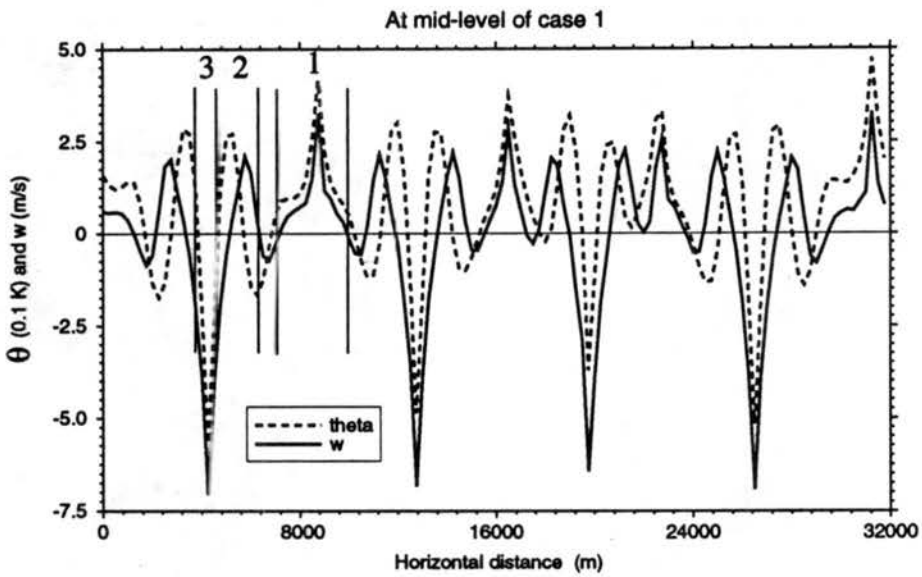

FIGURE 4.26: A composite structure of temperature (0.1 K) and vertical velocity (m/s) at the mid-level of case 1.

3), and small-scale convection is suppressed by the small-scale warm cores (negative heat flux in area 2).

As a matter of fact, although the average potential temperatures in updrafts and downdrafts each include stable layers, the stratification in the mesoscale updraft and downdraft cores (the peaks of 1 and 3 indicated in Fig, 4.26, respectively) is unstable. The potential temperature distribution for the cores is shown in Fig. 4.27. The mean profiles for case 1 in Fig. 4.24 are reproduced here for comparison. The locally unstable stratification in the cores 1 and 3 allows vertical, or counter-mean-gradient transport of heat. It is also worth pointing out that near the small-scale warm cores (e.g., 2 in Fig. 4.26), the phase difference of potential temperature and vertical velocity is about $\pi/2$, which indicates that gravity waves are excited by strong downdrafts, and propagate away

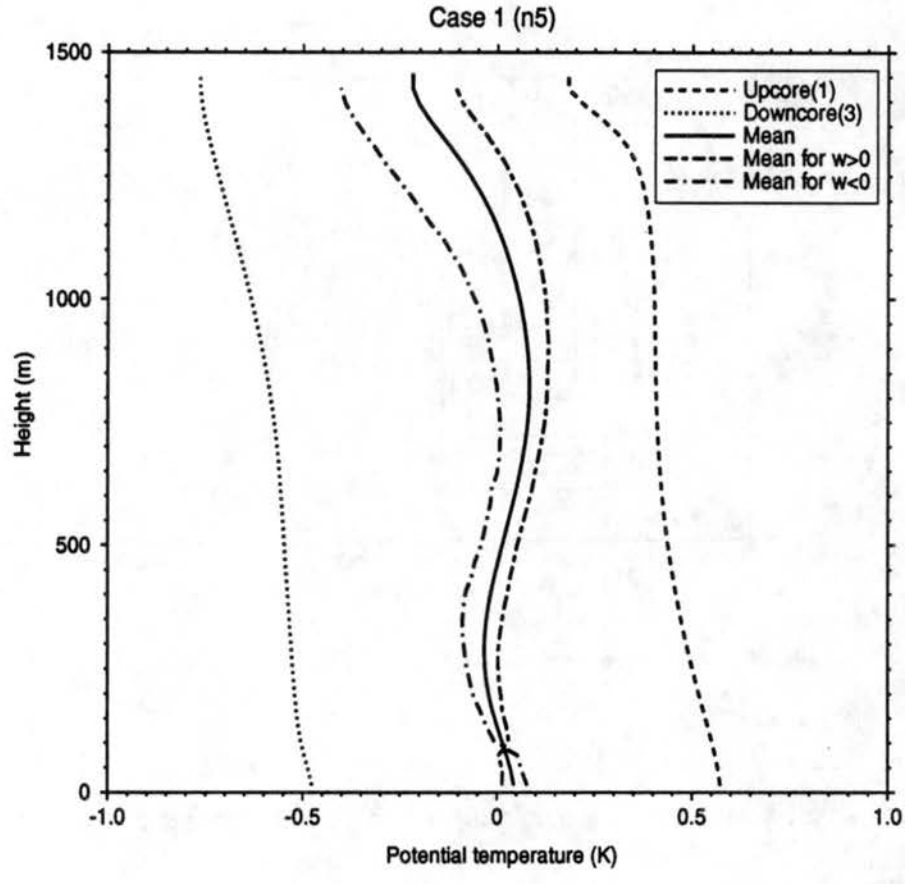

FIGURE 4.27: The potential temperature distribution from case 1.

from the cold core 1. The gravity waves disappear at warm cores, such as 3, where stratification is unstable, and their energy is converted back to CKE.

However, we have not explained yet why the two-scale structure, as found in section 4.4.3.1, exists only when asymmetric heating exists. This can be investigated by trajectory analysis. A passive parcel is "placed" at the center of the domain (x=16 km and z=750 m) at the beginning of the 22nd hour. It is then advected by the resolved vertical and horizontal wind. Its trajectory, cooling rate, and potential temperature are recorded until the end of experiment at the end of the 24th hour. Figs. 4.28 to 4.32 show

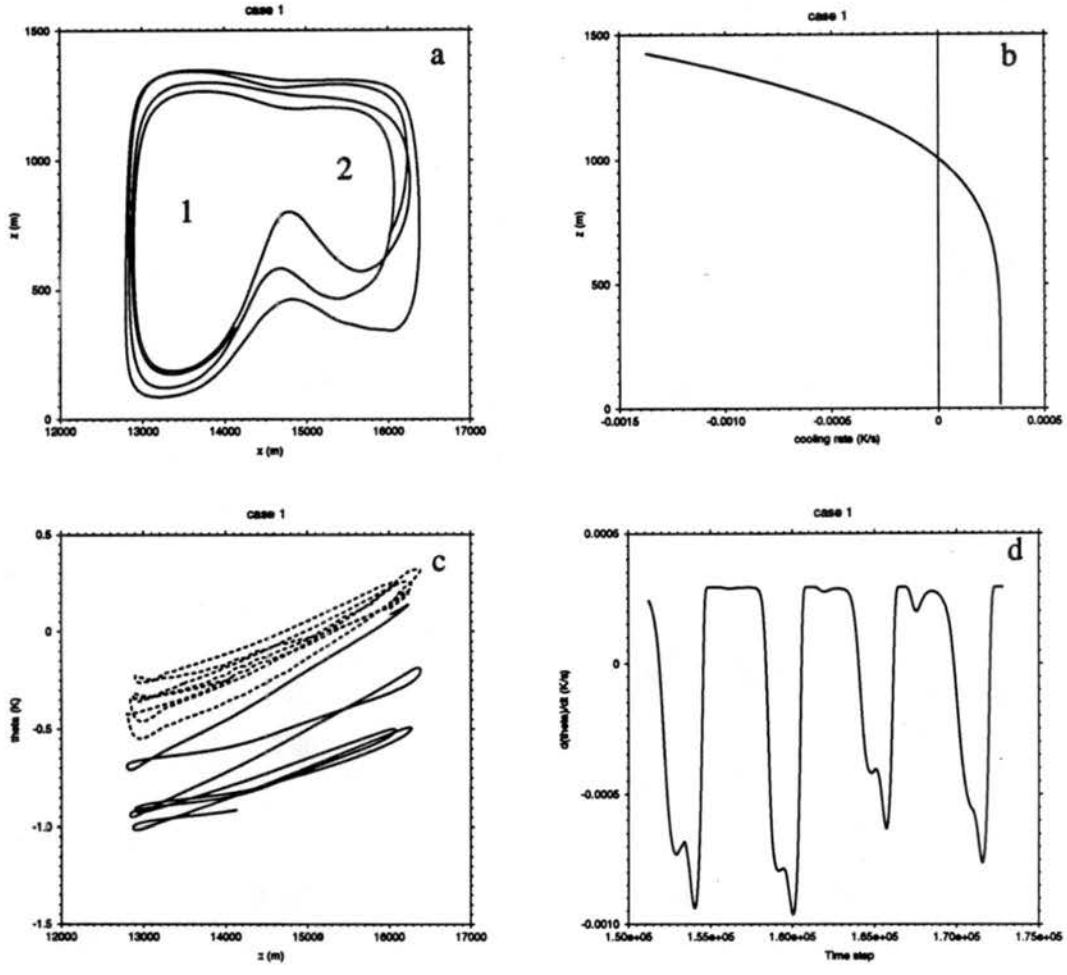

FIGURE 4.28: Case 1: (a) trajectory and two small cells encircled by the trajectory (indicated by 1 and 2); (b) imposed internal heating/cooling rate Q; (c) the potential temperature that the parcel would have if only Q is considered (solid line), and the potential temperature of the parcel interpolated from its environment (dashed line); and (d) the instantaneous value of Q at where the parcel is located. (See footnote on page 192 for more explanation).

the results for the five cases. The circulations representing these trajectories are indicated by arrows in Figs. 4.10 to 4.14, respectively. These trajectories are very representative of the circulation patterns of these cases. Let us look at case 1 (Figs. 4.28 and 4.10) first. The trajectory in Fig. 4.28a includes one mesoscale cell and two small-scale cells, as shown by Fig. 4.10. The two small-scale cells are indicated as 1 and 2 in Fig. 4.28a. Cell 1, which is closer to a downdraft, is stronger than cell 2, which is closer to an updraft.

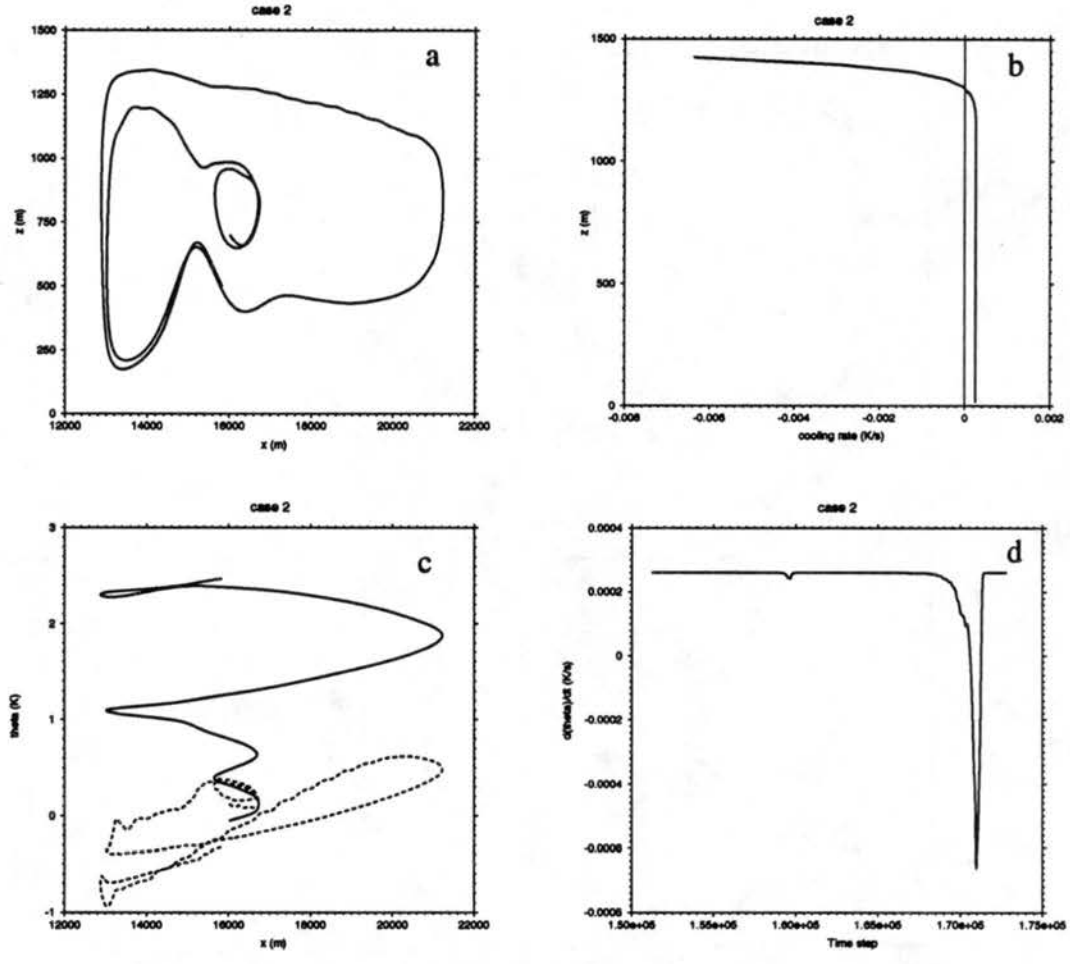

FIGURE 4.29: As in Fig. 4.28 but for case 2.

The parcel moves counter-clockwise (Fig. 4.28a). It experiences heating or cooling, depending on its height (Fig. 4.28b). Since the cooling layer is deep, it experiences strong cooling much of time during the three hours (Fig. 4.28d). This results in the cooling of the parcel if diffusion is not considered† (Fig. 4.28c, solid line). However, diffusion warms up the parcel so that its potential temperature follows a similar pattern (Fig. 4.28c, dashed line). The parcel is cooled while it stays near the model top, until it is

†. This is done by using $d\theta/dt = \dot{Q}$ for the passive parcel so that diffusion can be excluded. The $\dot{Q}$ of the parcel (panel d in Fi.gs. 4.28-4.32) is known after the location of the parcel is determined by $dx/dt = u$, and $dz/dt = w$.

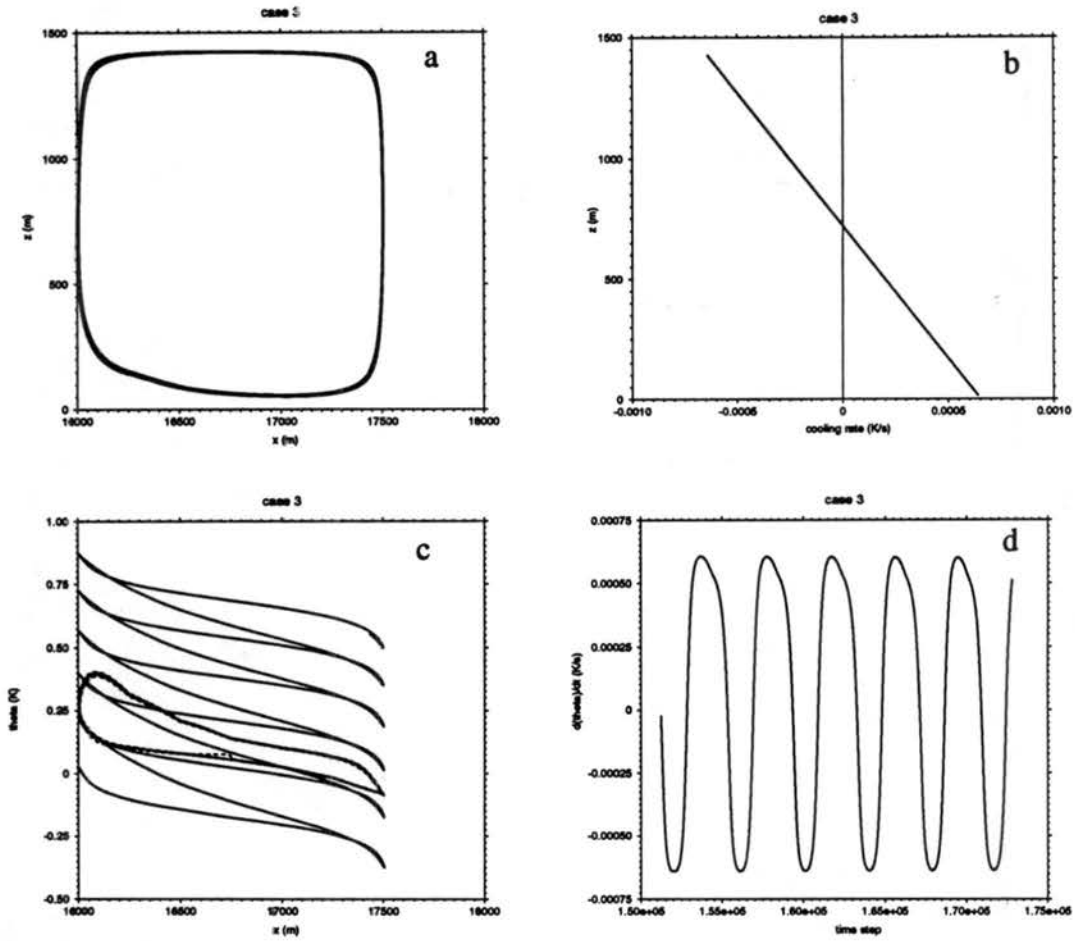

FIGURE 4.30: As in Fig. 4.28 but for case 3.

cold enough to join a downdraft. When it reaches the bottom, it is colder than the air above it. It then moves upward along the direction of cell 1. It is gradually warmed in the lower part of the layer. However, since the air above it is so stable (the small-scale warm core) that it cannot break through, it is pushed downward by the local downward motion related to cell 2. Gravity waves may also help the parcel move up and down during this period. It finally rises when it has gained enough buoyancy through the low-level warming, while at the same time it has moved horizontally. In this way, the parcel's

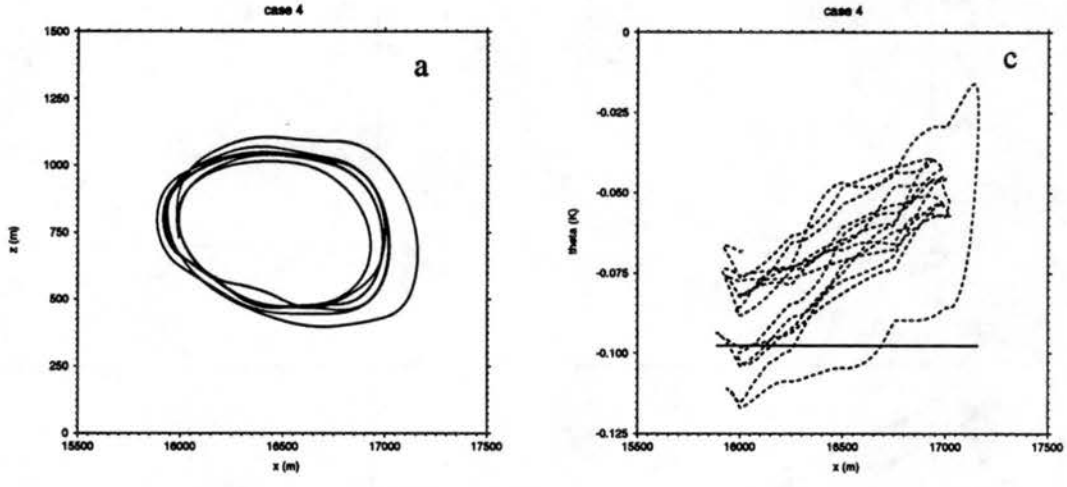

FIGURE 4.31: As in Fig. 4.28 except for case 4.

small-scale circulation is suppressed by the local stable layer, and it is forced to participate in a mesoscale circulation.

Cases 2 and 5 (Figs. 4.29 and 4.32) can be analyzed similarly. The parcel in case 2 (Fig. 4.29a) experiences both small-scale and mesoscale circulations. The small-scale circulation is preferred when the cooling rate experienced by the parcel is small, while the mesoscale circulation is preferred when the parcel undergoes strong cooling (Fig. 4.29d). This is not hard to understand. A parcel which is cooled most strongly can

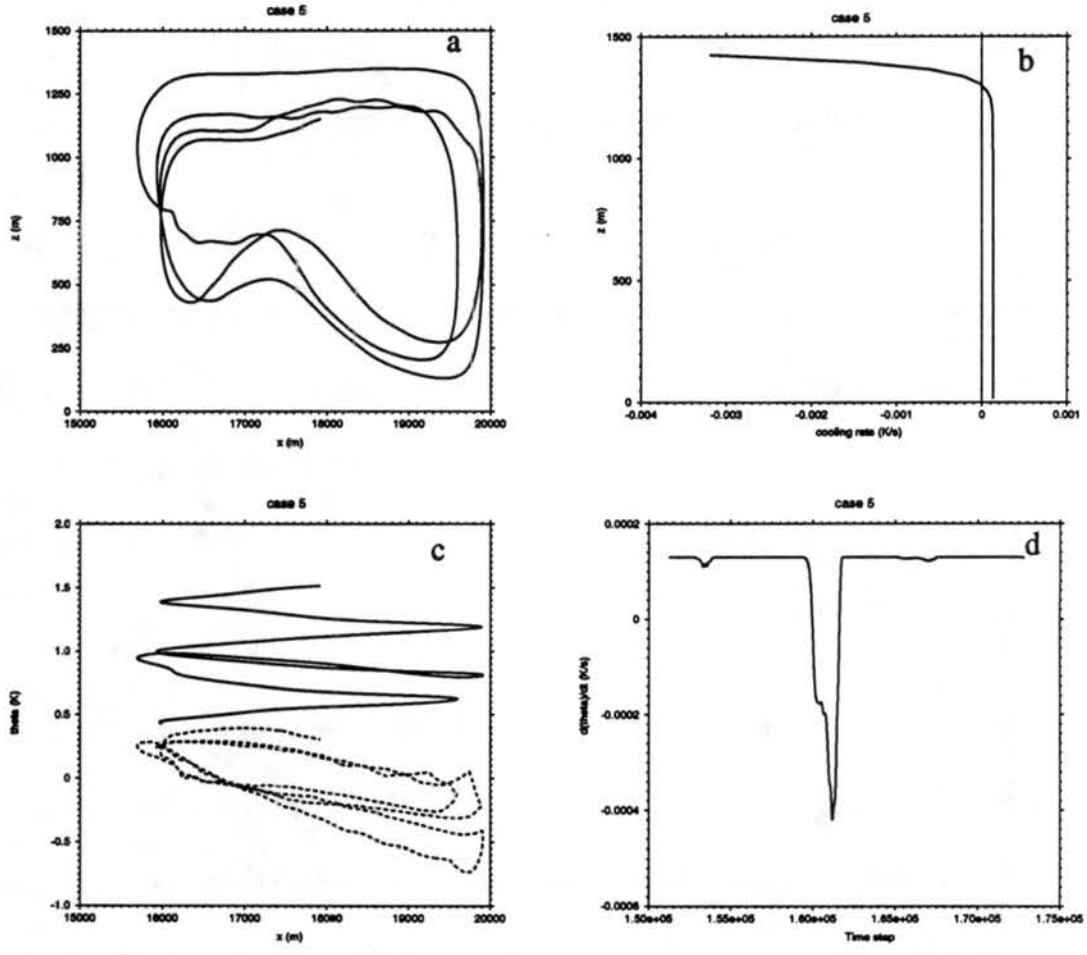

FIGURE 4.32: As in Fig. 4.28 except for case 5.

penetrate more readily to the bottom of the layer, and takes a long time to regain its buoyancy. Therefore it moves farther horizontally, and forms a mesoscale circulation.

More asymmetric heating implies a stronger cooling near the top in our cases. Therefore a longer time is required to warm the parcel. In this way, more asymmetric heating results in larger cells.

In case 3, for which the heating is symmetric, a parcel cooled at the top can be warmed up at the bottom at the same rate. There is no chance for another scale to

develop. However, we cannot explain why its single circulation pattern is small-scale, rather than mesoscale, as implied by the linear and weakly nonlinear theory. Perhaps it is because the parcel cannot sustain its buoyancy for a long time.

Case 4 is different from all the cases discussed above (Fig. 4.31). The parcel only circles near the center of the layer. Since in this case the heating is at the upper and lower boundaries, this parcel near the center can only obtain energy from the local diffusion, and it does not penetrate the stable layers at the upper levels of the updraft and the lower levels of the downdraft (Fig. 4.24d). Therefore in this case it is also hard to develop mesoscale cells.

The above trajectory analysis shows qualitatively how asymmetric internal heating generates mesoscale convection and why more asymmetric heating generates larger mesoscale cells. In these analyses we have assumed that the temperature structure is steady. Although we have discussed how the horizontally averaged stratification is maintained by the prescribed heating and vertical transport of heat due to motion, we did not discuss how the basic state stratification is produced. Since the basic state and motion always change interactively, a nonsteady-state analysis may be required. This is beyond the scope of this thesis. Instead, we will analyze the potential temperature budget in the next section to further understand the steady temperature structure. In the rest of this section, we still assume that the basic state for each case already exists, and further study what kind of basic state is preferred by mesoscale circulations.

An unstable layer exists above the stable layer in cases 1, 2 and 5, in which mesoscale cells dominate. This unstable layer is necessary to generate cold narrow

downdrafts, or small-scale CKE, which can penetrate through a stable layer (see 4.4.3.2). Otherwise the stable stratification would gradually kill the turbulence. The small-scale CKE can then be partly converted to mesoscale CKE through the processes discussed in the trajectory analysis. The trajectory analysis is consistent with the results shown in Fig. 4.22, i.e., mesoscale CKE is mainly represented by the horizontal advection near the top and bottom. Note that closed MCC can exist even if the surface heating is relatively strong, as in case 5. The trajectory analysis indicates that, as long as surface heating is not so strong that a parcel can recover its buoyancy before it travels a mesoscale distance, mesoscale circulation may appear.

The above analysis shows that a stable layer which selects the scales of the updrafts, together with an unstable layer near the top which generates the small-scale downdrafts, comprise a basic state which favors the formation of closed MCC. This kind of potential temperature profile is not unusual in the real atmosphere. Fig. 4.33 shows two soundings observed four days apart on the island of Porto Santo during ASTEX in 1992. Here the moist static energy h is conserved during adiabatic processes. The dry static stability is determined by the gradient of potential temperature θ. The moist static stability is determined by the gradient of saturation static energy h^*. The soundings show both dry statically stable (noted by 1 in Fig. 4.33) and moist statically stable (noted by 2 in Fig. 4.33) conditions in the cloud layer. A small stable kink is also indicated by 3. This kink is often observed near cloud base. An unstable layer at cloud top, as indicated by 4, is obvious in both cases. However, people generally believe that this unstable layer cannot exist in nature, and that it must be due to observational errors resulting from bulb wetting. Here we do not want to argue whether this unstable layer can possibly exist or

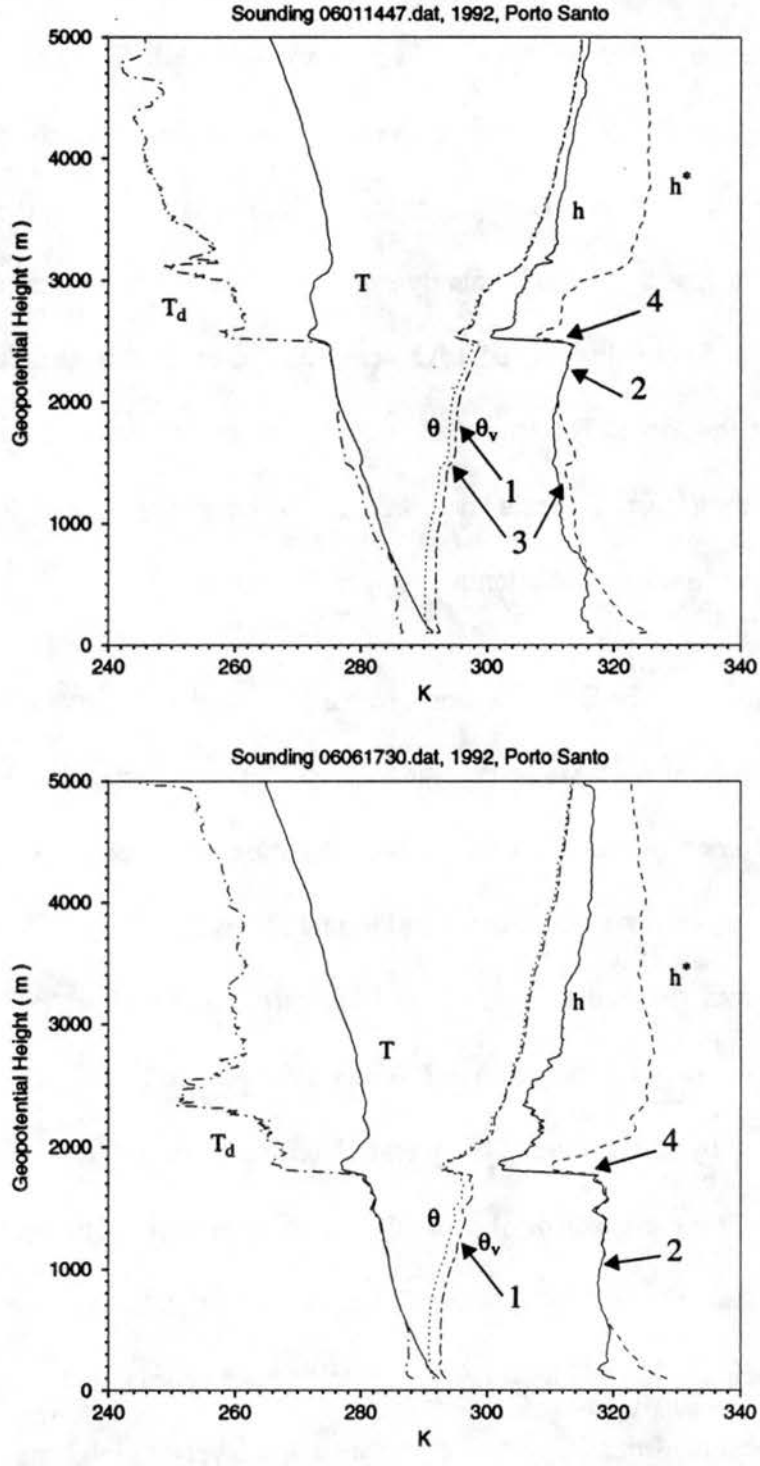

FIGURE 4.33: Soundings observed during ASTEX.

not. Our "need" for this unstable layer is that we require a mechanism to generate convection near cloud top. As long as cloud-top cooling can drive convection, rather than mostly being balanced by the local heating, such as due to entrainment warming, then together with the statically stable layer, the mechanism we discussed in this section will work to generate mesoscale convection. As a matter of fact, we do not even need a stable layer to extend through the whole cloud layer, as in Fig. 4.33. What we need is a stable layer somewhere in the middle of the PBL so that the coldest parcels near the bottom, which penetrate from the top, can be blocked by the stable layer for a while until they move far enough away horizontally to gain enough buoyancy to penetrate upward. This stable layer could be a cloud-base inversion which is produced either by solar radiation or drizzling, as long as it is weak enough to allow vertical transport of heat and moisture, but strong enough to suppress the vertical motion of the coldest parcels at the bottom which originate from cold downdrafts. Such weak inversion layers are often observed in the stratocumulus-topped boundary layers (e.g., Nicholls and Leighton, 1986; Betts, 1989). Therefore, although the mechanism we suggest is based on our simple idealized model, the essential elements required for this mechanism to work do exist in the real atmosphere. We conclude that this mechanism can be applied qualitatively to the atmosphere to explain the formation of MCC. It would be interesting to look at other data, such as satellite imagery, to see whether mesoscale cloud patches appeared during the time the soundings were observed.

4.4.3.4 θ-budget analysis

The preceding analysis motivates further study of the simulated potential temperature structure. Diffusion and advection, together with the internal heating, determine the θ-budget, as shown in Fig. 4.34. Advection dominates in all cases, except that in case 2 diffusion largely balances the strong cooling at the top, and in case 4 diffusion and advection balance each other since there is no internal heating. This dominance of advection cannot be represented by the weakly nonlinear theory, in which diffusion is orders of magnitude stronger than advection. To see to what extent mesoscale convection is represented by the weakly nonlinear theory, and how it helps to build up the potential temperature distribution, we decomposed the budget into horizontal advection, vertical advection, horizontal diffusion, vertical diffusion, and their mesoscale components. Only the results from case 1, which is very representative of both mesoscale and small-scale motions, are discussed below.

Figs. 4.35 and 4.36 show the distributions of the budget terms. The upper panel shows the total, and the lower panel shows the mesoscale component, for each term. Small-scale motions are vigorous in and around the downdraft cores. There is warm horizontal advection in the upper part of the cores, which tends to push warm air into the cores, and cold advection at the lower part of the cores, which tends to push cold air out of the cores (also see Fig. 4.10). This tends to stabilize the cores. Vertical advection has the opposite sign, in contrast. There is cold vertical advection in the upper parts of the cores, which brings the very cold air from the top downward due to negative buoyancy, and warm advection in the lower parts of the cores, which warms up the cold air that has

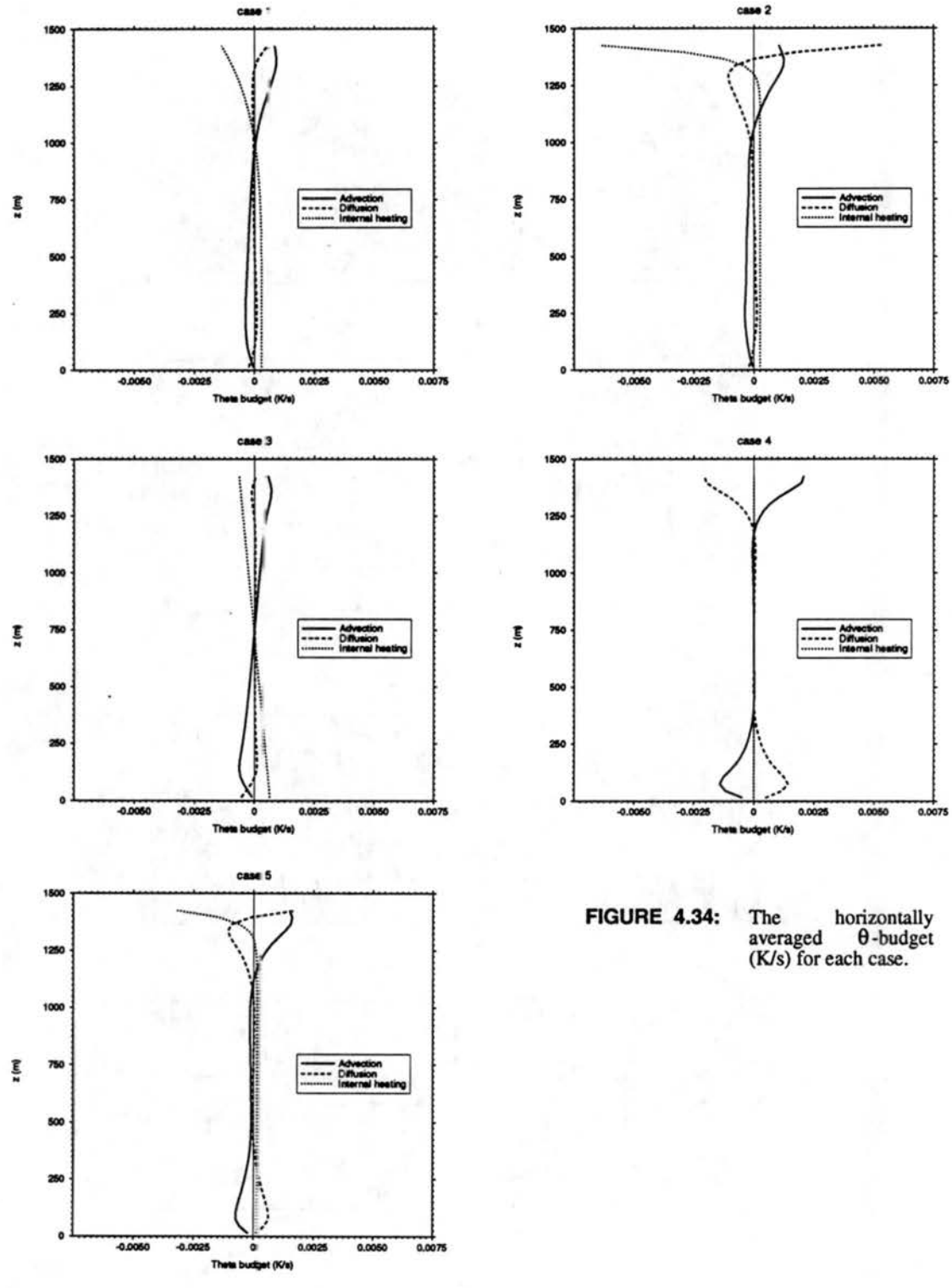

FIGURE 4.34: The horizontally averaged θ-budget (K/s) for each case.

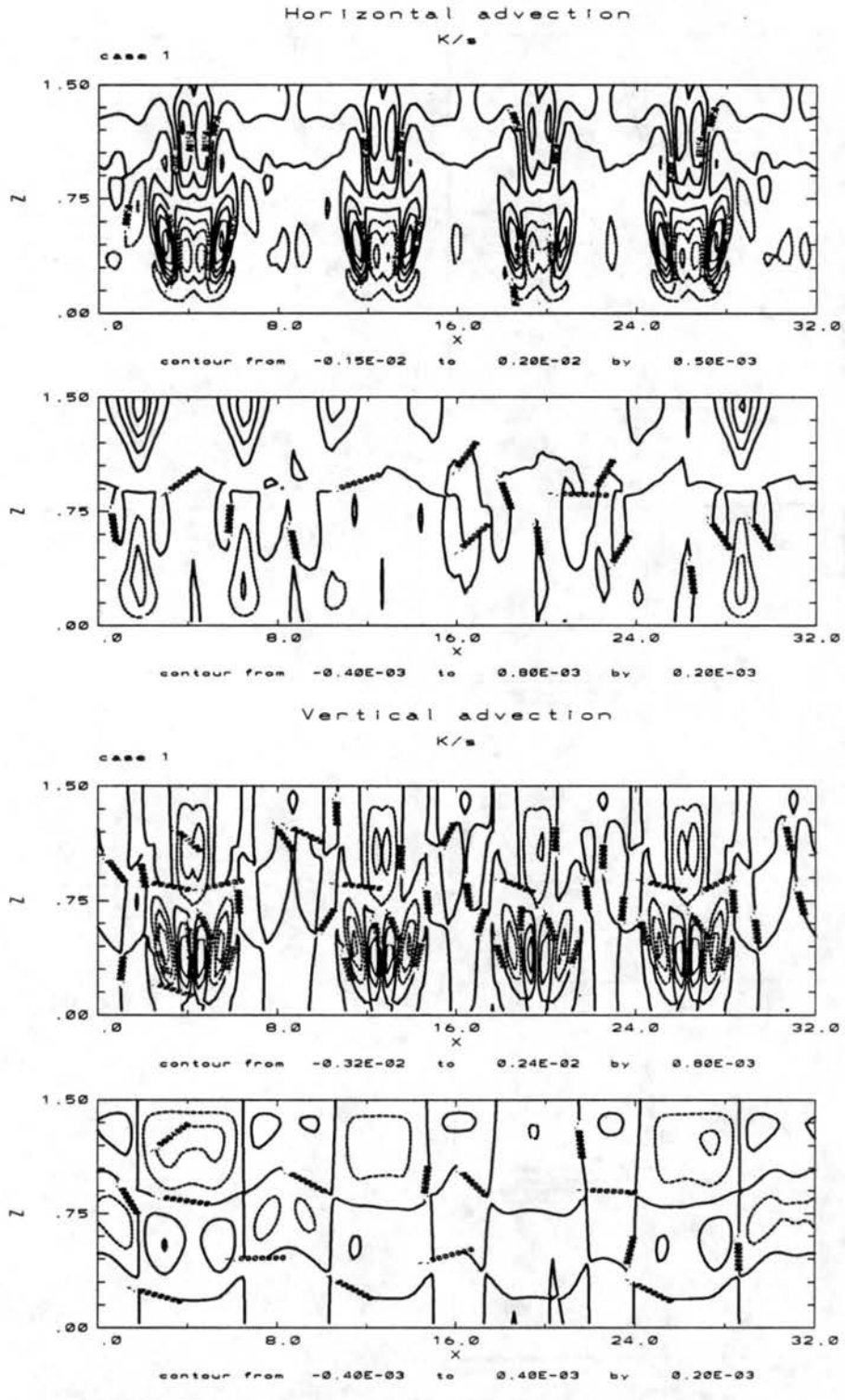

FIGURE 4.35: Total and mesoscale advections for θ-budget.

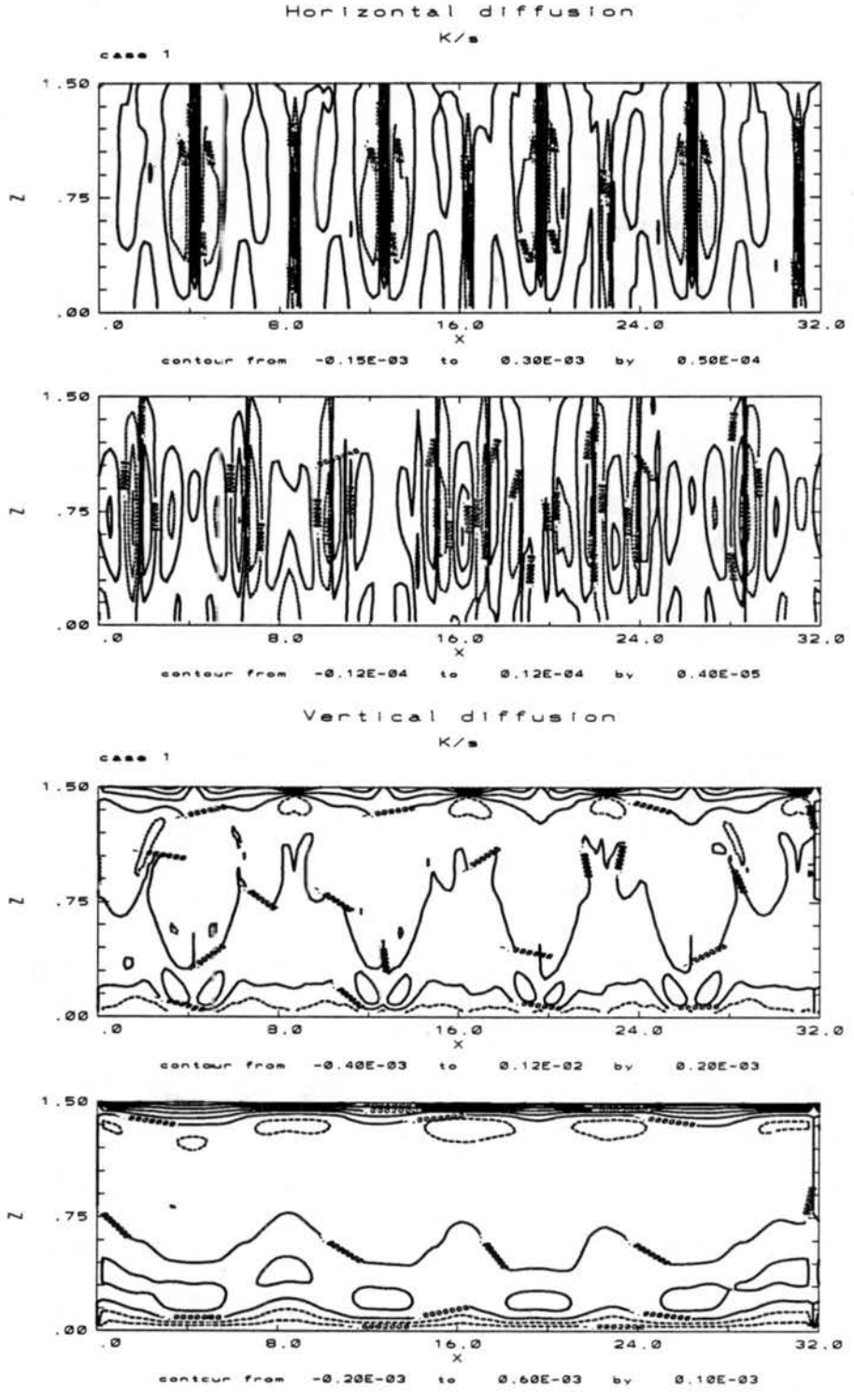

FIGURE 4.33: Total and mesoscale diffusion for θ-budget.

penetrated to the bottom. This term destabilizes the core. These two local advections have the same magnitude, however, and mostly cancel each other. Diffusion is an order of magnitude smaller than advection, except near the top and bottom. Relatively large horizontal diffusion exists in the cores, which tends to decrease the strong horizontal temperature gradient in the cores. The vertical diffusion is very weak in the cores due to the small vertical temperature gradient there. However, it is strong near the top and bottom, tending to decrease the vertical temperature gradient there.

The above analysis has shown that advection, or the "splash" of cold air at the bottom of downdrafts, is essential in maintaining the mid-level stable layer. The vigorous small-scale convection around the lower part of downdrafts is limited under the local stable layer (see Fig. 4.35, or CKE in Fig. 4.22). Small-scale cells transport heat vertically, and deposit the heat in the stable layer. This kind of stable layer which is generated and maintained by motion seems unusual in the atmosphere, since with such a strong cloud-top cooling, observations often show that the PBL is well mixed. However, Rothermel and Agee (1980) did observe that the air-sea temperature difference changes under one closed cell, i.e., at 100 m above sea surface, the air temperature is colder than the SST near downdrafts, and warmer than the SST at the cell center. This observation supports our mechanism that cold parcels originated from cold downdrafts are gradually warmed up when they move towards the cell center, either by surface heating, internal heating, or diffusion. As long as there is a stable layer in the middle of PBL, such as that discussed in last section, the mechanism discussed in our trajectory analysis can work.

The mesoscale contributions to these terms are very distinctive. There is still warm horizontal advection near the top. However, it is located at both sides of the cold cores, which tends to build up the temperature gradient above the cores, or to enhance negative buoyancy there. The vertical advection now has the same sign as the horizontal advection. At the upper part, it advects warm air at where warm horizontal advection occurs, and also advects cold air inside the core. The total mesoscale advection then enhances the horizontal temperature gradient, or negative buoyancy, at the top where the cold cores are rooted, and destabilizes the stratification inside the cores. Therefore, mesoscale advection enhances the strength of the downdrafts, which in turn provide more energy to generate updrafts. This is just what we expect in convection. The mesoscale horizontal diffusion is an order of magnitude smaller than other mesoscale terms. The vertical mesoscale diffusion, however, is of the same magnitude as the mesoscale advection terms.

The analysis above tells us that, first, the mesoscale advection is as important as mesoscale diffusion. This difference from the weakly nonlinear theory, in which diffusion is required to be an order of magnitude larger than advection, explains why a very asymmetric cell cannot be found by the weakly nonlinear theory. Second, mesoscale advection enhances the downdrafts by increasing the horizontal temperature gradient above and destabilizing the vertical static stability of downdrafts. Therefore, once a mesoscale circulation is initiated by the mechanism we discussed, it will strengthen itself by enhancing the strength of the downdrafts, until a steady state is reached.

4.4.4 The sensitivity of the results to horizontal domain size

To see whether the scale of our mesoscale cells are artificially selected by the domain size, we ran three cases with all parameters exactly the same as case 1, except that the horizontal domain size was changed to 16 km, 64 km and 128 km, respectively. The potential temperature and stream function distributions are shown in Figs. 4.37 and 4.38, respectively. It is obvious that the number of cells doubles with a doubling of horizontal domain size. There are 2, 4, 8, and 16 cells for horizontal domain sizes of 16, 32, 64 and 128 km, respectively. The magnitudes of potential temperatures and stream functions are the same, and their detailed structures are very similar. Therefore, we can conclude that the size and pattern of the cells obtained do not depend on the horizontal domain size in our model.

4.4.5 Discussion

Based on the above analysis, we can provide a conceptual model for the generation of MCC, as shown in Fig. 4.39: Cloud-top cooling constantly generates small-scale convection. A weak inversion, such as a cloud-base inversion, exists inside the PBL. The strongest downdrafts bring cold air from the top to the bottom. Cold air moves both vertically and horizontally. At the same time, this cold air is warmed up by surface heating, internal heating, or diffusion in the lower part of the PBL. The less cold parcels in this cold air may gain buoyancy by the warming in a short time, and flow into other small-scale cells. However, those extremely cold parcels may need a longer time to be warmed up to finally be able to rise through the stable layer. During the time they are

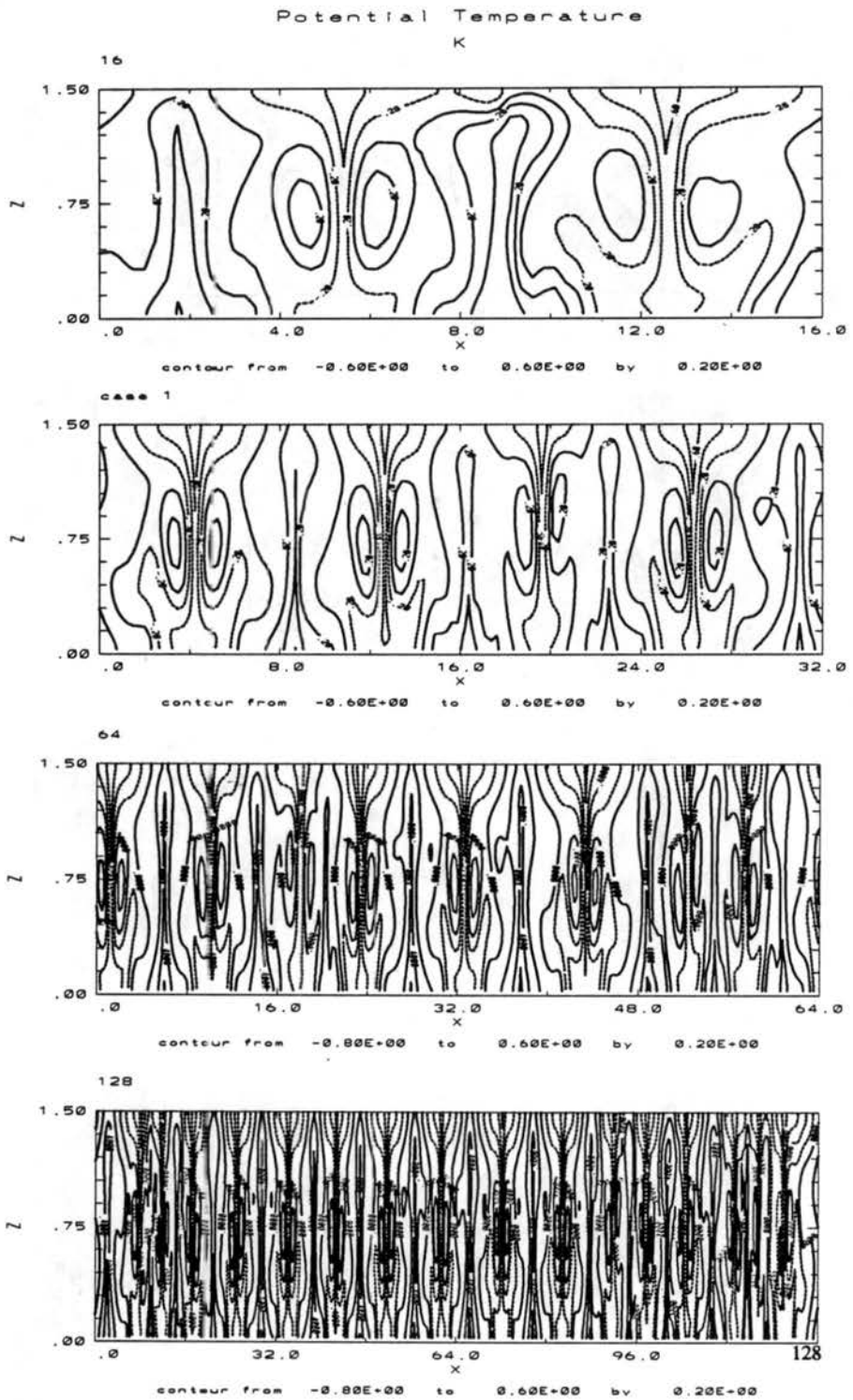

FIGURE 4.37: The potential temperature distribution for the different domain sizes for case 1. Note the difference of the horizontal scale between different panels.

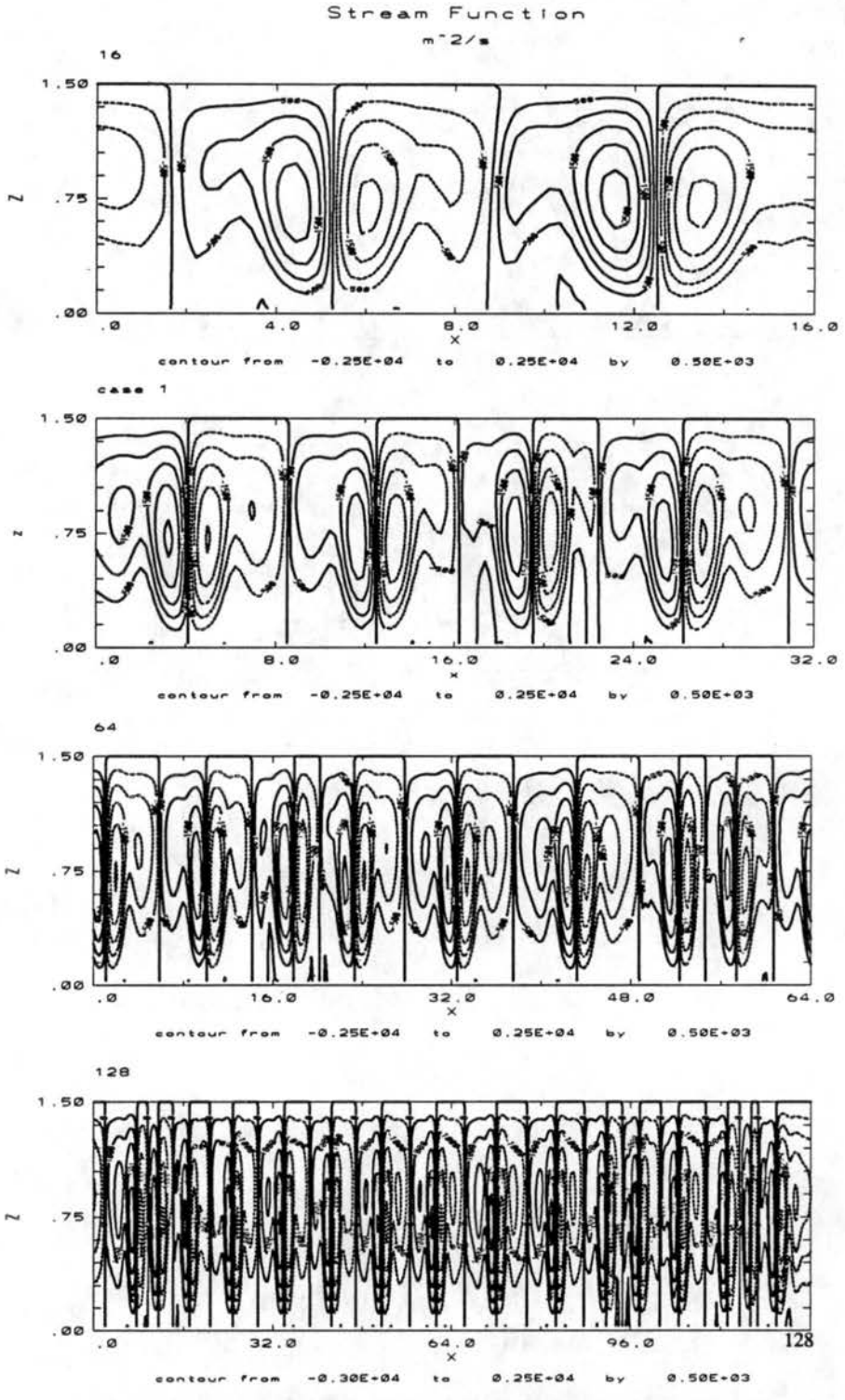

FIGURE 4.38: The stream function for the different domain sizes for case 1. Note the difference of horizontal scale between different panels.

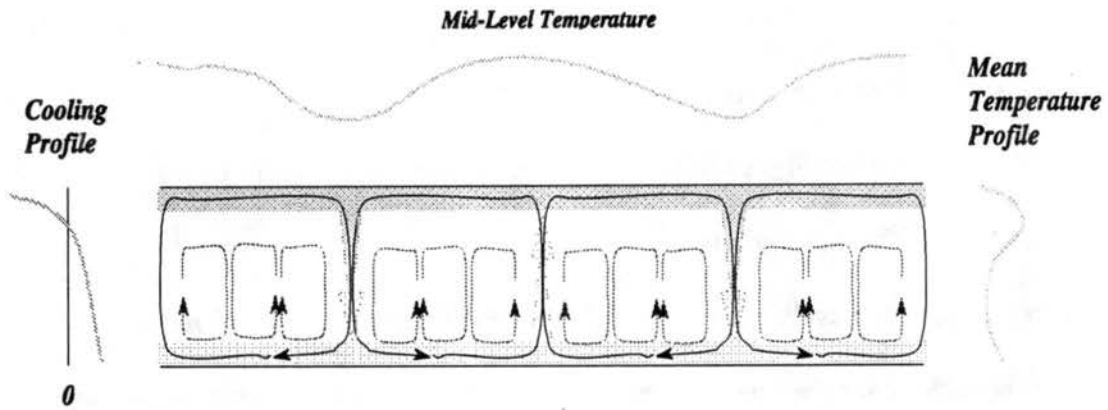

FIGURE 4.39: A conceptual model for closed MCC. See discussion in the text.

warmed up, they may move up somewhat due to a small warming, but be pushed down by other weaker downdrafts when the parcels' buoyancy is consumed by the stable layer. In this way, small-scale convection deposits heat into the weak inversion layer. However, the parcels remain in quasi-horizontal motion, so that when they are finally warm enough to rise through the stable layer by an updraft of another small-scale cell, they have moved a mesoscale distance horizontally. In this way, mesoscale convection is maintained. Near cloud top, cold parcels transported by the mesoscale circulation may join small-scale circulations at anytime, when they have enough negative buoyancy to sink. On the other hand, warm parcels from updrafts of small-scale cells may also join the mesoscale advection near cloud top at any time, and experience cloud-top cooling. Nevertheless, mesoscale advection near cloud top may statistically, in a Reynolds-averaged sense, "move" cold parcels to downdrafts which generate CKE for both small-scale and

mesoscale circulations, enhance the downdrafts, and therefore enhance the mesoscale circulation, until a steady state is reached.

Nonlinear processes are crucial in this mechanism. These processes include the counter-gradient transport of heat, and mesoscale horizontal advection. The nonlinear processes explain why asymmetric internal heating, or cloud-top cooling, is essential to generate MCC, and a relatively more asymmetric heating, or stronger cloud-top cooling, can generate relatively broader MCC. This is because the vertical motion of cold parcels can be limited by the inversion maintained by the counter-gradient transport of heat, and then can stay near the bottom longer. This permits a parcel to move over a mesoscale distance due to horizontal advection.

It is also shown from our numerical results that a constant heat flux boundary condition may not be necessary for the formation of MCC, although it can give a mesoscale mode in the linear analysis as emphasized by Fiedler (1985). Under a constant heat flux boundary condition without internal heating, only small-scale cells are present (Fig. 4.13).

The neglect of nonlinear processes may be one of the reasons that Fiedler could not obtain MCC in some of his studies. Fiedler (1993) claimed that a three-dimensional model is necessary to simulate MCC. This may be true for a low-Rayleigh-number case ($R_a/R_{ac} < 10$). A low-Rayleigh-number case is comparable to our weakly nonlinear case, in which linear processes may work at the leading order. Nonlinear motions may be harder to develop in the 2-D case than in 3-D case. As discussed in section 4.3.4, the dominance of linear processes requires a large diffusion coefficient. This may be why an

unusually large diffusion coefficient was required by Fiedler to explain some of his theoretical and numerical results (Fiedler, 1985; van Delden, 1985b; Fiedler, 1989). One of the reasons that Fiedler preferred to use low Rayleigh numbers in his simulations is that the convective heat flux carried by MCC is generally small, and hence mesoscale convection is weak and could be slightly supercritical (Fiedler, 1989). However, in the mechanism we have discovered, these mesoscale motions cannot be separated from the small-scale motions. Mesoscale motions result from interactions between the basic state and small-scale convection. The mechanism for the open MCC generated by latent heat release, as reviewed in the introduction, also relies on interactions between the basic state and the small-scale convection generated from a warm surface. Therefore, it is more reasonable to study MCC with a large Rayleigh number so that it can develop in a more realistic fully nonlinear environment, as in our study. Other works, such as those of Helfand and Kalnay (1983) and Rothermel and Agee (1986), also point in this direction.

Our mechanism may be applicable to the atmosphere, even though it has been found by using our simple idealized model. The only two basic requirements for this mechanism to work are cloud-top cooling, which is required to generate turbulence, and a stable layer in the middle of the PBL, which can suppress vertical motion in small eddies. Cloud-top cooling is produced by radiative cooling and evaporative cooling, and the stable layer may be the weak cloud-base inversion, or an inversion like the one shown in Fig. 4.33. These features are observed in the STBL quite often. Moreover, this model also agrees with observations in other aspects:

(1). Mesoscale components of the horizontal wind, temperature and moisture are observed more often than in vertical velocity (e.g., Rothermel and Agee, 1980; Nucciarone and Young, 1991). In our model, the mesoscale downdraft can be associated with the downdraft of one small cell, and the mesoscale updraft can be associated with the updraft of another small cell. Therefore it is hard to observe by aircraft.

(2). Mesoscale cloud patterns are composed of small-scale cumuli, as mentioned at the very beginning of this chapter (Krueger Fritz, 1961; Hubert, 1966). The coexistence of small-scale and mesoscale convection in our model allows this pattern to appear.

(3). Closed MCC is observed over both cold and warm water, and appears most frequently over cold water (e.g., Agee, 1987). This also agrees with our model. A warm surface may not destroy closed MCC, as long as it is not so warm as to regenerate the positive buoyancy of very cold parcels in a very short time, or over a very short distance. Cold water permits the easier development of closed MCC. Even if surface warming is strong, closed MCC still has a chance to develop, as long as the inversion inside the PBL is also strong enough.

Due to the simplicity of our model, we cannot test the relative importance of radiative cooling and evaporative cooling. Also, the effects of latent heating in clouds are not included. Large scale convergence is not yet considered, nor the importance of a large-scale prevailing flow. However, the qualitative agreement of our model with observations is very encouraging.

4.5 Conclusions

The role of cloud-top cooling in the formation of closed MCC has been studied both theoretically and numerically by means of a simple 2-D nonlinear model. The theoretical results obtained by weakly nonlinear methods show that cooling at the top favors the formation of closed MCC. However, the asymmetry of the cells is limited by the weakly nonlinear assumption. Fully nonlinear numerical simulations show that nonlinear processes are very important for generating MCC. The relation between cloud-top cooling and MCC is revealed in our model results. Basically, MCC appears only when the internal heating is asymmetric. A more asymmetric heating results in broader MCC. Without asymmetric internal heating, constant heat flux boundary conditions cannot generate MCC. Further experiments are required to see if a constant heat flux boundary condition is necessary, as suggested by linear theory.

Based on our model results, we have suggested a mechanism for the formation of closed MCC. Cloud-top cooling, together with a weak stable layer inside the PBL, offer a favorable state for the formation of closed MCC. Cloud-top cooling generates small-scale turbulence, while the weak stable layer suppresses small-scale convection of very cold parcels. Mesoscale motion is initiated by the horizontal motion of the cold parcels. Once mesoscale convection has been initiated, mesoscale advection increases the negative buoyancy at the tops of downdrafts, enhancing the downdrafts, helping to build up the potential energy which is lost in the sinking motion, and further enhancing the closed MCC.

This conceptual model agrees qualitatively with observations in many aspects, and therefore may be applicable to the atmosphere. This mechanism allows cloud-top cooling, surface heating, and heating/cooling inside the STBL, such as solar warming and drizzling, which are all often observed in the STBL, to work together to generate and maintain MCC.

The improvement of our model is a goal for the future. We want to include moisture, more realistic boundary conditions, large scale convergence, and even cloud microphysics. Other studies, such as running an existing complicated model to ascertain more realistically the effects of radiative and evaporative cooling, or to run a 3-D model to see the differences between 2-D convection and 3-D convection, would also be extensions of the present work.

CHAPTER 5

Conclusions and Future Research

5.1 Conclusions

The cloud-top processes, by our definition, include cloud-top radiative cooling, entrainment mixing warming, and evaporative cooling. Their effects on both small-scale and mesoscale convection in the stratocumulus-topped boundary layer (STBL) have been studied analytically, numerically, as well as through data analysis. The review in chapter 1 has shown that cloud-top processes can drive convection in STBL, and are important for determining the STBL's structure. Their effects on small-scale convection have been studied in chapters 2 and 3, and their effects on mesoscale convection have been studied in chapter 4.

The cloud-top processes are first studied in terms of "bulk" properties in chapter 2. Turbulent fluxes generated by these processes are parameterized in terms of the "jumps" of the related mean-state quantities across the entrainment layer. Besides the jumps, two parameters are introduced into our parameterization: One is the entrainment rate, E. This parameter represents the effects of all the processes that contribute to the turbulent fluxes near cloud-top, such as turbulence driven from below, local wind shear, cloud-top

radiative cooling, evaporative cooling due to entrainment mixing, and strength of inversion. The other is the "bulk" mixing fraction, χ_E. This parameter represents the fraction of free atmosphere air entrained from above inversion in downdrafts. It is obvious that χ_E is related to E. However, by introducing χ_E as an independent parameter, the effects of cloud-top processes on other properties, such as the fractional cloudiness, the convective mass flux, the mean structure and turbulent fluxes inside the STBL, are explicitly represented in terms of χ_E and E in our analytical model. Therefore, as a first step, we have avoided detailed description of the cloud-top processes at micro-scales (~10 m), such as the dependence of radiative cooling on the local liquid water content, and evaporative cooling in a single parcel. This parameterization has been tested using a set of LES data.

By using the entrainment layer and surface layer as the "boundaries" of the STBL, we have developed an analytical second-order bulk boundary-layer model which is able to determine the structures of cloud and subcloud layers, as well as fractional cloudiness. For the first time we have determined the fractional cloudiness analytically based on physics, although the results need further testing against observations or LES results.

Further detailed analyses of cloud-top processes on the micro-scale are given in chapter 3. The LES field that was used to test the parameterization in chapter 2 is used here for the detailed analysis. We first defined the mixing fraction for each parcel, χ. Based on the definition of χ, we systematically developed a method which can distinguish the effects of cloud-top radiative cooling, evaporative cooling, and entrainment warming. We further investigated mixing processes, as well as the physical

meaning of χ_E, as used in last chapter. In a case study, we found from the LES-generated STBL that the relative importance of cloud-top radiative cooling and evaporative cooling depends on the mixing fraction, χ. As an average for downdrafts, radiative cooling dominates over evaporative cooling in this simulated case.

The work in chapters 2 and 3 has shown that cloud-top processes can drive small-scale convection. It has not answered yet, however, whether or not cloud-top processes can drive mesoscale convection. Chapter 4 concentrates on this problem. Through both analytical and numerical studies by means of the 2-D Boussinesq equations, we found that cloud-top cooling can generate closed MCC. Nonlinear processes, which are shown as the mesoscale advection and the interactions between convection and basic state, are also crucial for generating and maintaining closed MCC. Based on our results, we proposed a conceptual model for the formation of closed MCC. Cloud-top cooling is required to generate TKE, as well as to provide cold parcels which can reach the bottom of the STBL. A weak stable layer inside STBL is required to suppress small-scale convection, and allow mesoscale convection to develop. The cold parcels must move horizontally a mesoscale distance before they gain enough buoyancy to penetrate through the stable layer. Once mesoscale circulation is formed, its advection helps to maintain narrow cold downdrafts, which in turn support the mesoscale convection.

The two ingredients of our conceptual model, i.e., cloud-top cooling and a weak stable layer inside STBL, are common in the atmosphere. The cloud-top cooling can be radiative cooling and/or evaporative cooling. The weak stable layer can be the cloud-base inversion produced by either solar radiation or drizzle. The model agrees qualitatively

with observations in many respects, especially in that it allows closed MCC to occur over a warm ocean. Therefore this model, for the first time, suggests how the processes that are often observed in an STBL, such as infrared radiative cooling, solar radiative heating, entrainment, drizzling, and surface heating, can work together to explain the formation of closed MCC. Among these processes, however, cloud-top cooling is the only process that generates TKE for closed MCC.

To summarize, cloud-top cooling can drive both small-scale and mesoscale convection in the STBL. The effects of small-scale convection, generated by cloud-top processes, on the STBL structure can be parameterized in our analytical model. Detailed analysis of cloud-top cooling showed that downdrafts at cloud top are mainly generated by the cooling. Nonlinear processes must be involved to transfer small-scale TKE generated by cloud-top cooling to mesoscale TKE. This anti-cascade of TKE is not due to the nonlinear processes inherent in 2-D turbulence. Rather, it is a result of interactions between convection and the basic state. Therefore, it should also occur in 3-D convection.

5.2 Future research

5.2.1 The second-order bulk boundary-layer model

The analytical second-order bulk boundary-layer model has been built in an attempt to parameterize the PBL for large-scale models, as well as to understand the physics of complex situations. Before this model is practically useful, we need to further understand several parameters in the model.

The key parameters for surface and entrainment layers are χ_V, V, χ_E, and E, as explained in chapter 2. When σ and M_c are assumed to be independent of height, the values of χ_V and χ_E can be obtained analytically, which in turn allows σ and M_c to be solved analytically. However, ambiguity exists in the expressions of χ_V and χ_E. We need further observational or LES data to add more constraints on χ_V and χ_E.

Furthermore, the model should allow σ and M_c to vary with height. This is possible as long as the dissipation rate in the entrainment layer and surface layer is known, as discussed in Appendix A. Further study is needed to see whether or not the dissipation rates in the entrainment layer and surface layer can be represented in terms of a constant parameter, as assumed in the derivation.

Another parameter which is related to dissipation inside the PBL, is the dissipation time scale, τ_{dis}. This parameter is critical for determining the fluxes and mean structure inside the PBL, the PBL depth, fractional cloudiness, and convective mass flux in our model. How this parameter is determined for different situations in the atmosphere is also a remaining problem.

Once these parameters have been determined for different kinds of atmospheric PBL, the final step of the work is to apply the model to a large-scale model as parameterization of the PBL.

5.2.2 MCC

The nonlinear 2-D Boussinesq model helped us to physically understand the effects of cloud-top cooling on mesoscale convection. However, this model is very idealized, and most importantly, it does not include cloudiness, except that "cloud-top" cooling is included by an imposed internal heating profile. Several paths of research can be followed from here.

5.2.2.1 Upgrading the present model

The model discussed in chapter 4 can be upgraded step by step, as follows.

(1) We add moisture, and still prescribe the internal heating/cooling profile. The appearance of clouds may affect buoyancy at the upper part of PBL.

(2) Based on (1), we add cloud-top entrainment. The entrainment warming may partly balance cloud-top cooling, as discussed in chapters 1 and 3, and therefore may slow down the convection generated by cloud-top cooling.

(3) Based on (2), we add interactive radiation. Interactive radiation can determine the cloud-top radiative cooling and cloud-base warming, so that they do not need to be prescribed anymore. At this point, the mechanism we suggested in our conceptual model in chapter 4 can be fully tested.

(4) As an extra step, we may add subgrid-scale condensation. Subgrid-scale condensation can give detailed cloud-top evaporative cooling and drizzling effects.

Moreover, the study may not be limited to the PBL with large cloud amounts. A PBL with small cloud amounts may also be studied by this model.

5.2.2.2 Using an existing model

Instead of upgrading our simple model, we can also use an existing complicated model. We have been using the cloud ensemble model (CEM) developed by Krueger (1985, 1988) to study MCC. This model includes all of the physics that we plan to include in future versions of our simple model. Further study may be based on this model.

5.2.2.3 Developing a 3-D model

Although MCC can be studied in a 2-D framework, it nevertheless is a 3-D phenomenon. To prove that the mechanism we suggested is realistic for the atmosphere, a 3-D simulation is necessary. We expect that a 3-D model can still show closed MCC as long as a suitable basic state is given.

5.2.3 Other aspects

One of the purposes of studying MCC is to understand under what conditions the clouds transit from a solid deck to broken pattern, and finally to small cumuli. The PBLs of these different cloud regimes are very different, and so are the heat and moisture fluxes. Closed MCC may be one of the transient states between a solid cloud deck and small cumuli, as shown in Fig.1.2. We have tried to understand how a solid cloud deck is broken into mesoscale cloud patches. Further study is necessary to understand how these

mesoscale cloud patches are broken into cumuli. Therefore, after MCC is further understood, we may extend our research to the trade-wind-cumulus PBL. The data we obtained during ASTEX may be used for this study.

References

Agee, E. M., 1984: Observations from space and thermal convection - a historical perspective. *Bull. Am. Meteor. Soc.*, **65**, 938-949.

Agee, E. M., 1987: Mesoscale cellular convection over the oceans. Dyn. *of Atmos. and Oceans*, **10**, 317-341.

Agee, E. M., and T.S. Chen, 1973: A model for investigating eddy viscosity effects on mesoscale cellular convection. *J. Atmos. Sci.*, **30**, 180-189.

Agee, E. M., T.S., Chen, and K.E. Dowell, 1973: A review of mesoscale cellular convection. *Bull. Amer. Met. Soc.*, **54**, 1004-1012.

Agee, E. M., and K. E. Dowell, 1974: Observational studies of mesoscale cellular convection. *J. Appl. Met.*, **13**, 46-53.

Agee, E. M., and F.E. Lomax, 1978: Structure of the mixed layer and inversion layer associated with patterns of mesoscale cellular convection during AMTEX 75. *J. Atmos. Sci.*, **35**, 2281-2301.

Albrecht, B. A., 1979: A model of the thermodynamic structure of the trade-wind boundary layer: Part II. Applications. *J. Atmos. Sci.*, **36**, 90-98.

Albrecht,, B. A., 1991: Fractional cloudiness and cloud-top entrainment instability. *J. Atmos. Sci.*, **48**, 1519-1525.

Albrecht, B. A., R. S. Penc, and W. H. Schubert, 1985: An observational study of cloud-topped mixed layers. *J. Atmos. Sci.*, **42**, 800-822.

Albrecht, B. A., D. A. Randall, and S. Nicholls, 1988: Observations of marine stratocumulus clouds during FIRE. *Bull. Am. Meteor. Soc.*, **69**, 618-626.

Antonia, R. A., and A. J. Chambers, 1978: Note on the temperature ramp structure in the marine surface layer. *Bound.-Layer Meteor.*, **15**, 347-355.

Antonia, R. A., A. J. Chambers, C. A. Friehe, and C. W. Van Atta, 1979: Temperature ramps in the atmospheric surface layer. *J. Atmos. Sci.*, **36**, 99-108.

Antonia, R. A., S. Rajagopalan and A. J. Chambers, 1983: Conditional sampling of turbulence in the atmospheric surface layer. *J. Climate Appl. Meteor.*, **22**, 69-78.

Arakawa, A., 1966: Computational design for long-term numerical integration of the equations of fluid motion: Two-dimensional incompressible flow. Part I., *J. Comp. Phys.*, **1**, 119-143.

Arakawa, A., 1969: Parameterization of cumulus convection. Proc. WMO/IUGG Symp. Numerical Weather Prediction, Tokyo, 26 November - 4 December, 1968, *Japan Meteor. Agency. IV*, **8**, 1-6.

Arakawa, A., 1975: Modeling clouds and cloud processes for use in climate models. In The Physical Basis of Climate and Climate Modelling. *GARP Publications Series* **No. 16**, 181-197, ICSU/WMO, Geneva.

Asai, T., 1967: On the characteristic of cellular cumulus convection. *J. Met. Soc. Japan*, **45**, 251-260.

Asai, T., and I. Nakasuji, 1977: On the prefered mode of cumulus convection in a conditionally unstable atmosphere. *J. Met. Soc. Japan*, **55**, 151-167.

Asai, T., and I. Nakasuji, 1982: A further study of the prefered mode of cumulus convection in a conditionally unstable atmosphere. *J. Met. Soc. Japan*, **60**, 425-431.

Baker, M. B., and J. Latham, 1979: The evolution of the droplet spectra and the rate of production of embryonic raindrops in small cumulus clouds. *J. Atmos. Sci.*, **36**, 1612-1615.

Ball, F. K., 1960: Control of inversion height by surface heating. *Quart. J. Roy. Meteor. Soc.*, **80**, 339-358.

Benoit, R., 1976: *A comprehensive parameterization of the atmospheric boundary layer for general circulation models*. Ph.D. dissertation, McGill University, and National Center for Atmospheric Research cooperative thesis No. 39, 278 pp.

Betts, A. K., 1973: Non-precipitating cumulus convection and its parameterization. *Quart. J. Roy. Meteor. Soc.*, **99**, 178-196.

Betts, A. K., 1983: Thermodynamics of mixed stratocumulus layers: Saturation point budgets. *J. Atmos. Sci.*, **40**, 2655-2670.

Betts, A. K., 1985: Mixing line analysis of clouds and cloudy boundary layers. *J. Atmos. Sci.*, **42**, 2751-2763.

Betts, A. K., 1989: Idealized stratocumulus model for cloud layer thickness. *Tellus*, **41A**, 246-254.

Betts, A. K., and B. A., Albrecht, 1987: Conserved variable analysis of boundary layer thermodynamic structure over the tropical oceans. *J. Atmos. Sci.*, **44**, 83-99.

Betts, A. K., and R. Boers, 1991: A cloudiness transition in a marine boundary layer. *J. Atmos. Sci.*, **47**, 1480-1497.

Bjerknes, J., 1938: Saturated ascent of air through a dry-adiabatically descending environment. *Quart. J. R. Met. Soc.*, **64**, 325-330.

Blaskovic, M., R. Davies, and J. B. Snider, 1991: Diurnal variation of marine stratocumulus over San Nicolas island during July 1987. *Mon. Wea. Rev.*, **119**, 1469-1478.

Bluth, R. T., and B. A. Albrecht, 1993: ASTEX and MAGE June 1992 experiment summary. Part I - Mission summaries. Pennsylvania State University, Department of Meteorology, 286pp.

Bougeault, P., 1985: The diurnal cycle of the marine stratocumulus layer: A higher-order model study. *J. Atmos. Sci.*, **42**, 2826-2843.

Brandt, A., 1977: Multi-level adaptive solutions to boundary-value problems. *Math. Comp.*, **31**, 333-390.

Bretherton, C. S., 1987: A theory for non-precipitating moist convection between two parallel plates. Part I: Thermodynamics and "linear" solutions. *J. Atmos. Sci.*, **44**, 1809-1827.

Bretherton, C. S., 1988: A theory for nonprecipitating convection between two parallel plates. Part II: Nonlinear theory and cloud field organization. *J. Atmos. Sci.*, **45**, 2391-2415.

Bretherton, C. S., 1993: Marine boundary layer dynamics during ASTEX. *Presented at the ECMWF/GCSS Workshop on Parameterization of the Cloud Topped Boundary Layer, June, 1993*. Atmospheric Science Department, University of Washington, Seattle.

Brost, R. A., D. H. Lenschow, and J. C. Wyngaard, 1982a: Marine stratocumulus layers. Part I: Mean conditions. *J. Atmos. Sci.*, **39**, 800-817.

Brost, R. A., J. C. Wyngaard, and D. H. Lenschow, 1982b: Marine stratocumulus layers. Part II: Turbulence budgets. *J. Atmos. Sci.*, **39**, 818-836.

Brugge, R., and M.W. moncrieff, 1985: The effect of physical processes on numerical simulations of two dimensional cellular convection. *Beitr. Phys. Atmos.*, **58**, 417-440.

Burden, R.L., and J.D. Faires, 1985: *Numerical analysis*. Prindle, Weber & Schmidt. 676pp.

Burt, W. V., and E. M. Agee, 1977: Buoy and satellite observations of mesoscale cellular convection during AMTEX 75. *Bound.-layer Meteor.*, **12**, 3-24.

Businger, J. A., J. C. Wyngaard, Y. Izumi, and E. F. Bradley, 1971: Flux-profile relationships in the atmospheric surface layer. *J. Atmos. Sci.*, **18**, 181-189.

Cahalan, R. F., and J. B. Snider, 1989: Marine stratocumulus structure. *Remote Sens. Environ.*, **28**, 95-107.

Caughey, S. J., and S. G. Palmer, 1979: Some aspects of turbulence structure through the depth of the convective boundary layer. *Quart. J. Roy. Meteor. Soc.*, **105**, 811-827.

Caughey, S. J., B. A. Crease, and W. T. Roach, 1982: A field study of nocturnal stratocumulus: II. Turbulence structure and entrainment. *Quart. J. Roy. Meteor. Soc.*, **108**, 125-144.

Caughey, S. J., and M. Kitchen, 1984: Simultaneous measurements of the turbulent and microphysical structure of nocturnal stratocumulus cloud. *Quart. J. Roy. Meteor. Soc.*, **110**, 13-34.

Chandrasekhar, S., 1961: *Hydrodynamic and hydromagnetic stability.* Oxford at the Clarenton Press. 654 pp.

Chapman, C.J., and M.R.E. Proctor, 1980: Nonlinear Rayleigh-Benard convection with poorly conducting boundaries. *J Fluid Mech.*, **101**, 759-782.

Chatfield, R. B., and R. A. Brost, 1987: A two-stream model of the vertical transport of trace species in the convective boundary layer. *J. Geophys. Res.*, **92**, 13263-13276.

Chen, C., and W. R. Cotton, 1983: A one-dimensional simulation of the stratocumulus-capped mixed layer. *Bound.-Layer Meteor.*, **25**, 289-293.

Childress, S., M. Levandowsky, and E.A. Spiegel, 1975: Pattern formation in a suspension of swimming micro-organisms: equations and stability theory. *J. Fluid Mech.*, **63**, 591-613.

Chlond, A., 1988: Numerical and analytical studies of diabatic heating effect upon flatness of boundary layer rolls. *Beitr. Phys. Atmos.*, **61**, 312-329.

Clark, T., T. Hauf, and J.P. Kuttner, 1986: Convectively forced internal gravity waves: results from two-dimensional numerical experiments. *Quart. J. R. Met. Soc.*, **112**, 899-925.

Coulman, C. E., 1978: Boundary-layer evolution and nocturnal inversion dispersal, Part II. *Bound. Layer Meteor.*, **14**, 493-513.

Cox, S., C. Cornwall, W. Cotton, J. Davis, J. Kleist, T. McKee, Q. Shao, D. Randall, W. Schubert, D. Wood, S. Frisch, M. Hardesty, R. Kropfli, J. Snider and P. Anikin, 1993: CSU/NOAA-WPL FIRE II - ASTEX field experiment: Description of field deployment phase. *Atmos. Sci. Paper No. 523*, Colorado State University, Ft. Collins, Colorado, 100pp.

Cox, S., S. Gillies, A. Heidinger, and C. Keith, 1993: CSU ASTEX surface data sets from Porto Santo (June 1-28, 1992). *Atmos. Sci. Paper No. 530*, Colorado State University, Ft. Collins, Colorado, 140pp.

Curry, J. A., 1986: Interactions among turbulence, radiation and microphysics in arctic stratus clouds. *J. Atmos. Sci.*, **43**, 90-106.

Deardorff, J. W., 1972: Parameterization of the planetary boundary layer for use in general circulation models. *Mon. Wea. Rev.*, **100**, 93-106.

Deardorff, J. W., 1976: On the entrainment rate of a stratocumulus-topped mixed layer in a strong inversion. *Quart. J. Roy. Meteor. Soc.*, **102**, 563-582.

Deardorff, J. W., 1980: Cloud-top entrainment instability. *J. Atmos. Sci.*, **37**, 131-147.

Deardorff, J. W., 1981: On the distribution of mean radiative cooling at the top of a stratocumulus-capped mixed layer. *Quart. J. Roy. Meteor. Soc.*, **107**, 191-202.

Durran, D.R., 1991: The third-order Adams-Bashforth method: An attractive alternative to leapfrog time differencing. *Mon. Wea. Rev.*, **119**, 702-720.

Duynkerke, P. G., 1993: The stability of cloud top with regard to entrainment: amendment of the theory of cloud top entrainment instability. *J. Atmos. Sci.*, **50**, 495-502.

Fiedler, B.H., 1984: The mesoscale stability of entrainment into cloud-topped mixed layers. *J. Atmos. Sci.*, **41**, 92-101.

Fiedler, B.H., 1985: Mesoscale cellular convection: Is it convection? *Tellus*, **37A**, 163-175.

Fiedler, B.H., 1989: Scale selection in nonlinear thermal convection between poorly conducting boundaries. *Geophys. & Astrophys. Fluid Dyn.*, **46**, 191-201.

Fiedler, B.H., 1990: Transitions to broad cells in a nonlinear thermal convection system. *Geophys. & Astrophys. Fluid Dyn.*, **50**, 195-201.

Fiedler, B.H., 1993: Cell broading in three-dimensional thermal convection between poorly conducting boundaries. Will appear in *Beitr. Phys. Atmos.*, **66**, No. 3.

Fravalo, D., Y. Fouquart, and R. Rosset, 1981: The sensitivity of a model of low stratiform clouds to radiation. *J. Atmos. Sci.*, **38**, 1049-1062.

Frisch, A. S., and J. A.Businger, 1973: A study of convective elements in the atmospheric surface layer. *Bound.-Layer Meteor.*, **3**, 301-328.

Fulton, S.R., P.E. Ciesielski, and W.H. Schubert, 1986: Multigrid methods for elliptic problems: A review. *Mon. Wea. Rev.*, **114**, 943-959.

Greenhut, G. K. and S. J. S. Khalsa, 1982: Updraft and downdraft events in the atmospheric boundary layer over the equatorial Pacific Ocean, *J. Atmos. Sci.*, **39**, 1803-1818.

Grossman, R. L., 1984: Bivariate conditional sampling of moisture flux over a tropical ocean. *J. Atmos. Sci.*, **41**, 3238-3253.

Hamming, R.W., 1983: *Digital filters*. Prentice-Hall, Inc., 257pp.

Hanson, H. P., 1981: On mixing by trade-wind cumuli. J. Atmos. Sci., 38, 1003-1014.

Hanson, H., 1984: On mixed layer modelling of the stratocumulus topped marine boundary layer. *J. Atmos. Sci.*, **41**, 1226-1236.

Hanson, H.P., and P.L Gruber, 1982: Effect of marine stratocumulus clouds on the ocean-surface heat budget. *J. Atmos. Sci.*, **39**, 897-908.

Hardy, K.R., and H. Ottersten, 1969: Radar investigations of convective patterns in the clear atmosphere. *J. Atmos. Sci.*, **26**, 666-672.

Helfand, H.M., and E. Kalnay, 1983: A model to determine open or closed cellular convection. *J. Atmos. Sci.*, **40**, 631-650.

Hein, P. F., S. K. Cox, W. H. Schubert, C. M. Johnson-Pasqua, D. P. Duda, T. A. Guinn, M. Mulloy, T. B. McKee, W. L. Smith, and J. D. Kleist, 1988: The CSU tethered balloon data set of the FIRE marine stratocumulus IFO. *Dept. of Atmos. Sci. Paper No. 432*, Colorado State University, 33 pp.

Higgnett, P, 1991: Observations of diurnal variation in a cloud-capped marine boundary layer. *J. Atmos. Sci.*, **48**, 1474-1482.

Huang, X.Y., 1990: The organization of moist convection by internal gravity waves. *Tellus*, **42A**, 270-285.

Hubert, L.F., 1966: *Mesoscale cellular convection.* U.S. Dept. of Commerce, Environmental Science Services Administration, Meteorological Satellite Laboratory, Rept. No. 37.

Hurle, D.T.J., E. Jakeman, and E.R. Pike, 1967: On the solution of the Benard problem with boundaries of finite conductivity. *Proc. R. Soc.*, **A, 296**, 469-475.

James, D. G., 1959: Observations from aircraft of temperatures and humidities near stratocumulus clouds. *Quart. J. Roy. Meteor. Soc.*, **85**, 120-130.

Kahn, P. H., and J. A. Businger, 1979: The effect of radiative flux divergence on entrainment of a saturated convective boundary layer. *Quart. J. Roy. Meteor. Soc.*, **105**, 303-306.

Kaimal, J. C., 1974: Translation speed of convective plumes in the atmospheric surface

layer. *Quart. J. Roy. Meteor. Soc.*, **100**, 46-52.

Kaimal, J. C., and J. A. Businger, 1970: Case studies of a convective plume and a dust devil. *J. Appl. Meteor.*, **9**, 612-620.

Khalsa, S. J. S., 1980: Surface-layer intermittency investigated with conditional sampling. *Bound.-Layer Meteor.*, **19**, 135-153.

Khalsa, S. J. S., 1993: Direct sampling of entrainment events in a marine stratocumulus layer. *J. Atmos. Sci.*, **50**, 1734-1750.

Khalsa, S. J. S., and J. A. Businger, 1977: The drag coefficient as determined by the dissipation method and its relation to intermittent convection in the surface layer. *Bound.-Layer Meteor.*, **12**, 273-297.

Khalsa, S. J. S., and G. K. Greenhut, 1985: Conditional sampling of updrafts and downdrafts in the marine atmospheric boundary layer. *J. Atmos. Sci.*, **42**, 2550-2562.

Kondo, J., 1975: Air-sea bulk transfer coefficients in diabatic conditions. *Bound.-Layer Meteor.*, **9**, 91-112.

Konrad, T.G., 1970: The dynamics of the convective process in clear air as seen by radar. *J. Atmos. Sci.*, **27**, 1138-1147.

Kraus, P. H., and E. Schaller, 1978a: Steady-state characteristics of inversions capping a well-mixed PBL. *Bound.-Layer Meteor.*, **14**, 83-104.

Kraus, P. H., and E. Schaller, 1978b: A note on the closure in Lilly-type inversion models. *Tellus*, **30**, 284-288.

Krishnamurti, R., 1975a: On cellular cloud patterns. Part I: Mathematical model. *J. Atmos. Sci.*, **32**, 1353-1363.

Krishnamurti, R., 1975b: On cellular cloud patterns. Part II: Laboratory model. *J. Atmos. Sci.*, **32**, 1364-1372.

Krishnamurti, R., 1975c: On cellular cloud patterns. Part III: Aplicability of mathematical and laboratory models. *J. Atmos. Sci.*, **32**, 1373-1383.

Krueger, A.F., and S. Fritz, 1961: Cellular cloud patterns revealed by TIROS I. *Tellus*, **13**,1-7.

Krueger, S. K., 1985: Numerical simulation of tropical cumulus clouds and their interaction with the subcloud layer. Ph. D. thesis, University of California, Los Angeles, 205pp.

Krueger, S. K, 1988: Numerical simulation of tropical cumulus and their interaction with the subcloud layer. *J. Atmos. Sci.*, **45**, 2221-2250.

Krueger, S. K., 1993: Linear eddy modeling of entrainment and mixing in stratus clouds. *J. Atmos. Sci.*, **50**, 3078-3090.

Kuo, H.-C., and W. H. Schubert, 1988: Stability of cloud-topped boundary layers. *Quart. J. Roy. Meteor. Soc.*, **114**, 887-916.

Kuo, H.L., 1961: Convection in a conditionally unstable atmosphere. *Tellus*, **13**, 441-459.

Kuo, H.L., 1965: Further studies of the properties of cellular convection in a conditionally unstable atmosphere. *Tellus*, **17**, 413-433.

Lamb, R. G., 1978: A numerical simulation of dispersion from an elevated point source in the convective planetary boundary layer. *Atmos. Environ.*, **12**, 1297-1304.

Lee, T. F., J. Rosenthal, and R. A. Helvey, 1980: Coastal stratus phenomena observed by GOES satellite. *Preprints Second Conf. Coastal Meteorology.* Los Angeles, Amer. Meteor. Soc., 271-281.

LeMone, M. A., 1990: Some observations of vertical velocity skewness in the convective planetary boundary layer. *J. Atmos. Sci.*, **47**, 1163-1169.

Lenschow, D. H., and P. L. Stephens, 1980: The role of thermals in the convective boundary layer. *Bound. Layer Meteor.*, **19**, 509-532.

Lenschow, D. H., and P. L. Stephens, 1982: Mean vertical velocity and turbulence intensity inside and outside thermals. *Atmos. Env.*, **16**, 761-674.

Lilly, D.K., 1960: On the theory of disturbances in a conditionally unstable atmosphere. *Mon. Wea. Rev.*, **88**, 1-17.

Lilly, D. K., 1968: Models of cloud-topped mixed layers under a strong inversion. *Quart. J. Roy. Meteor. Soc.*, **94**, 292-309.

Lilly, D. K., and W. H. Schubert, 1980: The effects of radiative cooling in a cloud-topped mixed layer. *J. Atmos. Sci.*, **37**, 482-487.

Liu, W. T., K. B. Katsaros, and J. A. Businger, 1979: Bulk parameterization of air-sea exchanges of heat and water vapor including the molecular constraints of the interface. *J. Atmos. Sci.*, **36**, 1722-1735.

MacVean, M. K., 1993: A numerical investigation of the criterion for cloud-top entrainment instability. *J. Atmos. Sci.*, **50**, 2481-2495.

MacVean, M. K., and P. J. Mason, 1990: Cloud-top entrainment instability through small-scale mixing and its parameterization in numerical models. *J. Atmos. Sci.*, **47**, 1012-1030.

Mahrt, L., and J. Paumier, 1982: Cloud-top entrainment instability observed in AMTEX. *J. Atmos. Sci.*, **38**, 622-634.

Mahrt, L., and J. Paumier, 1984: Heat transport in the atmospheric boundary layer. *J. Atmos. Sci.*, **41**, 3061-3075.

Manton, M. J., 1977: On the structure of convection. *Bound. Layer Meteor.*, **12**, 491-503.

Moeng, C.-H., 1979: Stability of a turbulent layer cloud within the planetary boundary layer. Ph. D. dissertation. University of California, Los Angeles.

Moeng, C.-H., 1984: A large-eddy simulation model for the study of planetary boundary-layer turbulence. *J. Atmos. Sci.*, **41**, 2052-2062.

Moeng, C.-H., 1986: Large-eddy simulation of a stratus-topped boundary layer. Part I: Structure and budgets. *J. Atmos. Sci.*, **43**, 2886-2900.

Moeng, C.-H., and A. Arakawa, 1980: A numerical study of a marine subtropical stratus cloud layer and its stability. *J. Atmos. Sci.*, **37**, 2661 - 2676.

Moeng, C.-H., and D.A. Randall, 1984: Problems in simulating the stratocumulus-topped mixed layer with a third-order closure model. *J. Atmos. Sci.*, **41**, 1588 - 1600.

Moeng, C.-H., and R. Rotunno, 1990: Vertical-velocity skewness in the buoyancy-driven boundary layer. *J. Atmos. Sci.*, **47**, 1149-1162.

Moeng, C.-H., and U. Schumann, 1991: Composite structure of plumes in stratus-topped boundary layers. *J. Atmos. Sci.*, **48**, 2280-2291.

Moeng, C.-H., S.-H., Shen, and D. A., Randall, 1992: Physical processes within the nocturnal stratus-topped boundary layer. *J. Atmos. Sci.*, **49**, 2384-2401.

Moyer, K. A., and G. S. Young, 1991: Observations of vertical velocity skewness within the marine stratocumulus-topped boundary layer. *J. Atmos. Sci.*, **48**, 403-410.

Neiburger, M., 1960: The relation of air mass structure to the field of motion over the

Eastern North Pacific Ocean in summer. *Tellus*, **12**, 31-40.

Neiburger, M., D.S. Johnson, and C.-W. Chien, 1961: *Studies of structure of the atmosphere over the eastern Pacific ocean in summer. I. The inversion over the eastern north Pacific Ocean.* University of California Press.

Nicholls, S., 1984: The dynamics of stratocumulus: aircraft observations and comparisons with a mixed layer model. *Quart. J. Roy. Meteor. Soc.*, **110**, 783-820.

Nicholls, S., 1989: The structure of radiatively driven convection in stratocumulus. *Quart. J. Roy. Meteor. Soc.*, **115**, 487-511.

Nicholls, S., and J. Leighton, 1986: An observational study of the structure of stratiform cloud sheets: Part I. Structure. *Quart. J. Roy. Meteor. Soc.*, **112**, 431-460.

Nicholls, S., and J. D. Turton, 1986: An observational study of the structure of stratiform cloud sheets. Part II. Entrainment. *Quart. J. Roy. Meteor. Soc.*, **112**, 461-480.

Nieustadt, F. T. M and J. A. Businger, 1984: Radiative cooling near the top of a cloudy mixed layer. *Quart. J. Roy. Meteor. Soc.*, **110**, 1073-1078.

Nucciarone, J. J., and G. S. Young, 1991: Aircraft measurements of turbulence spectra and variance dissipation in the marine stratocumulus-topped boundary layer. *J. Atmos. Sci.*, **48**, 2382-2392.

Oerlemans, J., 1986: Convection in a conditionally unstable atmosphere: a re-investigation of Bjerknes' slice method. *Beitr. Phys. Atmos.*, **59**, 41-53.

Oliver, D. A., W. S. Lewellen, and G. G. Williamson, 1978: The interaction between turbulent and radiative transport in the development of fog and low-level stratus. *J. Atmos. Sci.*, **35**, 301-316.

Paluch, I. R., and D. H. Lenschow, 1991: Stratiform cloud formation in the marine boundary layer.*J. Atmos. Sci.*, **48**, 2141-2158.

Penc, R. S., and B. A. Albrecht, 1986: Parametric representation of heat and moisture fluxes in cloud-topped mixed layers. *Bound. Layer Meteor.*, **38**, 225-248.

Phong-Anant, D., R. A. Antonia, A. J. Chambers, and S. Rajagopalan, 1980: Features of the organized motion in the atmospheric surface layer. *J. Geophys. Res.*, **85**, 424-432.

Priestley, C. H. B., 1959: *Turbulent transfer in the lower atmosphere*. The University of Chicago Press, 130pp.

Priestley, C.H.B., 1963: Width-height ratio of large convection cells. *Tellus*, **14**, 123-124.

Ramanathan V., 1987a: The role of earth radiation budget studies in climate and general circulation research. *J. Geophys. Res.*, **92**, 4075-4095.

Ramanathan V., 1987b: Atmospheric general circulation and its low frequency variance: radiative influences. *Short and Medium-Range Numerical Weather Prediction.*, 151-175.

Rand, H.A., and C.S. Bretherton, 1993: The relevance of the mesoscale entrainment instability to the marine cloud topped atmospheric boundary layer. *J. Atmos. Sci.*, **50**, 1152-1158.

Randall, D. A., 1976: *The interaction of the planetary boundary layer with large-scale circulations.* Ph.D. Thesis, UCLA, 247 pp.

Randall, D. A., 1980 a: Conditional instability of the first kind, upside-down. *J. Atmos. Sci.*, **37**, 125-130.

Randall, D. A., 1980 b: Entrainment into a stratocumulus layer with distributed radiative

cooling. *J. Atmos. Sci.*, **37**, 148-159.

Randall, D. A., 1987: Turbulent fluxes of liquid water and buoyancy in partly cloudy layers. *J. Atmos. Sci.*, **44**, 850-858.

Randall, D. A., J. A. Abeles, and T. G. Corsetti, 1985: Seasonal simulations of the planetary boundary layer and boundary-layer stratocumulus clouds with a general circulation model. *J. Atmos. Sci.*, **42**, 641-676.

Randall, D. A., J. A. Coakley Jr., C. W. Fairall, R. A. Kropfli, and D. H. Lenschow, 1984: Outlook for research on subtropical marine stratiform clouds. *Bull. Amer. Meteor. Soc.*, **65**, 1290-1301.

Randall, D. A., Q. Shao, and C.-H. Moeng, 1992: A second-order bulk boundary-layer model. *J. Atmos. Sci.*, **49**, 1903 - 1923.

Ray, D., 1965: Cellular convection with nonisotropic eddies. *Tellus*, **17**, 434-439.

Rayment, R., and C. J. Readings, 1974: A case study of the structure and energetics of an inversion. *Quart. J. Roy. Meteor. Soc.*, **100**, 221-233.

Riehl, H., T. C. Yeh, J. S. Malkus, and N. E. LaSeur, 1951: The northeast trade of the Pacific Ocean. *Quart. J. Roy. Meteor. Soc.*, **77**, 598-626.

Roach, W. T., R. Brown, S. J. Caughey, B. A. Crease, and A. Slingo, 1982: A field study of nocturnal stratocumulus: I. Mean structure and budgets. *Quart. J. Roy. Meteor. Soc.*, **108**, 103-123.

Rogers, D., and J. W. Telford, 1986: Metastable stratus tops. *Quart. J. Roy. Meteor. Soc.*, **112**, 481-500.

Rosmond, T.E., 1973: Mesoscale cellular convection. *J. Atmos. Sci.*, **30**, 1392-1409.

Rothermal, J., and E.M., Agee, 1980: Aircraft investigation of mesoscale cellular convection during AMTEX 75. *J. Atmos. Sci.*, **37**, 1027-1040.

Rothermal, J., and E.M., Agee, 1986: A numerical study of atmospheric convective scaling. *J. Atmos. Sci.*, **43**, 1185-1197.

Sasaki, Y., 1970: Influences of thermal boundary layer on atmospheric cellular convection. *J. Meteorol. Soc. Japan*, **48**, 492-502.

Schaller, B., and H. Kraus, 1981: The role of radiation in an inversion-capped planetary boundary layer. *Bound.-Layer Meteoro.*, **20**, 497-513.

Schmidt, H., and U. Schumann, 1989: Coherent structure of the convective boundary layer derived from large-eddy simulations. *J. Fluid Mech.*, **200**, 511-562.

Schols, J. L. J., A. E. Jansen and J. G. Krom, 1985: Characteristics of turbulent structures in the unstable atmospheric surface layer. *Bound.-Layer Meteor.*, **33**, 173-196.

Schubert, W. H., 1976: Experiments with Lilly's c;oud-topped mixed layer model. *J. Atmos. Sci.*, **33**, 436 - 446.

Schubert, W. H., P. E. Ciesielski, T. B. McKee, J. D. Kleist, S. K. Cox, C. M. Johnson-Pasqua, and W. L. Smith, Jr., 1987: Analysis of boundary layer sounding data from the FIRE marine stratocumulus project. *Dept. of Atmos. Sci. Paper No. 419*, Colorado State University, 101 pp.

Schubert, W. H., S. Cox, T. McKee, D. Randall, P. Ciesielski, J. Kliest, and E. Stevens, 1992: Analysis of sounding data from Porto Santo island during ASTEX. *Atmos. Sci. Paper No. 512*, Colorado State University, Ft. Collins, Colorado, 100pp.

Schubert, W.H., J.S. Wakefield, E.J. Steiner, and S.K. Cox, 1979a: Marine stratocumulus convection. Part I: Governing equations and horizontally homogeneous solutions. *J. Atmos. Sci.*, **36**, 1286 - 1307.

Schubert, W.H., J.S. Wakefield, E.J. Steiner, and S.K. Cox, 1979b: Marine stratocumulus convection. Part II: Horizontally inhomogeneous solutions. *J. Atmos. Sci.*, **36**, 1308 - 1324.

Schumann, U., and C.-H. Moeng, 1991 a: Plume fluxes in clear and cloudy convective boundary layers. *J. Atmos. Sci.*, **48**, 1746 - 1757.

Schumann, U., and C.-H. Moeng, 1991 b: Plume budgets in clear and cloudy convective boundary layers. *J. Atmos. Sci.*, **48**, 1758 - 1770.

Shao, Q., and D.A. Randall, 1992: Stratocumulus simulations with a third-order closure model. *Preprints, Tenth Symposium on Turbulence and Diffusion*, September 29-October 2, 1992, Portland, Oregon.

Shao, Q., D. A. Randall, and C.-H. Moeng, 1993: Plume generation in the entrainment and ventilation layers. *J. Atmos. Sci.*, Submitted.

Shen, S., and C.-H. Moeng, 1993: Comparison of LES stratus-topped boundary flow with aircraft measurements. *Bound.-Layer Meteor.*, **65**, 29-53.

Sheu, P.J., and E.M. Agee, 1977: Kinematic analysis and air-sea heat flux associated with mesoscale cellular convection during AMTEX 75. *J. Atmos. Sci.*, **34**, 793-801.

Sheu, P.J., E.M. Agee, and J.J. Tribbia, 1980: A numerical study of physical processes affecting convective cellular geometry. *J. Met. Soc. Japan*, **58**, 489-499.

Siems, S. T., C. S. Bretherton, M. B. Baker, S. Shy, and R. T. Breidenthal, 1990: Buoyancy reversal and cloudtop entrainment instability. *Quart. J. Roy. Meteor. Soc.*, **116**, 705-

739.

Sykes, R. I., and D. S. Henn, 1988: On the numerical computation of two-dimensional convective flow. *J. Atmos. Sci.*, **45**, 1961-1964.

Slingo, A., R. Brown, and C. L. Wrench, 1982: A field study of nocturnal stratocumulus: III. High-resolution radiative and microphysical observations. *Quart. J. Roy. Meteor. Soc.*, **108**, 145-165.

Sparrow, E.M., R.J. Goldstein, and V.K. Jonsson, 1964: Thermal instability in a horizontal fluid layer: effect of boundary conditions and non-linear temperature profile. *J. Fluid Mech.*, **18**, 513-528.

Stommel, H., 1947: A summary of the theory of convection cells. *Annals of the New York Academy of Sciences*. **48**, 715-726.

Stowe, L.L., H.Y.M. Yeh, T.F. Eck, C.G. Wellemeyer, H.L. Kyle, and the Nimbus-7 Cloud Data Processing Team, 1989: Nimbus-7 global cloud climatology. Part II: First year results. *J. climate*, **2**, 671-709.

Suarez, M. J., A. Arakawa, and D. A. Randall, 1983: Parameterization of the planetary boundary layer in the UCLA general circulation model: Formulation and results. *Mon. Wea. Rev.*, **111**, 2224-2243.

Taylor, R. J., 1958: Thermal structures in the lowest layers of the atmosphere. *Aust. J. Phys.*, **11**, 168-176.

Telford, J. W., and S. K. Chai, 1980: A new aspect of condensation theory. *Pure Appl. Geophys.*, **118**, 720-742.

Twomey, S., 1983: Radiative effects in California stratus. *Beitr. Phys. Atmosph.*, **56**, 429-439.

Van Delden, A., 1985a: On the prefered mode of cumulus convection. *Beitr. Phys. Atmos.*, **58**, 202-219.

Van Delden, A., 1985b: Comments on mesoscale cellular convection: Is it convection? *Tellus*, **37A**, 487-488.

Wakefield, J.S., and W.H. Schubert, 1976: Design and execution of the marine stratocumulus experiment. Atmos. Sci. Pap. No. 256, Colorado State University, 74pp.

Wang, S., and B. A. Albrecht, 1986: A stratocumulus model with an internal circulation. *J. Atmos. Sci.*, **43**, 2374-2391.

Wang, S., and B. A. Albrecht, 1990: A mean-gradient model of the dry convective boundary layer. *J. Atmos. Sci.*, **46**, 126-138.

Wang, Q., and B. A. Albrecht, 1993: Observations of cloud-top entrainment in marine stratocumulus. Submitted to *J. Atmos. Sci.*

Wang, S., and Q. Wang, 1993: The effects of drizzle on the stratus-topped marine boundary layer in a one-dimensional higher-order turbulence closure model. Submitted to *J. Atmos. Sci.*.

Wilczak, J. M., 1984: Large-scale eddies in the unstably stratified atmospheric surface layer. Part I: Velocity and temperature structure. *J. Atmos. Sci.*, **41**, 3537-3550.

Wilczak, J. M., and J. A. Businger, 1984: Large-scale eddies in the unstably stratified atmospheric surface layer. Part II: Turbulent pressure fluctuations and the budgets of heat flux, stress and turbulent kinetic energy. *J. Atmos. Sci.*, **41**, 3551-3567.

WMO, 1956: *International Cloud Atlas*, Vol. 1, World Meteor. Organization, Geneva.

APPENDICES

A. Scalar Variance Budgets For the Ventilation and Entrainment Layers

In Section 3, we derived constraints on M_c and σ by forcing the convective mass flux model be consistent with the fluxes of ψ due to entrainment and ventilation. We now derive additional constraints by use of the conservation principle for $\overline{\psi'^2}$, as applied to the ventilation and entrainment layers.

Because $\overline{\psi}$ varies rapidly across the top of the ventilation layer and the base of the entrainment layer, there is vigorous variance production in these regions, but there is also rapid variance dissipation by small eddies. The variance budget for the ventilation layer can be approximated by

$$2\int_{z_{S-}}^{z_S} \varepsilon_\psi \rho dz = 2\,(F_\psi)_S\,(\overline{\psi_{S-}} - \overline{\psi_S}) - (\overline{\rho w'\psi'\psi'})_S \qquad \text{(A.1)}$$

The lhs of (A.1) represents dissipation. The first term on the rhs represents gradient production, and the second represents downward transport into the ventilation layer by triple correlations. We have neglected the terms representing the local time rate of change and advection by the mean flow.

Similarly, the variance budget for the entrainment layer can be expressed as

$$2\int_{z_B}^{z_{B+}} \varepsilon_\psi \rho dz = -\,(F_\psi)_B \Delta\overline{\psi} + (\overline{\rho w'\psi'\psi'})_B - E\,(\overline{\psi'^2})_B + 2\int_{z_B}^{z_{B+}} \overline{\psi' S_\psi'}\, dz \qquad \text{(A.2)}$$

The lhs and the first two terms on the rhs of (A.2) are closely analogous to those of (A.1). In the gradient production term of (A.2), the minus sign appears because of the definition of $\Delta\overline{\psi}$. The factor of two that appears in the production term of (A.1) is not present in the corresponding term of (A.2), because although the turbulent flux of ψ is nearly constant across the ventilation layer, it drops from $(F_\psi)_B$ to zero across the entrainment layer, so that its average value for the entrainment layer is *half* of $(F_\psi)_B$. The second term of (A.2) represents the transport of variance into the entrainment layer by triple correlations. The fourth term represents the rate at which scalar variance is provided to the newly entrained air. The fifth term represents variance production due to fluctuations of S_ψ in the entrainment layer. There is a close analogy between (A.2) and (3.5).

Recall from Section 2 that the plume-scale variance of ψ is given by

$$\overline{\psi'^2} = \sigma(1-\sigma)\,(\psi_u - \psi_d)^2 \tag{A.3}$$

and that the plume-scale variance transport can be written as

$$\rho\overline{w'\psi'\psi'} = M_c(1-2\sigma)\,(\psi_u - \psi_d)^2 \tag{A.4}$$

For the LES results shown in Fig. 3, σ is so close to 1/2 at both levels S and B that the only safe conclusion is that variance production and dissipation are closely balanced in both the entrainment and ventilation layers. If $(\rho\overline{w'\psi'\psi'})_S = (\rho\overline{w'\psi'\psi'})_B$, the variance flux passes through the interior of the PBL without convergence or divergence.

These ideas may have some relevance to mesoscale cellular convection, if our mass flux model can be applied to the mesoscale convective circulations. For the case of open cellular convection, surface heating is believed to dominate (e.g., Arakawa, 1975) and observations suggest that $\sigma_B << 1$. According to our model, the entrainment layer with $\sigma_B << 1$ is dissipating more variance than it produces. This seems physically plausible for open cells. For closed cellular convection, cloud-top cooling is believed to be dominant (Arakawa, 1975) and observations suggest that $\sigma \approx 1$. According to our model, the entrainment layer with $\sigma \approx 1$ is producing more variance than it is dissipating. This seems physically plausible for closed cells.

We now define nondimensional measures of the dissipation rates, denoted by k_V and k_E, respectively:

$$2\int_{z_{S-}}^{z_S} \varepsilon_\psi \rho dz \equiv k_V V \sigma_S (1-\sigma_S)\,(\psi_u - \psi_d)_S^2 \tag{A.5}$$

$$2\int_{z_B}^{z_{B+}} \varepsilon_\psi \rho dz \equiv k_E E \sigma_B (1-\sigma_B)\,(\psi_u - \psi_d)_B^2 \tag{A.6}$$

Rapid variance dissipation rates in the ventilation and entrainment layers correspond to large values of k_V and k_E, respectively. Note from (A.3) that the rhs of (A.5-6) are proportional to $\overline{\psi^2}$ for the ventilation and entrainment layers, respectively. The definitions of k_V and k_E, given by (A.5-6), are motivated by the idea that the rates of variance dissipation in the ventilation and entrainment layers should be related to the actual values of the variances at the edges of those layers.

Using the results of Section 3 with (A.4-5), we rewrite (A.1) as

$$\sigma_S = \frac{2-\chi_V}{k_V \chi_V^2 + 2(1-\chi_V)} \tag{A.7}$$

All reference to ψ has dropped out of (A.7), indicating that k_V is independent of species.

Now turning to the entrainment layer, we can use (A.3), (A.4), and (A.6) with the results of Section 3 to rewrite (A.2) as

$$\begin{aligned}(\psi_u - \psi_d)_B^2 \chi_E M_{c,B} \{-k_E(1-\sigma_B) + \chi_E^{-1}[\chi_E^{-1}\sigma_B + (1-2\sigma_B)] - (1-\sigma_B)\} \\ + (\psi_u - \psi_d)_B \frac{M_{c,B}}{E}\int_{z_b}^{z_{B+}} \overline{S_\psi} dz + \int_{z_B}^{z_{B+}} \overline{\psi' S'}_\psi dz = 0\end{aligned} \tag{A.8}$$

We require that (A.8) hold for all species, including those for which S_ψ is zero. It follows that

$$\sigma_B = \frac{k_E \chi_E^2 - \chi_E + \chi_E^2}{1 + k_E \chi_E^2 - 2\chi_E + \chi_E^2} \tag{A.9}$$

Again, all reference to υ has dropped out, showing that k_E is independent of species.

Since (A.8 - 9) must apply for all species, including those for which S_ψ is *not* zero, we conclude that

$$2\int_{z_B}^{z_{B+}} \overline{\psi' S'_\psi} dz = -\frac{(F_\psi)_B}{E_B} \int_{z_B}^{z_{B+}} \overline{S_\psi} dz \tag{A.10}$$

Using (A.10), we can determine the rate at which fluctuations of S_ψ in the entrainment layer generate fluctuations of ψ there.

Using the results derived above, we can show that the ratio of dissipation to production, for the ventilation layer, satisfies

$$\frac{2\int_{z_{S-}}^{z_S} \varepsilon_\psi \rho dz}{2(F_\psi)_S(\overline{\psi}_{S-} - \overline{\psi}_S)} = 1 - \left[\frac{\chi_V(1-2\sigma_S)}{2(1-\sigma_S)}\right] \tag{A.11}$$

The corresponding ratio for the entrainment layer is

$$\frac{2\int_{z_B}^{z_{B+}} \varepsilon_\psi \rho dz}{-(F_\psi)_B \Delta\psi - E(\overline{\psi'^2})_B + 2\int_{z_B}^{z_{B+}} \overline{\psi' S'_\psi} dz} = 1 + \left[\frac{\chi_E(1-2\sigma_B)}{\sigma_B - \chi_E^2(1-\sigma_B)}\right] \tag{A.12}$$

Note from (A.11) and (A.12) that, since χ_V and χ_E are both on the order of 10^{-2}, and if σ is close to 1/2, dissipation and production must nearly balance in the ventilation and entrainment layers. Such near balances are observed (e.g., Caughey and Palmer, 1979), and have been predicted through LES (see for example Fig. 7 of Moeng and Wyngaard, 1989).

Now combine (A.7) with (3.4), to obtain a quadratic equation for χ_V. The solutions, which are both physically relevant, are given by

$$\chi_V = \frac{2G_V + k_V \pm \sqrt{k_V^2 - 8G_V^2 k_V + 4G_V^2}}{2k_V G_V} \tag{A.13}$$

Using (3.4), we can obtain the corresponding solutions for σ_S:

$$\sigma_S = \frac{(k_V - 2G_V) \mp \sqrt{k_V^2 - 8G_V^2 k_V + 4G_V^2}}{2k_V} \tag{A.14}$$

The condition that the discriminant in (A.13) and (A.14) be non-negative implies that k_V must be sufficiently large, for a given G_V. The discriminant vanishes for

$$k_V = (k_V)_{\min} = 4G_V^2 + 2G_V\sqrt{4G_V^2 - 1} \tag{A.15}$$

For convenience, let

$$r_V = \frac{k_V}{(k_V)_{\min}} \tag{A.16}$$

FIGURE A.1: Plots of χ_V and σ_S against k_V and r_V, as given by (A.13) and (A.15). Panels (a) and (b) are for the choice of the plus sign on the discriminant, and panels (c) and (d) are for the choice of the minus sign.

Fig.A.1 shows plots of χ_V and σ_S against G_V and r_V. Both solutions are shown. Note that, for sufficiently large G_V, σ_S depends only on r_V. For $G_V >> 1$, the following approximate relations hold:

$$(k_V)_{\min} \approx 8G_V^2 \tag{A.17}$$

$$\sigma_S \approx \frac{r_V \mp \sqrt{r_V(r_V-1)}}{2r_V} \tag{A.18}$$

$$\chi_V \approx \frac{r_V \pm \sqrt{r_V(r_V-1)}}{2r_V G_V} \tag{A.19}$$

From (A.18), we conclude that

$$\frac{1}{2} \le \sigma \le 1 \text{ with the choice of the minus, or}$$

$$0 \le \sigma \le \frac{1}{2} \text{ with the choice of the plus.} \tag{A.20}$$

By substituting (A.17 - 19) back into (A.1) and (A.5), we can show that the approximation $G_V >> 1$, on which (A.17-19) are based, corresponds to a balance between dissipation and production.

A parallel analysis for the entrainment layer leads to

$$\chi_E = \frac{2G_E + k_E + 1 \pm k_E^2\sqrt{k_E^2 + (2-4G_E^2)\,k_E + 1}}{2G_E(1+k_E)} \tag{A.21}$$

and

$$\sigma_B = \frac{2G_E + k_E + 1 \pm k_E^2\sqrt{k_E^2 + (2-4G_E^2)\,k_E + 1}}{2(1+k_E)} \tag{A.22}$$

Again, both solutions are physically relevant. The condition that the discriminant in (A.21 - 22) be non-negative implies that k_E must be sufficiently large. The discriminant vanishes for

$$k_E = (k_E)_{\min} = 2G_E^2 - 1 + 2G_E\sqrt{G_E^2 - 1} \tag{A.23}$$

Let

$$r_E = \frac{k_E}{(k_E)_{\min}} \tag{A.24}$$

FIGURE A.2: Plots of χ_E and σ_B against k_E and r_E, as given by (A.21) and (A.22). Panels (a) and (b) are for the choice of the plus sign on the discriminant, and panels (c) and (d) are for the choice of the minus sign.

Fig.A.2 shows plots of χ_E and σ_B against G_E and r_E. The situation is very similar to that found for the ventilation layer. For sufficiently large G_E, σ_B appears to depend only on r_E. We can demonstrate that, for $G_E >> 1$, the following approximate relations hold:

$$(k_E)_{\min} \approx 4G_E^2 \tag{A.25}$$

$$\sigma_B \approx \frac{r_E \pm \sqrt{r_E(r_E-1)}}{2r_E} \tag{A.26}$$

$$\chi_E \approx \frac{r_E \pm \sqrt{r_E(r_E-1)}}{2r_E G_E} \tag{A.27}$$

FIGURE A.3: Plot of σ_B as a function of r_E, or of σ_S, or of both, as a function of r_V.

Note that (A.26 - 27) closely parallel (A.19). Fig. A.3 shows σ_B as a function of r_E, and/or σ_S as a function of r_V, as given by (A.18) and/or (A.26).

From (A.26), we can conclude that

$$\frac{1}{2} \leq \sigma \leq 1 \text{ with the choice of the plus, and}$$

$$0 \leq \sigma \leq \frac{1}{2} \text{ with the choice of the minus.} \tag{A.28}$$

The main results of this Appendix are (A.18-19) and (A.26-27). Our expressions for σ_S and σ_B automatically satisfy $0 < \sigma < 1$. If r_V and r_E were known, we could find σ_S, σ_B, and χ_E and χ_E. The values of $M_{c,S}$ and $M_{c,B}$ would follow immediately from (3.4) and (3.9), respectively. The interior value of M_c could be obtained by an approach analogous to that used in Section 4. We would thus be in a position to allow σ to vary linearly with height, and M_c to vary quadratically. This would allow improved agreement with the LES results presented in Fig. 2.3. Pursuit of this generalization of our model is left to the future.

B. A Method to Predict the Vertically Integrated Turbulence Kinetic Energy

The vertically integrated conservation law for the TKE can be written as

$$g^{-1}\delta p_M \frac{\partial e_M}{\partial t} + E e_M = B + S - D \tag{B.1}$$

Here B, S, and D represent production by buoyancy, production by shear, and dissipation, respectively, and δp_M is the pressure-thickness of the PBL.

The vertically integrated dissipation rate and the vertically averaged TKE are assumed to be related by

$$D = \rho_M (e_M / a_1)^{3/2} \tag{B.2}$$

where ρ_M is the vertically averaged PBL density, and $a_1 \cong 0.163$ is a dimensionless constant.

The buoyancy production integral, B, is of the form

$$B = \kappa \int_{p_{B+}}^{p_{S-}} \frac{F_{Sv}}{p} dp \tag{B.3}$$

where κ is Poisson's constant. This integral can be evaluated using the methods of Randall (1984).

The shear production integral, S, is of the form

$$S = \int_{p_{B+}}^{p_{S-}} \mathrm{F_V} \bullet \frac{\partial}{\partial p} \overline{\mathrm{V}}\, dp \tag{B.4}$$

We divide this integral into three parts: shear production in the surface layer, in the interior of the PBL, and in the entrainment layer. The surface layer shear production is approximately given by

$$\int_{p_S}^{p_{S-}} \mathrm{F_V} \bullet \frac{\partial}{\partial p}\overline{\mathrm{V}}\, dp \;=\; (\mathrm{F_V})_S \bullet \overline{\mathrm{V}}_S \;=\; \left|(\mathrm{F_V})_S\right| \bullet \left|\overline{\mathrm{V}}_S\right| \tag{B.5}$$

Here the second equality follows from the assumption that the surface stress in parallel to the surface wind.

The interior shear production can be evaluated by straightforward methods once the profiles of the stress and the wind are known.

Finally, the entrainment layer shear production is approximately given by

$$\int_{p_{B+}}^{p_B} \mathrm{F_V} \bullet \frac{\partial}{\partial p}\overline{\mathrm{V}}\, dp \;=\; \frac{1}{2}\left|(\mathrm{F_V})_B\right| \bullet \left|\Delta\overline{\mathrm{V}}\right| \;=\; \frac{1}{2}E\left|\Delta\overline{\mathrm{V}}\right|^2 \tag{B.6}$$

In (B.6), the factor of 1/2 arises because $\boldsymbol{F_V}$ decreases from $(\boldsymbol{F_V})_B$ to zero across the entrainment layer, so that its average value inside the entrainment layer is $(\boldsymbol{F_V})_B / 2$. The second equality comes from applying (3.5) to the momentum budget of the entrainment layer.

C. Motivation for (5.8 - 9)

Dropping the time-dependence of (5.3) and simplifying, we obtain

$$\frac{(1-2\sigma)}{M_c}\frac{\partial F_\psi}{\partial p} - \frac{\sigma(1-\sigma)}{g\tau_{dis}M_c^2}F_\psi = -\frac{\partial\overline{\psi}}{\partial p} \tag{C.1}$$

This is basically the same as (5.7), except that we have not introduced δp_*. We solve (C.1) as a first-order ordinary differential equation for F_ψ, assuming constant coefficients and a constant value of $\partial\overline{\psi}/\partial p$. The solution is

$$F_\psi = \frac{g\tau_{dis}M_c^2}{\sigma(1-\sigma)}\frac{\partial\overline{\psi}}{\partial p} + Aexp\left[\frac{\sigma(1-\sigma)\ (p-p_B)}{g\tau_{dis}M_c(1-2\sigma)}\right] \tag{C.2}$$

where A is the constant of integration. Notice that the quantity $(1-2\sigma)$ appears in the denominator of the argument of the exponential. As σ passes through 1/2, the argument of the exponential diverges to plus and minus infinity -- unacceptable behavior. We cannot solve this problem by choosing $A = 0$, because then F_ψ would be independent of height and could not satisfy its boundary conditions at the surface and the PBL top.

Our interpretation is that τ_{dis} must depend on σ. This is acceptable, since the σ dependence of τ_{dis} is not known a priori. *We choose the σ dependence of τ_{dis} in such a way that F_ψ varies continuously with σ.*

This we can do by taking τ_{dis} proportional to $(1-2\sigma)$; that is,

$$\hat{\tau} \equiv (1-2\sigma)\,\tau_{dis}, \tag{C.3a}$$

where $\hat{\tau}$ is a constant (i.e., independent of σ). Then (C.2) is replaced by

$$F_\psi = \frac{M_c\delta p_*}{(1-2\sigma)}\frac{\partial\overline{\psi}}{\partial p} + Aexp\left[\frac{(p-p_B)}{\delta p_*}\right], \tag{C.4a}$$

where

$$\delta p_* = \frac{g\hat{\tau}M_c}{\sigma(1-\sigma)}. \tag{C.5a}$$

Inspection of (C.4a) shows that the flux does indeed vary continuously with σ. This approach is unacceptable, however, because (C.3a) will inevitably give negative and hence physically impossible values of τ_{dis} for some values of σ.

We can ensure nonnegative τ_{dis} and also make F_ψ vary continuously with σ by choosing

$$\hat{\tau} \equiv (1-2\sigma)^2 \tau_{dis}, \tag{C.3b}$$

with $\hat{\tau}$ positive and independent of σ. The solution of (C.1) is then

$$F_\psi = M_c\left[\frac{\delta p_*}{(1-2\sigma)}\frac{\partial\overline{\psi}}{\partial p} + A exp\left(\frac{p-p_B}{\delta p_*}\right)\right]. \tag{C.4b}$$

where

$$\delta p_* \equiv \frac{gM_c\hat{\tau}}{\sigma(1-\sigma)\ (1-2\sigma)}. \tag{C.5b}$$

We have used (C.3b) and (C.5b) in section (5).

This is the line of reasoning that led us to adopt (4.5.9), with $\hat{\tau}$ independent of σ.

An implication of (5.9) is that τ_{dis} becomes infinite (that is, the variance dissipation rate goes to zero) for $\sigma = 1/2$. Of course, this is at best an idealization of how nature works. From the LES results, we estimate that $(1-2\sigma) \sim 10^{-1}$ or 10^{-2}, which, together with the results shown in Fig.2.6, suggests that for this particular case $\hat{\tau}$ is on the order of 1 - 10 sec.

Why should τ_{dis} increase as σ approaches 1/2? A possible physical interpretation is that the largest (absolute) convective vertical velocities increase as σ departs from 1/2.

For example, if $\sigma \ll 1$, the *updraft* vertical velocities must be relatively vigorous, implying strong lateral shears and suggesting strong lateral mixing and variance dissipation. Similarly, for σ close to unity, the *downdraft* vertical velocities must be relatively vigorous. The intensity of the individual drafts is minimized for $\sigma = 1/2$, suggesting that the dissipation rate is minimized then too.

We must also ask why $\hat{\tau}$ is so short. From (5.2) and (5.9) the dissipation rate can be written as

$$\varepsilon_{\psi} = (1-2\sigma)^2 \left(\frac{\overline{\psi'^2}}{\hat{\tau}} \right). \tag{C.6}$$

We can interpret $\overline{\psi'^2}/\hat{\tau}$ as the intense *local* dissipation rate in those portions of the convective circulations where dissipation actually occurs and $(1-2\sigma)^2$ as the fraction of the domain within which dissipation is localized. The volume-averaged dissipation rate is then given by (C.6).

D. Calculation of Thermodynamic Variables From the Tethered Balloon Data

From Eq. (43) of Bolton (1980), we have

$$\theta_E = T\left(\frac{1000}{p}\right)^{0.2854\,(1-0.28\,q_v)} \times exp\left[\left(\frac{3.376}{T_L} - 0.00254\right) q_v \times 10^3 \times (1 + 0.81 \times q_v)\right] \quad \text{(D.1)}$$

where T_L is the temperature which a parcel would attain if lifted adiabatically to its condensation level and is given by

$$T_L = \frac{2840}{3.5\ lnT - lne - 4.805} + 55\ \text{(K)}, \quad \text{(D.2)}$$

The accuracy of (A.1) is about 0.3 K.

The vapor mixing ratio satisfies

$$q_v = \left[q_s(T_w) - \frac{c_{pd}}{L_w}(T - T_w)\right] / \left[1 + \frac{c_{pd}}{L_w} \times 0.887\,(T - T_w)\right],$$

$$q_s(T_w) = 0.622 \frac{e_s(T_w)}{p - e_s(T_w)},$$

$$e_s(T_w) = 6.112\ exp\left[\frac{17.67\,(T_w - 273.15)}{T_w - 29.65}\right], \quad \text{(D.3)}$$

where T_W (in K) is the wet-bulb temperature. q_v and q_s are in g g^{-1}, and e_s is in mb. The liquid water mixing ratio is

$$q_l \approx \frac{R_m T \rho_l}{p}, \quad \text{(D.4)}$$

where ρ_l is the density of liquid water. The total mixing ratio is, therefore

$$q(T) = q_v(T) + q_l(T) \tag{D.5}$$

The constants used in these calculations are as follows:

$$\begin{aligned} &c_{pm} \approx c_{pd}(p,T)\ (1+0.887\ q_v), c_{pd} = 1005.7\ J\ kg^{-1}\ K^{-1}, \\ &R_M \approx R_d(1+0.608\ q_v), \qquad R_d = 287.04\ J\ kg^{-1}\ K^{-1}, \\ &L_w \approx [2.501 - 0.00237\,(T-273.15)] \times 10^6 J\ kg^{-1}. \end{aligned} \tag{D.6}$$

Fluctuations of the liquid water static energy are related to those of the equivalent potential temperature by

$$dh \equiv \frac{c_p T_v}{\theta_e} d\theta_e. \tag{D.7}$$

E. A numerical method for choosing the boundaries Of the ventilation and entrainment layers

The results obtained in this paper depend very much on the boundaries we defined for the ventilation layer and entrainment layer, namely levels S-, S, B and B+. We adopted the levels defined in RSM for the LES data, which were based on the subgrid turbulent flux and mean structure of the total moisture.

As discussed in Section 2, the mixing fraction defined by (3.1) and (3.12) implies that the parcels have the mean properties of the "boundaries" before mixing ($\chi = 0$ or $\chi = 1$). This requires that most, if not all, of the parcels at a boundary have the mean properties of that boundary, i.e., statistically, the pdf has maxima at $\chi = 0$ (for boundaries S and B) and at $\chi = 1$ (for boundaries S- and B+). At the same time, the narrower the range of χ is, the closer the properties of the parcels are to the mean properties at that level, or the more independent the properties at level $\chi = 0$ are from those at level $\chi = 1$, and the better (3.1) and (3.12) apply. Therefore, the pdf of $-\chi$ can represent two things: First, the value of the pdf at $\chi = 0$ (or $\chi = 1$) represents what percentage of the parcels at that boundary have the mean property of the level; second, the diversity of χ, or the width of the pdf, represents how independent the properties at that boundary are from the other boundary. For example, if χ is very diverse, or the profile of the pdf is very wide, some parcels at the boundary (say level S or level B) must have properties very close to the mean state at the other boundary (say level S- or level B+, respectively). The two boundaries are then not two independent pools, providing two kinds of parcels used for mixing. This would conflict with our assumption for (3.1) and (3.12).

To see whether the boundaries defined by RSM are proper for our purpose, we calculated various pdfs on the boundaries by adjusting the depths of the ventilation layer and entrainment layer in an analysis of the LES results. In the present paper we have used together six grid levels, including the boundaries, with four levels in between S- and

S, and another four levels in between B and B+. For the ventilation layer, since S- is fixed, we adjusted level S so that the grid levels in between S- and S were two, three and five. Similarly, for the entrainment layer, since level B is below the cloud top, where the convective mixing is strong, we simply fixed level B, and adjusted level B+ so that the grid levels in between B and B+ were two, three and five. The results are shown in Figs. E1 and E2, respectively.

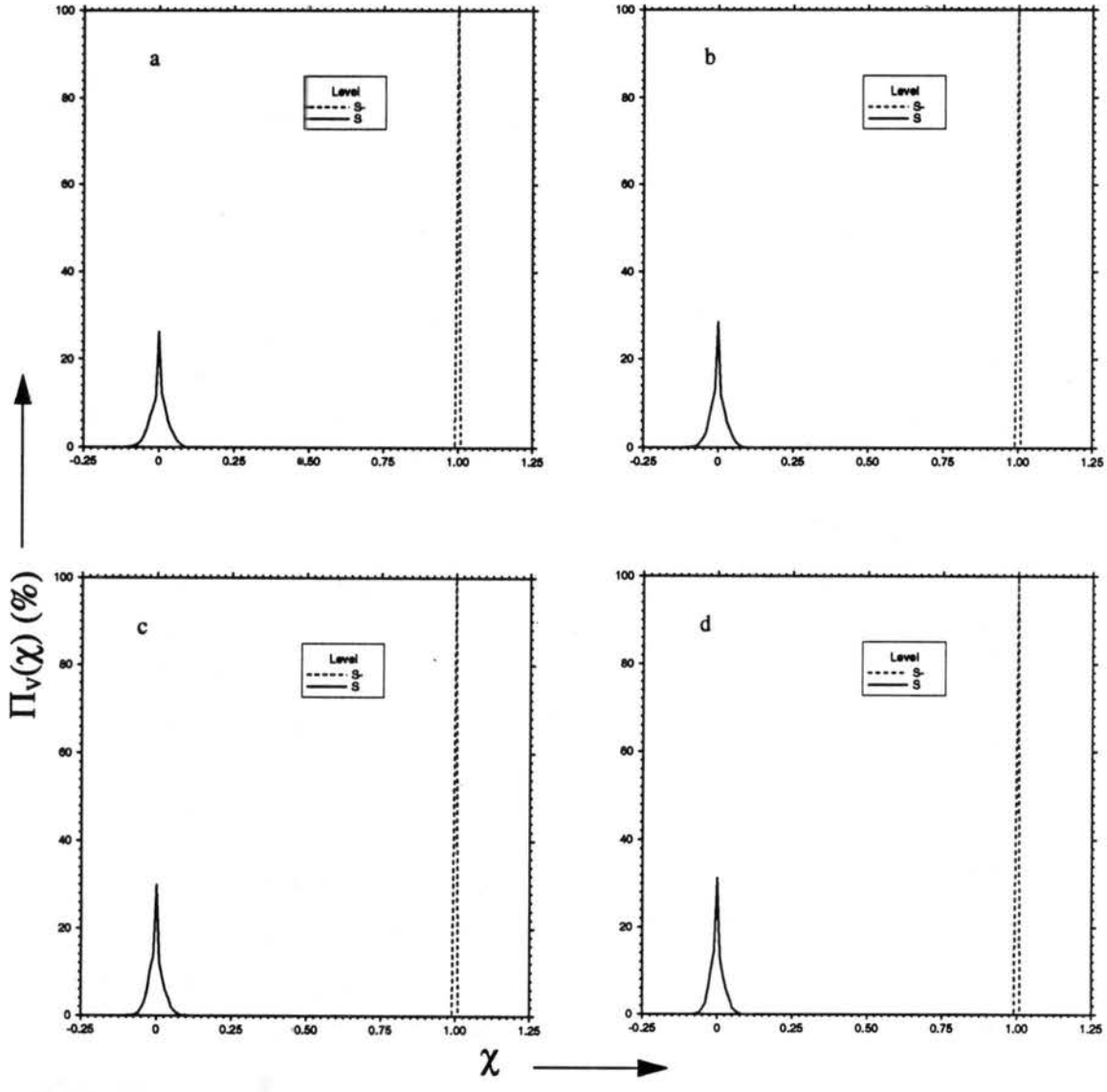

FIGURE E.1: The pdf at level S and S-.

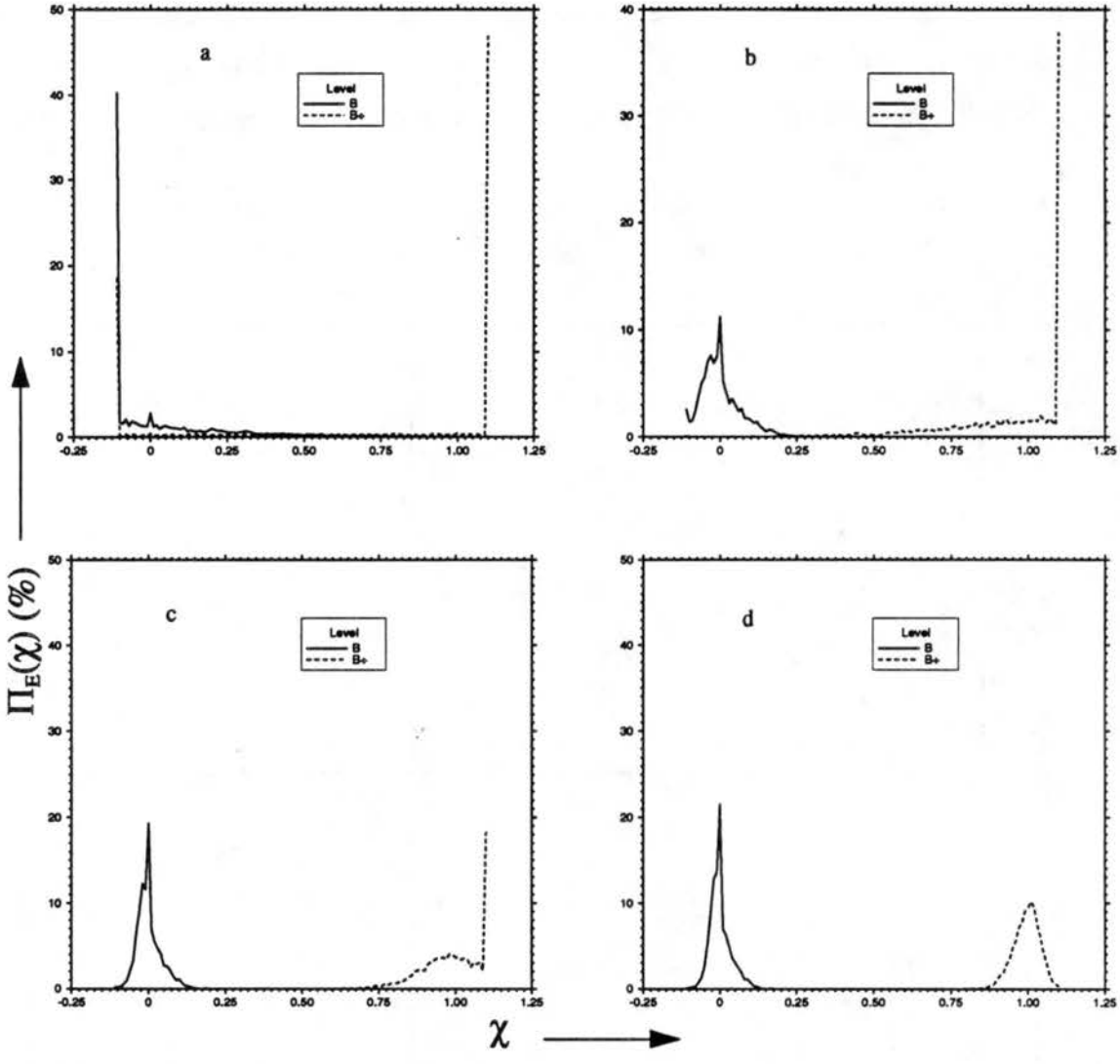

FIGURE E.2: The pdf at level B and B+.

The pdf at level S- is simply a constant of 100 because it is a homogeneous surface, as is shown in Fig. E.1. The pdf at level S does not change much from Fig. E.1a to d. This is because the gradient of the mean q_t profile is sharp only in a very shallow layer below the lowest S level defined in Fig. E.1 (namely model level 4, which is 31.25m above S-). The levels above that sharp gradient layer are almost well mixed. The pdf are all narrow and sharp. Therefore, any level S shown in Fig. E.1 is proper for our purpose.

The pdf at the boundaries of the entrainment layer changes a lot from Fig.E.2a to d. It is obvious that the choices for level B+ in Figs.E.2 a and b are not proper. The level B+ used in Fig.E.2c, which is the one we used in the present paper, is acceptable because both pdfs have peaks at $\chi = 0$ and $\chi = 1$ respectively, and the two pdf-profiles are far apart without overlapping, or they are relatively narrow. The best one is that in Fig. E.2d, in which the pdfs are all very sharp, and centered at $\chi = 0$ and $\chi = 1$, respectively.

The above analysis is only based on the pdf, or the assumption required by (3.1) and (3.12). Some other factors could be taken into account, such as the profiles of the subgrid turbulent fluxes and the reasonableness of the thicknesses of the entrainment and ventilation layers. The pdf analysis gives good guidance for the choice of levels S, B and B+, however.

F. An example to calculate α

An example of the calculation of $Q(Z)$, $W(Z)$, $S(Z)$ and $U(Z)$ and α by *Mathematica* is shown below. *ckf* represents $(c_b K_H)/F_0$, *ax* represents $F(n)/F_0$.

```
Clear [a,n,gs,pr,q,b1,b2,ar,dtdz,PP,rc,fQ,Q,QQ,
       fW,W,WW,fS,S,S1,ds1,ds2,eqn,a3,b3,c3,d3,
       SS,fU,U,U1,du1,du2,a4,b4,c4,d4,
       UU,CA,CB,CC,CD,x1,x2,alfa,adf,ckf,ax]

ckf=0

ax=1

n=5

pr=1;

q=0;

b1=0;

b2=0;

adf=ax (1+n)^(2+1/n) / n;

dtdz[z_]=-(adf z (1-z^n) / (n+1)-ckf);


PP[z_]=-(2 z^4 - 5 z^3 + 3 z^2)/48;


rc=-(2880*(1 + n)*(4 + n)*(5 + n)*(6 + n))/
 ((1080*ckf - 310*adf*n + 1746*ckf*n - 75*adf*n^2 +
 801*ckf*n^2 - 5*adf*n^3 + 144*ckf*n^3 +
```

```
 9*ckf*n^4));


fQ[z_]=-(rc PP[z] (-dtdz[z] + q ) + 1);

Integrate[%,z];

Integrate[%,z];

Simplify[%];

Q[z_]=% + b1;

QQ[z_,b1_]=Q[z];


fW[z_]=-rc D[PP[z],z];

Integrate[%,z];

Integrate[%,z];

W[z_]=% + b2;

WW[z_,b2_]=W[z];


fS[z_]=-2 rc W[z] + rc^2 (PP[z] D[PP[z],{z,3}] - D[PP[z],z]
D[PP[z],{z,2}])/pr;

Simplify[%];

Integrate[%,z];

Integrate[%,z];

Integrate[%,z];

Integrate[%,z];

Simplify[%];

S[z_]=%;
```

F. An example to calculate

```
S1[z_,a3_,b3_,c3_,d3_]=S[z] + a3 z^3 + b3 z^2 + c3 z + d3;

ds1[z_]=D[S1[z,a3,b3,c3,d3],z];

ds2[z_]=D[S1[z,a3,b3,c3,d3],{z,2}];

eqn = { S1[0,a3,b3,c3,d3] == 0, S1[1,a3,b3,c3,d3] == 0,

     ds1[0] == 0, ds2[1] == 0 };

Solve[eqn,{a3,b3,c3,d3}];


xxxx = Simplify[%];

a3 = xxxx[[1,1,2]];

b3 = xxxx[[1,2,2]];

c3 = xxxx[[1,3,2]];

d3 = xxxx[[1,4,2]];

SS[z_]=S1[z,a3,b3,c3,d3];


fU[z_]=-rc Q[z] -2 rc D[PP[z],{z,2}];

Simplify[%];

Integrate[%,z];

Integrate[%,z];

Integrate[%,z];

Integrate[%,z];

Simplify[%];

U[z_]=%;

U1[z_,a4_,b4_,c4_,d4_]=U[z] + a4 z^3 + b4 z^2 + c4 z + d4;
```

```
du1[z_]=D[U1[z,a4,b4,c4,d4],z];

du2[z_]=D[U1[z,a4,b4,c4,d4],{z,2}];

eqn = { U1[0,a4,b4,c4,d4] == 0, U1[1,a4,b4,c4,d4] == 0,

        du1[0] == 0, du2[1] == 0 };

Solve[eqn,{a4,b4,c4,d4}];


xxxx = Simplify[%];

a4 = xxxx[[1,1,2]];

b4 = xxxx[[1,2,2]];

c4 = xxxx[[1,3,2]];

d4 = xxxx[[1,4,2]];


UU[z_]=U1[z,a4,b4,c4,d4];


mfun[z_]={QQ[z,b1],WW[z,b2],SS[z],UU[z]}


CA=1/rc;

Simplify[%];

x1[z_]=UU[z] (-dtdz[z] + q) + QQ[z,b1];

CB= - Integrate[x1[z], {z,0,1}];

Simplify[%];

CC=rc^2 Integrate[PP[z]^2, {z,0,1}];

Simplify[%];
```

F. An example to calculate

```
x2[z_]=rc PP[z] D[QQ[z,b1],z] - (SS[z] (-dtdz[z] + q) + 2
WW[z,b2]);

CD=Integrate[x2[z], {z,0,1}];

Simplify[%];

mcoef={CA,CB,CC,CD}

N[%]


alfa=CD/Sqrt[CB CC];

mcons={rc,alfa}

N[%]
```

G. The profile of the filter used to select mesoscale contributions

The (2N+1)-point running average gives the filter function as (Hamming, 1983)

$$H(n) = \frac{\sin\left[2\pi n\left(N+1/2\right)/N_0\right]}{(2N+1)\sin\left(\pi n/N_0\right)} \tag{A.8}$$

where N_0 is the total horizontal grid points, n is the wave number defined as $n = L/\lambda$, and L is the domain size, λ is the wave length. For a 19-points running average, $N = 9$.

The profile of $H(n)$ is given in Fig. G.1. Aliasing error exists in this filter. The

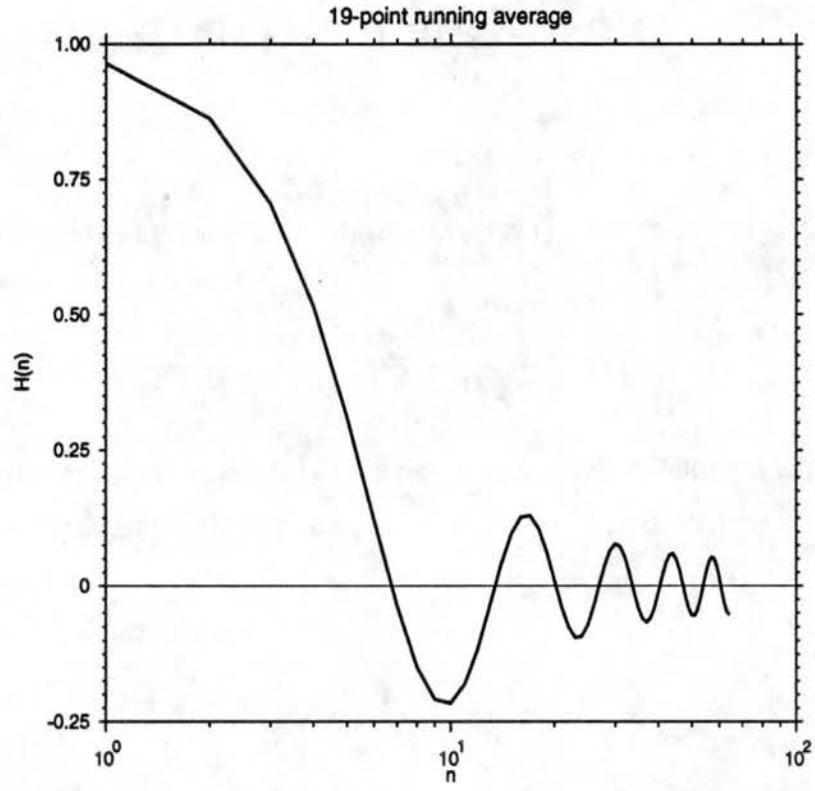

FIGURE G.1: The profile of the filter used to select the mesoscale contribution.

amplitudes of waves with wave number larger than 6 are greatly damped.